In-plane thermo-mechanical behavior of curved steel beams with constant curvature

Jean Marcos Teixeira de Souza

Dissertation presented to the Superior School of Technology and Management of the Polytechnic Institute of Bragança as a requirement for the Master of Science degree in Construction Engineering, in the scope of double degree with the Federal Technological University of Paraná.

Supervised by:

Prof. Luís Manuel Ribeiro de Mesquita

Prof. Marina Rocha Pinto Portela Nunes

Bragança

2020

Comportamento termo-mecânico de vigas de aço curvas com curvatura constante

Jean Marcos Teixeira de Souza

Dissertação apresentada à Escola Superior de Tecnologia e de Gestão do Instituto Politécnico de Bragança para obtenção do Grau de Mestre em Engenharia da Construção, no âmbito da dupla diplomação com a Universidade Tecnológica Federal do Paraná.

Trabalho orientado por:

Prof. Luís Manuel Ribeiro de Mesquita

Prof. Marina Rocha Pinto Portela Nunes

Bragança

2020

Acknowledgements

First of all, I would like to thank my family, my father Alcione, my mother Matilde and my sister Paola, for always supporting me during the long academic journey I have been in for the last few years, and for teaching me to persevere and believe in myself even when it might seem too hard to cope with.

My most honest thank you to my supervisor Dr. Luís Mesquita, for the dedication in tutoring and guiding me through this dissertation, and to my co-supervisor Dr. Marina Rocha for the support and attention given at moments of need.

To the Superior School of Technology and Management of the Polytechnic Institute of Bragança, for the structural and material support necessary for this investigation work. A special acknowledgement to the Federal Technological University of Paraná for the opportunity of studying and researching at an European institution via the double degree program.

To the Structures and Strength of Materials Laboratory staff, specially Eng. Luísa Barreira, for the help conducting this research and the availability to attend the needs of this project, as well as my lab work colleagues, specially my friend Paulo Bortolozzo, who helped me in so many ways in this thesis, and Alexandre Fernandes for always helping when I needed the most.

To my dear friends Marianne, Tatiane, Letícia, André and Ingrid, for the emotional support and amazing friendship during this time outside of our home country. A special thank you for my incredible friend Catia Alexandra, for encouraging and supporting my work, and making me feel at home and safe even with my family far away. And, to every person involved in this thesis who were not mentioned above, thank you.

Abstract

Curved steel beams and arches are structures originated from mechanical processes of curving straight members, usually I or H profiles, in order to get a desired geometry to attend aesthetics or project requirements. This type of elements behave differently when compared to regular straight members, with specific instability modes and different responses to various types of loading conditions. For these reasons, such structural members may react distinctively when submitted to fire conditions or elevated temperatures. This paper studies the stability and collapse load of steel curved beams and arches, curved by their major axes, through numerical Finite Element analyses for in-plane buckling at natural and elevated temperatures, simulating a fire event. Firstly, it was developed an analytical method to compute the internal forces based in energy methods for pin-supported arches under two point loads applied at one fourth of the length measured from the supports. Subsequently, linear elastic and nonlinear elasto-plastic buckling and ultimate load analyses were performed at both natural and elevated temperature conditions with the *ANSYS Mechanical APDL* Finite Element software package, for a variety of span and rise-to-span ratio values, support conditions and steel classes. These results were then compared to critical buckling load formulations found in the literature and to simplified methods presented in Eurocode 3 for elements under bending moments and axial forces. It is seen that support conditions play an important role in the thermo-mechanical response of steel arches, where fixed supports yielded much higher critical load results for every geometry and temperature case. However, even though superior steel classes provide higher resistant loads, regarding responses to thermal loads it was found that support condition is also more significant in

this case. Moreover, the standard Eurocode 3 methodology for straight members was compared to the numerical results, which showed a good fit for lower bound loads except for higher slendernesses under elevated temperatures, where numerical solutions yielded result points under the standard resistance curves. Also, an analytical and experimental study on the cold-curving process of straight steel beams into arches using point loads was conducted, aiming to analytically define a post-curving residual stress profile and investigate the influence of elastic *springback* in the final shape of an arch.
Keywords: Curved Beams, Arches, Steel, Temperature, Finite Element Method

Resumo

Vigas curvas e arcos de aço são estruturas originadas de processos mecânicos de curvamento de membros retos em curvos, geralmente perfis I ou H, a fim de obter a geometria desejada para atender a requisitos estéticos ou de projeto. Esse tipo de elemento comporta-se de maneira diferente quando comparado a membros retos regulares, com modos de instabilidade específicos e respostas diferentes a várias condições de carregamento. Por esses motivos, esses membros estruturais podem também reagir diferentemente quando submetidos a condições de incêndio ou temperaturas elevadas. Este trabalho estuda a estabilidade e a carga de colapso de vigas e arcos curvos de aço, curvados em seus eixos de maior resistência, através de análises numéricas de elementos finitos para encurvadura no plano à temperaturas ambiente e elevadas, simulando um evento de incêndio. Primeiramente, foi desenvolvido um método analítico para calcular as forças internas baseadas em métodos de energia para arcos bi-rotulados sob cargas pontuais aplicadas em um quarto do comprimento medido a partir dos suportes. Posteriormente, foram realizadas análises de encurvadura linear elástica e de carga última não-linear elasto-plástica em condições de temperatura naturais e elevada com o pacote de software *ANSYS Mechanical APDL* de elementos finitos, para uma variedade de valores de vão e relação altura-vão, condições de suporte e classes de aço. Esses resultados foram comparados com as formulações de carga crítica de encurvadura encontradas na literatura e com os métodos simplificados apresentados no Eurocódigo 3 para elementos submetidos a momentos fletores e forças axiais. Observa-se que as condições de suporte desempenham um papel importante na resposta termomecânica dos arcos de aço, onde

os suportes fixos produzem resultados de carga crítica muito mais altos para cada caso de geometria e temperatura. Ademais, embora classes de aço superiores proporcionem maior resistência mecânica, em relação às respostas à cargas térmicas, verificou-se que a condição de suporte também é mais significativa neste caso. Além disso, a metodologia padrão do Eurocódigo 3 para membros retos foi comparada com os resultados numéricos, que mostraram um bom ajuste com os limites impostos pela metodologia padrão, exceto para esbeltezas mais altas sob temperaturas elevadas, onde as soluções numéricas produziram resultados abaixo das curvas de resistência padrão. Também, um estudo experimental e analítico foi conduzido acerca do processo de curvamento a frio de vigas de aço retas em arcos utilizando cargas concentradas, com objetivo de definir analiticamente um perfil de tensões residuais pós-curvamento e investigar a influência do retorno elástico na forma final de um arco.
Palavras-chave: Vigas Curvas, Arcos, Aço, Temperatura, Método dos Elementos Finitos

Contents

List of Tables

List of Figures

List of Symbols

A	Cross-sectional area
A_f	Flange area
A_m	Surface area of a member per unit length
A_m/V	Section factor for unprotected steel members
A_v	Shear area
b_f	Flange width
c	Plastification height in the cross-section
c_a	Specific heat
d	Web height neglecting root radii
e_0	Equivalent impercetion maximum amplitude
E	Young's modulus of the material
E_a	Elastic modulus of steel at normal temperature
$E_{a,\theta}$	Slope of the linear elastic range for steel at elevated temperature
f	Arch rise
f_y	Steel yield strength
f_{imp}	Imperfection corrective factor
G	Transverse elastic modulus
h_w	Web height
$\dot{h}_{net,c}$	Convective heat flux
$\dot{h}_{net,r}$	Radiative heat flux

I_y	Strong axis moment of inertia of the cross section
I_z	Weak axis moment of inertia of the cross section
I_T	Uniform torsion modulus of the cross section
I_w	Warping constant of the cross section
i_y	Radius of gyrations in the strong axis
k_{sh}	Shadow effect coefficient
k_{yy}	Interaction coefficient for y axis bending moments
k_{zz}	Interaction coefficient for z axis bending moments
L	Arch horizontal span, linear length
L_b	Buckling length
M_{cr}	Critical lateral-torsional buckling bending moment
M_{Ed}	Design applied bending moment
M_{ep}	Elasto-plastic bending moment
$M_{y,Ed}$	Design applied bending moment in the strong axis
$M_{z,Ed}$	Design applied bending moment in the weak axis
$M_{N,Rd}$	Reduced bending moment resistance due to axial force
$M_{N,y,Rd}$	Reduced bending moment resistance in the strong axis due to axial force
$M_{pl,y,Rd}$	Design bending moment plastic resistance in the strong axis
N_{Ed}	Design applied axial force
N_{cr}	Buckling critical axial force
$N_{pl,Rd}$	Design axial force plastic resistant
R	Radius of curvature of an arch
R_t	Total radius of curvature considering the elastic springback
r	Rolling root radius
t_f	Flange thickness

t_w	Web thickness
U	Internal deformation potential energy
v	Poisson's ratio
V_{Ed}	Design applied shear force
$V_{pl,Rd}$	Design shear force plastic resistance
W_{el}	Elastic modulus of the cross-section
W_{pl}	Plastic modulus of the cross-section
α	Half internal angle of an arch
α_F	Internal angle of the loading point
γ_{M0}	Resistance of cross-section reduction factor
γ_{M1}	Resistance to instability reduction factor
δ_{max}	Maximum displacement sum
$\Delta l/l$	Thermal elongation
Δt	Time increment
σ	Stress
σ_{c1}	Compressive residual stresses in the flange
σ_{c2}	Compressive residual stresses in the web
σ_r	Residual stress maximum magnitude
σ_{rrf}	Rolling residual stress in the flange
σ_{rrw}	Rolling residual stress in the web
σ_t	Tensile residual stress
ε	Strain
ε_y	Yield strain
ε_u	Ultimate strain
$\varepsilon_{p,\theta}$	Proportional limit strain at temperature θ_a
$\varepsilon_{y,\theta}$	Yield strain at temperature θ_a
$\varepsilon_{t,\theta}$	Limit strain at temperature θ_a
$\varepsilon_{u,\theta}$	Ultimate strain at temperature θ_a
θ_a	Steel temperature

θ_g	Gas temperature in a fire event
λ	Nondimensional slenderness
λ_θ	Nondimensional slenderness at temperature θ_a
λ_a	Steel conductivity
ρ_a	Steel density
χ	Buckling reduction coefficient
ASCI	American Steel Construction Institute
EC3	Eurocode 3
EC3-1-1	Eurocode 3 part 1-1: General rules and rules for buildings
EC3-1-2	Eurocode 3 part 1-2: Structural fire design
EC3-2	Eurocode 3 part 2: Design of bridges
Dif. %	Percentage difference
ECCS	European Convention for Constructional Steelwork
FEM	Finite Element Method

Chapter 1

Introduction

1.1 Historical context

Siderurgy products like wrought and cast iron have been used for construction since the 17th century, in a diverse range of structures, [1]. Arch and truss bridges took advantage of the favorable mechanical properties of ferrous materials to overcome spans that other components could not with the available technology at the time.

Steel, although being known and used since ancient times, has started to be employed in construction only later, when mass production became popular in Europe and prices decreased to a point where steel replaced iron and has been one of the main construction materials ever since, [1].

In this aspect, curved steel in a variety of shapes is employed in a wide range of structures, providing an aesthetic appeal and sense os spaceness to the buildings where they are present, escaping from the traditional view of straight geometry. Curved steel beams and arches, besides the architectural benefits of the curved geometry, are performance-efficient when vertical in-plane loads are applied, because this structural element combines compression and bending moment resistance, utilizing the full potential of the cross section, [2].

For these reasons, curved steel beams become an interesting option for small- to

medium-span structures like bridges, roofs, convention and sports centers, and large building elements, for example. Figure 1.1 shows two examples of curved steel beams in long-span buildings.

(a) Auto dealership curved roof structure.

(b) Bellsouth Lindbergh Center, Atlanta - USA.

Figure 1.1: Examples of curved steel beams in buildings, [3].

However, a downside of steel as a building material is its behavior upon an increase in temperature, like when a steel member is submitted to fire. Under these conditions, it suffers from a decrease in elasticity proportionally to the change in temperature, which leads to extreme deformation and eventual collapse. Additionally, the yield and ultimate stresses are also reduced, causing the structure to fail upon smaller loads if the effect of fire has not been accounted for during the design phase, [1, 4].

The main concern when designing a building for fire safety is the lives and well-being of people and possible occupants during the event of fire, e.g. firefighter, residents. As a secondary concern stands the integrity of building components and material goods present in the fire environment, [5, 6]. With these aspects in mind, fire safety verifications are based on how long the structure is able to support the applied loads coupled with the effects of elevated temperatures on resistance, allowing the building to be properly evacuated and valuable material to be protected.

Statiscally, the occurance of fatalities during fire events in buildings around the world, mainly in North America and Europe, has decreased over the years since regulatory measures were implemented, as displayed in Figure 1.2. This is due to extensive

research and investigation on structural response and people's behavior in the presence of fire danger, whose research findings were then included in modern building and design codes, [7, 8].

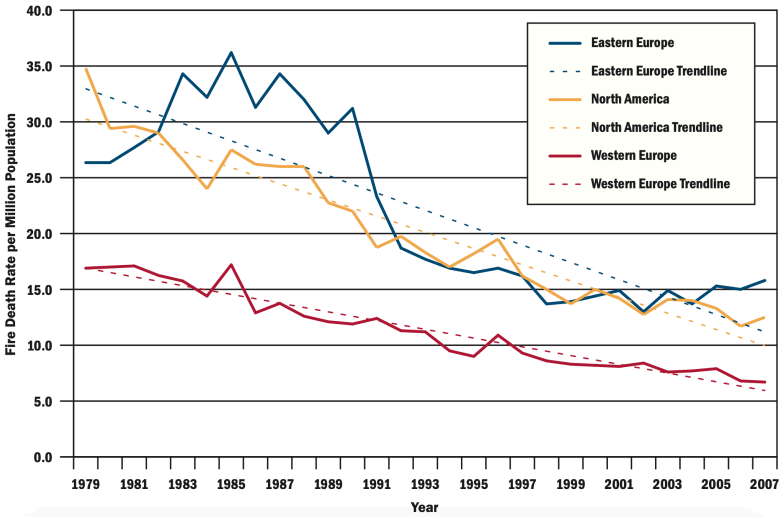

Figure 1.2: International fire death rates over time, [8].

In Europe, around 2 million domestic fires are reported yearly, and it is estimated that around 20.000 deaths and half a million injuries occur as a direct result, [8]. However, since some countries do not possess a proper database for fire reporting and analytics, these data might underestimate the real impact of building fires.

1.2 Scope and main goals

Bearing in mind the facts presented above, this dissertation paper aims to study via numerical and experimental analyses the stability and thermo-mechanical behavior of steel arches and curved beams produced by I/H double-symmetrical sections curved by their major axis, submitted to different temperature levels and support conditions. Furthermore, a comparison between the investigated results and standard structural safety verifications based on Eurocode 3 will be made. In order to reach these main goals, specific objectives include:

1. Study the current standard methodologies regarding design and safety of steel arches for both natural and elevated temperatures based on Eurocode 3;

2. Investigate existing formulations for in-plane buckling critical load of arches found in the literature;

3. Employ a numerical linear and nonlinear model to analyze the in-plane buckling load of these same arches and compare the results with literature formulations;

4. Compare the obtained numerical results to standard design methodologies for natural and elevated temperature steel members under bending moments and axial forces.

5. Analyse the effects of varying different geometrical parameters and identify the relevant factors that influence the thermo-mechanical behavior of steel arches and curved beams.

1.3 Thesis outline

This dissertation paper is organized in 6 chapters. In the Introduction, a general panorama about fires and steel construction is given, with special attention to curved structural steel members.

Chapter 2 presents the literature review about curved steel beams and arches, their specificities and general characteristics, common applications in buildings and curving processes, as well as instability modes and phenomena that are specific to curved beams and arches. Furthermore, it is presented in this chapter the state-of-the-art, describing current studies and investigations about the scope of this dissertation.

Chapter 3 presents the design and safety verifications of steel arches and elements submitted to combined axial force and bending moments based on the Eurocode 3 parts 1 and 8 for members under natural temperature and elevated temperatures, respectively.

Chapter 4 studies the in-plane stability behavior of steel curved members. The main goal of this chapter is to study the elastic buckling critical load and nonlinear ultimate load for arches under symmetrical concentrated forces through numerical approaches and energy methods, for a diversity of support conditions, steel classes, imperfection magnitudes and temperature levels. The results are then compared to those from the literature. Also, nonlinear solutions are employed, whose results are later compared to both linear elastic solutions and standard design simplified methods given in Eurocode 3 for both natural and elevated temperature cases.

Chapter 5 presents the experimental setup developed in order to study the stress development and deformations during cold curving processes. Also, an analytical solution to find the residual stress profile after cold curving straight beams into arches was defined.

Chapter 6 summarizes the results of this study and the main conclusions, and gives suggestions for future studies in this subject.

Chapter 2

Literature review

2.1 Curved steel beams and arches

Curved steel beams are frequently used in load-bearing structures such as bridges, roofs and a variety of buildings, when most of the time the aesthetics and architectural design require curved elements, but also because these types of structures provide economically fit solutions depending on load types and building purposes, [9, 10]. Typically in current times, curved beams and arches for construction are produced from straight steel I/H beams by a diversity of bending processes, such as pyramid roller bending, incremental bending, hot bending and induction bending. Each bending method has its own production processes and particularities, and each of them generates different effects related to the curving technique, [2, 10].

La Poutré et al., [11], define arches and curved beams depending on load and support conditions. Arches are curved structures bent in elevation, bearing an in-plane load with supports that prevent outward spreading, developing compression stresses in its rib and reducing bending moment, which makes them a better choice for structural use, [12]. Curved beams differ from arches regarding the supports, where curved beams have at least one support that allows horizontal spreading. In this disseration, both curved beams and arches will be studied.

Arches and curved beams may have different shapes, according mainly to the type of applied loading conditions and architectural needs of the structure. Figure 2.1 shows some possible shapes for arches and curved beams. If the main goal for choosing a particular shape is to eliminate or minimize bending moments, catenaries are the wisest choice for constant loads per unit of length, parabolas for evenly distributed loads and circular shapes for radial loads, [13]. However, circular arches are currently the most employed shape despite not being the most fit solution in all cases, mainly because of its more practical and easier curving processes. For this same reason, this paper studies strictly circular steel arches and curved beams with constant curvature.

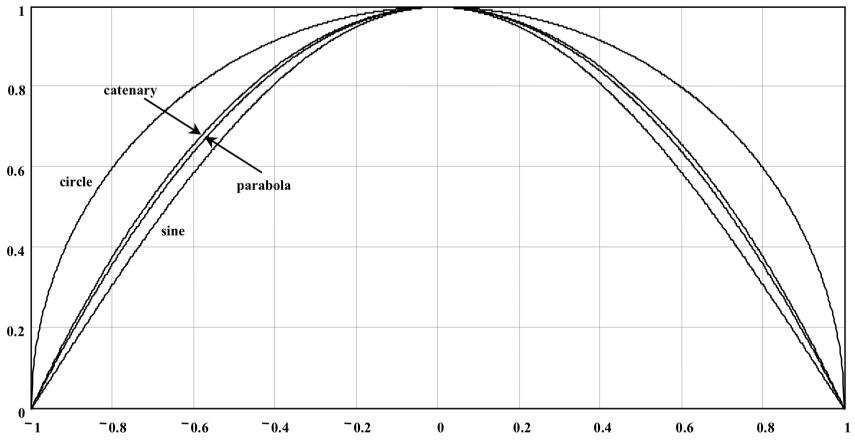

Figure 2.1: Some possible shapes of arches and curved beams, [13].

Generally, curved I/H-section members are submitted to vertical transverse loading, developing bending moments as well as compressing internal forces in order to resist the applied load. Depending on the rise-to-span ratio and load type, axial compression plays an important role on the arch resistance, causing in-plane instability phenomena such as cross-sectional buckling and global buckling, [9]. Additionally, out-of-plane instability phenomena may occur, in case the arch does not have proper lateral bracing, in a similar manner to laterally unrestrained steel beams, [14].

Despite its widespread use in all sorts of buildings, design rules for curved steel members are not included in a number of standards and design guides around the world. Eurocode 3 Part 1-1 for example, which is the European standard for general

steel construction and buildings, treats curved elements the same as straight members regarding sizing and safety verifications, even though the response to actions and stress distribution in curved elements may vary considerably compared to straight elements, [2, 15]. Safety verifications for arches are only included in Eurocode 3 Part 2, which is the European standard for bridge design, and it includes specific details for this type of construction that may not reflect properly on arches employed in other kinds of buildings. One example of behavior not included in design codes is the possibility of out-of-plane instability, as mentioned above, [11].

Historically, before the use of steel for construction purposes, curved members in structures were initially made of cast or wrought iron, [1]. In the first case, iron was cast into circular or curved shapes in liquid form, method that did not require any additional bending action after the iron was cold. Figure 2.2a shows an example of a curved structure of a metallic bridge made of cast iron, this one the Dom Luís I bridge, in the city of Porto, Portugal, [16]. In the second scenario, members of wrought iron were easily curved by smiths into a variety of shapes, because wrought iron is softer and easier to handle compared to cast iron or even steel, [2]. Figure 2.2b shows an example of a wrought iron curved structure, the Eiffel Tower, in Paris, France, [17].

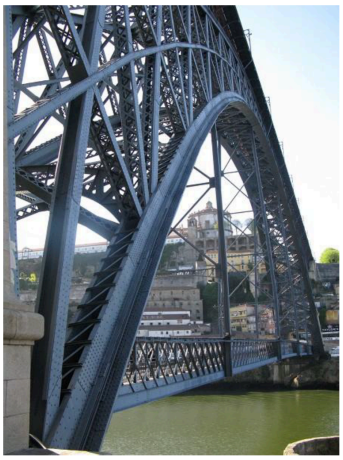

(a) Dom Luís I bridge, Porto, Portugal, [16].

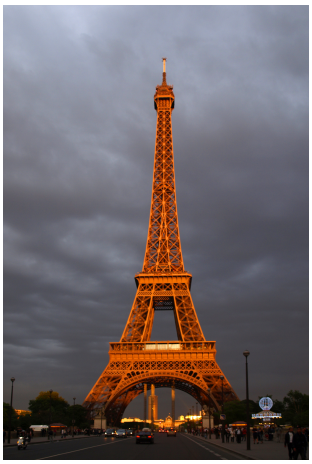

(b) Eiffel Tower, Paris, France, [17].

Figure 2.2: Example of (a) cast iron curved structure (b) wrought iron curved structure.

When steel first started to replace iron in general construction and load-bearing

structures, the problem of bending steel pieces became an important issue. There are two ways for bending a straight steel beam: vertical curving, also known as the hard-way bending, which consists on bending a straight beam about its major axis, used as vertical arches, and horizontal curving, also known as the easy-way bending, which consists on bending a straight beam in its minor axis, used as horizontal beams, commonly in floor structures, [18]. In this dissertation paper, the most common processes for curving members are detailed below.

In cold bending processes, which are the curving methods performed under natural temperature, the stress-strain curve of the material is modified by the application of strain. Figure 2.3a shows an idealized common stress-strain curve for conventional steel, and Figure 2.3b shows a stress-strain curve of cold-bent steel. Comparing both figures, it is possible to see in Figure 2.3b that after passing through the rolls there is an elastic unload (point C to D), and as the section is re-stressed, there is an elastic rise back to the previous stress point (point D to C), resuming to the original stress-strain path, [2]. In this process, a portion of the material's ductility has been consumed by the curving mechanism.

Antagonistically, in hot bending processes, some alteration in the material properties also occurs because of temperature changes during and after curving. If necessary, post-bending heat treatment might be used to correct properties of the steel, [2].

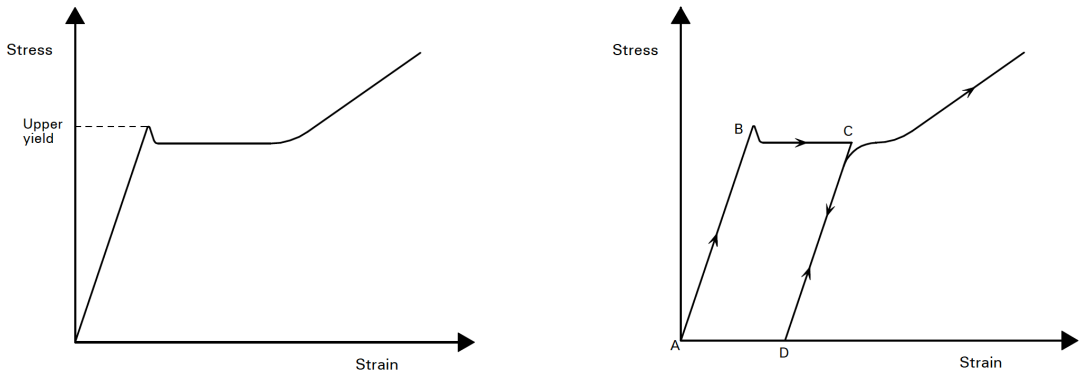

(a) Idealized stress-strain curve. (b) Cold-bent stress-strain curve.

Figure 2.3: Stress-strain curves for cold-bent steel, [2].

2.2 Curving processes and techniques

2.2.1 Roller bending

This curving method consists on passing a straight steel member, at natural temperature, through a pyramid-like arrange of rolls, as shown in Figure 2.4b, as the force is applied across the cross section. It requires repeated passes through the set of rolls to gradually bend the member, adjusting the distance between rolls as necessary, until the desired curvature is obtained, up to an angle of 360º, [2, 18]. After the completion of successive rolls, the tips of the beam might be cut off in order to provide constant curvature of the entire element, if needed. Figure 2.4a depicts the process of roller-bending an I-profile steel member.

(a) Roller-bending of an I beam.

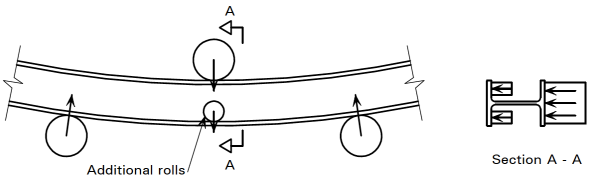

(b) Roller-bending scheme.

Figure 2.4: Roller bending process, [2]

An important effect in I/H profile members caused by roller bending is the possibility of local buckling of the web. The tension flanges tend to crush the web, and in order to prevent this, additional rolls can be installed on the set, compressing the tension flanges, [2]. Figure 2.4b also shows the proper position and force scheme of additional rolls applied on the tension flanges.

2.2.2 Incremental bending

As described by Dowswell, [18], ”incremental step bending is a cold-bending method that uses hydraulic rams to apply bending forces at several discrete, closely-spaced locations along the member”. Figure 2.5a shows a steel I-beam being bent by an hydraulic ram applying a point load in the middle of the span. This method is also called cambering, and it is commonly used in floor beams to compensate for deflections caused by heavy dead loads, [19].

(a) Cold incremental cambering of an I-beam

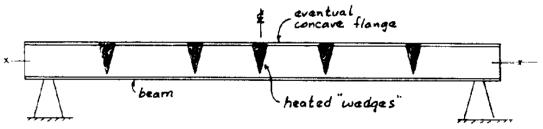

(b) Scheme of application of hot cambering in a beam, [20].

Figure 2.5: Roller bending process

Cambering can also be induced in a steel beam by applying heat (hot bending), where triangularly shaped segments of the beam are heated, in uniformly spaced points, causing the beam to bend due to differences of temperature between the flanges, as shown in Figure 2.5b, [21, 20].

2.2.3 Induction bending

In this curving method, a steel member is heated up to 1050ºC through the application of an electric current by an electric coil. Subsequently, the cross section is cooled after the passage through the electric coil, and a mechanical arm induces the curvature on the member, [2]. The length of the arm is adjustable, providing the curvature needed for the member. Figure 2.6a shows the functioning of an induction bending machine, and Figure 2.6b shows an actual induction machine bending a circular hollow section steel member.

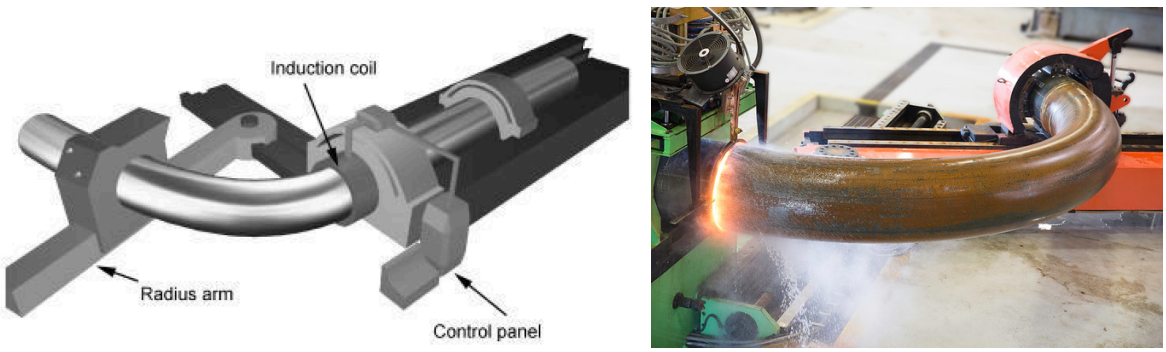

(a) Induction bending scheme (b) Induction bending machine

Figure 2.6: Induction bending scheme and machine, [2].

Although this method is more expensive compared to the others, it offers the possibility to curve pieces in smaller radii with lower cross-sectional distortion. Also, controlling dimensional requirements is far easier in hot bending, as well as bending special members with unusual geometries, [18].

There is also the possibility of combining induction bending and roller bending, where the mechanical arm is replaced by the pyramid-array of bending rollers . This combination is widely used in larger steel pieces, because in hot bending the length of the mechanical arm defines the maximum curvature that can be applied, [2].

2.3 Instability modes of arches and curved beams

Load-bearing members in a structure are conditioned to different types of loads, depending on the position of the member and where the loads are applied. Therefore, each type of member respond to loading with displacements. Compression members, for example, besides axial displacements, are prone to the occurance of buckling around its minor resistance axis, if lateral bracings are not provided. Steel I-beams, as they carry transverse loads and develop shear force and bending moments, are prone to lateral-torsional buckling, as well as local buckling of flanges and web.

Curved beams and arches, because of their particular geometry, have different

kinds of instability modes beyond those mentioned above. Additionally, modern design codes do not accomodate these differences in instability behavior, ignoring them when it comes to design and safety verifications, [11]. The Eurocode 3, [22], which is the European standard for steel construction, deals only with arched steel bridges in its part 2, providing simplified methods for buckling resistance verification and critical load calculation based on specific load and support conditions.

Vertical arches and curved beams, as they have two major dimensions (horizontal and vertical), are susceptible to three global modes of instability: in-plane snap-through buckling, in-plane bifurcational buckling and out-of-plane lateral torsional buckling, besides local buckling modes. Figure 2.7 shows a scheme of each global buckling mode for arches or curved beams.

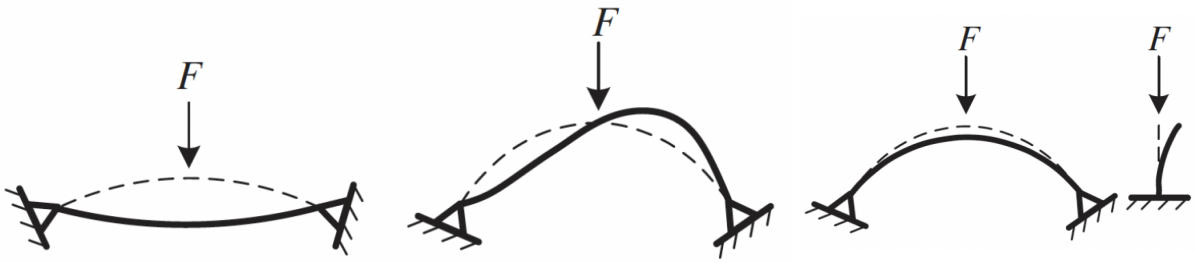

(a) In-plane snap-through. (b) In-plane bifurcational. (c) Out-of-plane.

Figure 2.7: Instability modes for arches and curved beams (adapted from La Poutré, [11]).

2.3.1 In-plane snap-through buckling

The snap-through buckling mode, also called limit-point buckling, occurs when the arch or curved beam is deformed at a point that it inverts its geometry as the load is applied. It happens in shallow arches when the compression forces are such that the arch suffers from a level of shortening that causes it to flip, and then starts to develop axial tension stresses as the load continues to be applied, as shown in Figure 2.7a, [13]. This instability mode is also called symmetrical buckling.

Figure 2.8 shows the typical load/displacement curve for the snap-through instability. This curve shows the nonlinear path of equilibrium, in which the increment of load reduces the stiffness until a limit point (point B), where the path is parallel to the horizontal axis. At this point, the deformation path reaches the limit where it passes from stable to an unstable condition, when a small increment of the load causes a large deformation of the arch. At point C the arch has totally inverted its geometry (deformed configuration in Figure 2.7a) and the load starts to increase again, inducing axial tension throughout the arch, [23].

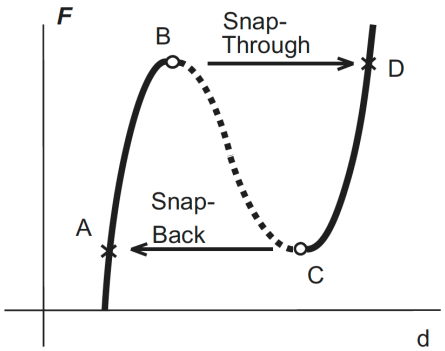

Figure 2.8: Force-displacement curve of snap-through buckling, [24].

In this type of buckling, members buckle in the same configuration since the application of loads until the maximum load is reached, without any sudden changes in the equilibrium path. This mode is also common in other non-straight structures subjected to external pressure, [25].

2.3.2 In-plane bifurcational buckling

The in-plane bifurcational instability mode, also known as anti-symmetrical buckling, is characterized by the sinusoidal shape of the deformed configuration after buckling, as shown in Figure 2.7b. This instability mode is associated to a bifurcation of equilibrium phenomenon, in which the deformations follow the same pattern prior to a critical load, for which the deformation changes to a different mode, [25, 23]. As a typical example, buckling behavior of a free-standing linear structural element subjected to a

uniform compressive force is classified as bifurcational, because before reaching the critical load, this element shortens due to compression, and right after the critical load is reached, it bends around its weak axis.

In curved structures, this instability mode usually happens in deeper arches, where the bending moments are substantially higher when compared to compression forces. Additionally, it is important to mention that bifurcational buckling presents an abrupt nature regarding the load-displacement path, which means that deformations after buckling are not present in the pre-buckling path and will show suddenly right after the bifurcation point, [23], as shown in Figure 2.9. In arches, this concept means that only right after the load reaches its critical value for this instability mode, the sinusoidal shape of transverse displacements will start to appear in the structure.

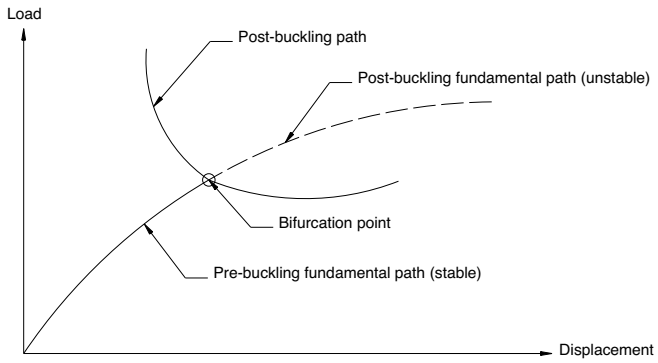

Figure 2.9: Load-displacement equilibrium path for bifurcational buckling.

2.3.3 Out-of-plane lateral torsional buckling

The out-of-plane buckling of arches is very similar to the lateral torsional buckling of laterally unrestrained beams. It is characterized by the occurance of lateral displacements out of the loading plane, acting along with the transverse in-plane deformations, as shown in Figure 2.10. In free-standing arches or ones without proper lateral bracing, it generally occurs before all other instability modes, depending on the out-of-plane support conditions and section properties, mainly its torsional resistance, [11, 14].

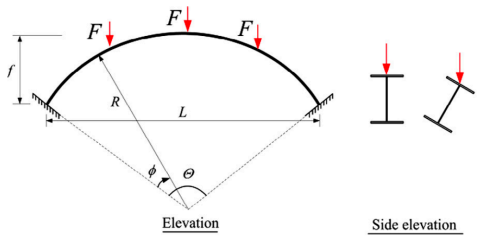

Figure 2.10: Out-of-plane displacements, [14].

During this mode of instability, a complex stress distribution arises due to an interaction of forces on the member. As buckling occurs, the arch or curved beam steps from supporting bending and axial forces to resisting bi-axial bending (around both weak and strong axes) coupled with torsion and unrestrained warping of the cross section, [11].

2.4 Geometrical imperfections

Geometrical imperfections are defined as discrepancies between the ideal and real geometries of a structural member, caused by inevitable flaws during production, transportation and manipulation processes. Even though modern standards for design and construction adress this issue by allowing small acceptable imperfections, they still need to be considered in design and safety verifications.

Regarding steel members formed by thin-walled plates, imperfections are classified mainly in local and global, according to type and magnitude, [26]. Local imperfections are characterized by lack of straightness between the forming plates of a section and wrinkles/distortions developed during cooling (for hot-rolled members) or handling operations. On the other hand, global imperfections in a member consist of undesired curvatures along the member's length, usually associated with transportation and storage maneuvers.

These imperfections may affect considerably the behavior of structures, [23]. Taking as an example, the approach for calculating the theoretical critical load for axially loaded columns under compression assumes nonexistent transverse displacements

up until the bifurcation point, which is when the column starts to deflect perpendicularly to its central axis, as depicted by the dotted line shown in Figure 2.11a. However, if geometrical imperfections are taken into consideration, the column already has initial deflections and exhibits nonlinear lateral displacements even before the critical load is reached, in a value substantially lower than the theoretical perfect-model critical buckling load. This behavior is displayed by the imperfect model curve in the lateral deflection *versus* load in Figure 2.11a.

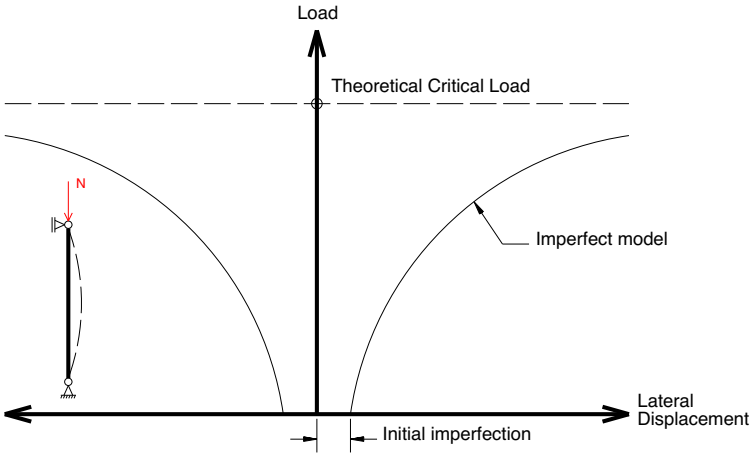

(a) Critical load for perfect and imperfect columns.

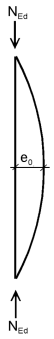

(b) Shape of initial imperfections for columns and beams, [27].

Figure 2.11: Imperfections in structural members.

Global bow imperfections are often modelled as sinusoidal displacements of the centroidal axis of the element, for beams and columns, as shown in Figure 2.11b by the maximum amplitude of bow displacements in an element (e_0). Eurocode 3 Part 1-1, [27], defines the maximum local bow imperfection e_0 to be considered in analyses for linear members under compression or flexural buckling depending on the buckling curve and type of analysis, as shown in Table 2.1, where L is the element length. The buckling curve is also given in EC3 part 1, and it depends on the steel strength, type of section, manufacturing process, plate thickness and buckling axis, [27].

Nonetheless, additionally to all the issues cited above, the processes of curving a straight steel member might cause more local and global distortions, increasing the magnitude of imperfections. Since this issue is not included in the imperfection factors

Buckling curve	Elastic analysis	Plastic analysis
a0	$L/350$	$L/300$
a	$L/300$	$L/250$
b	$L/250$	$L/200$
c	$L/200$	$L/150$
d	$L/150$	$L/100$

Table 2.1: Imperfection factors e_0 according to Eurocode 3 part 1, [27].

given in Table 2.1 for straight members, Eurocode 3 part 2 for the design of steel bridges determines new values for e_0 in arches for in-plane buckling depending on support conditions and presence of hinges, for the four buckling curves, as seen in Table 2.2.

	1	2	3			
		shape of imperfection (sinus or parabola)	e_0 according to classification of cross section to buckling curve			
			a	b	c	d
1	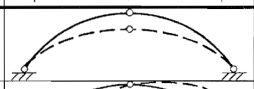	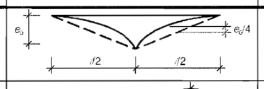	$\frac{s}{300}$	$\frac{s}{250}$	$\frac{s}{200}$	$\frac{s}{150}$
2	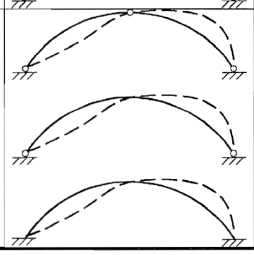	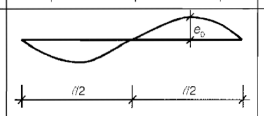	$\frac{\ell}{600}$	$\frac{\ell}{500}$	$\frac{\ell}{400}$	$\frac{\ell}{300}$

Table 2.2: Imperfection factors e_0 according to Eurocode 3 part 2, [22].

It is noticeable that in Eurocode 3 part 2 the imperfection factor values for design geometrical imperfections are lower when compared to those given in Eurocode 3 part 1-1 for linear elements. One of the reasons for this is the presence of additional residual stresses caused by the curving processes in arches and curved beams, forcing the admissible imperfections to be lower in order to avoid extreme deformations and possible buckling instability.

2.5 Residual stresses

Residual stresses, also called locked-in, are internal stresses present in a steel element even while no external loads are applied. These stresses are originated in the production processes, and are always in static equilibrium. However, this type of stress must be considered when designing a steel element, and for this reason, its influence has been included in building standards all over the world regarding behavior and stability of members, such as the Eurocode 3, [27], and the AISC Steel Construction Manual, [28]. In this context, residual stresses are often included in the allowed global geometrical imperfections as an equivalent imperfection factor or in buckling curves for determining the stability factors for members under compression or combined bending and compression.

Several studies investigated the stress distribution in hot formed sections. Young, [29], assumes a parabolic distribution of locked-in stresses as shown in Figure 2.12a. The maximum magnitude of compressive (σ_{c1} and σ_{c2}) and tensile (σ_t) residual stresses are given by Equations 2.1 to 2.3, and are only dependent on the cross section dimensions. ECCS, [30], assumes that the residual stresses vary linearly through the cross section components and depend only on the yield strength f_y of the steel, as depicted in Figure 2.12b for H and I sections with height-to-width ratios smaller and greater than 1,2, respectively.

$$\sigma_{c1} = -165\left(1 - \frac{h \cdot t_w}{2.4 \cdot b \cdot t_f}\right) \tag{2.1}$$

$$\sigma_{c2} = -100\left(1.5 - \frac{h \cdot t_w}{2.4 \cdot b \cdot t_f}\right) \tag{2.2}$$

$$\sigma_t = -100\left(0.7 - \frac{h \cdot t_w}{2 \cdot b \cdot t_f}\right) \tag{2.3}$$

In arches and curved beams, the curving process alters significantly the profile of original residual stresses from manufacturing, as part of the section reaches past the yield stress to impose permanent large plastic deformations in the straight member,

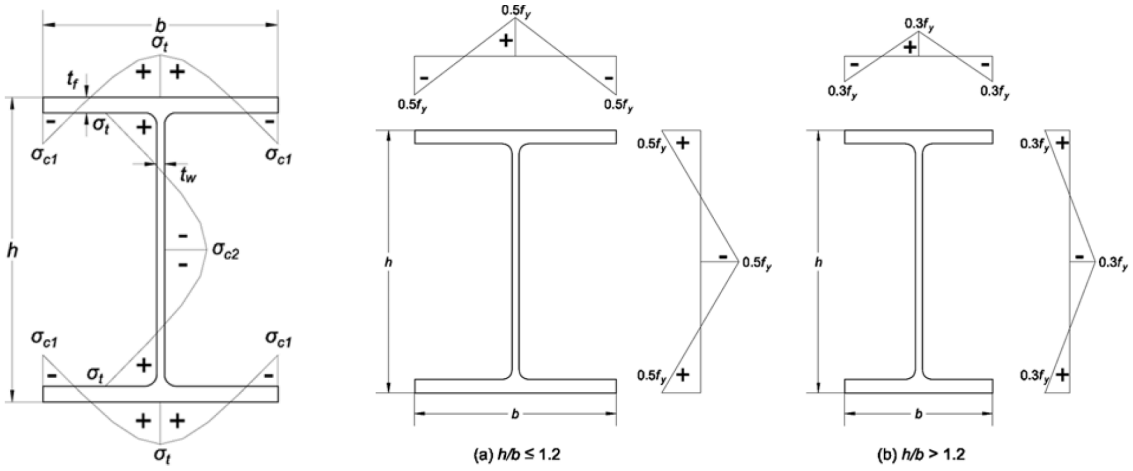

(a) According to Young, [29].

(b) According to the ECCS, [30].

Figure 2.12: Residual stress distributions in straight members.

[31]. When the curving loads are removed, the arch relaxes elastically (phenomenon also called *springback*) into its final curved shape. So, the final residual stress profile is given by the stress distribution during bending combined with the stress distribution during the elastic unloading, [32], and since they are in static equilibrium, the residual stresses satisfy the bending and axial equilibrium conditions in the cross section given by Equations 2.4 and 2.5, respectively, where σ_r is the residual stress distribution in the cross section of area A.

$$\int_A \sigma_r \cdot y \cdot dA = 0 \tag{2.4}$$

$$\int_A \sigma_r \cdot dA = 0 \tag{2.5}$$

For this reason, the plastic zone in the cross section, which depends on the final curvature radius, influences the magnitude of residual stresses in the web after cold curving. However, acccording to Pi and Trahair, [33], the flange residual stresses σ_{rrf} due to cold curving are comparatively smaller after the elastic unloading and are considered to be constant along the flange width, given by Equation 2.6, [32] for the case of roller bending.

$$\sigma_{rrf} = \sigma_y \left(\frac{Z_{px}}{Z_{ex}} - 1 \right) \tag{2.6}$$

In this expression, Z_{px} and Z_{ex} are the plastic and elastic moduli of the cross section. Figure 2.13 shows a typical stress pattern of an I profile after cold curving by rollers, where C and T stand for compression and tension, respectively. Pi and Trahair, [33], consider in their studies the maximum web residual stress after roller curving to be $\sigma_{rrw} = 0.9 f_y$. Nevertheless, this distribution of stresses may differ significantly when other types of curving techniques are employed, mainly because of differences in load application and support apparatus.

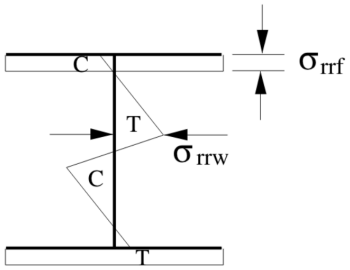

Figure 2.13: Residual stress patterns after cold roller curving of I section, [33].

Spoorenberg et al., [34], and Timoshenko, [35], also studied the changes in locked-in stresses after roller-bending a straight steel I-section member, with each respective residual stress model shown in Figures 2.14a and 2.14b. Both models suppose a linear distribution of stresses, but with different maximum magnitudes due to specific considerations made in each model.

For both models, it is assumed that the initial locked-in stresses of a straight member before roller bending are replaced in the curving process, because of the large plastic deformations necessary to obtain the desired radius of curvature of the arch, [31].

Timoshenko's model utilizes an analytical uniaxial beam model and assumes a bi-linear stress-strain relationship in order to simplify calculations, and for this reason the distribution over the flange width is considered to be constant and depends on α, which is the ratio between the plastic and elastic moduli of the cross section. It is noticeable

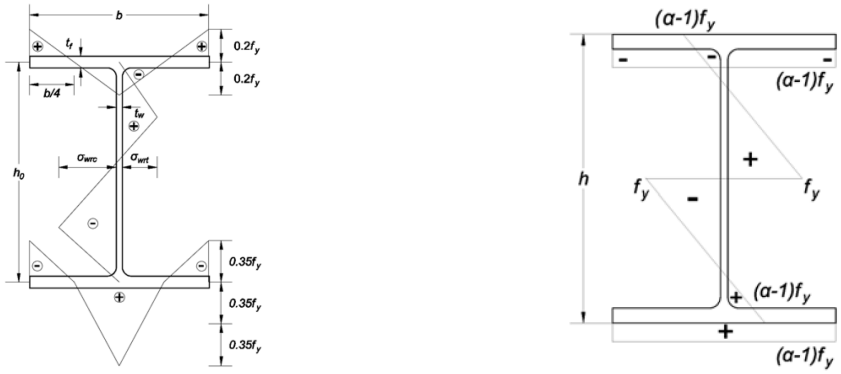

(a) According to Spoorenberg et al., [34]. (b) According to Timoshenko, [35].

Figure 2.14: Residual stress distributions in roller-bent members.

that this model is very similar to the one proposed by Pi and Trahair, [33], shown in Figure 2.13.

Spoorenberg et al., [34], performed experimental tests using the sectioning method in cold roller-bent members to measure residual stresses, and compared the results later on with numerical simulations of the curving process. Then, the residual stress model shown in Figure 2.14a was proposed based on the numerical and experimental results, with the maximum compressive σ_{wrc} and tensile σ_{wrt} stresses in the web given by Equations 2.7 and 2.8, respectively.

$$\sigma_{wrc} = \left(\frac{14bt_f}{30h_0t_w}\right) f_y \tag{2.7}$$

$$\sigma_{wrt} = \left(\frac{7bt_f}{30h_0t_w}\right) f_y \tag{2.8}$$

This model depends on the geometry of the cross section similarly to the straight member residual stress model by Young, [29], shown in Figure 2.12a, but also depends on the steel tensile strength, parameter not considered in Young's stress model. All residual stress models cited above consider the distribution along the thickness of the section components to be negligible.

2.6 State-of-the-art

Due to its large employment in metal structures worldwide, studies conducted to describe the mechanical behavior of steel curved beams and arches at room temperature and some at elevated temperatures have been done in order to aid design processes and safety verifications for this type of element. Some of these studies and their main results and findings are briefly described below.

Timoshenko in 1940, [35], investigated the effects on residual stress patterns due to cold roller bending of straight I/H hot formed steel profiles, included in Part II of his *Strength of Materials* book. Also, Timoshenko and Gere, in 1985 [36], studied the general elastic stability of structures of a diversity of shapes, comprising linear and nonlinear problems of buckling and bending of columns, rings, frames, thin bars and plates, etc. Nonetheless, the strength and behavior of curved bars and arches under uniform external pressure were also investigated, and equations for the critical in-plane buckling load were derived considering linear pre-buckling behavior and the center line of the bar to be inextensible.

Rajasekaran and Padmanabhan, in 1989 [37], developed a set of equations describing the behavior of thin-walled curved steel beams derived from large displacement beam theory and the principal of virtual work. Equations aiming to calculate three-dimensional strains and stresses, as well as equilibrium and in-plane and out-of-plane critical buckling load equations for curved beams were deducted. The results were then compared to those obtained by other authors for similar curved beam models.

Yang, Kuo and Yau, in 1991 [38], formulated a curved beam finite element model to predict the critical buckling load by approximating a curved beam by discretizing it into a series of straight-beam elements. Numerical testing was performed in order to validate the proposed model, and curved beams under either uniform bending, uniform compression and with clamped ends were tested.

Based on the studies and theories developed in years of research and cited above, Pi and Trahair, in 1999 [33], concerned with the lack of proper methods for designing

curved elements in construction standards, investigated the in-plane elastic buckling of pinned-pinned curved steel beams and arches under uniform compression and developed a design method for arches againts uniform compression through a nonlinear inelastic finite element model, and a modified interaction equation different from those given in design standards for elements under combined bending and compression. The results from this study, seen in Figure 2.15, show that the classical column and beam-column design approaches might overestimate the real buckling load of arches, mainly because of differences in internal force distribution and global behavior when compared to linear members.

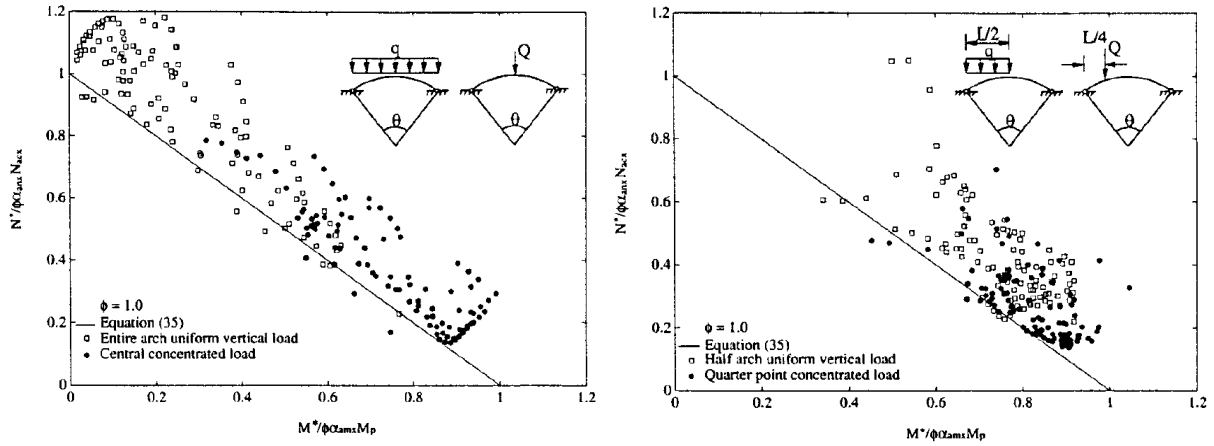

(a) Symmetrical loads. (b) Asymmetrical loads.

Figure 2.15: Strength results by Pi and Trahair, 1999, [33].

Similarly, Bradford, Uy and Pi, in 2002 [39], studied the in-plane behavior of both pinned-pinned and fixed-fixed steel arches with symmetric cross section under a central concentrated load, instead of a radial uniform distributed load as generally considered. Because of the nonuniform internal force distribution caused by the loading condition, the pre-buckling behavior might be nonlinear, and the effects of this nonlinearity are not covered in classical buckling solutions. it was found that this phenomenon occurs mainly in shallow arches, as they undergo greater axial deformations when compared to deeper arches.

Considering a different support condition case, Pi an Bradford, [40], in 2013 investigated through nonlinear elastic numerical simulations the structural and buckling behavior of pinned-fixed steel arches under uniform compression. The results of their research show that pinned-fixed arches deform unsymmetrically because of the reaction moment in the fixed end, as seen in the results shown in Figure 2.16, and the buckling mode is also affected by the support condition.

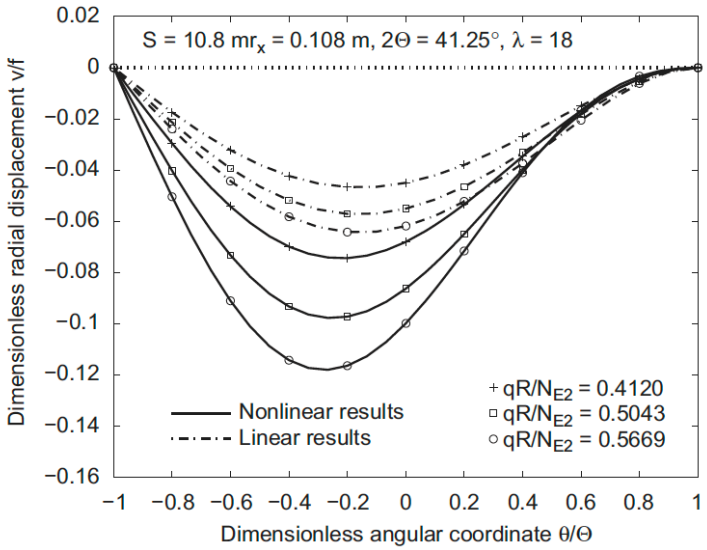

Figure 2.16: Nonlinear and linear displacements for pinned-fixed arches, [40].

In 2013, La Poutré et al., [11], experimentally researched the out-of-plane stability of roller bent steel arches at room temperature supporting a single load at the arch crown. A total of 15 specimens were tested, varying their geometrical characteristics. They concluded that, for free-standing or poorly laterally braced arches, the arch would become unstable in an out-of-plane instability mode before it reaches its in-plane buckling capacity. Pior to this study, Spoorenberg et al. [41] investigated the out-of-plane buckling capacity of free-standing arches under symmetric loads and a design rule for the imperfection parameter was proposed based on finite elemenet analyses and experimental results.

Later on, Dou et al., [42], conducted a study dealing with the flexural-torsional ultimate resistance of steel arches. The experiments employed arches with the same

length but different rise-to-span ratios under symmetrical three-point loads. They used finite element software *ANSYS* with element type *BEAM188* to predict the inelastic response of the tested arches. It was found that the numerical analyses provided good predictions of the out-of-plane resistance of the arches, and that in every test the arch failed in a S-shaped flexural-torsional buckling mode due to geometrical imperfections and out-of-plane boundary conditions.

Differently from the studies mentioned above, and since very limited research has been conducted in this area, Guo et al. in 2016, [43], investigated the structural behavior of pinned-pinned steel arches under concentrated loads exposed to fire conditions, through numerical simulations considering the influence of different horizontal restraints, fire fields, rise-to-span ratios and geometrical characteristics of the cross section. Steel mechanical properties under temperature cases were considered according to Eurocode 3 part 1-2, for fire resistance design. The results have shown that arches present a specific response to high temperature significantly different from the response of regular straight steel beams, and arches with rise-to-span ratios in a certain range withstand higher temperatures because of nonlinear optimal harmonization of combined load effects, as seen in Figure 2.17.

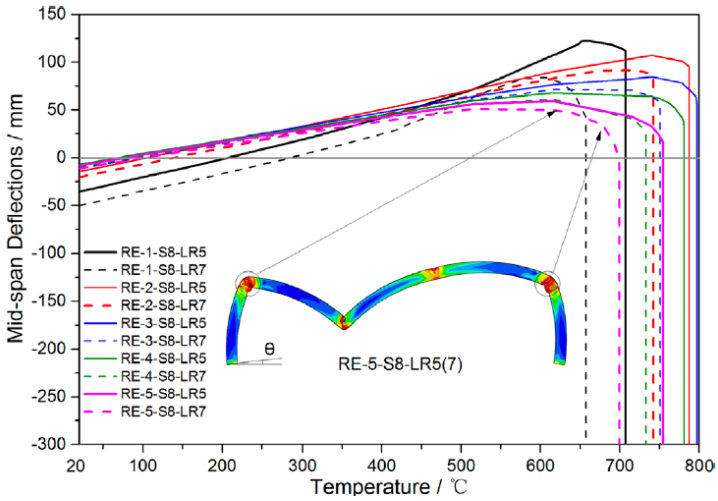

Figure 2.17: Mid-span displacements under various temperatures, [43].

Chapter 3

Standard strength and safety verifications for steel arches

Depending on support and loading conditions, steel arches may develop a wide range of internal force distributions. Moreover, except for radial uniform distributed loads, which develop uniform compression along the arch, and applied moments at both ends, which generate uniform bending, arches and curved beams withstand a combination of bending moments and axial forces when under general loading.

Safety verifications of steel arches under general loading at room temperature are made based on Eurocode 3 Part 1-1, [27], while the same verifications but at elevated temperatures as during fire conditions follow the methodology given by Eurocode 3 Part 1-2, [44], for fire structural design.

3.1 Elements under bending moments and axial force at room temperature

Safety verification for elements under general loading at natural temperature developing bending moments and axial compressive forces is conducted in two steps: verification of cross sectional resistance and verification against the occurence of global buckling

in compressed members.

Since arches and curved beams are generally fabricated from I/H profiles with adequate cross-section geometries regarding the necessary mechanical power to cold-bend a steel member, only cross sections of Classes 1 and 2 will be considered, allowing for plastic design according to Eurocode 3, [27].

Also, because this dissertation focuses on the in-plane resistance and stability of steel curved beams and arches curved by their strong axis (y), it will be considered that bending moments around the weak axis (z) are negligible and out-of-plane lateral torsional buckling is prevented by lateral constraints.

3.1.1 Resistance of cross-sections

The resistance of the cross section is verified by Equation 3.1, where M_{Ed} is the design bending moment and $M_{N,Rd}$ is the reduced bending moment resistance accounting for the axial compressive force effects on the cross section.

$$M_{Ed} \leq M_{N,Rd} \tag{3.1}$$

For double-symmetrical I and H profiles, both hot-rolled and welded, the reduced bending moment capacity is given by Equation 3.2.

$$M_{N,Rd} = M_{pl,y,Rd}\left(\frac{1-n}{1-0,5\cdot a}\right) \tag{3.2}$$

In which, $n = N_{Ed}/N_{pl,Rd}$ and $a = (A - 2b_f t_f)/A$, but also satisfying $a \leq 0,5$. However, bending moment values are excused from reduction when the following criteria are satisfied:

1. $N_{Ed} \leq 0,25 N_{pl,Rd}$

2. $N_{Ed} \leq 0,5 h_w t_w f_y/\gamma_{M0}$

Additionally, interaction between shear forces and bending moments must be accounted for if the design value of the shear force V_{Ed} exceeds 50% of the shear plastic resistance of the cross section $V_{pl,Rd}$, [27]. Should it be the case, the value of the resisting bending moment plus axial force $M_{N,y,Rd}$ must be calculated using a reduced yield strength value, given by $(1-\rho)f_y$, where $\rho = [(2V_{Ed}/V_{pl,Rd}) - 1]^2$. The plastic shear resistance of the cross section is given by Equation 3.3, where A_v is the shear area.

$$V_{pl,Rd} = \frac{A_v(f_y/\sqrt{3})}{\gamma_{M0}} \tag{3.3}$$

3.1.2 Buckling resistance

Eurocode 3 Part 1-1, [27], defines that, for double-symmetric section members under a combination of bending moments and axial compression, the safety verification for element stability and buckling resistance is given by the interaction expressions shown in Equations 3.4 and 3.5, for buckling around the y and z axes, respectively.

$$\frac{N_{Ed}}{\chi_y N_{Rk}/\gamma_{M1}} + k_{yy}\frac{M_{y,Ed} + \Delta M_{y,Ed}}{\chi_{LT} M_{y,Rk}/\gamma_{M1}} + k_{yz}\frac{M_{z,Ed} + \Delta M_{z,Ed}}{\chi_{LT} M_{z,Rk}/\gamma_{M1}} \leq 1,0 \tag{3.4}$$

$$\frac{N_{Ed}}{\chi_z N_{Rk}/\gamma_{M1}} + k_{zy}\frac{M_{y,Ed} + \Delta M_{y,Ed}}{\chi_{LT} M_{y,Rk}/\gamma_{M1}} + k_{zz}\frac{M_{z,Ed} + \Delta M_{z,Ed}}{\chi_{LT} M_{z,Rk}/\gamma_{M1}} \leq 1,0 \tag{3.5}$$

In these expressions,

- N_{Ed}, $M_{y,Ed}$ e $M_{z,Ed}$: design values of axial forces and bending moments around the y and z axes, respectively;
- N_{Rk}, $M_{y,Rk}$ e $M_{z,Rk}$: characteristic values of axial forces and bending moments around the y and z axes, respectively, given as $N_{Rk} = f_y A$, $M_{y,Rk} = f_y W_{pl,y}$ and $M_{z,Rk} = f_y W_{pl,z}$;
- $\Delta M_{y,Ed}$ and $\Delta M_{z,Ed}$: additional bending moments due to shift in centroidal axis of Class 4 cross-sections;

- χ_y and χ_z: resistance reduction coefficients due to flexural buckling around the y and z axes, respectively;
- χ_{LT}: out-of-plane lateral-torsional buckling reduction factor;
- k_{yy}, k_{yz}, k_{zy} and k_{zz}: interaction coefficients;
- γ_{M1}: buckling coefficient given as $\gamma_{M1} = 1,0$, [27].

Thus, considering the factors mentioned above regarding the scope of this study, χ_{LT} is treated as being 1.0, and $\Delta M_{y,Ed}$ and $\Delta M_{z,Ed}$ are neglected. Also, since no moments around the weak axis are present, the last fraction of the buckling resistance equations are to be ignored, given that $M_{z,Ed} = 0$, so Equations 3.4 and 3.5 can be rewritten into Equations 3.6 and 3.7.

$$\frac{N_{Ed}}{\chi_y N_{Rk}} + k_{yy}\frac{M_{y,Ed}}{M_{y,Rk}} \leq 1,0 \tag{3.6}$$

$$\frac{N_{Ed}}{\chi_z N_{Rk}} + k_{zy}\frac{M_{y,Ed}}{M_{y,Rk}} \leq 1,0 \tag{3.7}$$

The resistance reduction factors χ_y and χ_z due to flexural buckling, for each axis, are calculated by Equation 3.8.

$$\chi = \frac{1}{\Phi + \sqrt{\Phi^2 + \bar{\lambda}^2}} \tag{3.8}$$

In this equation,

$$\Phi = 0,5[1 + \alpha(\bar{\lambda} - 0,2) + \bar{\lambda}^2] \tag{3.9}$$

$$\bar{\lambda} = \sqrt{\frac{Af_y}{N_{cr}}} \tag{3.10}$$

The non-dimensional slenderness $\bar{\lambda}$ is calculated based on the critical elastic buckling load N_{cr} of the member, as well as its cross-sectional area A and steel yield strength f_y. For linear members, the buckling critical load is determined using classical Euler's

theory for elastic buckling considering a perfect column submitted to a compressive force, developing uniform compression throughout the member's length, as shown in Equation 3.11.

$$N_{cr} = \frac{n\pi^2 EI}{L_b^2} \tag{3.11}$$

In this equation, n is the buckling mode for which the critical load is being calculated. In practical cases, the buckling mode that yields the smallest critical load is considered for safety verifications, assuming then $n = 1$. L_b is the buckling length of the member, that depends on the member's length but also on the support conditions, as well as the buckling mode.

The coefficient α is an imperfection factor given in accordance to the appropriate buckling curve, obtained in Table 3.1. The selection of the buckling curve depends on section type and geometry, steel class and buckling axis, as shown in Table 3.2 for doubly-symmetric I/H rolled or welded sections.

Buckling curve	a_0	a	b	c	d
Imperfection factor α	0,13	0,21	0,34	0,49	0,76

Table 3.1: Imperfection factors for buckling curves, [27].

Cross section		Limits		Buckling about axis	Buckling curve: S 235, S 275, S 355, S 420	Buckling curve: S 460
Rolled sections	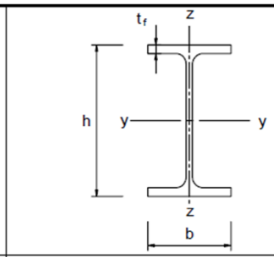	$h/b > 1{,}2$	$t_f \leq 40$ mm	y – y z – z	a b	a_0 a_0
			40 mm < $t_f \leq 100$	y – y z – z	b c	a a
		$h/b \leq 1{,}2$	$t_f \leq 100$ mm	y – y z – z	b c	a a
			$t_f > 100$ mm	y – y z – z	d d	c c
Welded I-sections	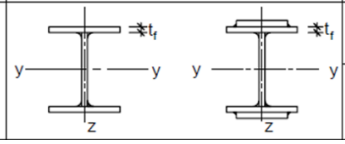		$t_f \leq 40$ mm	y – y z – z	b c	b c
			$t_f > 40$ mm	y – y z – z	c d	c d

Table 3.2: Selection of buckling curves, [27].

3.2 Elements under bending moments and axial force at elevated temperatures

3.2.1 Steel properties at elevated temperatures

As mentioned before, when unprotected steel structural members undergo fire conditions, the internal profile temperature rises, causing material properties crucial to structural resistance to be degraded. In this aspect, the most critical mechanical properties affected during the occurence of a fire event are the steel yield strength and elastic modulus, which affect directly the steel stress-strain behavior.

Taking these facts into consideration, the Eurocode 3 Part 1-2, [44], defines the steel thermal and mechanical properties depending on the temperature, to be employed in fire design and strength calculations of structures.

3.2.1.1 Strength and deformations

In order to account for alterations in strength and stiffness due to temperature changes, reduction factors in reference to yield strength and elastic modulus at 20°C are given in Eurocode 3 Part 1-2, so updated stress *versus* strain curves are determined for different levels of steel temperature.

Then, the effective yield strength $f_{y,\theta}$, proportional limit $f_{p,\theta}$ and slope of linear elastic range $E_{a,\theta}$ are calculated and a new stress-strain curve is defined for the required temperature level. This updated curve for general cases is shown in Figure 3.1, and it is divided in distinct ranges: the first range comprises the elastic regime following Hooke's Law, up until the proportional limit given by ($f_{p,\theta}$,$\varepsilon_{p,\theta}$). From this point on, steel behavior is considered nonlinear until the occurance of yielding in point ($f_{y,\theta}$,$\varepsilon_{y,\theta}$), for which stress is considered to be constant until limiting strain point $\varepsilon_{t,\theta}$ is reached. After this point, stress decreases linearly until collapse in ultimate strain $\varepsilon_{u,\theta}$.

The functions defining the relationships described above are calculated based on the equations given in Table 3.3.

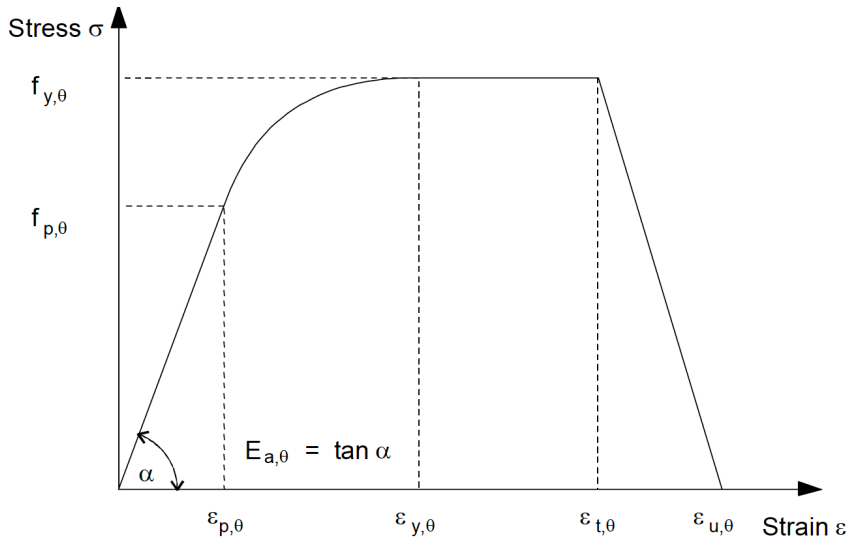

Figure 3.1: Stress-strain curves due to temperature changes, [44].

Strain range ε	**Stress** σ	**Tangent modulus**
$\varepsilon \leq \varepsilon_{p,\theta}$	$\varepsilon E_{a,\theta}$	$E_{a,\theta}$
$\varepsilon_{p,\theta} < \varepsilon < \varepsilon_{y,\theta}$	$f_{p,\theta} - c + (b/a)[a^2 - (\varepsilon_{y,\theta} - \varepsilon)^2]^{0.5}$	$\frac{b(\varepsilon_{y,\theta}-\varepsilon)}{a[a^2-(\varepsilon_{y,\theta}-\varepsilon)^2]^{0.5}}$
$\varepsilon_{y,\theta} \leq \varepsilon \leq \varepsilon_{t,\theta}$	$f_{y,\theta}$	0
$\varepsilon_{t,\theta} < \varepsilon < \varepsilon_{u,\theta}$	$f_{y,\theta}[1 - (\varepsilon - \varepsilon_{t,\theta})/(\varepsilon_{u,\theta} - \varepsilon_{t,\theta})]$	-
$\varepsilon = \varepsilon_{u,\theta}$	0	-

Table 3.3: Stress-strain parameters, [44].

In this table, the strain range limits are given by $\varepsilon_{p,\theta} = f_{p,\theta}/E_{a,\theta}$, $\varepsilon_{y,\theta} = 0,02$, $\varepsilon_{t,\theta} = 0,15$ and $\varepsilon_{u,\theta} = 0,20$. Additionally, parameters a, b and c are given by Equations 3.12 to 3.14.

$$a^2 = (\varepsilon_{y,\theta} - \varepsilon_{p,\theta})(\varepsilon_{y,\theta} - \varepsilon_{p,\theta} + c/E_{a,\theta}) \tag{3.12}$$

$$b^2 = c(\varepsilon_{y,\theta} - \varepsilon_{p,\theta})E_{a,\theta} + c^2 \tag{3.13}$$

$$c = \frac{(f_{y,\theta} - f_{p,\theta})^2}{(\varepsilon_{y,\theta} - \varepsilon_{p,\theta})E_{a,\theta} - 2(f_{y,\theta} - f_{p,\theta})} \tag{3.14}$$

Effective yield strength, proportional limit and elastic tangent modulus are determined by the reduction factors given in Table 3.4, for each temperature level. Figure 3.2 depicts how the reduction factors are affected as temperature increases. Also, it is

important to note that, for temperature levels not included in Table 3.4, linear interpolation must be used to obtain correct values for all reduction factors.

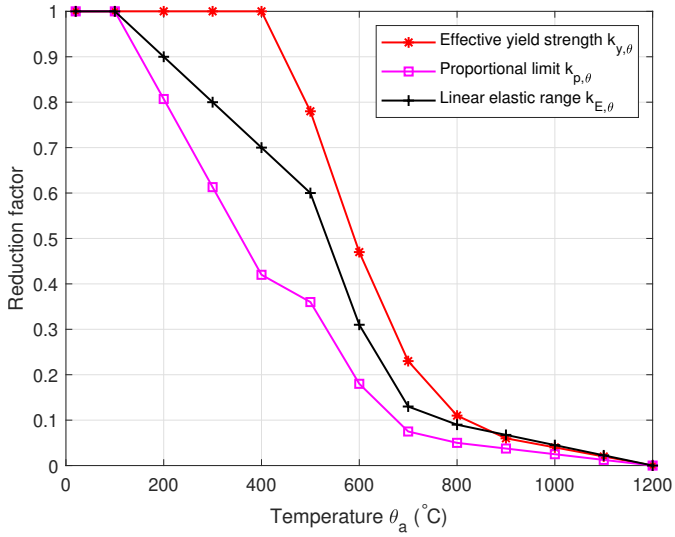

Figure 3.2: Reduction factors *versus* temperature.

Thus, for steel class S275 utilized in this paper, stress-strain curves obtained from the methodology exposed above are shown in Figure 3.3 for the range of temperatures given in Table 3.4.

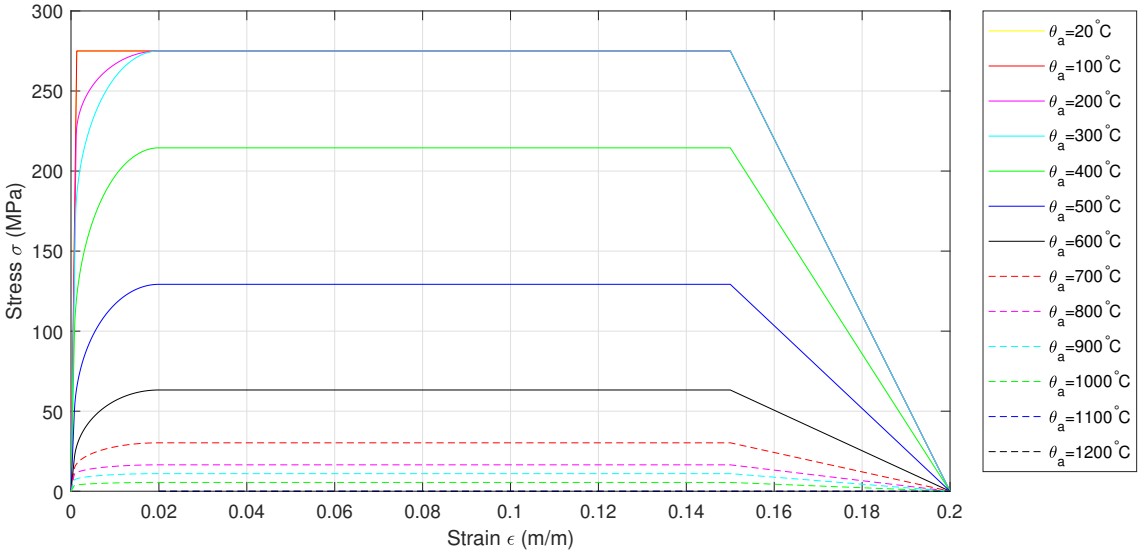

Figure 3.3: Stress-strain curves of S275 steel for various temperatures.

Temperature θ_a	**Effective yield strength** $k_{y,\theta} = f_{y,\theta}/f_y$	**Proportional limit** $k_{p,\theta} = f_{p,\theta}/f_y$	**Elastic modulus** $k_{E,\theta} = E_{a,\theta}/E_a$
20°C	1,000	1,000	1,000
100°C	1,000	1,000	1,000
200°C	1,000	0,807	0,900
300°C	1,000	0,613	0,800
400°C	1,000	0,420	0,700
500°C	0,780	0,360	0,600
600°C	0,470	0,180	0,310
700°C	0,230	0,075	0,130
800°C	0,110	0,050	0,090
900°C	0,060	0,0375	0,0675
1000°C	0,040	0,0250	0,0450
1100°C	0,020	0,0125	0,0225
1200°C	0,000	0,0000	0,0000

Table 3.4: Reduction factors due to steel temperature variation.

However, since the *ANSYS Mechanical APDL* FEM package does not allow negative stress-strain slopes, the portion between $\varepsilon_{t,\theta}$ and $\varepsilon_{u,\theta}$ is kept constant and parallel to the strain axis.

It is noticeable that for steel temperatures up until 100°C, mechanical properties are not affected by temperature changes. Although, during fire events, temperatures may get much higher than this value, so it is necessary to verify the safety of the building accordingly.

3.2.1.2 Relative thermal elongation

Thermal elongation occurs basically due to the inherent expansion of most solid materials when submitted to an increase in temperature. When this happens, material's molecules face an increase in kinetic energy and consequently vibrate more, creating separation between molecules that macroscopically show as variation of size in the member.

For carbon steels, relative thermal elongation $\Delta l/l$ is defined in three temperature ranges, as given in EC3 Part 1-2, [44] and shown in Equations 3.15 to 3.17, in m/m.

- $20°C \leq \theta_a < 750°C$:

$$\Delta l/l = 1,2 \times 10^{-5}\theta_a + 0,4 \times 10^{-8}\theta_a^2 - 2,416 \times 10^{-4} \tag{3.15}$$

- $750°C \leq \theta_a \leq 860°C$:

$$\Delta l/l = 1,1 \times 10^{-2} \tag{3.16}$$

- $860°C < \theta_a \leq 1200°C$:

$$\Delta l/l = 2 \times 10^{-5}\theta_a - 6,2 \times 10^{-3} \tag{3.17}$$

Figure 3.4 illustrates the variation of relative thermal elongation with temperature, as given by the equations above.

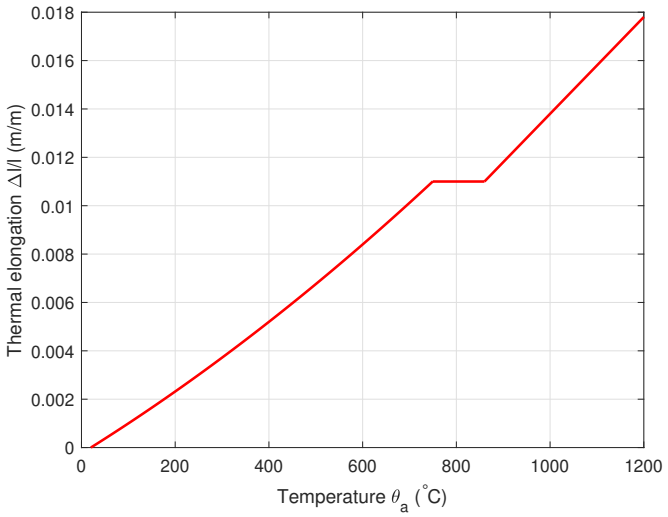

Figure 3.4: Thermal elongation as a function of temperature, [44].

3.2.1.3 Thermal conductivity

Thermal conductivity measures the material's ability to conduct heat through its interior when under a difference in temperature between two surfaces. For carbon steels,

thermal conductivity λ_a is defined in two temperature ranges, as given in EC3 Part 1-2, [44] and shown in Equations 3.18 and 3.19, in W/mK, which generate the plot shown in Figure 3.5.

- $20°C \leq \theta_a < 800°C$:

$$\lambda_a = 54 - 3,33 \times 10^{-2}\theta_a \tag{3.18}$$

- $800°C \leq \theta_a \leq 1200°C$:

$$\lambda_a = 27,3 \tag{3.19}$$

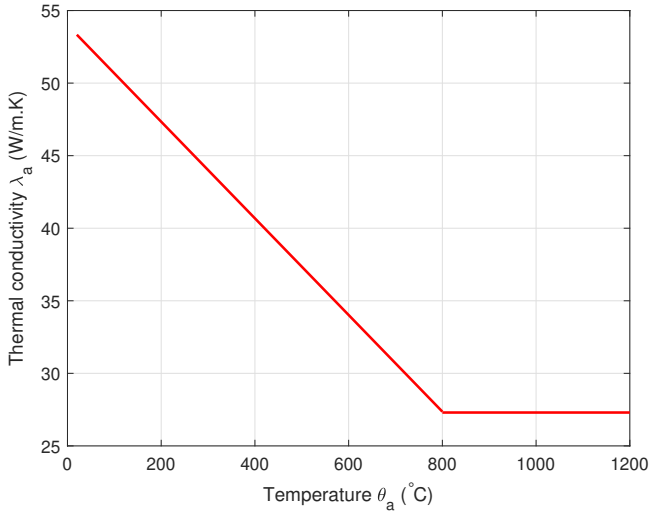

Figure 3.5: Thermal conductivity as a function of temperature, [44].

3.2.1.4 Specific heat

Specific heat is the amount of energy (measured in Joules) required to increase 1 Kelvin in temperature in 1 kilogram of mass for a material. For this reason, it is an important factor in the internal energy development calculation for fire design of steel members. It is defined by the EC3 Part 1-2, [44], in four temperature ranges, given by Equations

3.20 to 3.23, in J/kgK, which generate the plot shown in Figure 3.6. It can be seen that, between 600°C and 800°C, there is an abrupt increase in specific heat of carbon steel.

- $20°C \leq \theta_a < 600°C$:

$$c_a = 425 + 7,73 \times 10^{-1}\theta_a - 1,69 \times 10^{-3}\theta_a^2 + 2,22 \times 10^{-6}\theta_a^3 \tag{3.20}$$

- $600°C \leq \theta_a < 735°C$:

$$c_a = 666 + \frac{13002}{738 - \theta_a} \tag{3.21}$$

- $735°C \leq \theta_a < 900°C$:

$$c_a = 545 + \frac{17820}{\theta_a - 731} \tag{3.22}$$

- $900°C \leq \theta_a \leq 1200°C$:

$$c_a = 650 \tag{3.23}$$

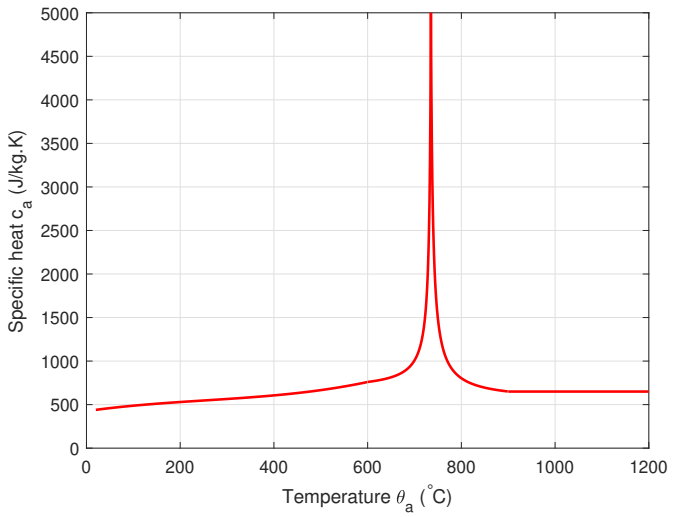

Figure 3.6: Specific heat as a function of temperature, [44].

3.2.2 Verification domains for fire safety

According to Eurocode 1 Part 1-2, [45], verifications for fire resistance in members can be carried out in three distinct domains: time, strength and temperature.

In the time domain, fire resistance is verified when the design value of the time resistance $t_{fi,d}$ of the structure is greater or equal to the required resistance time $t_{fi,requ}$. The required time is given based on the type of building and utilization characteristics, since the time necessary to fully evacuate larger or densely populated buildings is greater when compared to less utilized buildings, i.e. storage rooms or industrial constructions.

In the strength domain, the design fire resistance of the member $R_{fi,d,t}$ in the required time t must be greater or equal to the design effect of the relevant actions $E_{fi,d,t}$ at the same instant.

In the temperature domain, the design value of the material temperature θ_d must be smaller or equal to the design value of the critical temperature θ_{cr} of the material.

Generally, fire resistance of steel members ir verified according to the strength domain, because it provides a safety margin for evacuation since the resistance at a given temperature must always be greater than the effects of applied actions.

3.2.3 Internal temperature development in exposed steel members

Considering the worst case scenario during an event of fire, the increase in temperature $\Delta\theta_{a,t}$ of an unprotected internal steel member submitted to an equivalent uniform temperature distribution in the cross section, during a time interval Δt is calculated using Equation 3.24, [44].

$$\Delta\theta_{a,t} = k_{sh}\frac{A_m/V}{c_a\rho_a}\dot{h}_{net}\Delta t \tag{3.24}$$

In this equation, k_{sh} is the shadow factor, given by Equation 3.25 for I sections, A_m/V

is the section factor for unprotected members, c_a is the specific heat (given above, depending on temperature grade), ρ_a is the steel unit mass ($\rho_a = 7850\,kg/m^3$, independent of temperature) and $\dot{h}_{net}$ is the net heat flux per unit area.

$$k_{sh} = 0,9\frac{[A_m/V]_b}{[A_m/V]} \tag{3.25}$$

The value of $[A_m/V]_b$ is called the box factor for the section shadow effect. The ratio A_m/V depends on section geometry and surfaces exposed to fire. For an open sections (I and H profiles) subjected to fire on all sides, it is given by the ratio between section perimeter and area. On the other hand, for open sections subjected to fire in only three sides (as when I/H beams have encaseb webs in concrete floor slabs), it is given by the perimeter of the surfaces exposed to fire divided by the cross section area.

For other sections rather than I or H profiles, the shadow effect is calculated only by $k_{sh} = [A_m/V]_b/[A_m/V]$. However, considering $k_{sh} = 1,0$ leads to conservative results, and it can be used for non-conventional cross sections or fire exposure cases.

The net heat flux is obtained by the summation of convective $\dot{h}_{net,c}$ and radiative $\dot{h}_{net,r}$ heat fluxes (per unit surface area), given by Equations 3.26 and 3.27, respectively, in W/m^2. These expressions are obtained from the Eurocode 1 Part 1-2, [45], which provides guidelines for the computation of fire actions on structures and buildings.

$$\dot{h}_{net,c} = \alpha_c(\theta_g - \theta_m) \tag{3.26}$$

$$\dot{h}_{net,r} = \Phi\varepsilon_m\varepsilon_f\sigma[(\theta_r + 273)^4 - (\theta_m + 273)^4] \tag{3.27}$$

For the above equations, it is given that:

α_c: convection coefficient (W/m^{2}K);

θ_g: gas temperature ($^\circ$C);

θ_m: material surface temperature ($^\circ$C);

θ_r: effective radiation temperature of the fire environment ($^\circ$C);

Φ: section configuration factor;

ε_m: material surface emissivity (for steel $\varepsilon_m = 0.7$);

ε_f: fire emissivity ($\varepsilon_f = 1.0$);

σ: Stefan-Boltzmann constant ($\sigma = 5.67 \times 10^{-}8\, W/m^2K^4$).

When a member is fully fire-embedded, the effective radiation temperature θ_r can be replaced by the gas temperature θ_g. Also, the Eurocode 1 Part 1-2, [45], provides a simplified method for calculating Φ, although it can be considered as $\Phi = 1.0$ if no specific data are supplied. Additionally, the Eurocode 1 Part 1-2 determines that the time interval Δt must be at a maximum value of 5 seconds. The gas temperature θ_g is calculated from nominal fire curves that describe the evolution of a fire event over time.

3.2.4 Nominal temperature-time curves

In order to describe the phases and characteristics of fire event, nominal expressions correlating the gas temperature θ_g with time were derived from experimental results and numerical solutions of fluid dynamics problems, as well as specific characteristics of fire and material properties. Eurocode 1 Part 1-2, [45], defined three types of nominal fire curves to be used in fire design.

The standard temperature-time curve is given by Equation 3.28. This expression is widely used worldwide and is described by the international ISO 834 standard from 1994, [46]. This curve represents fire in cellulose-based materials, and is used for design of internal fires.

$$\theta_g = 20 + 345 log_{10}(8t + 1) \tag{3.28}$$

In the case of external members, which can be subjected to the influence of an internal fire or from compartments located at the sides or below the element under consideration, another expression for the gas temperature was developed, and it is shown in Equation 3.29.

$$\theta_g = 660(1 - 0.687e^{-0.32t} - 0.313e^{-3.8t}) + 20 \tag{3.29}$$

Also, when the event of fire involves the presence of hydrocarbon-based materials, which cause fires with higher intensity when compared to standard fires, a different expression given by Equation 3.30 is used for fire design purposes.

$$\theta_g = 1080(1 - 0.325e^{-0.167t} - 0.675e^{-2.5t}) + 20 \tag{3.30}$$

Figure 3.7 shows a comparison between the aforementioned temperature-time curves. It is noticeable that hydrocarbon fires reach higher temperatures overall and in a smaller period of time when compared to the standard and external fire cases. However, for fire duration times longer than approximately 3 hours (180 minutes) the standard fire curve yields greater temperature values than the hydrocarbon curve. Also, both external and hydrocarbon curves show virtually no change in temperature for fire duration times longer than approximately 30 minutes.

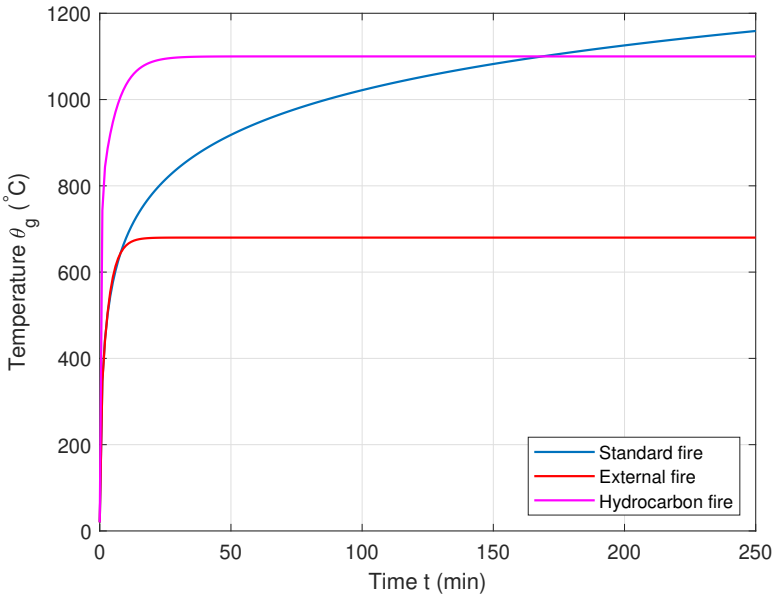

Figure 3.7: Nominal temperature-time curves, [45].

Nonetheless, all fire cases described above do not model a cooling phase inherent to natural fires as they extinguish, so the steel member temperature conservatively is considered to always increase.

3.2.5 Resistance and safety verification

Following the same methodology for strength and buckling safety verifications for elements under natural temperature given in Equations 3.4 and 3.5 in Section 3.1, in case of fire design of members under a combination of axial force and bending moment, verifications are made based on Equations 3.31 and 3.32.

$$\frac{N_{fi,Ed}}{\chi_{min,fi} A k_{y,\theta} \frac{f_y}{\gamma_{M,fi}}} + k_y \frac{M_{y,fi,Ed}}{W_{pl,y} k_{y,\theta} \frac{f_y}{\gamma_{M,fi}}} + k_z \frac{M_{z,fi,Ed}}{W_{pl,z} k_{y,\theta} \frac{f_y}{\gamma_{M,fi}}} \leq 1,0 \tag{3.31}$$

$$\frac{N_{fi,Ed}}{\chi_{z,fi} A k_{y,\theta} \frac{f_y}{\gamma_{M,fi}}} + k_{LT} \frac{M_{y,fi,Ed}}{\chi_{LT,fi} W_{pl,y} k_{y,\theta} \frac{f_y}{\gamma_{M,fi}}} + k_z \frac{M_{z,fi,Ed}}{W_{pl,z} k_{y,\theta} \frac{f_y}{\gamma_{M,fi}}} \leq 1,0 \tag{3.32}$$

In these expressions,

- $N_{fi,Ed}$, $M_{y,fi,Ed}$ e $M_{z,fi,Ed}$: design values of axial forces and bending moments around the y and z axes at moment t, respectively, for fire design;
- $\chi_{min,fi}$ and $\chi_{z,fi}$: resistance reduction coefficients due to flexural buckling for fire design;
- $k_{y,\theta}$: yield strength reduction factor for steel temperature θ_a reached at instant t according to Table 3.4;
- $\chi_{LT,fi}$: out-of-plane lateral-torsional buckling reduction factor for fire design;
- k_y, k_z and k_{LT}: interaction coefficients for fire design;
- $\gamma_{M1,fi}$: buckling coefficient for fire design given as $\gamma_{M1,fi} = 1,0$, [45].

Bearing in mind that, in the scope of this paper, out-of-plane deformations on the arches and curved beams are prevented by adequate lateral bracing, consequently it is considered that $\chi_{LT,fi} = 0$. Also, bending moments around the weak axis are neglected, making $M_{z,fi,Ed} = 0$. So, replacing the known variables into Equations 3.31 and 3.32 yield Equations 3.33 and 3.34.

$$\frac{N_{fi,Ed}}{\chi_{min,fi} A k_{y,\theta} f_y} + k_y \frac{M_{y,fi,Ed}}{W_{pl,y} k_{y,\theta} f_y} \leq 1,0 \tag{3.33}$$

$$\frac{N_{fi,Ed}}{\chi_{z,fi} A k_{y,\theta} f_y} + k_{LT} \frac{M_{y,fi,Ed}}{W_{pl,y} k_{y,\theta} f_y} \leq 1,0 \tag{3.34}$$

The flexural buckling reduction coefficients $\chi_{min,fi}$ and $\chi_{z,fi}$ are given by Equation 3.35.

$$\chi_{fi} = \frac{1}{\varphi_\theta + \sqrt{\varphi_\theta^2 + \bar{\lambda}_\theta^2}} \tag{3.35}$$

Where,

$$\varphi_\theta = 0,5[1 + \alpha \bar{\lambda}_\theta + \bar{\lambda}_\theta^2] \tag{3.36}$$

$$\alpha = 0,65\sqrt{235/f_y} \tag{3.37}$$

$$\bar{\lambda}_\theta = \bar{\lambda}[k_{y,\theta}/k_{E,\theta}]^{0,5} \tag{3.38}$$

In Equation 3.38, $\bar{\lambda}$ is given by Equation 3.10, which depends on the critical buckling load at natural temperature. The reduction factors for the yield strength $k_{y,\theta}$ and elastic modulus $k_{E,\theta}$ are given in Table 3.4 for the steel temperature reached at instant t.

Chapter 4

In-plane stability of steel arches

This chapter focuses on the elastic in-plane buckling critical load and stability investigation for pinned and fixed steel arches. Results obtained from prior studies found in the literature about buckling of steel arches and curved beams are compared to numerical *FEM* analyses via software *ANSYS Mechanical APDL*®, for arches under room temperature.

Linear and nonlinear formulations with respective *FEM* simulations were performed for a variety of arch spans and rise-to-span ratios, aiming to understand the influences of these main geometrical parameters on the buckling behavior. In this context, the main goal in each analysis is to find the critical load F_{cr} according to the load case described in the next section.

4.1 Elastic critical buckling load

One of the main parameters in the study of buckling is the critical load. This parameter marks the point when a loaded structure switches from a stable to an unstable equilibium condition, where small increments of load cause large deformations. Nonetheless, considering that generally for sufficiently slender members buckling occurs prior to the beginning of plastification, the elastic domain is used to study buckling behavior.

Moreover, two different approaches for determining the elastic critical buckling load in steel arches are commonly employed. The linear elastic approach makes simplifications regarding pre-buckling displacements, considering them to be linear so stresses can be easily determined. On the other hand, nonlinear elastic formulations of the buckling critical load take the effects of pre-buckling deformations and their nonlinear behavior into account, generally yielding lower values when compared to classical linear theories.

As demonstrated by previous investigation work on steel arches, [33, 39, 47], it is important to firstly distinguish two geometrical categories: shallow and deeper arches. This categorization is due to considerable differences in pre-buckling behavior, since shallow arches present nonlinearities and substantial deformations that may reduce buckling resistance, and for this reason classical linear theories for critical load may overestimate the resistance of shallow arches.

A classification method proven to be effective is based on the internal included angle α, where arches with $2\alpha < \pi/2$ are considered to be shallow, and when $2\alpha \geq \pi/2$ they are treated as deeper arches. Also, another significant parameter in this type of analysis is the modified slenderness λ_s, which depends on the cross-sectional properties and geometry of the arch, and it is given by Equation 4.1, [39], where i_y is the section radius of gyration for the strong axis and S is the developed arch length.

$$\lambda_s = \frac{S^2}{4 i_y R} = \frac{R\alpha^2}{i_y} \tag{4.1}$$

In the following sections, both linear and nonlinear buckling will be studied. Also, a comparison between results of critical load formulations for different loading cases will be done, followed by numerical simulations of arches under a combination of axial forces and bending moments.

4.1.1 Linear elastic critical load

Since arches may be subjected to a variety of loads developing different stress distributions along their length, a critical load expression for each specific load case would be laborous and unpractical to achieve. Thus, in order to resolve this problem, researchers seeked to develop conservative expressions for simpler loading conditions, providing lower bound values favoring safety in the design process.

In this aspect, the critical buckling load for circular arches under a uniform radially distributed load perpendicular to their central axis is oftenly used. This type of load generates a uniform compressive axial force throughout the arch, and in these cases bending moment is considered to be negligible.

Timoshenko and Gere, [36], determined the critical load for the case described above, from the differential equation describing buckling deflections, shown in Equation 4.2, where ω represents the arch radial deflection curve as a function of the angle θ.

$$\frac{d^2\omega}{d\theta^2} + \omega = -\frac{MR^2}{EI} \tag{4.2}$$

Considering that the applied bending moment M can be written as a product between the axial force at each section and the corresponding radial deflection, Equation 4.2 becomes

$$\frac{d^2\omega}{d\theta^2} + \omega + \frac{N\omega R^2}{EI} = 0 \tag{4.3}$$

Since this expression is a homogeneous second-order differential equation with independent coefficients, its solution in order to ω yields

$$\omega = C_1 cos(\sqrt{k}\theta) + C_2 sin(\sqrt{k}\theta) \tag{4.4}$$

In this expression, C_1 and C_2 are integration coefficients and k is given by

$$k = 1 + \frac{NR^2}{EI} \tag{4.5}$$

Applying the boundary condition from the pin support at $\theta = 0$ where $\omega = 0$, one gets $C_1 cos(\sqrt{k}0) + C_2 sin(\sqrt{k}0) = 0$, yielding $C_1 = 0$. On the opossite end, the pin support at $\theta = 2\alpha$ where also $\omega = 0$ yields $C_2 sin(\sqrt{k}2\alpha) = 0$. Thus, in order to avoid the trivial solution ($C_2 = 0$), the equality $sin(2\alpha\sqrt{k}) = 0$ must be valid.

Then, considering that the buckled shape follows an anti-symmetrical sinusoidal curve (as seen in Figure 2.7b) and that the centerline of the arch is inextensible (neglecting axial deformations), this previous expression results in $2\alpha\sqrt{k} = \pi$.

From Equation 4.5, the axial critical force N_{cr} is determined as a function of the arch radius R, internal half included angle α and flexural stiffness EI, as shown in Equation 4.6.

$$N_{cr} = \frac{EI}{R^2}\left(\frac{\pi^2}{\alpha^2} - 1\right) \tag{4.6}$$

Following a different methodology using the membrane and bending strain formulation, [47], the longitudinal strain at an arbitrary point P at a given vertical coordinate along the cross-section is given by

$$\varepsilon_P = \varepsilon_m + \varepsilon_b \tag{4.7}$$

In this expression, the membrane strain is given by $\varepsilon_m = v' - \omega + \frac{1}{2}(\omega' + v)^2$, and the bending strain is $\varepsilon_b = -y(\omega'' + v')/R$. In these expressions, ω and v are the radial and axial dimensionless displacements, respectively.

Then, the energy equation for in-plane buckling is derived establishing that the second variation of total potential energy of the arch is null, as

$$\frac{1}{2}\int_{-\alpha}^{+\alpha}\left[EA(v_b' - \omega_b)^2 + \frac{EI(\omega_b'' + v_b')^2}{R^2} - N(\omega_b' + v_b)^2\right]Rd\theta = 0 \tag{4.8}$$

Calling the Euler-Lagrange second-order partial differential equations of variational calculus that make this functional stationary, which means that the solution leads to the functions that make the total potential energy to be minimum, the differential equilibrium

equations for both radial and axial directions are obtained, as shown in Equations 4.9 and 4.10, respectively, [47].

$$[-N(\omega_b' + v_b)]' + EA(v_b' - \omega_b) - \left[\frac{EI(\omega_b'' + v_b')}{R^2}\right]'' = 0 \tag{4.9}$$

$$- N(\omega_b' + v_b) - [EA(v_b' - \omega_b)]' - \left[\frac{EI(\omega_b'' + v_b')}{R^2}\right]' = 0 \tag{4.10}$$

Assuming that the centerline of the arch is inextensible ($(v_b' - \omega_b) = 0$) and applying the proper boundary conditions for a pinned-pinned arch where $\omega_b'' = 0$ at $\theta = -\alpha$ and $\theta = +\alpha$, [47], the lowest anti-symmetrical critical load is given in Equation 4.11.

$$N_{cr} = \frac{\pi^2 EI}{(S/2)^2} \tag{4.11}$$

In the case of fixed-ended arches, a parameter k is introduced in Equation 4.11 to account for in-plane rotation restriction imposed by the fixed supports, yielding Equation 4.12. This parameter increases alongside the internal included angle, reaching a maximum value of $k = 1,5$ when $2\alpha = \pi$. When $2\alpha = 0$ the structure becomes a fixed column and $k = 1,43$, [47]. Since this variation is not very significant, and favoring stability safety, the smaller value of this parameters is usually adopted.

$$N_{cr} = \frac{k^2 \pi^2 EI}{(S/2)^2} \tag{4.12}$$

Rewritting both these above expressions as functions of the radius and half internal angle based on the developed arch length $S = 2\alpha R$, Equations 4.11 and 4.12 become

$$N_{cr} = \frac{\pi^2 EI}{R^2 \alpha^2} \tag{4.13}$$

$$N_{cr} = \frac{k^2 \pi^2 EI}{R^2 \alpha^2} \tag{4.14}$$

Additionally to these formulations, the Annex D.3 in Eurocode 3 Part 2, [22], regarding the design and safety of steel bridges deals with buckling of arch structures, and it provides a simplified method to determine the critical in-plane buckling load for arches of various geometries. This method is shown in Equation 4.15.

$$N_{cr} = \left(\frac{\pi}{\beta s}\right)^2 EI \tag{4.15}$$

In this expression, s is the half developed length given by $s = \alpha R$, and β is a buckling length factor depending on the arch rise-to-span ratio and loading case, and it is given in Figure 4.1 for pin- and fixed-supported elements.

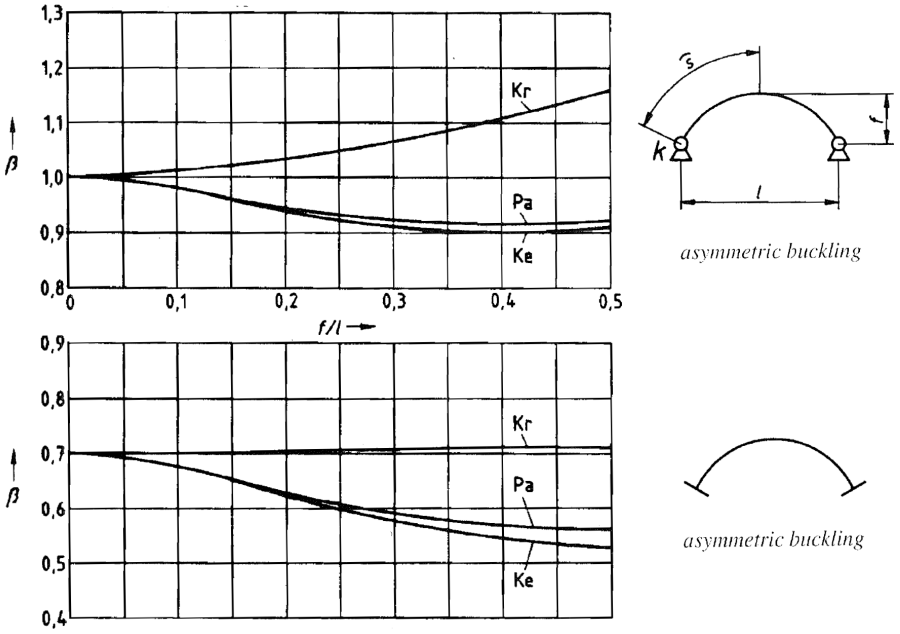

Figure 4.1: Buckling length factors according to Eurocode 3-2, [22].

In the image above, Pa, Ke and Kr are the curves for a parabolic, chain form and circular arch, respectively. Also, for circular arches it is assumed a radial loading that generates uniform compression, as is the case for the aforementioned methods.

4.1.2 Nonlinear elastic critical load

Bearing in mind the issues priorly stated in the critical load calculation for shallow arches, nonlinear elastic formulations are necessary to provide a reliable solution that takes into account the nonlinearities and significant arch deformations in the pre-buckling phase.

Pi, Bradford and Uy, [47], developed nonlinear critical buckling load expressions for both symmetrical and anti-symmetrical cases in shallow arches, also considering uniform compression. These formulations were obtained from the nonlinear equilibrium conditions, and are defined as reduction coefficients for the linear critical load given in Equations 4.13 and 4.14. Also, these results were validated by the authors in two different finite element programs, which strongly agreed both between *FEM* packages and with those obtained in the derived equations.

In the anti-symmetrical buckling case for pin-ended arches, pre-buckling displacements are symmetrical (for this type of loading) while post-buckling displacements are anti-symmetrical, so an analytical solution is easily obtained, and it is given in Equation 4.16.

$$N_{cr} = \frac{9 \pm \sqrt{(2\pi^2+6)^2 - \frac{12(2\pi^2+15)\pi^4}{\lambda_s^2}}}{2\pi^2+15} \left(\frac{\pi^2 EI}{R^2\alpha^2}\right) \tag{4.16}$$

For the symmetrical snap-through expression in pin-ended arches, both pre- and post-buckling displacements are symmetrical, so a solution for the critical load is obtained by a rather complicated iterative process, [47]. However, the authors proposed a approximation expression for the critical symmetrical load, as seen in Equation 4.17.

$$N_{cr} = \left(0,15 + 0,006\lambda_s^2\right) \left(\frac{\pi^2 EI}{R^2\alpha^2}\right) \tag{4.17}$$

In both expressions above, the reduction coefficient depends on the modified slenderness λ_s of the arch, previously defined in Equation 4.1. This parameter is also used to set a domain for each buckling mode. A real solution for Equation 4.16 exists when

$\lambda_s \geq 7,83$ so the anti-symmetrical mode may occur, and when $\lambda_s \leq 9,38$ a real solution for the symmetrical mode exists in Equation 4.17. In the interval $7,83 \leq \lambda_s \leq 9,38$ both solutions are real, so either buckling mode may occur.

In the same manner as for pinned arches, in the case of fixed shallow arches an anti-symmetrical critical load expression was obtained based on the nonlinear equilibrium equations, and it is shown in Equation 4.18.

$$N_{cr} = \frac{3 \pm 2\sqrt{1 - \frac{15(1.43\pi)^2}{\lambda_s^2}}}{5} \left(\frac{k^2 \pi^2 EI}{R^2 \alpha^2} \right) \tag{4.18}$$

For symmetrical buckling of fixed shallow arches, a simplified solution was proposed following the same method for a pinned shallow arch. This solution in shown in Equation 4.19.

$$N_{cr} = \left(0,36 + 0,0011\lambda_s^2\right) \left(\frac{\pi^2 EI}{R^2 \alpha^2} \right) \tag{4.19}$$

Considering the real solutions to these equations, the symmetrical buckling mode only occurs for modified slendernesses below $\lambda_s \leq 18,60$, and the anti-symmetrical mode occurs when $\lambda_s \leq 17,40$. When $17,40 \leq \lambda_s \leq 18,60$, both buckling modes may occur.

4.2 Analyzed loading cases and geometries

Considering that arches are prone to non-usual loading cases, a investigation for arches under bending and compression will be carried out, and later compared to the critical buckling formulations previously defined for uniform compression.

For this, a symmetrical load configuration of two point loads F located at quarter span was employed. Figure 4.2 describes the general geometry, dimensions and load-support condition of the analyzed cases.

In this figure, L is the arch span, f is the arch rise, R is the arch radius, α is the half

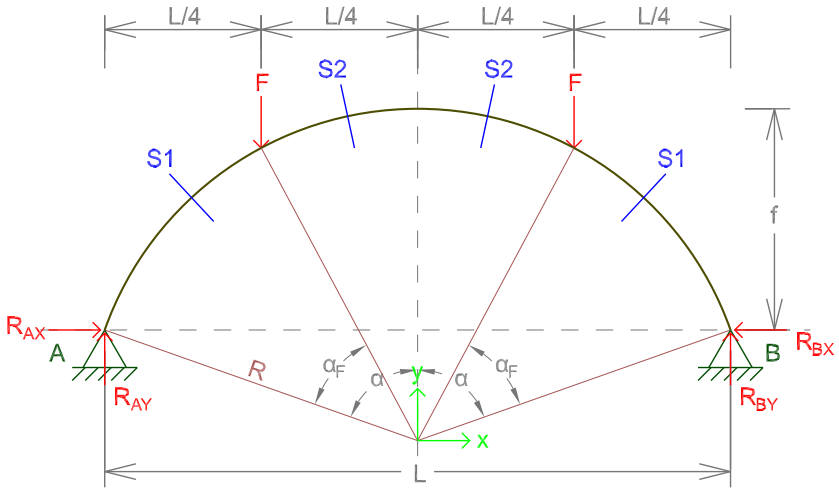

Figure 4.2: Geometry of analyzed arches.

internal angle, α_F is the internal angle of the load position and F is the applied load. The radius is determined based on span and rise, as given in Equation 4.20.

$$R = \frac{(L/2)^2 + f^2}{2f} \tag{4.20}$$

The half internal angle is calculated from the horizontal length and radius, as shown in Equation 4.21.

$$\alpha = sin^{-1}\left(\frac{L/2}{R}\right) \tag{4.21}$$

The internal angle of the line connecting the load position point and the origin, measured from the support, is calculated from the half internal angle and radius, as exhibited in Equation 4.22.

$$\alpha_F = \alpha - sin^{-1}\left(\frac{L/4}{R}\right) \tag{4.22}$$

All investigated arches were considered to be made of IPE 100 hot-rolled profiles. Cross sectional dimensions are shown in Figure 4.3.

Then, the first step in the path to study buckling behavior of the aforementioned

IPE100
$b_f = 55,0\,mm$
$t_f = 5,7\,mm$
$h_i = 88,6\,mm$
$t_w = 4,1\,mm$
$d = 74,6\,mm$
$h = 100,0\,mm$
$r = 7,0\,mm$
$A = 1030\,mm^2$
$i_y = 0,0407\,mm$

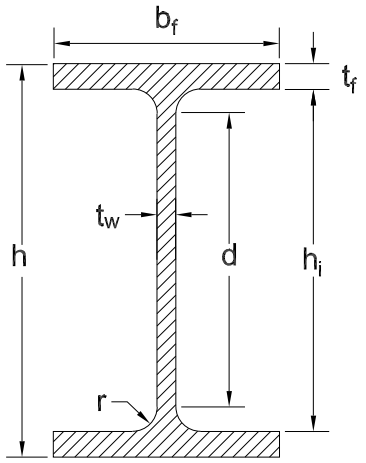

Figure 4.3: IPE100 section dimensions.

arches is to determine the distribution of internal forces along their length, which requires the solution of all reaction forces at the supports. Also, these solutions will provide a way to compare the results from this study to the current standard verifications for this type of structure.

4.2.1 Reactions and internal forces

From Figure 4.2, one notices that for pinned-pinned arches, there are four unknown reaction forces, being two horizontal (R_{AX} and R_{BX}) and two vertical (R_{AY} and R_{BY}). Considering the horizontal direction to be the x axis and vertical direction to be the y axis, with origin at center point of the arch, the in-plane two-dimensional equilibrium conditions are, in order, the summation of forces in the horizontal direction equals zero ($\sum F_X = 0$), summation of forces in the vertical direction equals zero ($\sum F_Y = 0$) and summation of moments about the left support (A) equals zero ($\sum M_A = 0$), it is found that:

$$\sum F_X = 0 = R_{AX} - R_{BX} \rightarrow R_{AX} = R_{BX} \tag{4.23}$$

$$\sum F_Y = 0 = R_{AY} + R_{BY} - F - F \rightarrow R_{AY} + R_{BY} = 2F \tag{4.24}$$

$$\sum M_A = 0 = R_{BY}.L - F\left(\frac{3L}{4}\right) - F\left(\frac{L}{4}\right) \rightarrow R_{BY}.L = F.L \tag{4.25}$$

From Equation 4.25, one can easily notice that $R_{BY} = F$. Replacing this result in Equation 4.24 yields $R_{AY} = 2F - R_{BY} = F$. However, it is still necessary to determine the horizontal reactions, henceforth denoted as $R_{AX} = R_{BX} = H$. For this, Castigliano's Theorem is employed in order to find the indeterminate reaction. This theorem states that the first partial derivative of the strain energy U in a member, with respect to an applied force F, is equal to the displacement δ_F in the point of application and along the line of action of the respective applied force, [48]. This theorem is summarized in Equation 4.26.

$$\frac{\partial U}{\partial F} = \delta_F \tag{4.26}$$

Bearing in mind that, in the arch ends, vertical and horizontal displacements are null because of the supports ($\delta_F = 0$) and the horizontal unknown reaction H is acting on these points, this theorem is strategically applied at point A, yielding

$$\frac{\partial U}{\partial H} = 0 \tag{4.27}$$

The strain energy in a general body submitted to a multiaxial stress state where deformations are in the elastic range is calculated by Equation 4.28, where V is the body's volume.

$$U = \int_V \left[\frac{1}{2E}(\sigma_x^2 + \sigma_y^2 + \sigma_z^2) - \frac{\nu}{E}(\sigma_x\sigma_y + \sigma_y\sigma_z + \sigma_x\sigma_z) + \frac{1}{2G}(\tau_{xy}^2 + \tau_{yz}^2 + \tau_{xz}^2)\right] dV \tag{4.28}$$

Considering the arch configuration shown in Figure 4.2, some simplifications and assumptions are made. Firstly, since the arch is modeled as a two-dimensional structure, axial stresses along the y and z axes are neglected, as well as the yz and xz components of the shear stresses, yielding $\sigma_y = \sigma_z = \tau_{yz} = \tau_{xz} = 0$. Nonetheless, shear

stress τ_{xy} can be neglected for its magnitude is minor when compared to other stress components should the member be slender enough, as frequently occurs in arches and curved beams.

Also, taking into account that the material follows Hooke's Law, stress components can be rewritten in terms of internal forces. The bending stress caused by a moment M is given as $\sigma_M = My/I$, where y is the distance of an arbitrary infinitesimal element to the neutral axis and I is the moment of inertia. Axial stress caused by a normal force N is given as $\sigma_N = N/A$. Thus, Equation 4.28 is then rewriten in the form of Equation 4.29.

$$U = \int_V \left[\frac{1}{2E} \left(\frac{My}{I} \right)^2 + \frac{1}{2E} \left(\frac{N}{A} \right)^2 \right] dV \tag{4.29}$$

Since arches and curved beams are prismatic elements, their volume may be determined by $V = AS$, given that A is the cross-sectional area and S is the arch developed length, given as $S = R\theta$, where θ is the internal angle. Thus, considering the radius R to be constant along the arch, one gets $dV = d(AR\theta) = RdAd\theta$, and Equation 4.29 becomes

$$U = \int_\theta \int_A \left[\frac{M^2 y^2 R}{2EI^2} + \frac{N^2 R}{2EA^2} \right] dAd\theta \tag{4.30}$$

From the geometrical definition of the moment of inertia,

$$I = \int_A y^2 dA \tag{4.31}$$

Which is replaced in the bending moment term of Equation 4.30. Finally, taking that the cross-sectional area is also constant along the member, the expression for determining the total strain energy for circular arches is given in Equation 4.32.

$$U = \int_\theta \frac{M^2}{2EI} Rd\theta + \int_\theta \frac{N^2}{2EA} Rd\theta \tag{4.32}$$

As seen in Figure 4.2, the arches investigated in the scope of this dissertation are

submitted to in-plane symmetrical loads and supports. For this reason, two different general sections (S1 and S2) perpendicular to the element longitudinal axis were drawn in order to obtain the internal force expressions for half of the arch, since the other half presents the same respective force distribution.

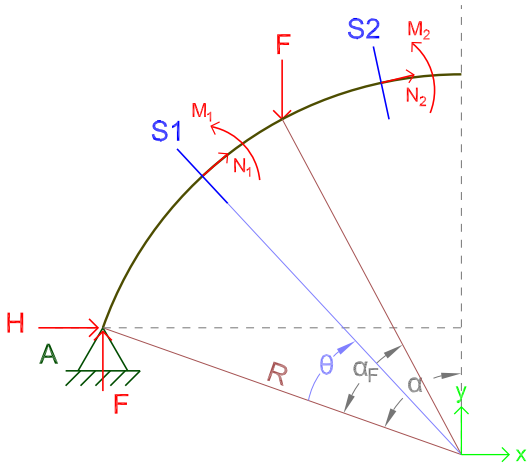

Figure 4.4: Internal forces and general sections.

In each analyzed section, internal forces N_1, N_2, M_1 and M_2 represent the axial force and bending moment distribution for the respective angular position θ. Section S1 is comprised between $0 \leq \theta \leq \alpha_F$, and section S2 between $\alpha_F \leq \theta \leq \alpha$, as exhibited in Figure 4.4.

In this aspect, Equation 4.32 can be reorganized with proper integration limits and divided into the respective internal force distributions, resulting in the expression shown in Equation 4.33.

$$U = 2\left[\int_0^{\alpha_F} \frac{M_1^2}{2EI} Rd\theta + \int_0^{\alpha_F} \frac{N_1^2}{2EA} Rd\theta + \int_{\alpha_F}^{\alpha} \frac{M_2^2}{2EI} Rd\theta + \int_{\alpha_F}^{\alpha} \frac{N_2^2}{2EA} Rd\theta\right] \tag{4.33}$$

Differentiating the expression above in order to H, one gets

$$\frac{\partial U}{\partial H} = 2\left[\int_0^{\alpha_F} \frac{M_1}{EI}\frac{\partial M_1}{\partial H}Rd\theta + \int_0^{\alpha_F} \frac{N_1}{EA}\frac{\partial N_1}{\partial H}Rd\theta + \int_{\alpha_F}^{\alpha} \frac{M_2}{EI}\frac{\partial M_2}{\partial H}Rd\theta + \int_{\alpha_F}^{\alpha} \frac{N_2}{EA}\frac{\partial N_2}{\partial H}Rd\theta\right] \tag{4.34}$$

Therefore, the expressions for internal forces are determined based on the applied loading in each section and the general geometry of the arch, and are given in Equations 4.35 through 4.38.

$$N_1 = -Hcos(\alpha - \theta) - Fsin(\alpha - \theta) \tag{4.35}$$

$$M_1 = HR\left[cos(\alpha - \theta) - cos(\alpha)\right] - F\left[\frac{L}{2} - Rsin(\alpha - \theta)\right] \tag{4.36}$$

$$N_2 = -Hcos(\alpha - \theta) \tag{4.37}$$

$$M_2 = HR\left[cos(\alpha - \theta) - cos(\alpha)\right] - \frac{FL}{4} \tag{4.38}$$

As seen in Equation 4.34, the derivatives of the internal force expressions with respect to H are needed to calculate the horizontal reaction. These derivatives are given in Equations 4.39 through 4.42.

$$\frac{\partial N_1}{\partial H} = -cos(\alpha - \theta) \tag{4.39}$$

$$\frac{\partial M_1}{\partial H} = R\left[cos(\alpha - \theta) - cos(\alpha)\right] \tag{4.40}$$

$$\frac{\partial N_2}{\partial H} = -cos(\alpha - \theta) \tag{4.41}$$

$$\frac{\partial M_2}{\partial H} = R\left[cos(\alpha - \theta) - cos(\alpha)\right] \tag{4.42}$$

Substituting these expressions above into Equation 4.34, applying the boundary condition $\partial U/\partial H = 0$ cited above and solving the respective integrals, an expression for the horizontal reaction H is obtained as a function of geometric and material properties. This expression in shown in Equation 4.43.

$$\begin{aligned}
&\frac{2FR\left(\frac{sin(\alpha)^2}{2}-\frac{sin(\alpha-\alpha_F)^2}{2}\right)}{EA}+\frac{2RH\left(\frac{\alpha}{2}-\frac{\alpha_F}{2}+\frac{sin(2\alpha-2\alpha_F)}{4}\right)}{EA}-\frac{2FR^3\left(\frac{cos(\alpha)^2}{2}-\frac{cos(\alpha-\alpha_F)^2}{2}\right)}{EI}\\
&+\frac{2R^3H\left(\alpha_F-\frac{3sin(2\alpha)}{4}+sin\left(2\alpha-\alpha_F\right)-\frac{sin(2\alpha-2\alpha_F)}{4}-sin\left(\alpha_F\right)+\frac{\alpha_F cos(2\alpha)}{2}\right)}{EI}\\
&+\frac{2R^3H\left(\frac{\alpha}{2}-\frac{\alpha_F}{2}+\frac{sin(2\alpha-2\alpha_F)}{4}\right)}{EI}+\frac{2RH\left(\frac{\alpha_F}{2}+\frac{sin(2\alpha)}{4}-\frac{sin(2\alpha-2\alpha_F)}{4}\right)}{EA}-\frac{FLR^2sin\left(\alpha-\alpha_F\right)}{2EI}\\
&+\frac{2FR^3cos\left(\alpha\right)\left(cos\left(\alpha\right)-cos\left(\alpha-\alpha_F\right)\right)}{EI}+\frac{2R^3Hcos\left(\alpha\right)^2\left(\alpha-\alpha_F\right)}{EI}\\
&-\frac{4R^3Hsin\left(\alpha-\alpha_F\right)cos\left(\alpha\right)}{EI}+\frac{FLR^2\left(sin\left(\alpha-\alpha_F\right)-sin\left(\alpha\right)\right)}{EI}+\frac{FLR^2\alpha_F cos\left(\alpha\right)}{EI}+\\
&\frac{FLR^2cos\left(\alpha\right)\left(\alpha-\alpha_F\right)}{2EI}=0
\end{aligned} \tag{4.43}$$

Solving Equation 4.43 in order to H yields

$$\begin{aligned}
H=-F\Bigg(&\frac{Icos\left(2\alpha-2\alpha_F\right)+2AR^2-Icos\left(2\alpha\right)-2AR^2cos\left(\alpha_F\right)+AR^2cos\left(2\alpha\right)}{2I\alpha+Isin\left(2\alpha\right)-3AR^2sin\left(2\alpha\right)+4AR^2\alpha+2AR^2\alpha cos\left(2\alpha\right)}\\
&\frac{-2AR^2cos\left(2\alpha-\alpha_F\right)+AR^2cos\left(2\alpha-2\alpha_F\right)-2ALRsin\left(\alpha\right)+ALRsin\left(\alpha-\alpha_F\right)}{2I\alpha+Isin\left(2\alpha\right)-3AR^2sin\left(2\alpha\right)+4AR^2\alpha+2AR^2\alpha cos\left(2\alpha\right)}\\
&\frac{+ALR\alpha cos\left(\alpha\right)+ALR\alpha_F cos\left(\alpha\right)}{2I\alpha+Isin\left(2\alpha\right)-3AR^2sin\left(2\alpha\right)+4AR^2\alpha+2AR^2\alpha cos\left(2\alpha\right)}\Bigg)
\end{aligned} \tag{4.44}$$

Table 4.1 and Figure 4.5 show the horizontal reaction results normalized to the applied load F from Equation 4.44 as a function of the rise-to-span ratio for different arch span values. It is clear that the horizontal reaction decreases as f/L ratios increase, but it is not significantly affected by the span length.

Since all reaction forces are determined, it is possible to obtain the axial force and bending moment diagrams, as well as their respective maximum values. Figures 4.6

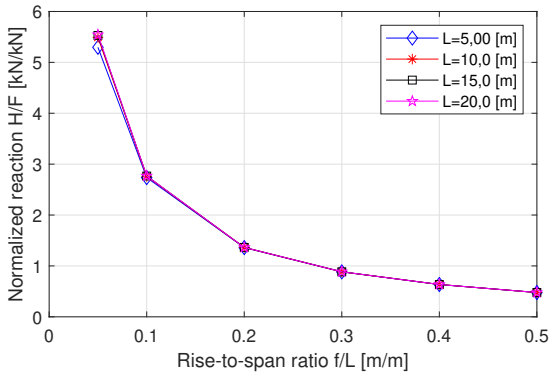

Figure 4.5: Normalized horizontal reaction

f/L	L=5m	L=10m	L=15m	L=20m
0,05	5,296	5,492	5,529	5,543
0,10	2,736	2,762	2,767	2,768
0,20	1,360	1,364	1,364	1,364
0,30	0,884	0,885	0,885	0,885
0,40	0,635	0,635	0,635	0,635
0,50	0,477	0,477	0,477	0,477

Table 4.1: Horizontal reaction values

and 4.7 show the axial forces and bending moments, respectively, calculated from Equations 4.35 through 4.38 and normalized in respect to F along the arch internal angle also normalized in respect to the half internal angle α.

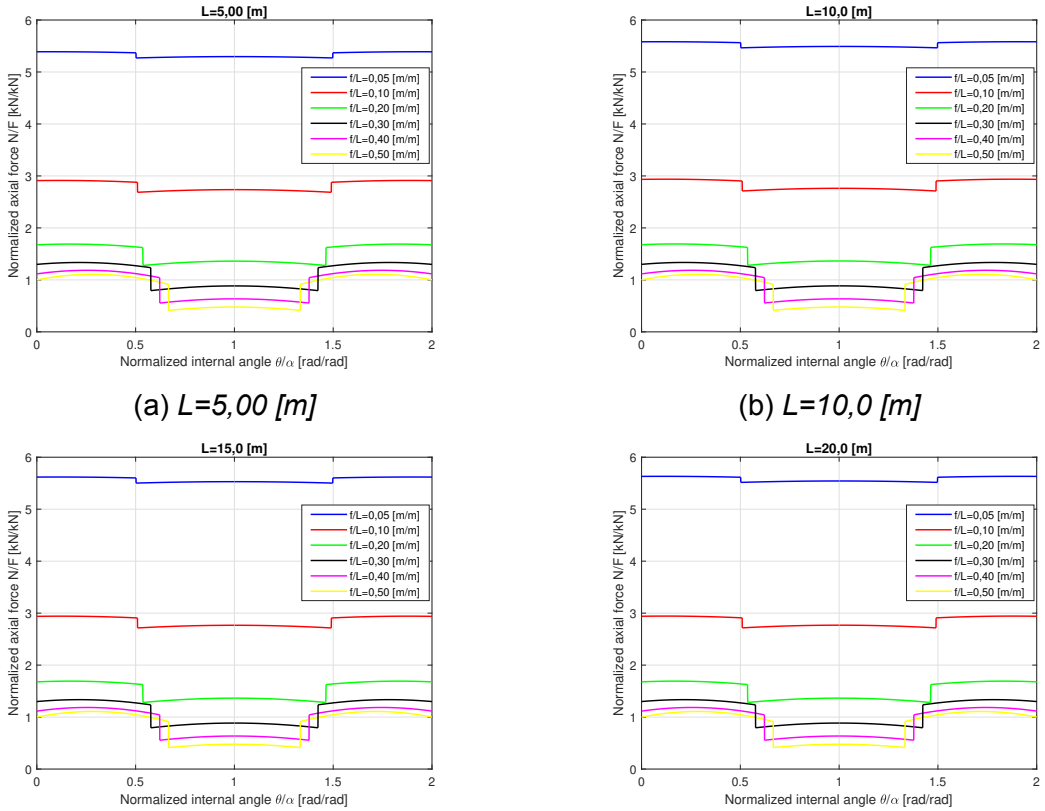

(a) *L=5,00 [m]*

(b) *L=10,0 [m]*

(c) *L=15,0 [m]*

(d) *L=20,0 [m]*

Figure 4.6: Axial internal force distribution.

In Figure 4.6, one easily notices that axial forces tend to be greater for smaller rise-to-span ratios, reaching almost six times the applied load for arches with $f/L = 0,05$ [m/m]. Nonetheless, little variation was found for different span values, following the same pattern as the horizontal reaction behavior mentioned above, where a 5 [m] span displayed slightly lower results when compared to greater spans. Also worth mentioning, the axial force distribution along the arch is more uniform for smaller rise-to-span ratios, but exhibits greater values closer to the supports in every case.

As for bending moment distributions, the arch span L is now much more important when compared to axial forces, since it is explicitly present in their respective expressions in Equations 4.36 and 4.38. Figure 4.7 shows the bending moments developed along the arch for different span values.

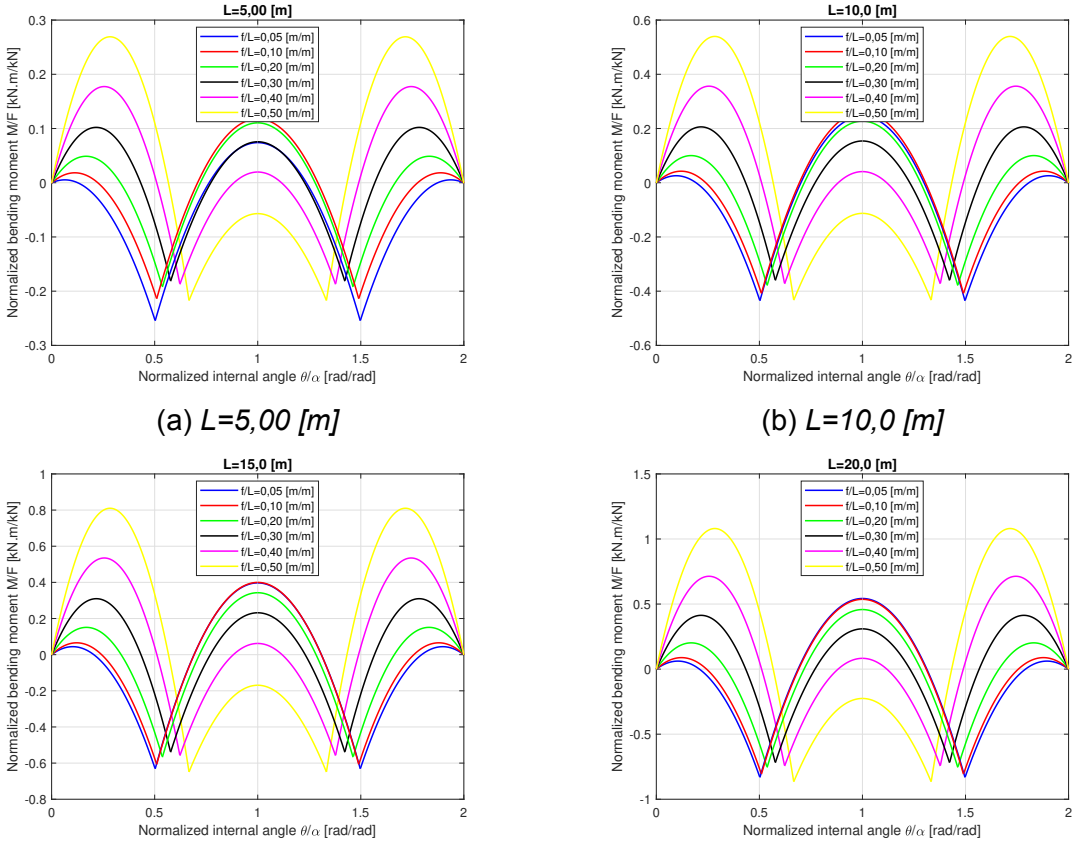

(a) *L=5,00 [m]*

(b) *L=10,0 [m]*

(c) *L=15,0 [m]*

(d) *L=20,0 [m]*

Figure 4.7: Bending moments distribution.

As seen in these images, in every span case the bending moment distribution followed a similar behavior, although peak values resulted more than three times higher for 20 [m] when compared to 5 [m] spans. Negative bending moment peaks happen at the loading points ($\theta = \pm\alpha_F$) in every studied case. Positive bending moment peaks vary in each studied span, where greater spans presented positive maximum moments in the support-load sections (section *S1*), and smaller spans exhibited the opposite behavior.

4.3 Numerical investigation

In this section, buckling behavior and critical load were studied with a numerical approach for both shallow and deeper arches under combinations of bending moments and axial forces at different levels, supported on both ends by pin supports allowing end rotations while preventing horizontal and vertical displacements, as already defined in the previous section.

For all numerical simulations, finite element software *ANSYS Mechanical APDL 2019R2* was employed. This software is used in a variety of contexts where the Finite Element Method is applicable. In structural analysis, this method consists on creating a mathematical model describing the analyzed structure by dividing it into a number of smaller finite elements, applying structural properties and pertinent physical laws in order to find an approximate solution. The smaller is the size of discretization, the closer an approximate solution tends to be from the real analytical result.

For this reason, finite element analyses are suitable for solving complex engineering problems where analytical solutions are not possible or too complicated to be determined. However, as mentioned above, a proper discretization needed to get a reliable result requires a great number os elements, for which computational implementations of this method became widely used in both scientifical and commercial fields.

In buckling analyses, there are two distinct solution techniques, [49], a linear eigenvalue buckling and a nonlinear ultimate load analysis. The first one calculates the theoretical bifurcation point of an ideal linear structure based on the eigenvectors and eigenvalues mathematical concept, determining the critical buckling loads (eigenvalues) with their respective buckling modes (eigenvectors). This method generally leads to unconservative results, since geometrical and material nonlinearities are not considered in the solution. The second method consists on a nonlinear static analysis with incremental load application where the structure equilibrium is calculated in the deformed configuration for each iteration (load increment) until a load level that causes the structure to be unstable is reached. Differently from the eigenvalue formulation, this technique is capable of including material nonlinearities, plastic behavior, geometrical imperfections and large displacements, which is why it is widely recommended for real engineering problems.

A comparison between both methods is shown in the load-displacement diagram in Figure 4.8, where F is the applied load and u is the displacement. It is noticeable that in bifurcation eigenvalue processes, the assumptions that geometry and material behavior are always linear lead to overcalculated values of the critical buckling load.

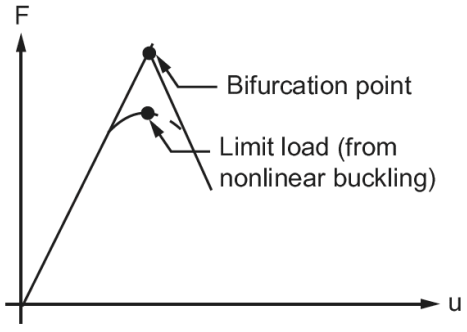

Figure 4.8: Linear and nonlinear buckling analyses, [49].

In this investigation, both methods were used to predict the linear critical and nonlinear ultimate buckling loads for a variety of arch geometries, support cases and steel classes. Moreover, the influence of imperfections and steel grades are studied in the

ultimate load simulations. These parameters and respective results, as well as a detailed description of the finite element model utilized in the numerical simulations are subsequently outlined.

4.3.1 Finite element model

A steel arch can be considered as a beam with a curved central axis, developing axial forces and bending moments to vertical in-plane loads. For this reason, finite element type *BEAM189* was selected for this numerical investigation.

This element type is a three-dimensional beam element based on the Timoshenko beam theory, which includes shear deformations, with both linear and nonlinear capabilities, [50]. It is composed by 3 nodes, one at each end (nodes I and J) and one central node (node K), with 2 integration points along the length. Each element node has 7 degrees of freedom, being translation in the x, y and z directions and rotation around the x, y and z axes, and warping of the cross-section, assumed to be unrestrained.

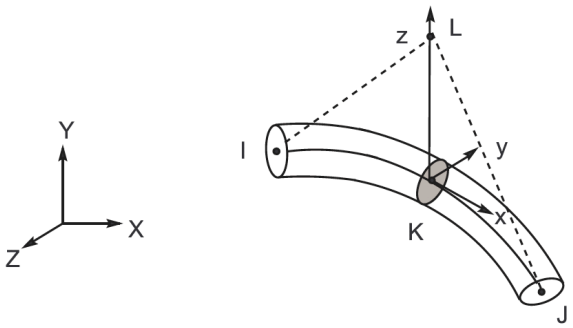

Figure 4.9: *BEAM189* element geometry, [50].

The mesh size along the length chosen after proper evaluation for both eigenvalue and nonlinear simulations is 0,02 [m]. The cross-section mesh was divided in rectangular cells, in a 4x4 array for both half flanges and web, as seen in Figure 4.10a. The overall mesh aspect is shown in Figure 4.10b. Cross-sectional dimensions for the IPE100 profiles employed in this paper are shown in Figure 4.3, where the rolling root radii between flanges and web were neglected.

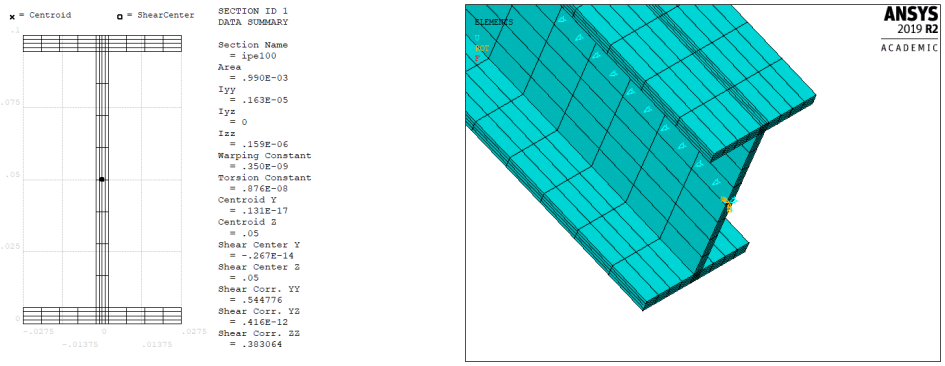

(a) Section meshing (b) Element meshing

Figure 4.10: Meshing details.

In order to evaluate the influence of the longitudinal mesh size in buckling results, a mesh refinement study was made simulating a pinned-pinned arch with a span of $L = 10,0$ [m] and rise $f = 1,00$ [m], for mesh sizes of a quarter (0,005 [m]), half (0,01 [m]) and double (0,04 [m]) of the chosen size. Table 4.2 shows the results for the eigenvalue critical load $F_{cr,eigen}$ and nonlinear ultimate load F_{ult} for each considered mesh size.

Mesh [m]	**# of Nodes**	$F_{cr,eigen}$ [N]	F_{ult} [N]	ΔF_{ult} [%]
0,005	5638	44902,60	21306,64	-0,467
0,01	2823	44902,60	21330,37	-0,356
0,02	1412	44902,60	21406,64	-
0,04	709	44902,60	21543,94	0,641

Table 4.2: Mesh size refinement.

These results show that for eigenvalue solutions the critical load found for each mesh size was the same. In nonlinear simulations, the results showed little variation, since the maximum error relative to the chosen mesh size in the ultimate load ΔF_{ult} were 0,641 [%]. Figure 4.11 shows a comparison between the vertical displacement paths on the loading node for each mesh refinement case. It is clearly noticeable that, except in the 0,04 [m] mesh size, all cases generated similar results with a negligible difference.

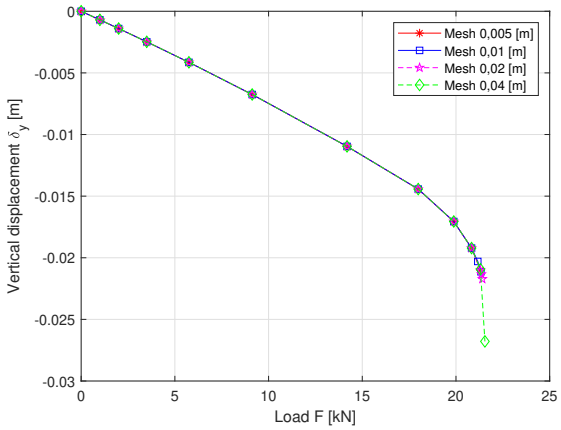

Figure 4.11: Vertical displacements in mesh refinement.

4.3.2 Linear eigenvalue buckling results

In this section, results from linear eigenvalue buckling simulations will be presented for two arch support conditions: pinned-pinned and fixed-fixed. For each support case, arches with rise-to-span ratios from 0,05 to 0,50 [m/m] and span of 5, 10, 15 and 20 [m] were studied, all made of IPE100 steel sections, whose elastic modulus is 210 [GPa].

Figure 4.12 shows the numerical critical load results for arches with different rise-to-span ratios. It is seen that ratios around 0,3 displayed the highest loads for every studied span and support condition with a considerable difference when compared to other ratios, which becomes more significant for smaller span values. Table A.1 in Appendix A summarizes the linear numerical results for every studied geometry.

This behavior might be explained by the strong negative influence of nonlinear axial forces in shallow arches, which causes substantial axial displacements inducing the arches to unstable earlier than deeper arches in linear critical load simulations. However, when the arch is too deep, bending displacements cause the same effect as axial displacements do in shallow arches, leading to smaller buckling loads.

Also, fixed arches yielded much higher critical loads when compared to pinned-pinned arches, around two times higher. These results show that stiffer supports enhance the in-plane stability of arches, and modelling arches as pinned-pinned structures

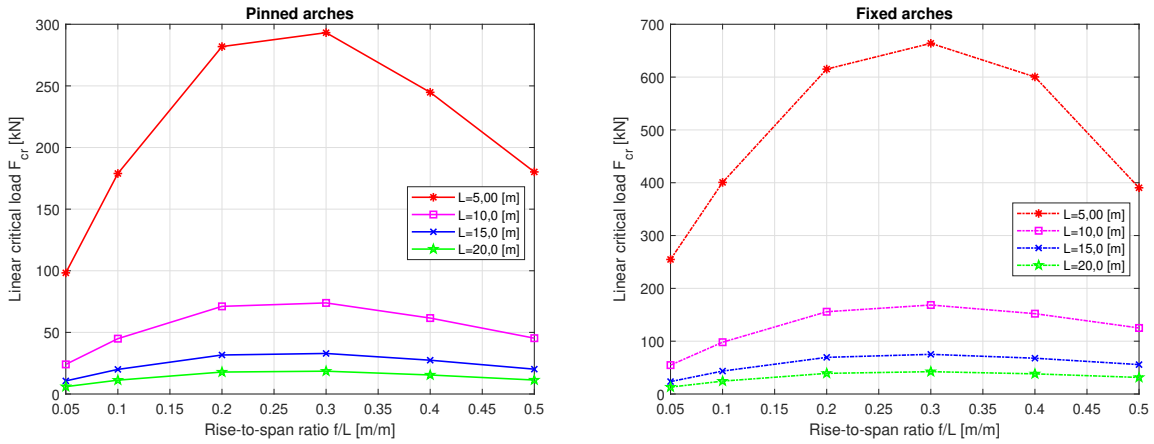

(a) Pinned supports.

(b) Fixed supports.

Figure 4.12: Critical load results versus rise-to-span ratio.

favors safety when designing these type of elements against in-plane buckling.

Furthermore, considering the same cross-sections in each case, larger spans resulted in smaller in-plane critical load values. Moreover, the differences in load between shallow and deeper arches decreased, since bending moments increase substantially for larger spans when compared to axial forces, which makes bending deformations much more important when compared to axial shortening in the pre-buckling phase.

Figures 4.13 and 4.14 show the buckling modes for both pinned and fixed supports, respectively, for spans of 5 and 20 [m] and rise-to-span ratios of 0,05, 0,30 and 0,50 [m/m]. All buckling mode shapes are anti-symmetrical, agreeing with literature results, [33, 47, 51], stating that only arches with modified slendernesses under $\lambda_s < 7,38$ would buckle in a symmetrical mode, which is not the case in this study since all simulated arches are above this slenderness limit.

These buckling mode results show a slight different shape in fixed arches, which is due to the fact that fixed supports prevent rotation around the bending axis as well, influencing in the buckled shape of the structure, which also enhances its buckling critical load. The buckling mode shape for each studied geometry and support condition is shown in Figures B.1 through B.8 in Appendix B.

Moreover, a comparison was made between the numerical critical loads found in this

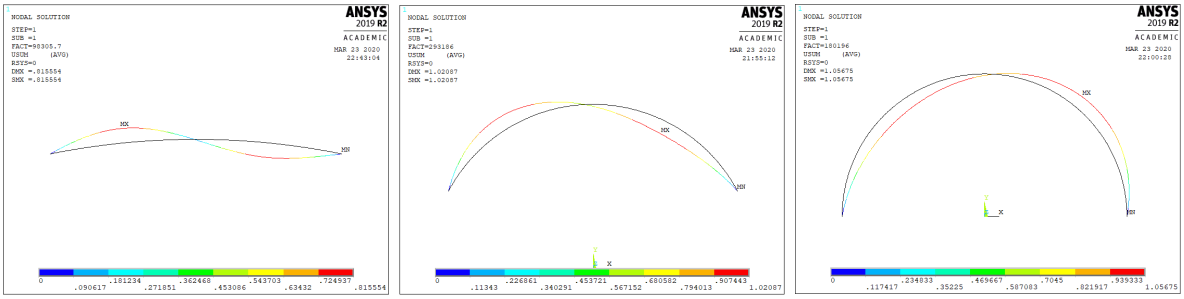

(a) *L=5 [m], f/L=0,05* (b) *L=5 [m], f/L=0,30* (c) *L=5 [m], f/L=0,50*

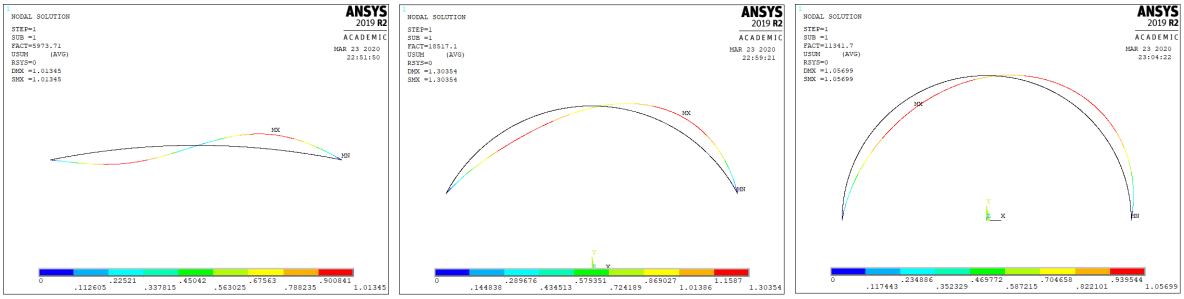

(d) *L=20 [m], f/L=0,05* (e) *L=20 [m], f/L=0,30* (f) *L=20 [m], f/L=0,50*

Figure 4.13: Buckling modes for pinned arches.

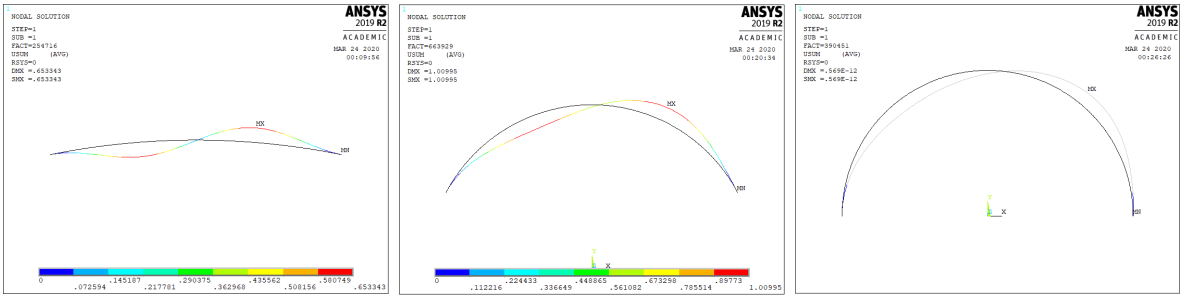

(a) *L=5 [m], f/L=0,05* (b) *L=5 [m], f/L=0,30* (c) *L=5 [m], f/L=0,50*

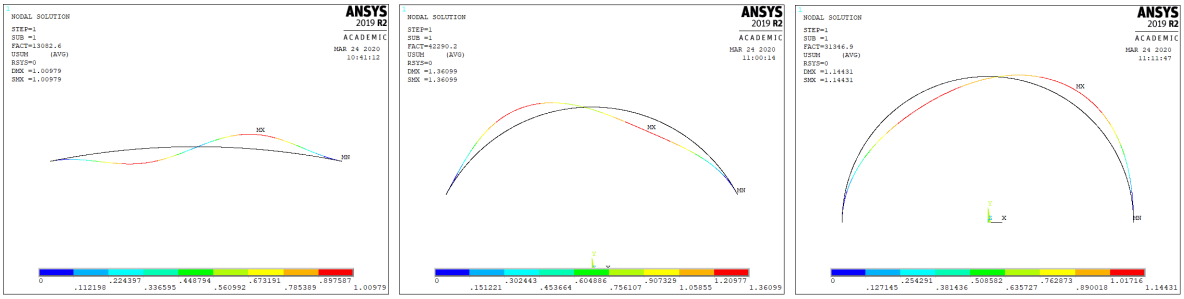

(d) *L=20 [m], f/L=0,05* (e) *L=20 [m], f/L=0,30* (f) *L=20 [m], f/L=0,50*

Figure 4.14: Buckling modes for fixed arches.

study and the results collected from the critical load formulations found in the literature stated in Section 4.1. Since these formulations treat axial forces as uniform along the arch length and determine the axial critical load N_{cr}, the linear elastic structural analysis conducted in Section 4.2.1 was used to link this parameter to the applied critical force F_{cr} for pinned arches under two point loads, using the maximum axial forces for each case.

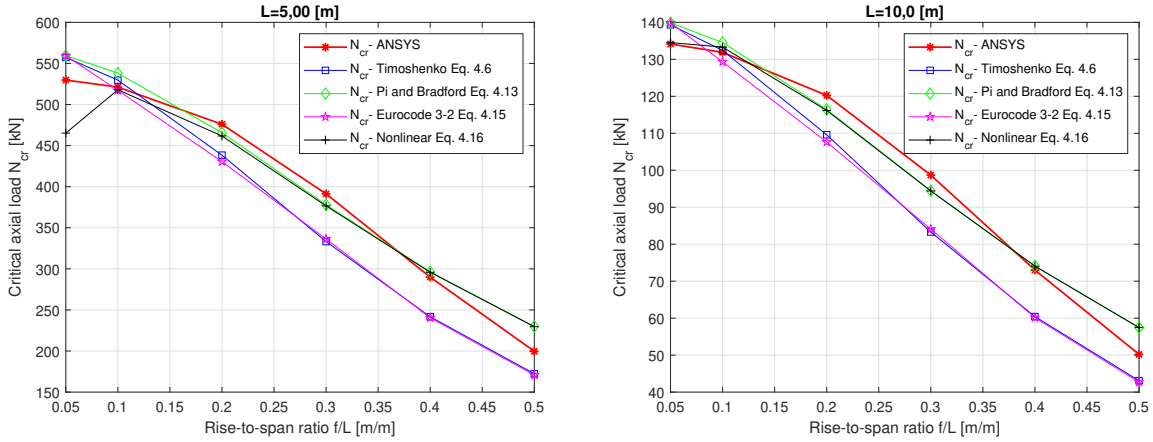

(a) *L=5,00 [m]* (b) *L=10,0 [m]*

(c) *L=15,0 [m]* (d) *L=20,0 [m]*

Figure 4.15: Critical linear axial loads.

Figure 4.15 shows the axial critical load results N_{cr} for each studied span value and rise-to-span ratio. In every case, the critical buckling expressions found in the literature tend to underestimate the critical load for rise-to-span ratios over 0,15 [m/m]

and under 0,40 [m/m], except in the case of 5 [m] spans, where the nonlinear expression in Equation 4.16 for anti-symmetrical buckling of shallow arches yielded conservative results when compared to both numerical simulations and literature formulations.

Additionally, both linear and nonlinear theories developed by Pi, Bradford and Uy, [47], overestimated the critical load for rise-to-span ratios over 0,40 [m/m] for every span sample. On the other hand, the expression given by the Eurocode 3 part 2, [22], yielded good conservative results in every case and significantly below the numerical results, except for rise-to-span ratios below 0,10 [m/m]. This expression strongly agrees with the theory by Timoshenko and Gere, [36], for more slender arches.

4.3.3 Nonlinear ultimate load results

As discussed above, even though linear buckling theories provide a more practical approach to study the instability behavior of a structural member, they do not account for the real properties of both geometry and material, and therefore are not recommended for using in real-life safety verification of structures. Moreover, this type of analysis is required to study the thermo-mechanical behavior of a structure at elevated temperatures generated in an event of fire.

In this context, the present section demonstrates the results obtained from nonlinear ultimate load numerical simulations of the aforementioned arches, for different support conditions, steel classes, imperfection models and temperature levels. The analyzed geometries, solid model and finite element model are the same ones used in the linear eigenbuckling simulations described above.

For these nonlinear numerical simulations, an elastic-perfectly plastic rate independent without strain hardening material model was employed to simulate the stress-strain behavior of structural carbon steel of class S275 at natural temperature, as provisioned by the Eurocode 3, [27]. In order to facilitate convergence, the plastic portion of this model is given to have a slope of $E/10000$ [GPa], where E is the elastic modulus given as 210 [GPa]. According to this steel class, its yield strength is given as $f_y = 275$ [MPa].

This model is shown in Figure 4.16a, where $\varepsilon_y = 1,3095.10^{-3}$ [m/m] and $\varepsilon_u = 0,15$ [m/m].

Also, in-plane geometrical imperfections were incorporated into the numerical model aiming to replicate the effect of real imperfections in the arches. The imperfection pattern used in this numerical study is the equivalent imperfection model for arches given by the Eurocode 3 part 2, [22], which translates both geometrical imperfections and residual stresses into an equivalent shape of imperfection, whose amplitude e_0 depends on the cross-section classification and its respective buckling curve, as well as the arch span, as seen in Table 2.2. The shape of this equivalent imperfection model follows a sinusoidal curve, and it is shown in Figure 4.16b.

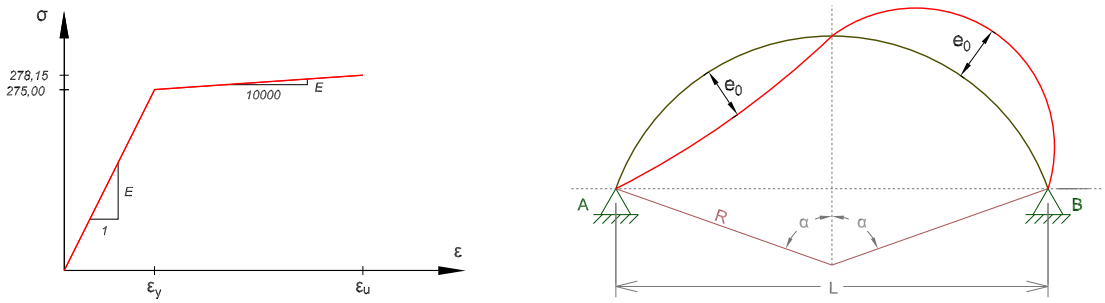

(a) Steel S275 material model.

(b) Equivalent imperfections shape.

Figure 4.16: Nonlinear geometrical and material properties.

Given that the IPE100 section is classified as Class 1 for both bending and compression, the buckling curve selected is curve **a**, resulting in an imperfection amplitude of $e_0 = L/600$ [m]. Hence, in order to associate the imperfection geometry to the numerical model, the buckled deformed shapes obtained in prior linear eigenbuckling simulations were used as a base model along with the *Update Geometry* command in *ANSYS Mechanical APDL*.

This technique consists on updating each individual node position of a numerical model according to a results file containing the deformed shape of a corresponding geometry, but respecting a factor that converts the displacements magnitude of the base model into the desired imperfection configuration.

As seen in Figures 4.13a through 4.13f, the deformed shape of pinned arches from

eigenbuckling simulations match the desired imperfection contour of Figure 4.16b, but with much larger displacements. For this reason, a conversion factor is determined and then applied to the entire deformed shape, so that the interest numerical model will match the shape and magnitude of the equivalent imperfection model proposed in Eurocode 3 part 2.

This conversion factor is calculated by Equation 4.45, where δ_{max} corresponds to the maximum displacement sum from the eigenbuckling study, and e_0 is the imperfection maximum magnitude.

$$f_{imp} = \frac{e_0}{\delta_{max}} \tag{4.45}$$

Furthermore, nonlinear analyses use the Newton-Raphson approach by default, which consists on applying load increments and determining the structure equilibrium in the deformed configuration for each load level, performing a linear solution in each load step, [49]. The analysis is carried out until a load level that causes large deformations with small load increments is found, either by plastification of the cross-section or buckling of the structure.

In this context, it is necessary to inform an appropriate load increment configuration, entered into the software as a *time increment*. For each nonlinear solution, a load increment of 0,50 [kN], with a minimum of 0,01 [kN] and maximum of 10 [kN] was defined. However, in order to prevent miscalculations and facilitate convergence of the solution, the automatic load stepping and bisection features were activated. These features automatically set a load increment in each load step, and if convergence is not reached, a smaller load step in defined and another solution attempt is made, [49].

In the next sections, the results from nonlinear simulations will be presented, for different geometrical configurations and temperature levels, in order to analyze the effects of different parameters that may affect considerably a steel arch. The elevated temperature simulations attempt to imitate as close as possible a fire event that arches

are prone to in real situations. These solutions will make it possible to properly understand structural behavior of steel arches as temperature increases and their resistance is affected.

4.3.3.1 Linear *versus* nonlinear solutions

Figure 4.17 shows a graphical comparison between linear and nonlinear solutions for the in-plane critical buckling load F_{cr} in arches with 5, 10, 15 and 20 [m] spans and rise-to-span ratios between 0,05 and 0,50 [m/m], for both fixed and pinned support conditions at natural temperature.

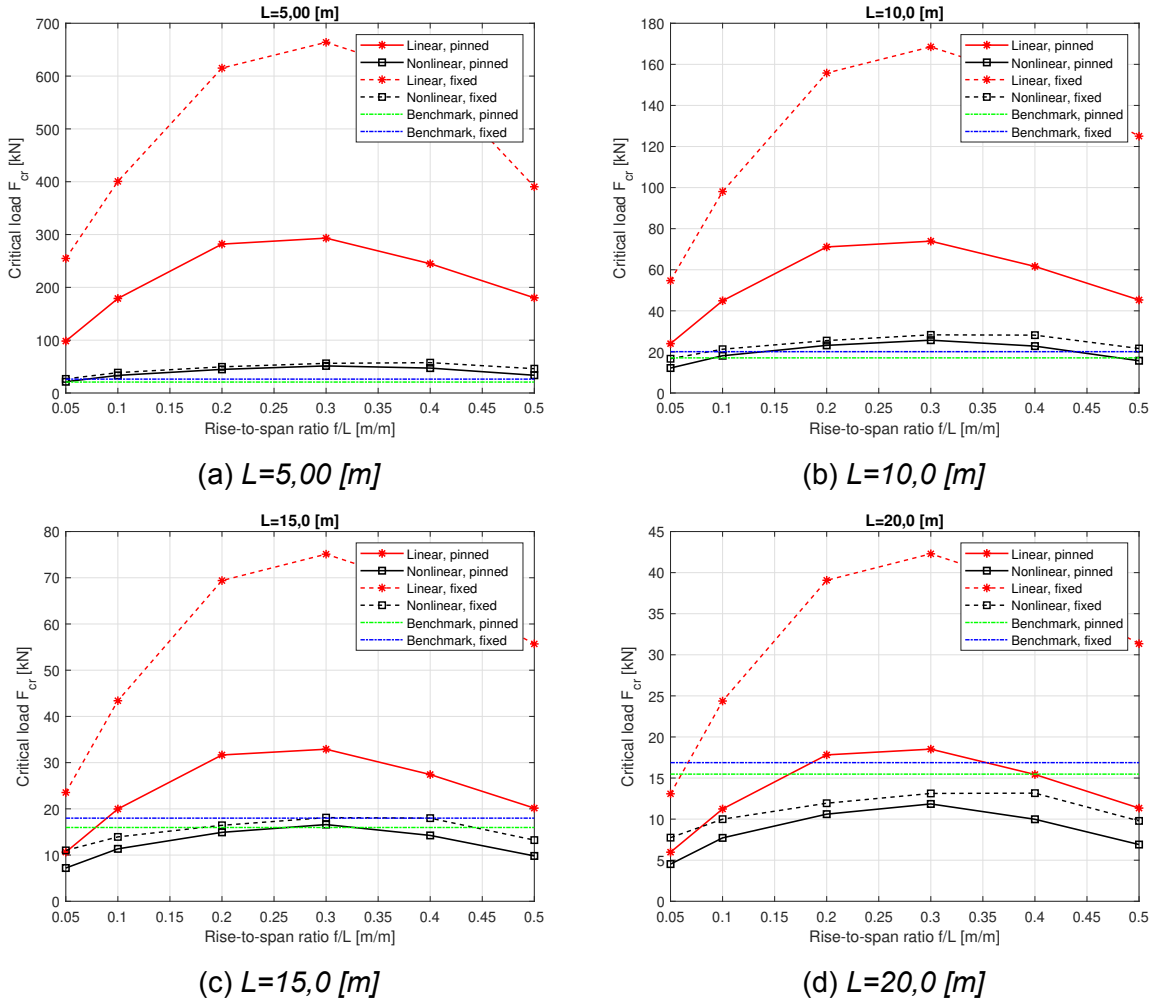

(a) *L=5,00 [m]* (b) *L=10,0 [m]*

(c) *L=15,0 [m]* (d) *L=20,0 [m]*

Figure 4.17: Linear *versus* nonlinear results.

In these images, it is clear that, even though they follow the same patterns for different rise-to-span ratios, linear solutions overestimate the critical load considerably, even more for fixed arches when compared to each corresponding nonlinear solution. The benchmark lines represent the cross-section plastification ultimate load of a straight beam of the same span and support condition as the respective simulated arches, also laterally restrained to avoid lateral-torsional buckling.

It is seen that, for small enough span values, arches actually endure higher ultimate point loads than straight beams, mostly because their geometry is more favorable regarding flexural displacements. Also, for larger spans, the linear and nonlinear loads for pinned arches are closer, indicating that linear theories for the critical load of arches better predict buckling behavior for more slender members.

Moreover, larger span arches become unstable before reaching their plastic load, explaining the reason that linear elastic theories produce moderately accurate results in these cases.

4.3.3.2 Influence of the support condition

In this section, besides the ultimate load, the collapse mode and vertical/horizontal displacements of pinned and fixed arches are investigated, targeting to better visualize the behavior phenomena around natural temperature instability of steel arches.

Table 4.3 compares the ultimate load (in [kN]) for 5, 10 and 20 [m] pinned and fixed arches of various rise-to-span ratios. As expected based on linear eigenvalue solutions, ultimate loads resulted higher for fixed arches in every span and rise-to-span case when compared to pinned supports.

However, the percentage difference between support conditions increased for larger spans, mostly because there is a more significant influence of bending moments, which are largely affected by the stiffness of the supports. An increase in stiffness favorably changes the bending moment distribution and displacement field along the member, enhancing its in-plane flexural resistance.

Span	Support	f/L=0,05	f/L=0,10	f/L=0,20	f/L=0,30	f/L=0,40	f/L=0,50
	Pinned	21,35	33,34	44,71	51,28	47,15	33,58
5m	Fixed	26,70	38,57	49,55	56,15	57,47	46,04
	Dif. %	20,03	13,55	9,76	8,67	17,95	27,06
	Pinned	12,16	18,14	23,19	25,71	22,83	15,71
10m	Fixed	16,67	21,32	25,52	28,31	28,17	21,66
	Dif. %	27,08	14,92	9,14	9,17	18,95	27,47
	Pinned	4,53	7,72	10,60	11,85	9,98	6,90
20m	Fixed	7,75	9,99	11,93	13,12	13,16	9,78
	Dif. %	41,54	22,78	11,14	9,74	24,16	29,42

Table 4.3: Nonlinear solution for different support conditions.

Also worth mentioning, the lowest percentage difference values occurred for rise-to-span ratios of 0,30 [m/m] in every studied span case, which also resulted the highest ultimate loads overall in both support conditions. This is due to the fact that this specific geometry combines relatively low axial forces and a moderate in-plane slenderness. In comparison, shallow arches have low slenderness values, but are prone to high axial compressive forces, while deeper arches possess the lowest compression forces but higher slenderness and bending moments. Thus, this geometry marks the optimal choice for arches under a combination of bending moments and compression at natural temperature.

Regarding the collapse modes, Figures 4.18 and 4.19 show, respectively, the final deformed shape (displacement sum) at the ultimate load of pinned and fixed arches of 5 and 20 [m] span and 0,05, 0,30 and 0,50 [m/m] rise-to-span ratios, since these are the critical geometry cases. These deformed shapes are scaled to 15 times. The deformed shapes for all studied geometries are shown from Figure B.9 to B.16 in Appendix B.

The most noticeable feature is that for the same geometry but different support condition the deformed shapes are similar, although slight differences appear. Pinned arches tend to show a more symmetrical deformation contour, while fixed arches presented more alternative shapes. Also, as expected, larger spans showed much larger deformations, mainly at the loading points at quarter span.

Additionally, in most of the cases maximum displacements occurred at one of the

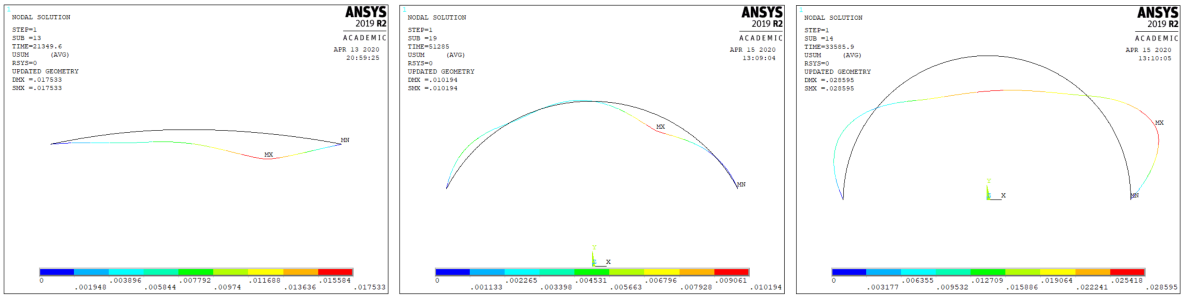

(a) *L=5 [m], f/L=0,05* (b) *L=5 [m], f/L=0,30* (c) *L=5 [m], f/L=0,50*

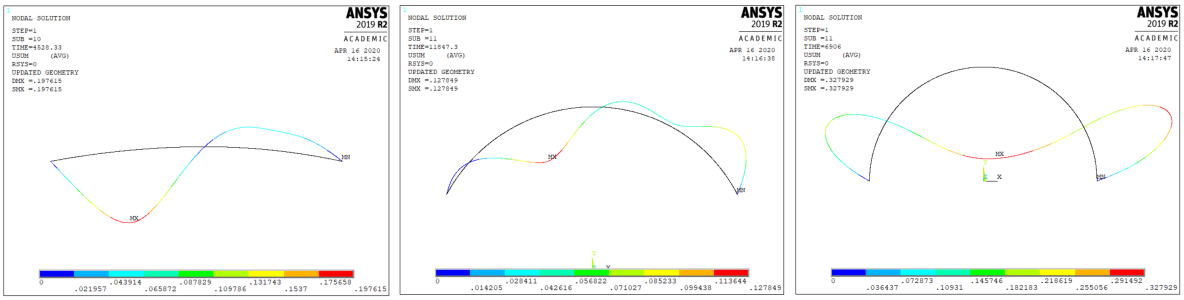

(d) *L=20 [m], f/L=0,05* (e) *L=20 [m], f/L=0,30* (f) *L=20 [m], f/L=0,50*

Figure 4.18: Deformed shapes of pinned arches.

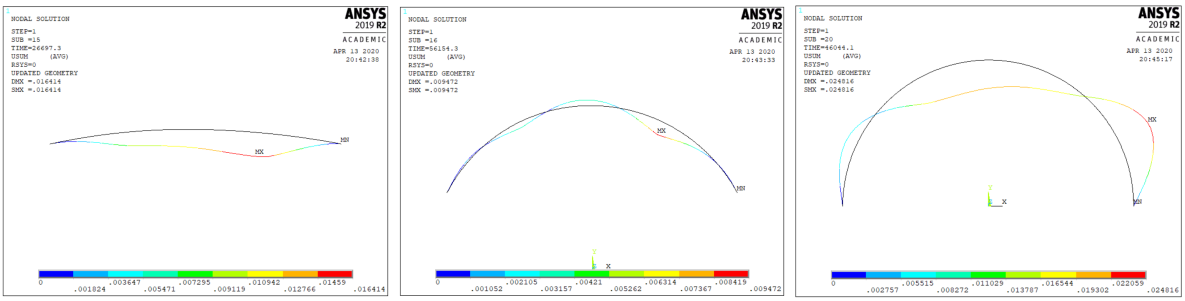

(a) *L=5 [m], f/L=0,05* (b) *L=5 [m], f/L=0,30* (c) *L=5 [m], f/L=0,50*

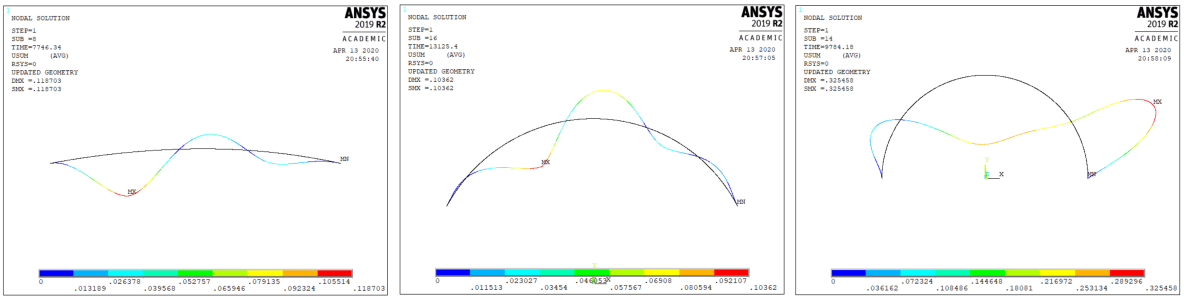

(d) *L=20 [m], f/L=0,05* (e) *L=20 [m], f/L=0,30* (f) *L=20 [m], f/L=0,50*

Figure 4.19: Deformed shapes of fixed arches.

load application points, except for more slender arches where anti-symmetrical deflections were more substantial.

As a manner of comparison, Figure 4.20 shows the load-vertical displacement (at the y axis direction) curves for both pinned (in blue) and fixed (in red) arches at the right load application point (see Figure 4.2). For the 5 [m] span, curves for different rise-to-span ratios show lower variations between support conditions if compared to those of 20 [m] arches. Also, for the 20 [m] arches with f/L=0,05 [m/m] the curves show distinct vertical displacement paths, meaning that the buckling shape resulted considerably discrepant from one another.

In the 20 [m] and 0,30 [m/m] case, there is a change in vertical displacement direction during the load application process for both pinned and fixed support cases, caused by anti-symmetrical buckling of the entire structure, as seen in Figures 4.18e and 4.19e.

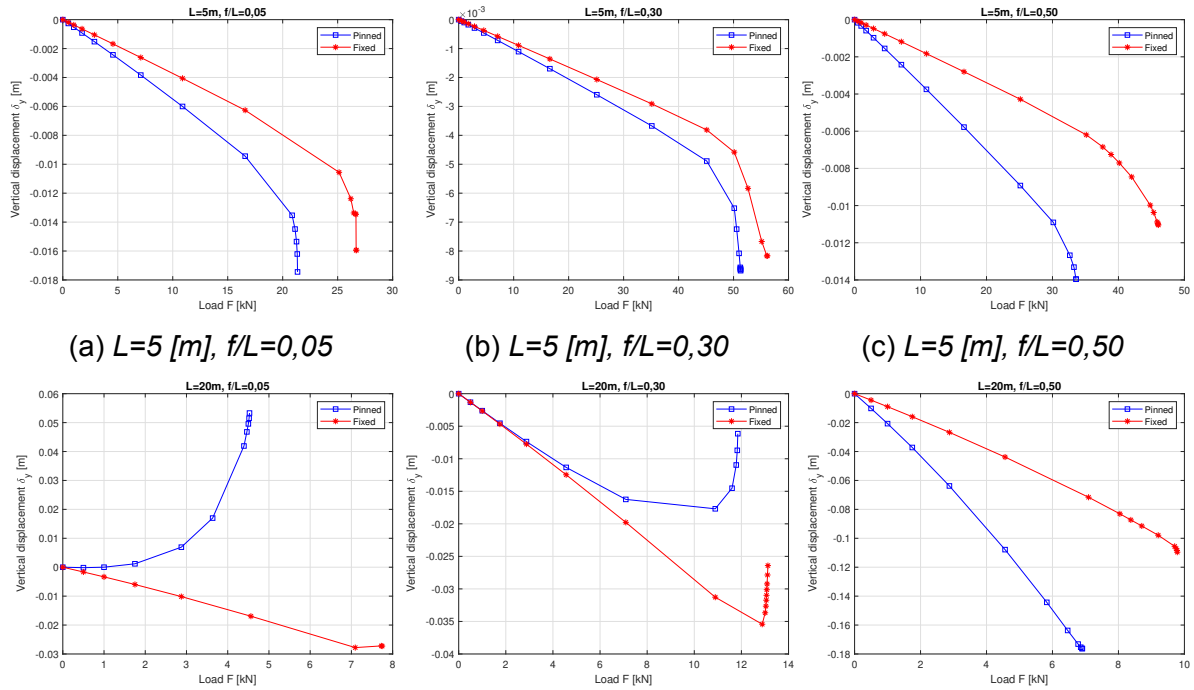

(a) *L=5 [m], f/L=0,05* (b) *L=5 [m], f/L=0,30* (c) *L=5 [m], f/L=0,50*

(d) *L=20 [m], f/L=0,05* (e) *L=20 [m], f/L=0,30* (f) *L=20 [m], f/L=0,50*

Figure 4.20: Vertical displacements.

Figure 4.21 shows the load-horizontal displacement (at the x axis direction) relationship also for both pinned (in magenta) and fixed (in green) support conditions. These curves show identical behavior when compared to each corresponding vertical displacement path, except for 0,50 [m/m] arches, where the side-sway deflection of anti-symmetrical displacements seen in Figures 4.18c, 4.19c, 4.18f and 4.19f occurring right from the beginning of the load application process generated these deflection paths.

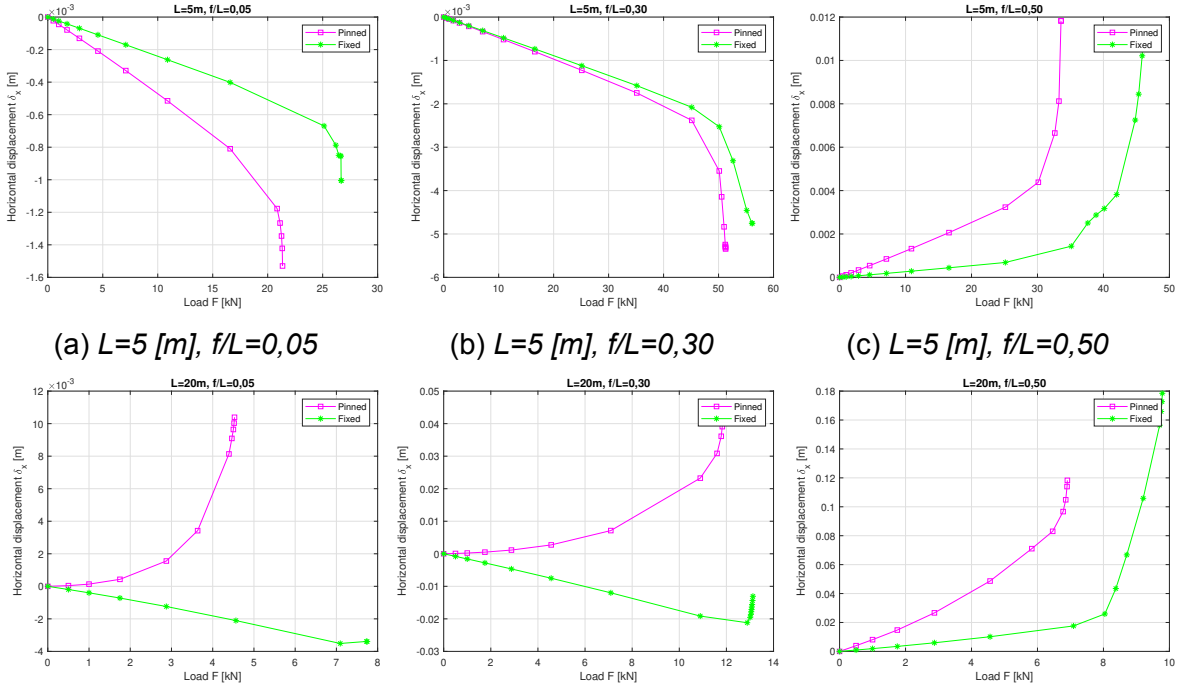

(a) *L=5 [m], f/L=0,05* (b) *L=5 [m], f/L=0,30* (c) *L=5 [m], f/L=0,50*

(d) *L=20 [m], f/L=0,05* (e) *L=20 [m], f/L=0,30* (f) *L=20 [m], f/L=0,50*

Figure 4.21: Horizontal displacements.

4.3.3.3 Influence of imperfections

Aiming to understand the influence of geometrical imperfections in the ultimate load of arches, a comparison study was made between similar arch geometries at natural temperature with and without in-plane imperfections incorporated into the numerical model.

For this, pinned arches of 5, 10 and 20 [m] spans with rise-to-span ratios between 0,05 and 0,50 [m/m] were simulated discarding the equivalent imperfections model described in the Section 4.3.3 ($e_0 = L/600$). Table 4.4 and Figure 4.22a show a comparison of the ultimate load results (in [kN]) between each imperfection case. Figure 4.22b graphically shows the evolution of percentage differences in ultimate loads as a function of the arch span and rise-to-span ratio.

Span	Case	f/L=0,05	f/L=0,10	f/L=0,20	f/L=0,30	f/L=0,40	f/L=0,50
5m	$e_0 = L/600$	21,35	33,34	44,71	51,29	47,15	33,59
	$e_0 = 0$	24,44	37,43	50,41	60,11	49,26	36,00
	Dif. %	12,64	10,91	11,30	14,68	4,28	6,70
10m	$e_0 = L/600$	12,16	18,14	23,19	25,71	22,83	15,71
	$e_0 = 0$	16,04	21,41	26,62	30,09	24,29	16,74
	Dif. %	24,20	15,28	12,88	14,54	6,00	6,16
20m	$e_0 = L/600$	4,53	7,72	10,60	11,85	9,98	6,91
	$e_0 = 0$	7,27	9,95	12,50	13,90	10,78	7,37
	Dif. %	37,71	22,46	15,18	14,75	7,43	6,30

Table 4.4: Influence of imperfection on the ultimate load.

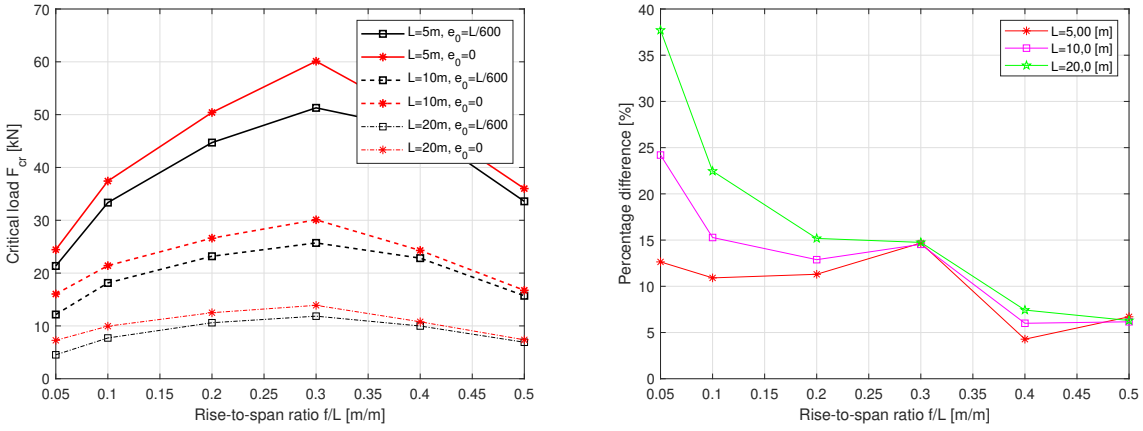

(a) Imperfection cases comparison

(b) Percentage difference evolution

Figure 4.22: Imperfection influence on ultimate resistance.

Based on this data, it is clear that imperfections play an important part on nonlinear numerical simulations, since perfect models yielded higher ultimate loads in every studied cases, and percentage differences of up to around 40% were found in this study,

for arches under this type of loading condition at natural temperature. The biggest percentage differences were found for smaller rise-to-span ratio, which increased for larges spans.

Figure 4.23 shows the deformed shapes of 5 and 20 [m] arches without imperfections. It is seen that in all cases a symmetrical deformed configuration was found, which is the opposite behavior when compared to the same arches but with equivalent geometrical imperfections shown in Figure 4.18.

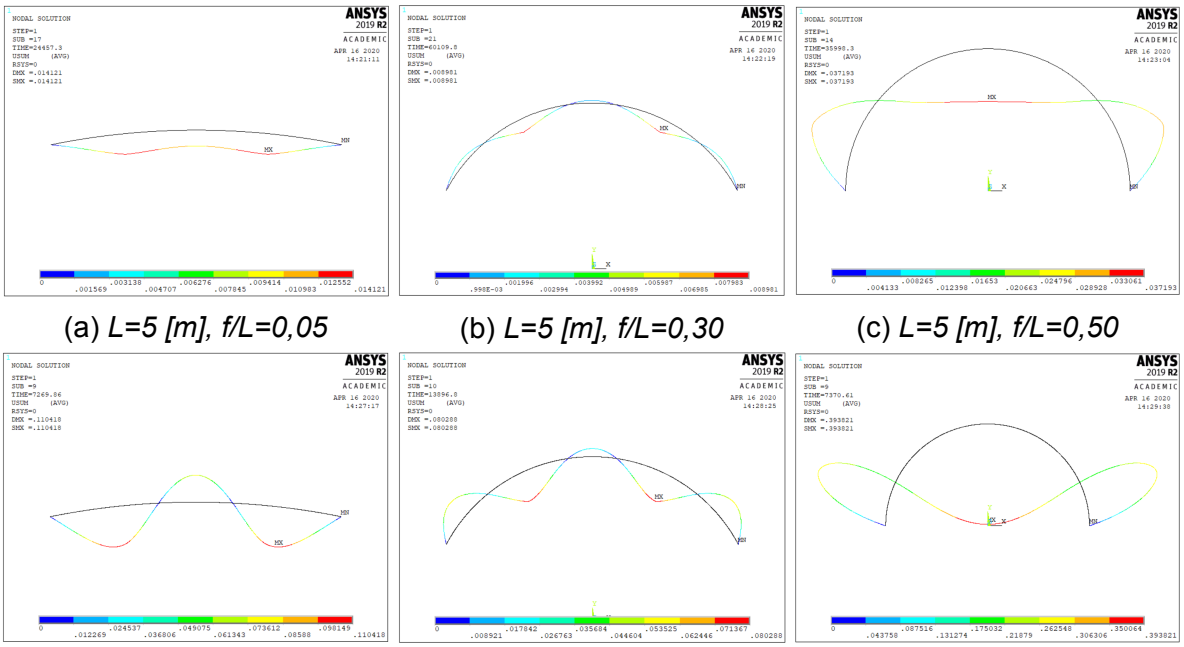

(a) *L=5 [m], f/L=0,05* (b) *L=5 [m], f/L=0,30* (c) *L=5 [m], f/L=0,50*

(d) *L=20 [m], f/L=0,05* (e) *L=20 [m], f/L=0,30* (f) *L=20 [m], f/L=0,50*

Figure 4.23: Deformed shapes of pinned arches without imperfections.

4.3.3.4 Ultimate load at elevated temperatures

In order to test the thermo-mechanical response of steel arches under elevated temperatures, nonlinear numerical solutions for three temperature levels were done, for 400, 600 and 700 [°C], in pinned and fixed arches of 5, 10, 15 and 20 [m] span and rise-to-span ratios ranging from 0,05 to 0,50 [m/m]. The temperature is uniformly applied in all nodes, while the loads linearly increase until a convergence level is reached, in the

same manner as natural temperature solutions.

These simulations took into account the various steel properties as functions of the temperature described in Section 3.2.1, namely the stress-strain relationship, relative thermal elongation (thermal strain), thermal conductivity and specific heat.

It was found during the simulation process that, when the thermal strain property was included, solutions for arches with 0,05 and 0,10 [m/m] ratios would not reach convergence. For this reason, exclusively in these geometry cases the thermal strain was neglected. However, an evaluation of the impact caused by this technique was done through numerical simulations of arches with and without the thermal strain incorporated into the material model, whose ultimate load results (in [kN]) are shown in Table 4.5. It is seen that percentage differences between simulations with and without thermal strain are negligible, since they resulted only as high as around 3%.

Temp.	Span	Condition	f/L=0,20	f/L=0,30	f/L=0,40
400 [°C]	**10m**	With	17,72	19,28	14,03
		Without	17,39	19,26	14,25
		Dif. %	1,87	0,14	-1,55
	15m	With	10,36	11,26	8,21
		Without	10,14	11,21	8,34
		Dif. %	2,10	0,44	-1,58
600 [°C]	**10m**	With	8,11	8,70	6,28
		Without	7,89	8,72	6,47
		Dif. %	2,68	-0,23	-3,10
	15m	With	4,71	5,04	3,65
		Without	4,56	5,03	3,74
		Dif. %	3,22	0,13	-2,48
700 [°C]	**10m**	With	3,73	3,96	2,88
		Without	3,63	3,98	2,96
		Dif. %	2,56	-0,47	-2,79
	15m	With	2,13	2,24	1,63
		Without	2,05	2,24	1,68
		Dif. %	3,31	-0,11	-3,23

Table 4.5: Comparison between thermal strain simulations.

Moreover, the equivalent imperfection model of $e_0 = L/600$ prior used in natural

temperature solutions was also implemented for elevated temperature studies using the linear eigenbuckling deformed shape as the base imperfection geometry.

Figures 4.24 and 4.25 show the ultimate load results of the aforementioned geometry and temperature cases, for pinned and fixed arches, respectively, all made of S275 steel.

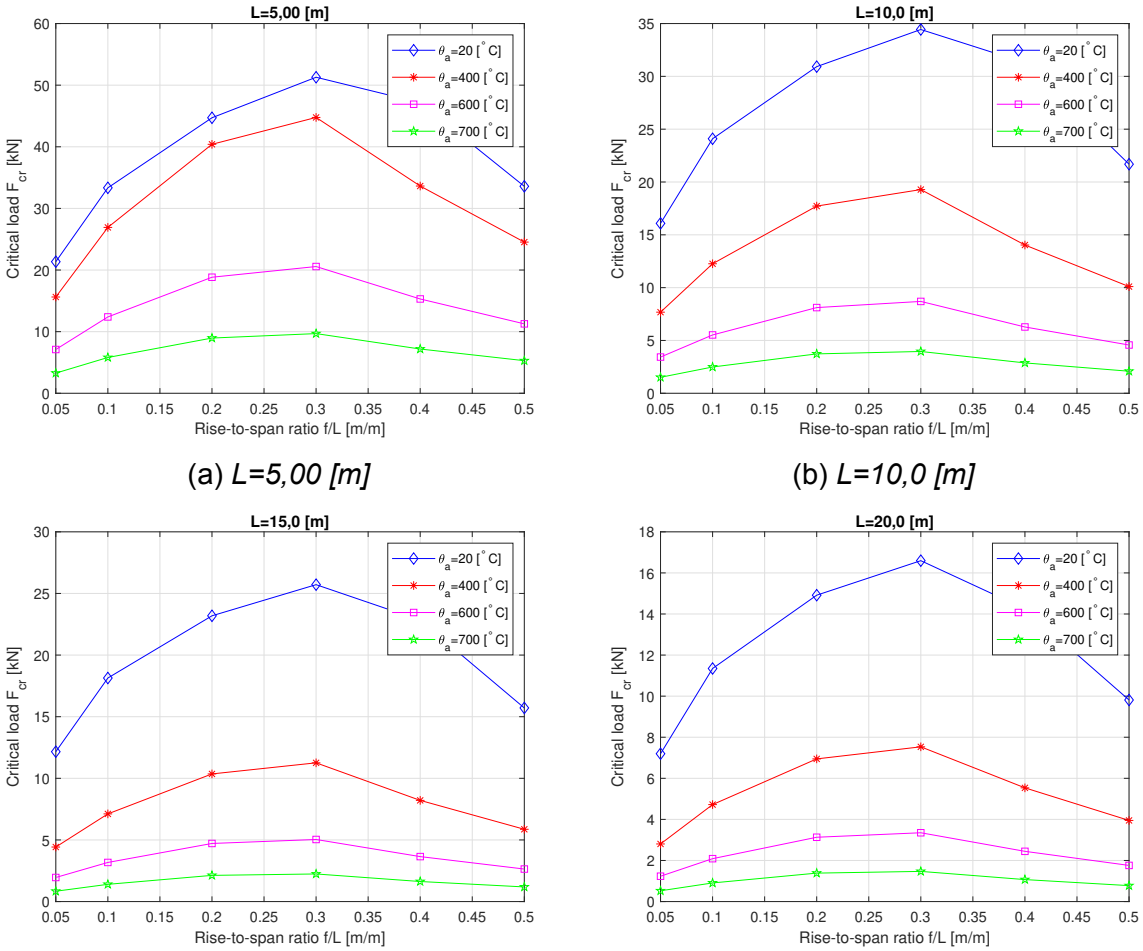

(a) *L=5,00 [m]* (b) *L=10,0 [m]*

(c) *L=15,0 [m]* (d) *L=20,0 [m]*

Figure 4.24: Ultimate load of pinned arches for different temperature levels.

It is seen that, as expected, even at elevated temperatures fixed arches yield considerably higher ultimate loads than pinned arches. Also, for the same geometrical properties, the differences between subsequent temperature levels in fixed arches is

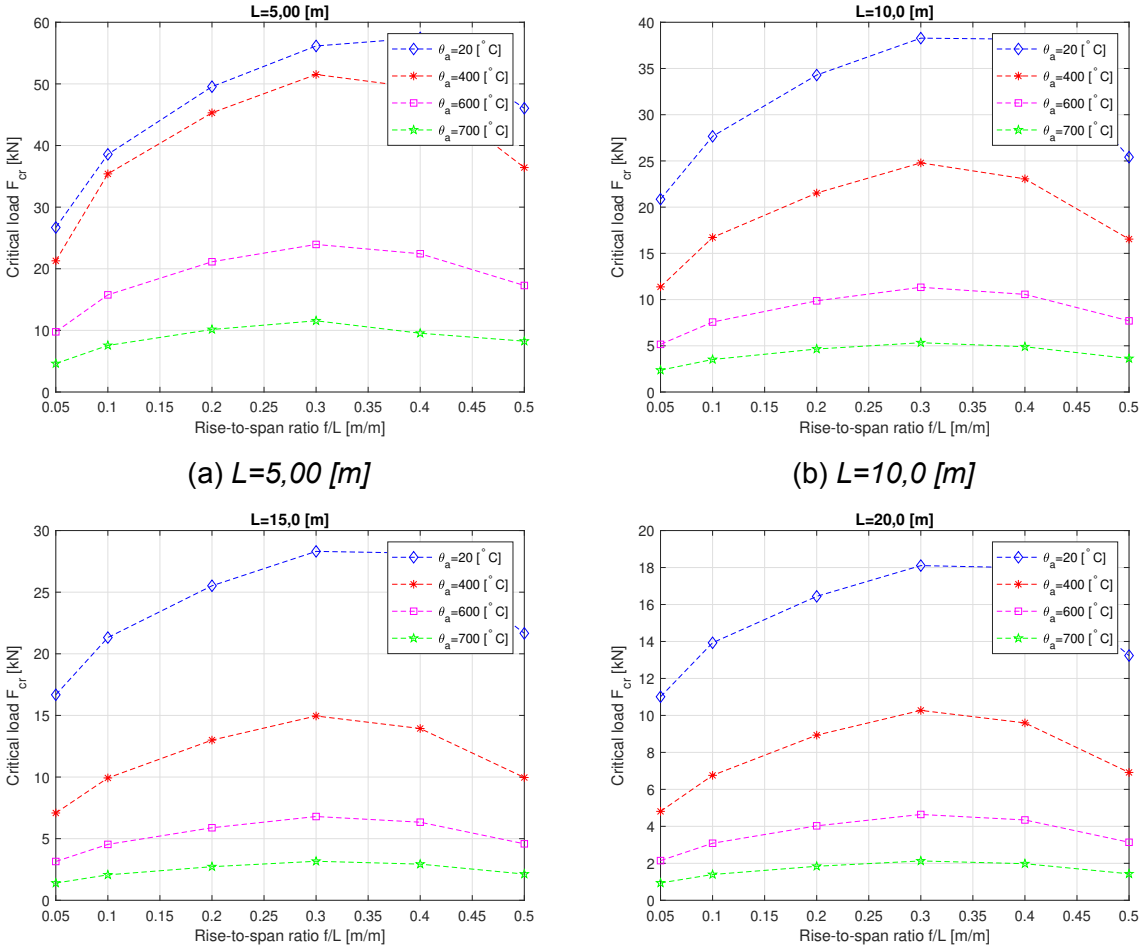

(a) *L=5,00 [m]*

(b) *L=10,0 [m]*

(c) *L=15,0 [m]*

(d) *L=20,0 [m]*

Figure 4.25: Ultimate load of fixed arches for different temperature levels.

lower for every span case, meaning that this support condition is less negatively affected by a rise in temperature.

As an example, Figure 4.26 exhibits the deformed buckled shapes of 5 [m] pinned arches for 20, 400, 600 and 700 [°C]. These images show that the buckled shape contours do not significantly change with temperature, except for the magnitude of displacements. Also, in the case where $f/L = 0,30$, a different deformed shape was found for elevated temperature cases, because of the more important effects of thermal strain caused by the temperature change.

In this context, Figures 4.27 and 4.28 show the vertical and horizontal load-displacement

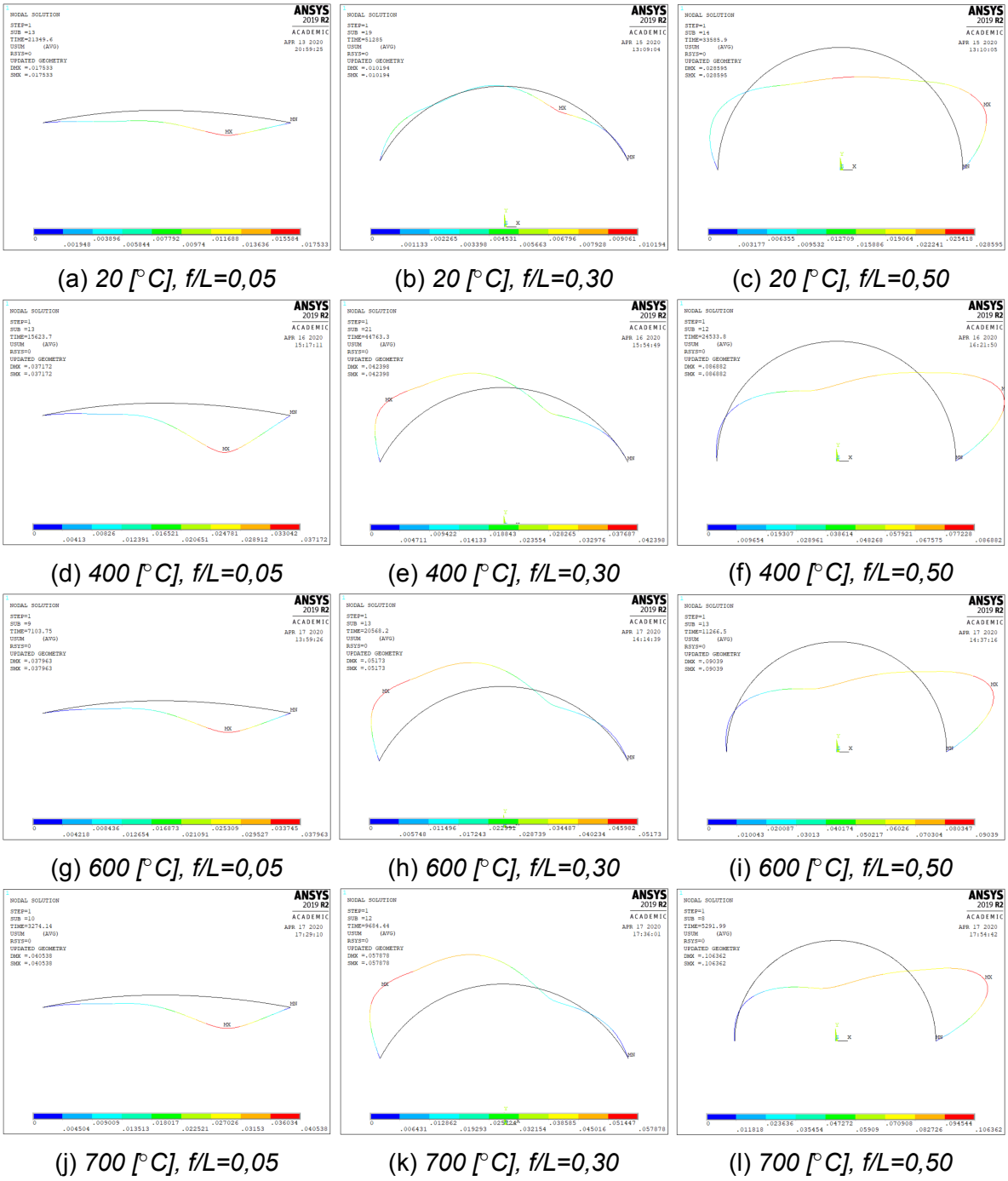

(a) *20 [°C], f/L=0,05* (b) *20 [°C], f/L=0,30* (c) *20 [°C], f/L=0,50*

(d) *400 [°C], f/L=0,05* (e) *400 [°C], f/L=0,30* (f) *400 [°C], f/L=0,50*

(g) *600 [°C], f/L=0,05* (h) *600 [°C], f/L=0,30* (i) *600 [°C], f/L=0,50*

(j) *700 [°C], f/L=0,05* (k) *700 [°C], f/L=0,30* (l) *700 [°C], f/L=0,50*

Figure 4.26: Deformed shapes of 5 [m] pinned arches at different temperature levels

paths of the load application point for different temperature levels in 5 [m] pinned arches with rise-to-span ratios of 0,05, 0,30 and 0,50 [m/m]. Both vertical and horizontal displacement paths of the 0,30 [m/m] arch, which takes thermal strains into account, show

an initial displacement caused by the temperature effect before any load is applied. This shows that, even though thermal strains do not interfere considerably on the ultimate load, it changes drastically the load-displacement behavior of a structure.

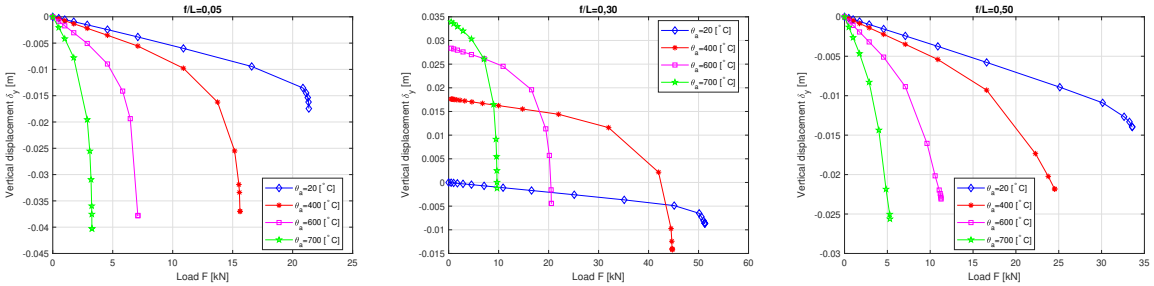

(a) *f/L=0,05* (b) *f/L=0,30* (c) *f/L=0,50*

Figure 4.27: Vertical displacements of 5 [m] pinned arches.

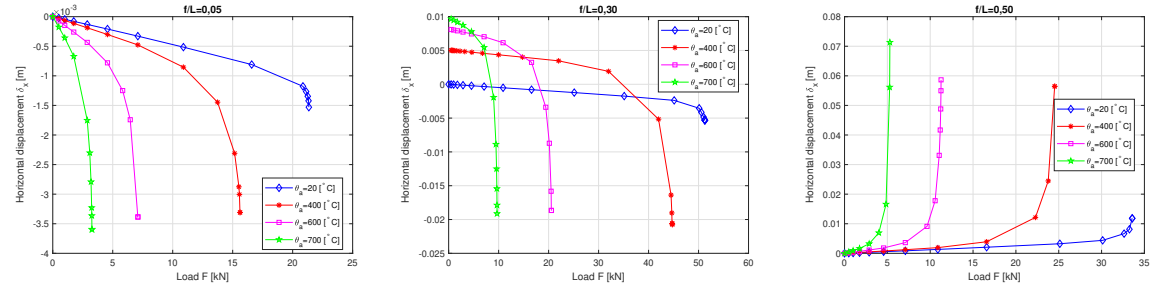

(a) *f/L=0,05* (b) *f/L=0,30* (c) *f/L=0,50*

Figure 4.28: Horizontal displacements of 5 [m] pinned arches.

In every condition stated above, both vertical and horizontal displacements increased substantially when compared to a natural temperature condition, adding to the fact that ultimate loads decreased as temperature increased.

As a manner of comparison, pinned arches made of S355 steel were tested against their in-plane failure under elevated temperatures of 400, 600 and 700 [°C]. This comparison allows to understand whether it is better to increase support stiffness or steel resistance when designing arches against fire and elevated temperature conditions.

Figures 4.29, 4.30 and 4.31 display the ultimate loads for each studied temperature condition and 5, 10, 15 and 20 [m] arch span, comparing results between pinned arches of S275 and S355 steel classes and fixed arches of S275 steel.

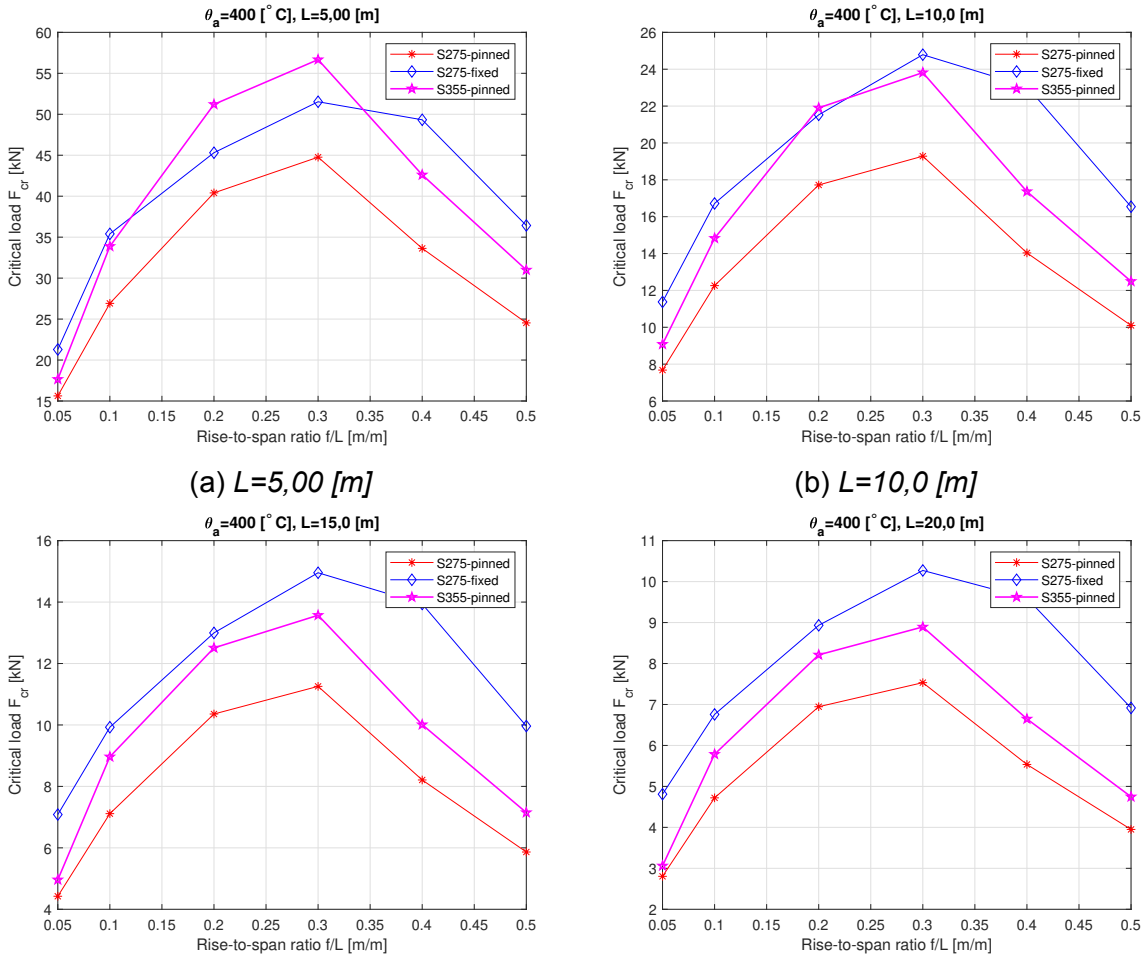

(a) *L=5,00 [m]* (b) *L=10,0 [m]*

(c) *L=15,0 [m]* (d) *L=20,0 [m]*

Figure 4.29: Steel class comparison at 400 [°C].

As expected, considering the same support condition, arches made of S355 steel yielded higher ultimate loads in every temperature condition, and exhibited the same behavior for different rise-to-span ratios.

However, these images also show that pinned S355 arches only surpass ultimate loads of fixed S275 arches for medium rise-to-span ratios and for 5 [m] spans, in every simulated temperature level. In every other span case, fixed S275 arches showed considerably higher loads than both other cases, specially for higher rise-to-span ratios.

Looking at the perspective of slenderness, the biggest differences in ultimate load between steel classes are observed for medium rise-to-span ratios, which decreased

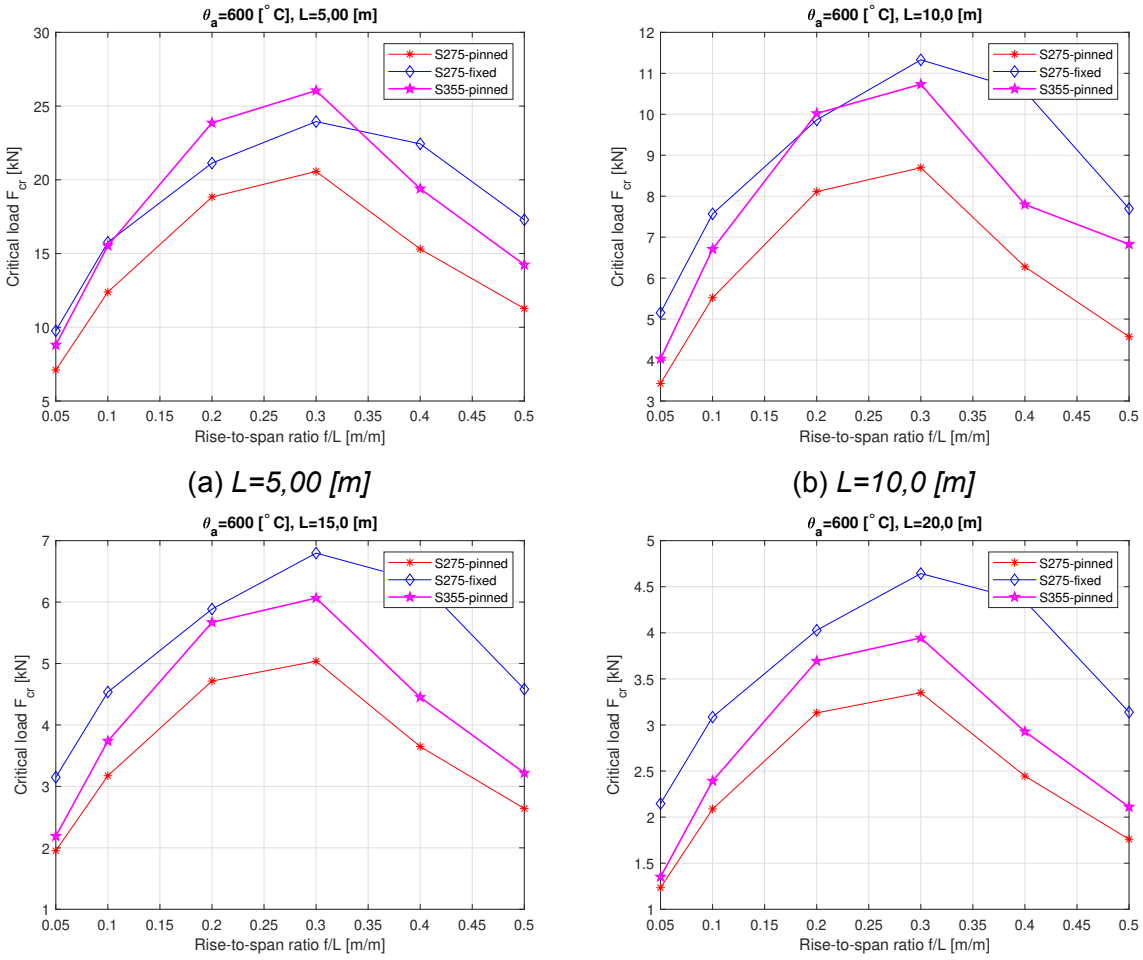

(a) *L=5,00 [m]* (b) *L=10,0 [m]*

(c) *L=15,0 [m]* (d) *L=20,0 [m]*

Figure 4.30: Steel class comparison at 600 [°C].

as rise-to-span ratios increased in every temperature/span case solution. This behavior might be explained by a combination of internal force distribution and buckling collapse mode. Generally, stocky arches collapse in the plastic or elasto-plastic domain, by a combination of elastic buckling and plastification of the cross-section. On the other hand, slender arches collapse by buckling in the elastic domain, before reaching the cross-section plastic load, in which the steel yield strength does not affect their behavior.

Analyzing buckling modes and vertical load-displacement behavior of the aforementioned steel/support conditions, Figures 4.32, 4.33 and 4.34 show the vertical displacement paths for 5 [m] arches under 400, 600 and 700 [°C], respectively. In every case,

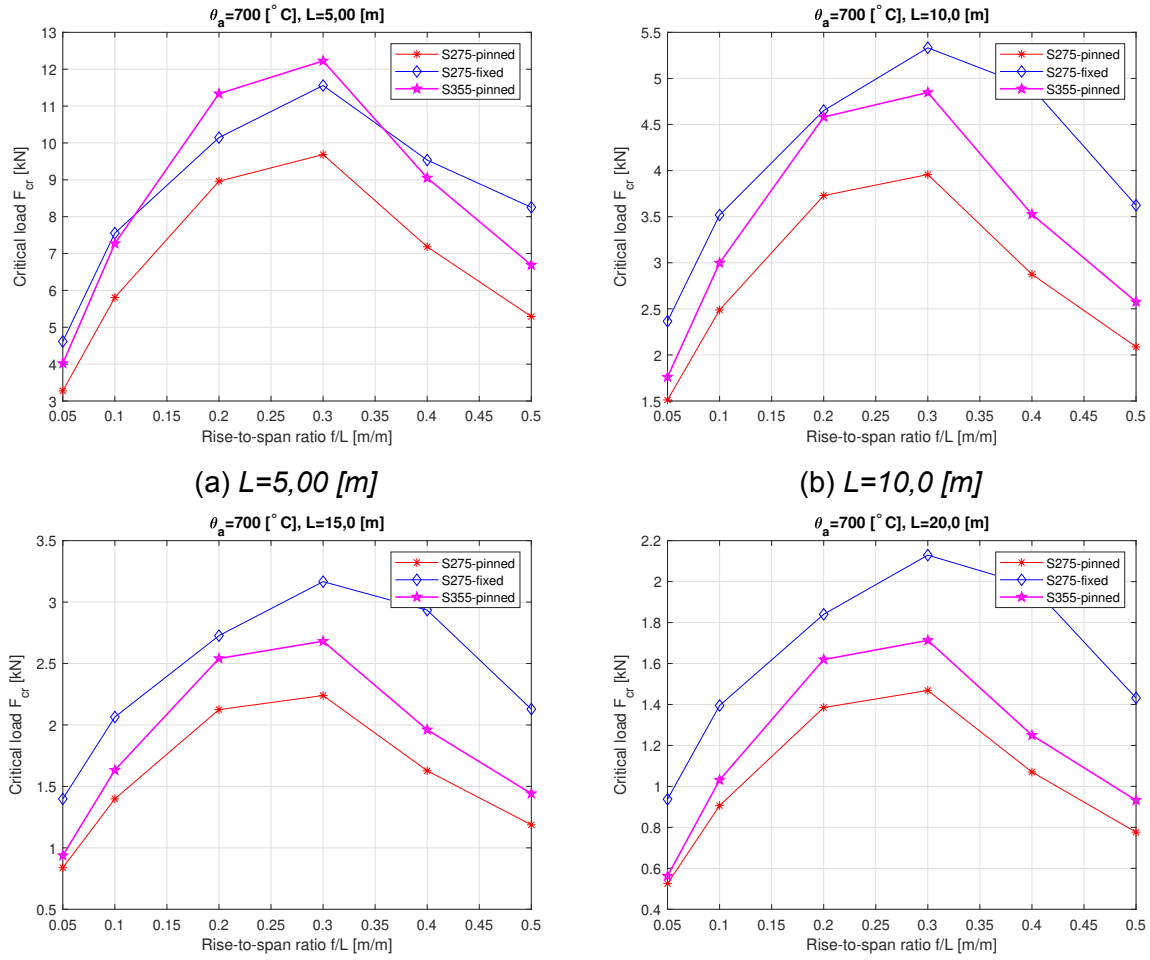

(a) *L=5,00 [m]* (b) *L=10,0 [m]*

(c) *L=15,0 [m]* (d) *L=20,0 [m]*

Figure 4.31: Steel class comparison at 700 [°C].

fixed arches of S275 steel developed smaller displacements than both other cases, despite following a similar load path.

Also, one easily notices that pinned arches of both S275 and S355 steel classes follow the same load-displacement path up until the beginning of cross-section plastification, after the most stressed fiber reaches its correspondent yield strength. After this point, a substantial difference in displacement is seen in every case.

In sum, it is clear that enhancing support stiffness for steel arches under bending moments and axial forces is a better option than switching to a higher steel class, since fixed arches provide higher ultimate loads and lower buckling displacements, even at

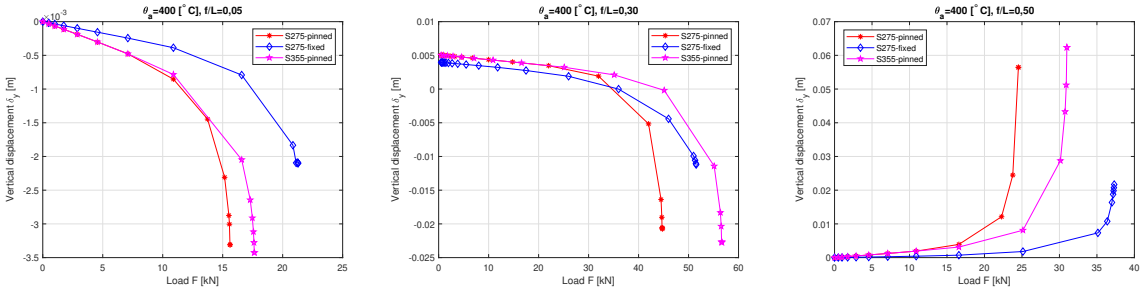

(a) *f/L=0,05* (b) *f/L=0,30* (c) *f/L=0,50*

Figure 4.32: Vertical displacements of 5 [m] pinned arches for different steel classes at 400 [°C].

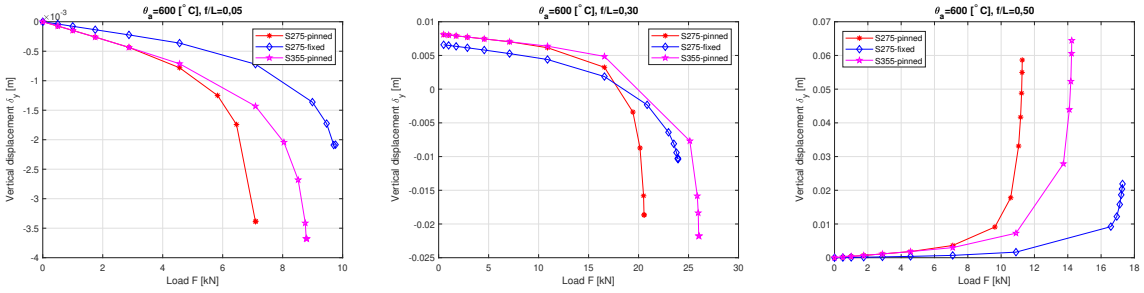

(a) *f/L=0,05* (b) *f/L=0,30* (c) *f/L=0,50*

Figure 4.33: Vertical displacements of 5 [m] pinned arches for different steel classes at 600 [°C].

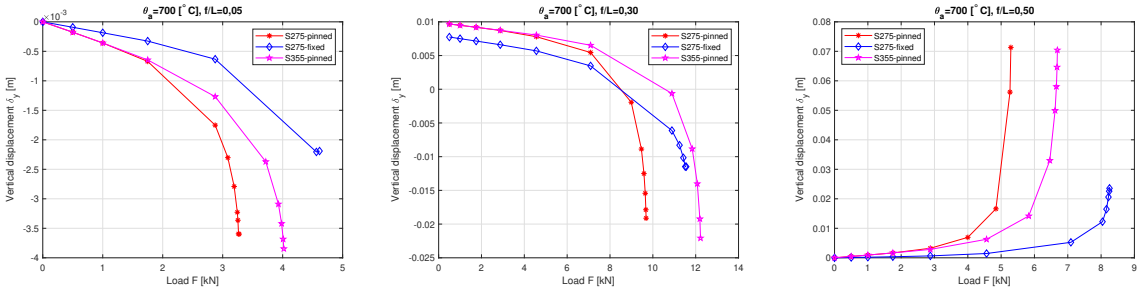

(a) *f/L=0,05* (b) *f/L=0,30* (c) *f/L=0,50*

Figure 4.34: Vertical displacements of 5 [m] pinned arches for different steel classes at 700 [°C].

elevated temperatures developed during a fire event. However, a perfectly fixed support is not achievable in normal construction due to inevitable deformations of joints and joint components.

4.3.4 Numerical results *versus* standard simplified methods

In this section, the standard safety and strength verifications given in Eurocode 3 parts 1-1 and 1-2, described in Sections 3.1.2 and 3.2.5, will be compared to the nonlinear ultimate load results obtained in the aforementioned numerical solutions, for both natural and elevated temperature cases.

4.3.4.1 Elements under natural temperature

For natural temperature analyses, Eurocode 3 part 1-1, [27], provides an interaction expression for members under axial forces and bending moments. Considering that this paper deals only with in-plane instability design of arches curved by their strong axis, some simplifications are made. These simplifications and the respective resulting expression are already demonstrated in Equation 3.6, in Section 3.1.2.

In this context, Figure 4.35 shows the normalized axial force in reference to the compression plastic capacity of the cross-section *versus* the normalized bending moment in reference to the plastic bending moment capacity of the cross-section, at natural temperature, for arches with 5, 10, 15 and 20 [m] spans and rise-to-span ratios from 0,05 to 0,50 [m/m].

In this image, each line represents the standard axial and bending moment interaction equation given in Eurocode 3-1-1 for straight members, while each point marks the numerical results from *ANSYS* arch simulations. For each line, a different flexural buckling reduction factor χ_y was calculated, depending on the arch non-dimensional slenderness, considering the imperfection curve **a**. Numerical internal forces were obtained using the *SMISC* table properties in *Element Line Results*, for the convergence ultimate load.

It is clear that, in every case, the standard interaction expression for linear elements yielded conservative results for the ultimate load, always favoring safety. Also, numerical results show that, for greater arch spans, bending moments are much more significant in the arch collapse for every studied rise-to-span ratio case.

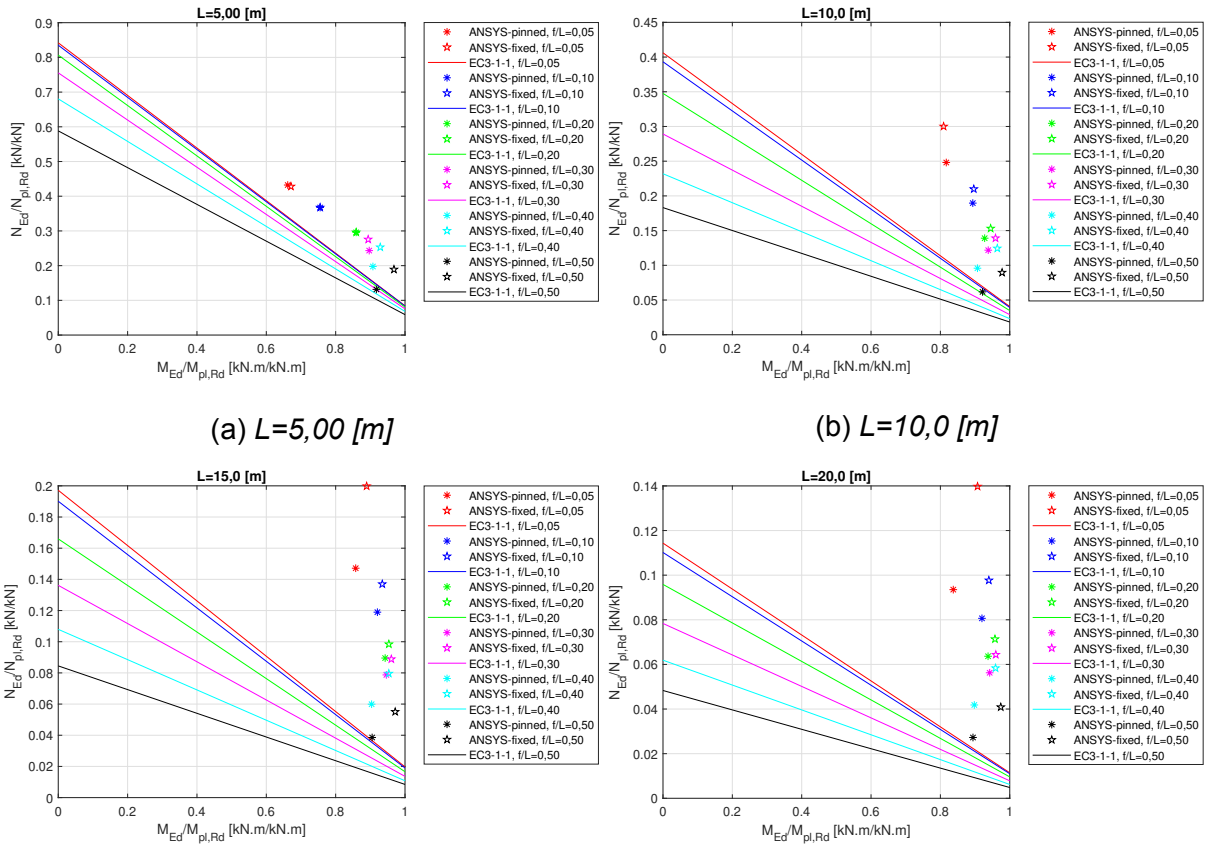

(a) *L=5,00 [m]* (b) *L=10,0 [m]*

(c) *L=15,0 [m]* (d) *L=20,0 [m]*

Figure 4.35: Normalized axial force *versus* normalized bending moment.

For smaller spans, numerical results approached the standard strength curves, specially for more slender arches. Nonetheless, a more uniform axial/bending moment relationship was found, due to the smaller contribution of bending moments and flexural displacements of instability phenomena.

4.3.4.2 Elements under elevated temperatures

As explained above in Section 3.2.5, an interaction expression for members under axial force and bending moments under elevated temperatures is given in Eurocode 3 part 1-2, [44]. This expression is similar to the one used in natural temperature safety verifications, but it contains the appropriate reduction factors due to temperature.

Following the same methodology as the previous section, a comparison between the standard verification and numerical results obtained in this study for temperature levels of 400, 600 and 700 [°C] are shown below.

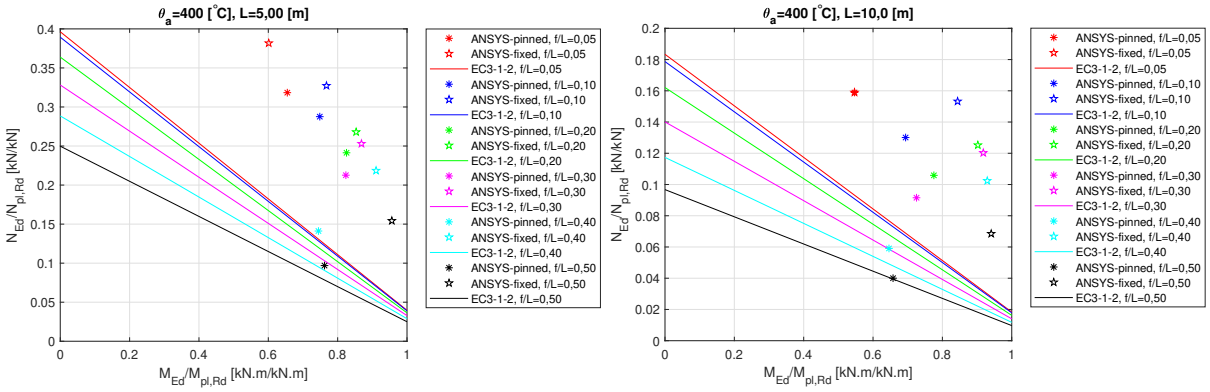

(a) *L=5,00 [m]* (b) *L=10,0 [m]*

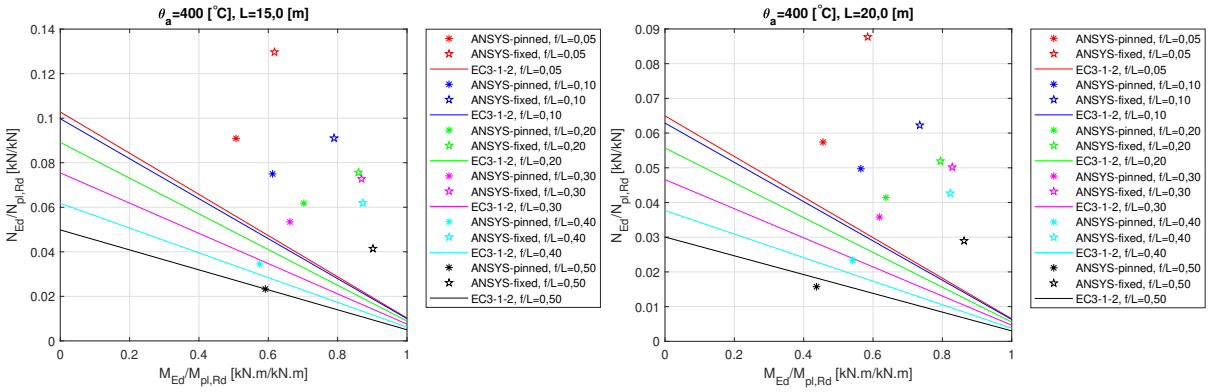

(c) *L=15,0 [m]* (d) *L=20,0 [m]*

Figure 4.36: Normalized axial force *versus* normalized bending moment at 400 [°C]

Figure 4.36 shows the numerical *versus* standard verifications for the 400 [°C] temperature level. It is seen that every case of fixed support yielded higher loads than the standard curve, and considerably higher than pinned arches of the same geometry. However, for the rise-to-span ratio cases of 0,40 and 0,50 [m/m], numerical solutions of pinned arches showed very close results with the standard Eurocode 3-1-2 curves in every span case, and in the 20 [m] span case the result for the 0,50 [m/m] geometry is under the standard curve.

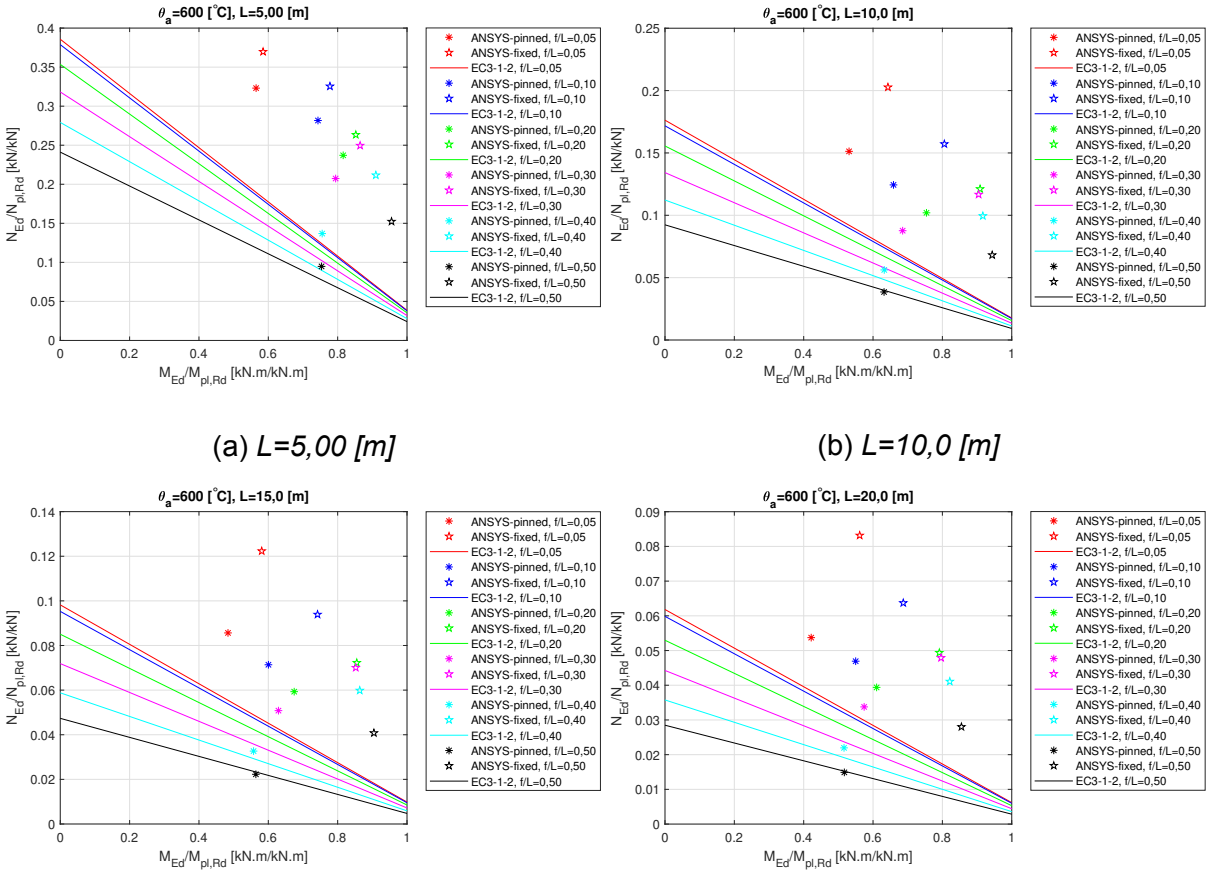

(a) *L=5,00 [m]* (b) *L=10,0 [m]*

(c) *L=15,0 [m]* (d) *L=20,0 [m]*

Figure 4.37: Normalized axial force *versus* normalized bending moment at 600 [°C]

Figure 4.37 shows the standard/numerical comparison for the 600 [°C] temperature level. A similar behavior as the 400 [°C] case regarding the differences between standard and numerical results is seen for this temperature level, although maximum values for both bending moments and axial forces dropped substantially, as expected. For the 700 [°C] temperatures, this same behavior was found, as seen in Figure 4.38.

Comparing every studied elevated temperature case with the natural temperature results, it is noticeable that for the same arch span, support condition and temperature level but different rise-to-span ratios, ultimate bending moments did not significantly change, while ultimate axial forces were severely reduced as temperatures rose.

Also, in every studied span case, more slender arches showed closer results to

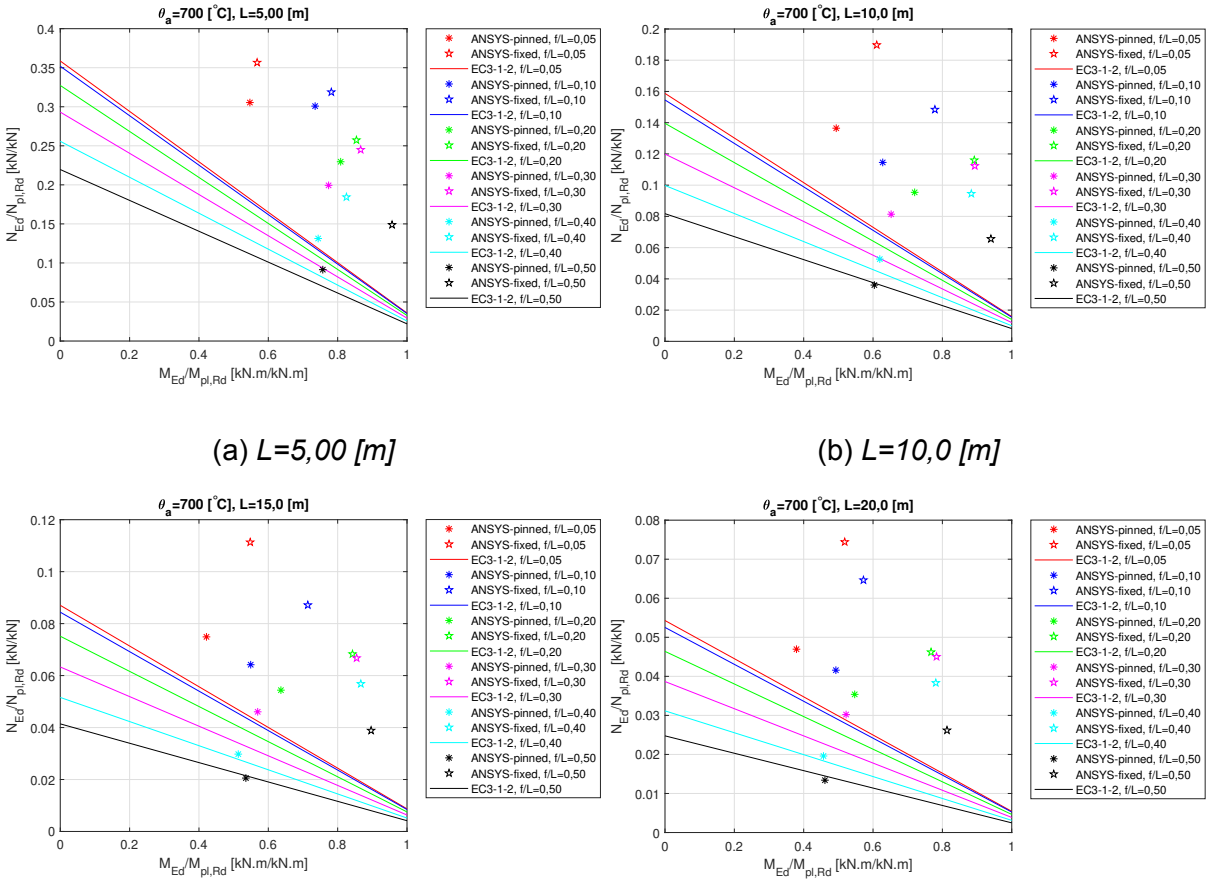

(a) *L=5,00 [m]* (b) *L=10,0 [m]*

(c) *L=15,0 [m]* (d) *L=20,0 [m]*

Figure 4.38: Normalized axial force *versus* normalized bending moment at 700 [°C]

the standard interaction equations from Eurocode 3, with some numerical solutions of pinned arches yielding ultimate internal forces below the respective standard curves. This behavior is due to the fact that these interaction expressions are determined based on straight elements, and do not account for the in-plane slenderness occurring in members with two major dimensions, such as arches and curved beams. In sum, the standard simplified methods given in Eurocode 3 Part 1-2 tend to overestimate buckling resistance for arches with high in-plane slendernesses.

Chapter 5

Stress development during mechanical cold-curving

Currently, methods for curving straight beams into arches have little scientific base, and these processes are done almost exclusively depending on experience of the operator and machine specificities, [19]. For this reason, curving methods generally require successive iterations until the proper geometry is achieved.

Nonetheless, since curving is done by applying mechanical or thermal loads on a straight member, this process affects how a structural piece behaves when used for its initial purpose, mainly because it changes the residual stress patterns on hot-rolled steel and might add imperfections and distortions that cause its resistance to decrease.

In this chapter, the displacement and strain during cold-curving and final residual stress pattern are investigated. Firstly, a theoretical approach was employed to determine important curving parameters and define a final residual stress profile. Then, an experimental setup was developed to curve real-scale IPE100 steel arches using a set of hydraulic rams at natural temperature. Finally, the experimental results are analyzed for vertical displacements and longitudinal strains.

5.1 Theoretical approach

In this section, a methodology is proposed to define the plastification zone related to the applied load and desired radius of curvature of an arch, and enabling the definition of the residual stress profile due to cold curving of each curved beam.

The first step is to relate the applied load to the stress pattern in the cross section. Considering a bi-linear elastic-perfectly plastic material behavior without strain hardening, Figure 5.1b, generating an elasto-plastic stress distribution as seen in Figure 5.1a, which comprises a plastic region ranging from the external surfaces towards the neutral axis of the section and a linear elastic region in between plastic zones, one can determine the bending moment related to this distribution by the cross section equilibrium condition stating that the summation of moments around the neutral axis due to stresses are equal to the applied bending moment.

Since all analyzed cross-sections are symmetrical around the neutral axis, and considering that the entire flange will reach past the yield strength, three distinct zones are defined: 1) plastic zone in the flange; 2) plastic zone in the web; 3) elastic zone in the web. These regions are shown in Figure 5.1a, neglecting the rolling root radius between flange and web.

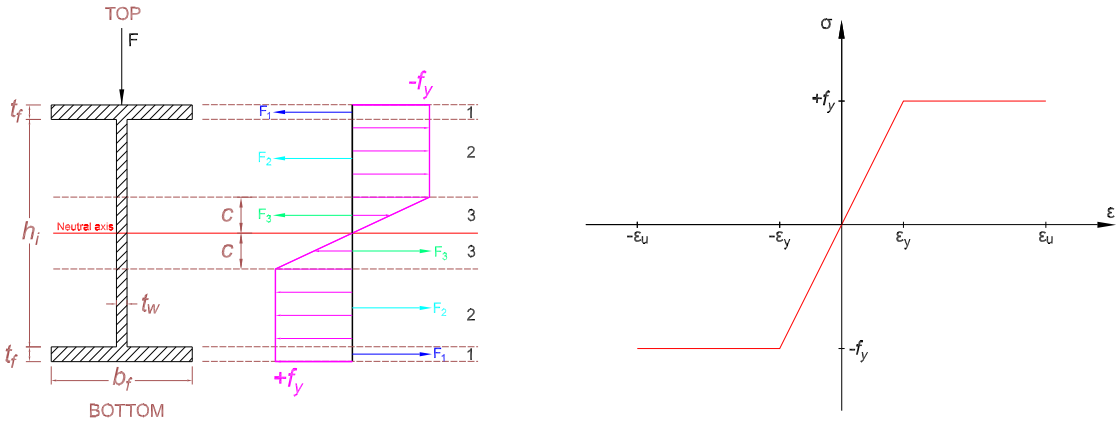

(a) Curving stress distribution (b) Bi-linear stress-strain material behavior

Figure 5.1: Stresses due to curving.

In this figure, $+f_y$ indicates the tension yield stress and $-f_y$ indicates its compression counterpart. Therefore, since the stresses are known along the cross-section, it is possible to calculate the couple moments $M = F \times d$ in each zone by transforming the stresses into concentrated forces by $F = \sigma A_z$, where A_z is the respective zone cross-section area. The distances d between forces depend on the section properties. The calculated couple moments for each zone are given in Equations 5.1 to 5.3.

$$M_1 = f_y b_f t_f (h_i + t_f) \tag{5.1}$$

$$M_2 = f_y t_w \left(\frac{h_i}{2} - c\right)\left(\frac{h_i}{2} + c\right) \tag{5.2}$$

$$M_3 = f_y t_w \left(\frac{2c^2}{3}\right) \tag{5.3}$$

From the cross-section equilibrium condition stated above, the applied elasto-plastic moment is equal to $M_{ep} = M_1 + M_2 + M_3$. Therefore, rearranging the terms in the expressions above, one gets

$$M_{ep} = f_y \left[b_f t_f (h_i + t_f) + t_w \left(\frac{h_i}{2} - c\right)\left(\frac{h_i}{2} + c\right) + t_w \left(\frac{2c^2}{3}\right)\right] \tag{5.4}$$

Equation 5.4 is the final expression for the applied elasto-plastic bending moment as a function of the elastic zone height c. Thus, as load is applied, this parameter c gets smaller until the entire cross-section reaches the yield strength and forms a plastic hinge, as shown in Figure 5.2 for an IPE100 section made of S275 steel. Nonetheless, as bending moments grow larger and the beam is bent, curvature increases causing the radius to decrease.

Then, as soon as loads are removed, the remaining elastic portion c of the cross-section deforms back to its initial form, causing a phenomenon called *springback*, where the beam recovers part of its curvature (increasing its radius) proportionally to the plastification level under which it was submitted, as seen in Figure 5.3.

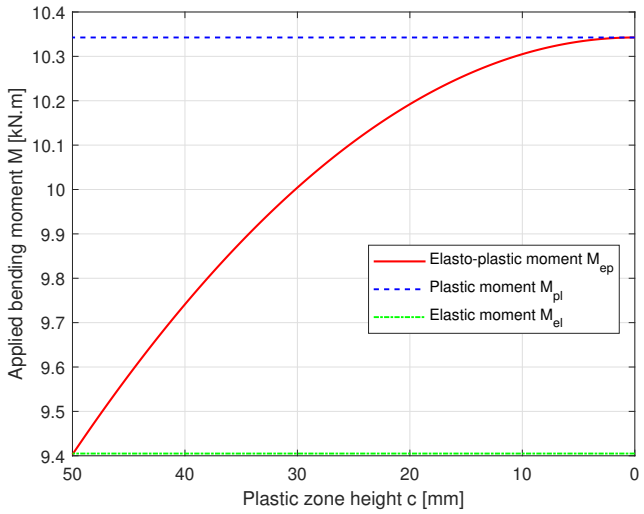

Figure 5.2: Elasto-plastic bending moment development.

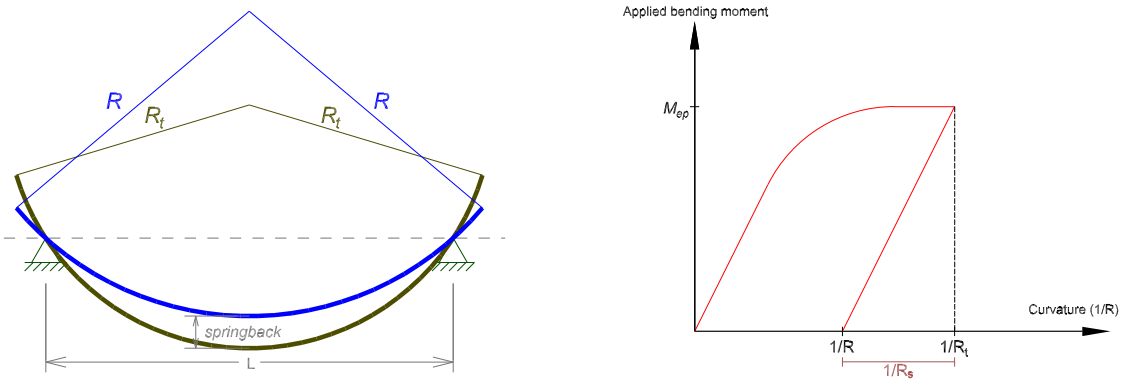

(a) Changes in radius during curving. (b) Moment *versus* curvature relationship, [52].

Figure 5.3: Beam curvature development.

Hence, the final curvature radius R is defined as a function of the total radius R_t reached during bending and the recovered *springback* radius R_s, as shown in Equation 5.5.

$$\frac{1}{R} = \frac{1}{R_t} - \frac{1}{R_s} \tag{5.5}$$

Henceforth, the radius of curvature for a deformed beam is related to the strain during bending as shown in Equation 5.6, for an element located at a distance y from the neutral axis for symmetrical cross-sections. Since this relationship is derived from

the geometrical definition of bending strain and radius of curvature, it is valid for both large and small radii.

$$\frac{1}{R} = \frac{\varepsilon}{y} \tag{5.6}$$

As seen in Figure 5.1a, at the elastic-plastic interface in $y = c$, stress is equal to f_y and material behavior is still considered to be elastic. Consequently, the relationship established in Equation 5.6 can be applied, as well as Hooke's Law $\varepsilon = \sigma/E$ for an elastic material. Therefore, combining both expressions, the curvature radius R_c at $y = c$ is given as

$$\frac{1}{R_c} = \frac{f_y}{Ec} \tag{5.7}$$

Nevertheless, since the interest variable in this methodology is the curvature of the center line of the beam, the radius R_c can be rewritten as a function of the total radius R_t as $R_c = R_t + c$, considering that c is located below the neutral axis, as shown in Figure 5.4. This happens because as the beam is deformed to R_t, the corresponding stress distribution generated in the process is the one shown in Figure 5.1a, where the plastification zone reaches $y = c$. Therefore, the total radius can be described as a function of c as

$$R_t = c\left(\frac{E}{f_y} - 1\right) \tag{5.8}$$

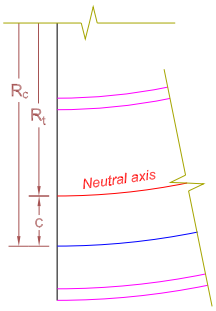

Figure 5.4: Radius R_c at $y = c$.

Also, bearing in mind that the *springback* follows an elastic behavior, Hooke's Law $\varepsilon = \sigma/E$ alongside the bending stress formula $\sigma = My/I$ are employed, and Equation 5.6 becomes

$$\frac{1}{R_s} = \frac{M_{ep}}{EI} \tag{5.9}$$

In the expression above, M_{ep} is the applied elasto-plastic bending moment calculated from Equation 5.4 and EI is the beam's bending stiffness. So, Equation 5.5 is used to define an expression of the plastic zone height c depending on the desired final curvature radius R and section/material properties. This expression is shown in Equation 5.10.

$$\frac{1}{R} = \frac{1}{c\left(\frac{E}{f_y} - 1\right)} - \frac{f_y}{EI}\left[b_f t_f (h_i + t_f) + t_w\left(\frac{h_i}{2} - c\right)\left(\frac{h_i}{2} + c\right) + t_w\left(\frac{2c^2}{3}\right)\right] \tag{5.10}$$

Even though the expression above does not have an analytical solution in order to c, it is possible to be solved by numerical iterative methods, such as Newton-Raphson. This method states that for a function $f(x)$ differentiable in its domain so $f'(x)$ exists, and given an initial value x_0, its root is given by

$$x_{k+1} = x_k - \frac{f(x_k)}{f'(x_k)} \tag{5.11}$$

For $k = 0, 1, 2, 3, ..$ until a desired convergence level is reached. This method is largely implemented in computational solutions such as the *fsolve* function in *MATLAB*. Then, once the parameter c is known, Equation 5.8 is utilized to determine the total radius R_t of the beam, that after releasing applied loads will elastically return back to the final desired radius R.

More importantly, this parameter c is essential for determining the final cold-bent residual stress profile for this type of curving procedure. This is done by summing the elasto-plastic stress profile on the cross-section at the bending procedure with the

elastic stress profile in the *springback* unloading step, after the loads are released. Figure 5.5 shows a scheme of this method and the final residual stress result.

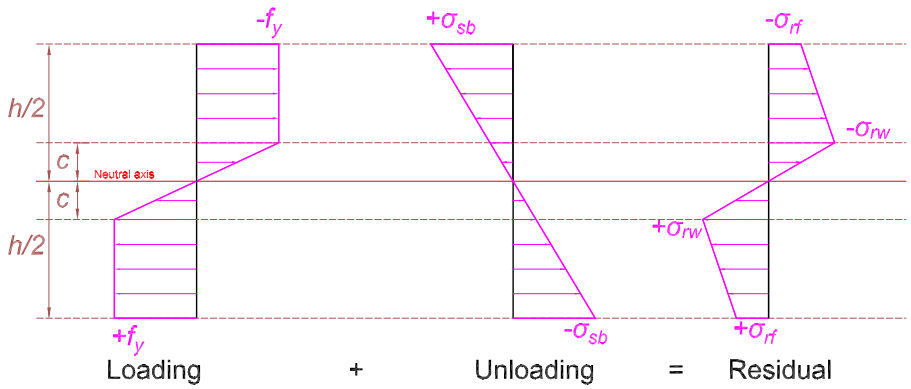

Figure 5.5: Cold-bent residual stresses.

In the unloading phase, the respective maximum stress magnitude σ_{sb} is calculated from the applied elasto-plastic bending moment M_{ep} by the elastic bending stress formula, as shown in Equation 5.12.

$$\sigma_{sb} = \frac{M_{ep} h}{2 I_y} \tag{5.12}$$

The maximum residual stresses in the flange σ_{rf} and in the web σ_{rw} shown in Figure 5.5 are given in Equations 5.13 and 5.14.

$$\sigma_{rf} = f_y - \sigma_{sb} \tag{5.13}$$

$$\sigma_{rw} = f_y - \frac{2 c \sigma_{sb}}{h} \tag{5.14}$$

In sum, the analytical method described above provides a practical manner to define a final residual stress profile as a function of the desired arch radius, which makes it possible to refine future numerical studies of in-plane stability of arches and curved beams with constant curvature.

5.2 Experimental setup

In this section, an experimental setup was developed to curve straight beams into arches at room temperature and investigate in real-time the vertical displacement and longitudinal strain behavior as two vertical point loads were applied. For this purpose, a straight IPE100 beam of S275 steel available at the Construction Materials Lab of the Polytechnic Institute of Bragança was used to produce the studied arches.

Mesquita, [53], studied the mechanical properties of the aforementioned IPE100 profiles of S275 steel grade. It was found that the yield strength f_y resulted as low as 292,85 [MPa], and went as high as 306,22 [MPa]. Also, the elastic modulus values E fluctuated around 200 [GPa]. These findings will be used throughout this experimental study, when necessary.

5.2.1 Specimen preparation and data acquisition

In order to measure elongation/shortening and vertical deflections of the specimens throughout load-applying procedures, strain gages and cable actuated position sensors were attached to the beams at strategic locations, which made it possible to check and verify important parameters for curving. Also, geometrical measurements of cross-section properties and lateral imperfections were taken.

5.2.1.1 Cross-section dimensions and lateral imperfections

Even though structural elements are mathematically modeled as perfect geometries, fabrication and logistical procedures inherently impose dimensional imperfections. For this experimental investigation, cross-sectional dimensions and lateral imperfections of the tested beam were previously measured with respective adequate procedures.

In order to measure these parameters, the specimen was properly marked with seven different sections of interest denoted as *S1* through *S7* along the beam's length, measured from a reference section previously marked at the middle. A general scheme

of the sections' locations is shown in Figure 5.6.

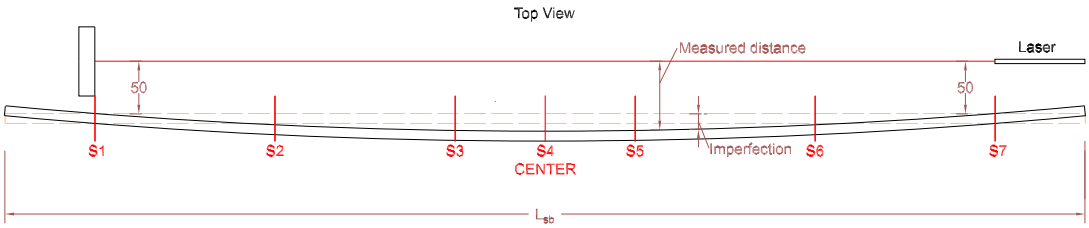

Figure 5.6: Geometry measuring setup.

In each section described above, the cross-sectional dimensions were measured using a caliper rule with 0,1 [mm] precision and maximum course of 200 [mm]. In order to measure web thickness t_w, a micrometer with 0,01 [mm] precision and 75 to 100 [mm] measuring range was employed. Both measuring devices and procedures are shown in Figures 5.7b and 5.7c. The cross-sectional dimensions measured are shown in Figure 5.7a, distinguishing between top and bottom flanges that were previously marked on the profile surfaces.

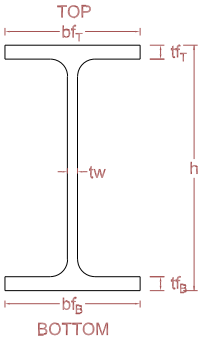

(a) Cross-section measured dimensions.

(b) Caliper.

(c) Micrometer.

Figure 5.7: Cross-section measuring apparatus.

Moreover, lateral imperfections of the specimen cited above were measured using a level laser positioned at section *S1* and pointed to section *S7*, at a lateral distance of 50 [mm] away from its bottom flange. This measuring setup is also shown in Figure 5.6.

Then, lateral distance from both top and bottom flanges to the projected laser was measured with a metallic ruler with 0,5 [mm] precision. Figure 5.8a shows a lateral view of the measured apparatus and procedure. In this aspect, lateral imperfection is given by subtracting the initial distance to the read value in each interest section. As seen in Figure 5.6, negative imperfection values mean that the shape of imperfection is in the opposite direction regarding the initial consideration.

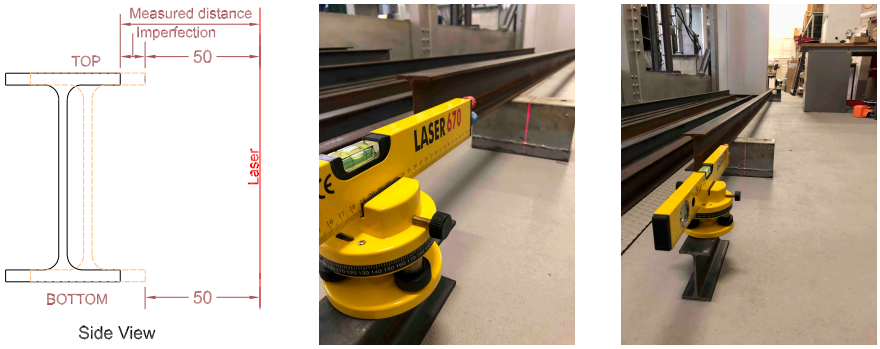

(a) Side view. (b) Laser. (c) Measuring setup.

Figure 5.8: Imperfection measuring apparatus.

The results of cross-section dimensions and lateral imperfections collected in the procedures mentioned above are shown in Tables 5.1 and 5.2, respectively. In these tables, *NM* stands for not measured, since sections *S1* and *S7* were reference sections for imperfection measurements.

Section	b_{fT}	t_{fT}	b_{fB}	t_{fB}	t_w	h
S1	54,80	6,20	55,00	6,20	4,25	100,80
S2	54,80	6,30	55,20	6,00	4,14	100,80
S3	55,00	6,30	55,20	6,00	4,16	100,60
S4	54,90	6,20	55,10	6,00	4,26	100,50
S5	54,80	6,40	55,00	6,00	4,09	100,70
S6	54,90	6,30	55,20	6,00	4,18	100,80
S7	54,80	6,30	55,10	6,00	4,13	100,80
Average	54,86	6,29	55,11	6,03	4,17	100,71
Std. Dev	0,079	0,069	0,090	0,076	0,063	0,1215

Table 5.1: Measured cross-sectional dimensions.

Section	Top	Bottom
S1	*NM*	*NM*
S2	0,50	1,00
S3	5,00	4,75
S4	5,00	4,50
S5	2,75	2,50
S6	0,75	0,50
S7	*NM*	*NM*

Table 5.2: Measured lateral imperfections.

5.2.1.2 Strain gauges

Strain gauges are currently one of the most reliable and practical devices for measuring strains in experimental stress analyses of a variety of objects. Basically, these devices measure the change of length ratio of the surface they are attached, in the direction they are pointed to, assuming that the surface strain is transferred without loss to the strain gage, [54].

In this experimental project, metal strain gauges were employed for the curving tests. This type of device consists on a metal grid placed in a carrier material connected to a signal reading machine, and its operation relies in the principle of strain-resistance relationship of electrical conductors, which says that the change in resistance r depends on the conductor's deformation ε and on the change in resistivity ϱ due to material micro-structural modifications, as shown in Equation 5.15.

$$\frac{dr}{r_0} = \varepsilon(1 + 2\upsilon) + \frac{d\varrho}{\varrho} \tag{5.15}$$

In this expression, r_0 is the initial resistance and υ is the Poisson's ratio of the conductor. For some metal alloys used for manufacturing strain gauges, micro-structural changes in resistivity may be considered to be negligible, [54], and the second term in Equation 5.15 vanishes, making it only dependable on the geometrical change of length. Then, the installed strain gages are connected to voltage or electric current measuring devices which automatically calculate the change in resistance and convert

these electrical readings into strain measurements.

For the specimens aforementioned, a group of four strain gauges was placed at the top flange and down the web in section *S4* (center of the beam) for each specimen, in an array as shown in Figure 5.9.

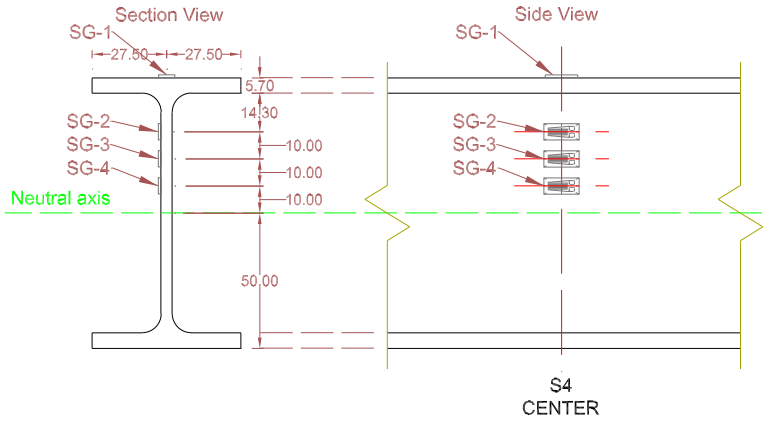

Figure 5.9: Locations of strain gauges along the section.

Before installing the strain gauges, the surfaces were properly sanded and cleaned with acetone and two cleaning agents *Conditioner A* and *Neutralizer 5A*, as seen in Figures 5.10a and 5.10b. Then, the correct position and direction (see Figure 5.9) of each strain gauge was marked (Figures 5.10c and 5.10d). After this, each strain gauge was glued to a previously prepared strip of glue tape and attached to the surface with a polymeric bonder (Figures 5.10e and 5.10f). Finally, the outlet wires were welded to extender wires connected to the reading machine, as seen in Figure 5.10g.

5.2.1.3 Cable actuated position sensors

These types of devices are used to measure linear position changes and velocities, by the means of translating cable movements into electrical signals read by an analogical or digital encoder. The measuring cable is connected to a rotary spool in one end, which is attached to a rotation sensor in the opposite end, [55].

Figure 5.11a shows an example of the position sensors used in this experimental investigation, with a measuring range of 0 to 1250 [mm]. A total of 3 position sensors

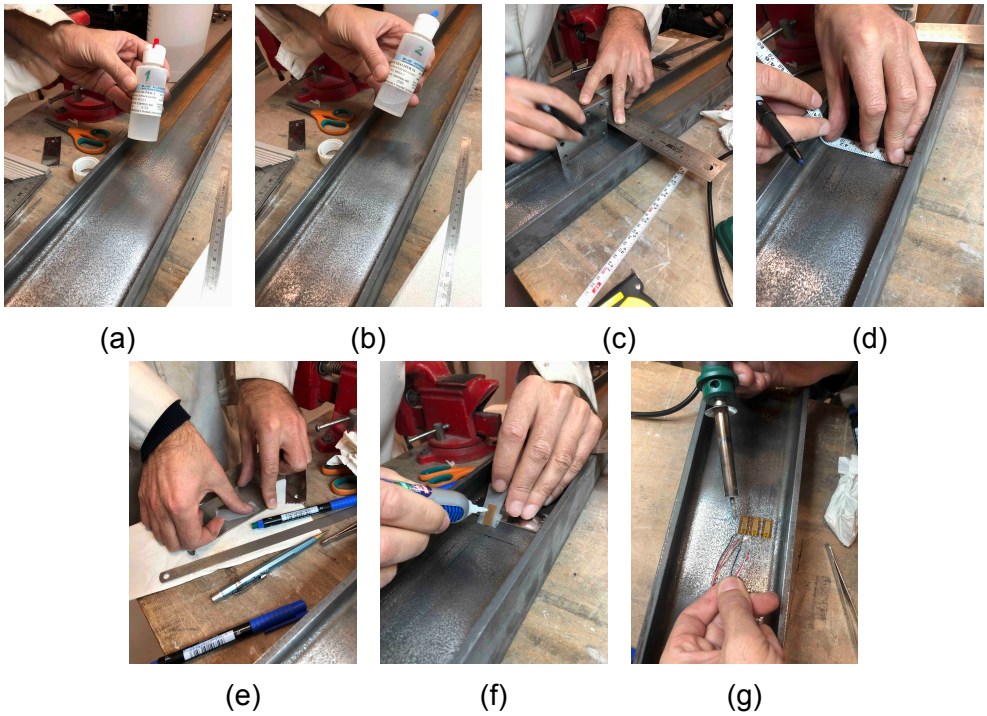

(a) (b) (c) (d)

(e) (f) (g)

Figure 5.10: Strain gauge installation procedures.

(a) (b) (c)

Figure 5.11: Position sensors.

were employed, located respectively under the beam at section *S4* (center of the beam) and under both loading points, as seen in Figures 5.11b and 5.11c.

Each sensor was bolted to a movable metal bar in order to adjust it to the desired position. In order to attach the measuring cable to the specimen, a supporting gadget was placed in the bottom flange of the beam, as seen in Figure 5.11c.

5.2.2 Curving procedure

For this project, the incremental bending method was chosen to curve the straight beams mentioned above. This method is detailed in Section 2.2.2, and it consists on the application of point loads transversely to the beam's strong axis (in the scope of this study) until the desired radius is achieved, which may take several load iterations.

5.2.2.1 Equipment and setup

A load testing machine located at the Structures and Strength of Materials Lab of the Polytechnic Institute of Bragança was employed, as seen in Figure 5.12a. This machine has a total length of 8,00 [m] and it is equipped with two longitudinally movable hydraulic rams, each with a load cell at its free end (see Figure 5.12b) capable of applying up to 100 [kN] and vertical displacement up to 239 [mm], as well as two movable support mechanisms capable of restraining horizontal, vertical and/or lateral displacements, as seen in Figure 5.12c.

(a) Load testing machine. (b) Load cell. (c) Support.

Figure 5.12: Load testing apparatus.

For the curving phase, both supports were placed 2,00 [m] away front the center of the machine, and both loading rams were placed 1,00 [m] away also from the center, creating a symmetrical loading setup. Nonetheless, in order to avoid the occurrence of lateral-torsional buckling while curving, discretely-spaced lateral restraints were provided along the beam. The complete setup with proper dimensions (in centimeters) is

shown in Figure 5.13.

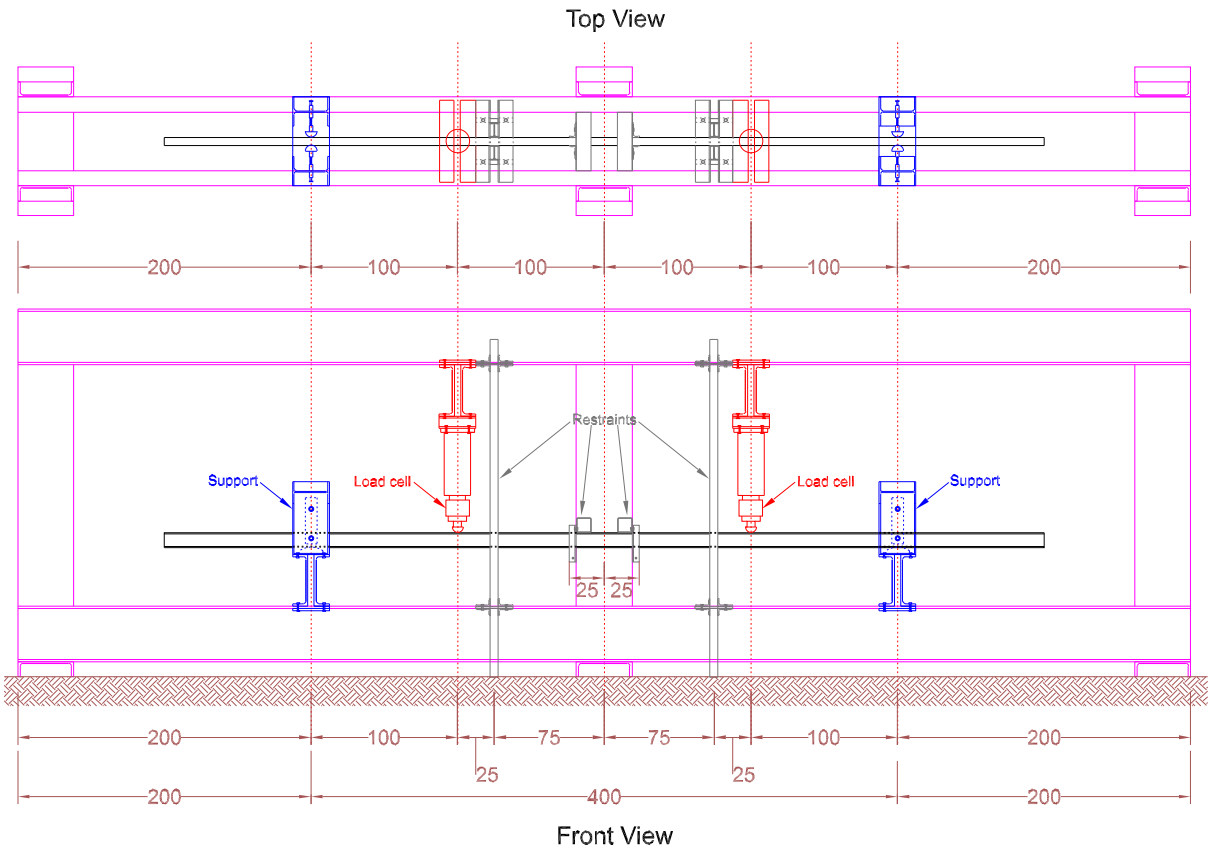

Figure 5.13: Curving setup.

Beyond installing lateral restraints, it is still necessary to check for lateral-torsional buckling in unrestrained sections of the beam to be curved. For this, the critical moment M_{cr} for a beam under uniform bending calculated by Equation 5.16 was determined for each unrestrained section. Even though in the sections closest to the supports a non-uniform moment distribution is seen, the uniform bending check represents a conservative approach, since the real corrected critical moment for these sections are proven to be higher than if considered to be under uniform bending.

$$M_{cr} = \frac{\pi}{L_b}\sqrt{GI_T EI_z\left(1 + \frac{\pi^2 EI_w}{L_b^2 GI_T}\right)} \tag{5.16}$$

In this expression, L_b is the buckling length of each respective section, G is the

transverse elastic modulus (for steel $G = E/2(1+v) = 76923,08\,MPa$), I_T is the uniform torsion modulus of the cross section, I_w is the warping constant of the cross section and I_z is the weak axis moment of inertia. For an IPE100 section used in this study, $I_T = 355,7.10^4\,mm^4$, $I_w = 3817.10^9\,mm^6$ and $I_z = 10820.10^4\,mm^4$. Table 5.3 shows the results of critical moment for every buckling length L_b, according to Figure 5.13.

L_b [m]	M_{cr} [kN.m]
1,25	16,56
0,70	38,66
0,50	68,03

Table 5.3: Critical moment for lateral-torsional buckling

Considering that an IPE100 profile has a plastic modulus around the strong axis of $W_{pl,y} = 39,4.10^3$ [mm^3], the plastic moment is determined by $M_{pl,y} = W_{pl,y} f_y = 39,4.10^3 \times 292,85 = 11,54$ [kN.m], safely considering the lower-bound value of the yield strength. Thus, comparing moment values it is noticeable that plastification of the cross-section occurs before lateral torsional buckling.

5.2.3 Experimental results

This section presents the experimental results obtained in curving processes of straight beams into arches. A load-deflection path for both the beam center point and load application points is shown in Figure 5.14a. For the center point of the beam, the average force between both load cells was taken, since there is not a load applied in this point.

In this picture, it is clear that *springback* displacements are important and must not be neglected when determining the final radius and residual stress patterns for curved steel beams. Also, it is seen that the *springback* unloading follows the same slope as the elastic loading path, agreeing with literature studies about the curving processes of straight beams into arches.

Figure 5.14b shows the average load (between both loading points) *versus* longitudinal strain (shortening) results collected from the strain gauges previously installed

in the beam, whose position and details are shown in Figure 5.9. Strain gauge *SG-1* is positioned at the top flange of the tested beam, which shows the greater values for compressive strains. It is seen that both strain and vertical displacement paths show similar loading and unloading behavior.

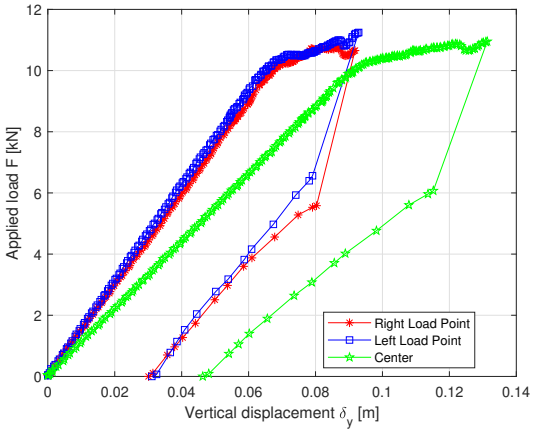

(a) Vertical displacements.

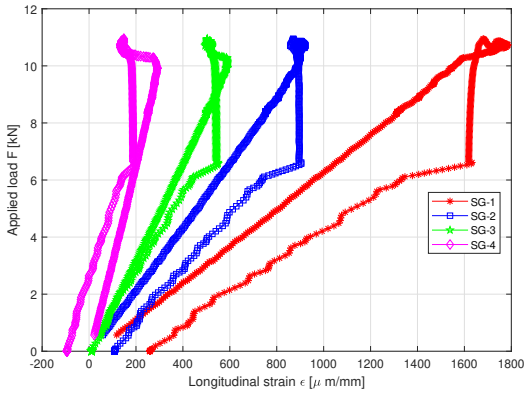

(b) Strain measurements.

Figure 5.14: Experimental results.

Also, it is clear that *springback* strains are significant, and even with high load levels, the remaining plastic deformation might be small, which requires several load iterations in order to get a desired curvature from a straight steel beam.

Nonetheless, when cold-curving a steel member with point loads, special attention must be given to avoid lateral torsional buckling, which is the reason why roller bending and induction bending are recommended for curving slender steel beams.

Chapter 6

Conclusions

This dissertation paper studied the in-plane thermo-mechanical behavior of steel arches and curved beams by their major axis via numerical linear and nonlinear *FEM* solutions. Various span and rise-to-span ratios were evaluated, for pinned and fixed support conditions and steel classes S275 and S355. Also, these geometries and properties were simulated at elevated temperature conditions, aiming to study how steel arches responds to the combination of mechanical and thermal loads.

Firstly, elastic simulations were compared to literature methods for predicting the elastic critical buckling load of arches. It was found that most methods yielded good results, mainly for moderately slender arches. However, for rise-to-span ratios under 0,10 [m/m], every studied literature formulation provided higher critical loads than numerical solutions, which makes them not reliable to use in these specific conditions.

Nonetheless, nonlinear solutions were employed to find the ultimate load for S275 steel arches. Comparing to linear buckling solutions, it was found that arches with moderate-to-high in-plane slendernesses buckle elastically before reaching their cross-section plastic capacity. For this reason, elastic methods are able to sufficiently predict critical loads for these restricted geometry cases.

In all instances, fixed arches yielded better buckling and collapse load results, up to around 40% higher than pinned supports, as well as smaller buckling displacements.

In elevated temperatures, it was observed that both pinned and fixed supports suffered considerable losses in resistance, those being much more accentuated in pinned arches since they are prone to higher in-plane displacements as temperatures rise.

Considering an upgrade of steel class, it was discovered that at elevated temperatures, in most of the cases fixed supports for S275 arches produced better results that pinned ones made of S355 steel, meaning that enhancing support stiffness generally induces superior thermo-mechanical behavior.

As a manner of comparison, the aforementioned elements were designed accordingly to standard simplified methods given in Eurocode 3 1-1 and 1-2 for linear members under bending moments and axial forces for natural and elevated temperatures. These simplified methods yielded conservative results for curved-axis members, except for arches with elevated normalized slendernesses at high temperatures, where numerical results were very close to standard curves and even lower for larger spans.

6.1 Suggestions for future investigation

Following the scope of this investigation work, additional points not covered in this thesis are open to future research, which are outlined below:

1. Conduct real-scale experimental tests on the in-plane stability of steel arches, both under natural and elevated temperature conditions;

2. Evaluate the influence of different load cases and cross-section geometries in both critical and ultimate collapse load of arches;

3. Analyze different residual stress profiles for curved members and how they influence their thermo-mechanical behavior;

Bibliography

[1] Walter Pfeil and Michèle Pfeil. *Estruturas de Aço: Dimensionamento Prático*. LTC, Rio de Janeiro, 8th edition, 2009.

[2] Charles King and David Brown. *Design of Curved Steel*. The Steel Construction Institute, 2001.

[3] American Institute of Steel Construction. *Curved Steel: A Reference for Architects and Engineers*, 2009.

[4] Wael F. Ragheb. Estimating the local buckling capacity of structural steel I-section columns at elevated temperatures. *Thin-Walled Structures*, 107:18 – 27, 2016.

[5] Richard G. Gewain, Nestor R. Iwankiw, and Farid Alfawakhiri. *Facts for Steel Buildings - Fire*. American Institute of Steel Construction, 2003.

[6] I. D. Bennetts and I. R. Thomas. Design of steel structures under fire conditions. *Progress in Structural Engineering and Materials*, 4(1):6–17, 2002.

[7] Stephanie Bryant and Isabel Preston. Focus on trends in fires and fire-related fatalities. page 26, 2017.

[8] National Fire Data Center. Fire Death Rate Trends: An International Perspective. 12(8):8, July 2011.

[9] R.C. Spoorenberg, H.H. Snijder, and J.C.D. Hoenderkamp. A theoretical method for calculating the collapse load of steel circular arches. *Engineering Structures*, 38:89 – 103, 2012.

[10] Ilias D. Thanasoulas, Cyril E. Douthe, Charis J. Gantes, and Xenofon A. Lignos. Influence of roller-bending on RHS steel arches: Experimental and numerical investigation. *Thin-Walled Structures*, 131:668 – 680, 2018.

[11] D.B. La Poutré, R.C. Spoorenberg, H.H. Snijder, and J.C.D. Hoenderkamp. Out-of-plane stability of roller bent steel arches — an experimental investigation. *Journal of Constructional Steel Research*, 81:20 – 34, 2013.

[12] N. S. Trahair. *Flexural-Torsional Buckling of Structures*. E FN Spon, 1993.

[13] J.A. Poutré, La. *Stability of steel arches*. TUE BCO rapporten. Technische Universiteit Eindhoven, 2001.

[14] Yan-Lin Guo, Si-Yuan Zhao, Yong-Lin Pi, Mark Andrew Bradford, and Chao Dou. An experimental study on out-of-plane inelastic buckling strength of fixed steel arches. *Engineering Structures*, 98:118 – 127, 2015.

[15] C.A. Dimopoulos and C.J. Gantes. Design of circular steel arches with hollow circular cross-sections according to EC3. *Journal of Constructional Steel Research*, 64(10):1077 – 1085, 2008.

[16] Joshua J. West. A critical analysis of the design and construction of the Luis I bridge, Porto. *Proceedings of Bridge Engineering 2 Conference*, April 2011.

[17] Council on Tall Buildings and Urban Habitat. Eiffel tower. *The Skyscraper Center*, 2019.

[18] Bo Dowswell. *Design Guide 33: Curved Member Design*. American Institute of Steel Construction, 2018.

[19] Antoine N. Gergess and Rajan Sen. Cambering structural steel I-girders using cold bending. *Journal of Constructional Steel Research*, 64(4):407 – 417, 2008.

[20] David T. Ricker. Cambering steel beams. *Engineering Journal*, 26, January 1989.

[21] Erin Criste. Beam cambering methods and costs. *Structure Magazine*, April 2009.

[22] European Committee for Standardization. *EN 1993-2 Eurocode 3: Design of steel structures - Part 2: Steel Bridges*, Brussels, 2006. CEN.

[23] António Reis and Dinar Camotim. *Estabilidade Estrutural*. McGraw Hill, Portugal, 2001.

[24] Yenny Chandra, Richard Wiebe, Ilinca Stanciulescu, Lawrence N. Virgin, Stephen M. Spottswood, and Thomas G. Eason. Characterizing dynamic transitions associated with snap-through of clamped shallow arches. *Journal of Sound and Vibration*, 332(22):5837 – 5855, 2013.

[25] Ronald D. Ziemian, editor. *Guide to Stability Design Criteria for Metal Structures*. John Wiley and Sons, 6th edition, 2010.

[26] Ehab Ellobody. Chapter 5 - Finite element analysis of steel and steel-concrete composite bridges. In Ehab Ellobody, editor, *Finite Element Analysis and Design of Steel and Steel-Concrete Composite Bridges*, pages 469 – 554. Butterworth-Heinemann, Oxford, 2014.

[27] European Committee for Standardization. *EN 1993-1 Eurocode 3: Design of steel structures - Part 1-1: General rules and rules for buildings*, Brussels, 2005. CEN.

[28] American Institute of Steel Construction. *Steel Construction Manual*, 15th edition, 2017.

[29] B. W. Young. Residual stresses in hot rolled members. *IABSE Reports of the Working Commisions*, 23:25–38, 1975.

[30] ECCS. Ultimate limit state calculations of sway frames with rigid joints. Technical report, Technical Working Group 8.2-System, European Convention for the Constructional Steelwork, Paris, 1984.

[31] Michalis Hadjioannou, Cyril Douthe, and Charis J. Gantes. Influence of cold bending on the resistance of wide flange members. *International Journal of Steel Structures*, 13(2):353–366, June 2013.

[32] Yong-Lin Pi, Mark Andrew Bradford, and Francis Tin-Loi. In-plane strength of steel arches. *Advanced Steel Construction*, 4:306–322, 2008.

[33] Y. L. Pi and N. S. Trahair. In-plane buckling and design of steel arches. *Journal of Structural Engineering*, pages 1291–1298, November 1999.

[34] R. C. Spoorenberg, H. H. Snijder, and J. C. D. Hoenderkamp. Proposed residual stress model for roller bent steel wide flange sections. *Journal of Constructional Steel Research*, 67(6):992–1000, 2011.

[35] S. P. Timoshenko. *Strength of materials. Part II: Advanced theory and problems*. D. Van Nostrand Company, Inc., New York, 1940.

[36] Stephen P. Timoshenko and James M. Gere. *Theory of Elastic Stability*. McGraw Hill, 2 edition, 1985.

[37] S. Rajasekaran and S. Padmanabhan. Equations of Curved Beams. *Journal of Engineering Mechanics*, 115(5):1094–1111, May 1989.

[38] Yeong-Bin Yang, Shyh-Rong Kuo, and Jong-Dar Yau. Use of Straight-Beam Approach to Study Buckling of Curved Beams. *Journal of Structural Engineering*, 117(7):1963–1978, July 1991.

[39] M. A. Bradford, B. Uy, and Y.-L. Pi. In-Plane Elastic Stability of Arches under a Central Concentrated Load. *Journal of Engineering Mechanics*, 128(7):710–719, July 2002.

[40] Yong-Lin Pi and Mark Andrew Bradford. Nonlinear elastic analysis and buckling of pinned–fixed arches. *International Journal of Mechanical Sciences*, 68:212–223, March 2013.

[41] R.C. Spoorenberg, H.H. Snijder, J.C.D. Hoenderkamp, and D. Beg. Design rules for out-of-plane stability of roller bent steel arches with FEM. *Journal of Constructional Steel Research*, 79:9–21, December 2012.

[42] Chao Dou, Yan-Lin Guo, Si-Yuan Zhao, and Yong-Lin Pi. Experimental Investigation into Flexural-Torsional Ultimate Resistance of Steel Circular Arches. *Journal of Structural Engineering*, 141(10):04015006, October 2015.

[43] Zhen Guo, Yongchao Wang, Nan Lu, Haidong Zhang, and Fei Zhu. Behaviour of a two-pinned steel arch at elevated temperatures. *Thin-Walled Structures*, 107:248–256, October 2016.

[44] European Committee for Standardization. *EN 1993-1 Eurocode 3: Design of steel structures - Part 1-2: General rules - Structural Fire Design*, Brussels, 2005. CEN.

[45] European Committee for Standardization. *EN 1991-1 Eurocode 1: Actions on structures - Part 1-2: General actions - Actions on structures exposed to fire*, Brussels, 2002. CEN.

[46] International Organization for Standardization. *ISO 834: Fire Resistance Tests-Elements of Building Constructions*, 2002.

[47] Yong-Lin Pi, Mark Andrew Bradford, and B. Uy. In-plane stability of arches. *International Journal of Solids and Structures*, 39:105–125, 2002.

[48] Olivier Andre Bauchau and J. I. Craig. *Structural analysis: with applications to aerospace structures*. Number v. 163 in Solid mechanics and its applications. Springer, Dordrecht ; New York, 2009.

[49] ANSYS Inc. *Mechanical APDL Structural Analysis Guide v15.0*, November 2013.

[50] S. Ahmad, B. M. Irons, and O. C. Zienkiewicz. *Theory Reference for the Mechanical APDL and Mechanical Applications*. ANSYS Inc., 2009.

[51] Yong-Lin Pi and Mark Andrew Bradford. Nonlinear elastic analysis and buckling of pinned–fixed arches. *International Journal of Mechanical Sciences*, 68:212–223, March 2013.

[52] Reham Saleh, Gamal Ali, and Abla El-Megharbel. Determination of Springback Values in Bending I-sections with Tresca Criteria. 14(3):15, 2015.

[53] Luís Manuel Ribeiro de Mesquita. *Estudo Experimental e Numérico do Comportamento de um Material Intumescente na Proteção Passiva de Elementos Estruturais Submetidos a Incêndio*. PhD thesis, Universidade do Porto, Porto, June 2015.

[54] Karl Hoffmann. *An Introduction to Measurements using Strain Gages*. Hottinger Baldwin Messtechnik GmbH, Darmstadt, December 1989.

[55] Daehie Hong, Keith J. Mueller, and Steven A. Velinsky. A Cable Extension Transducer Based Two-Dimensional Position Sensor for Industrial Applications. *Journal of Manufacturing Science and Engineering*, 124(1):105–108, February 2002.

Appendix A

Numerical results

Eigenbuckling critical load [kN]							
Support	**L [m]**	**f/L=0,05**	**f/L=0,10**	**f/L=0,20**	**f/L=0,30**	**f/L=0,40**	**f/L=0,40**
Pinned	5,00	98,31	178,92	281,89	293,19	244,77	180,20
	10,0	24,03	44,90	71,11	73,91	61,62	45,30
	15,0	10,64	19,97	31,66	32,90	27,42	20,16
	20,0	5,97	11,24	17,82	18,52	15,43	11,34
Fixed	5,00	254,72	400,61	615,13	663,93	600,33	390,45
	10,0	54,72	98,06	155,77	168,52	152,09	125,04
	15,0	23,54	43,39	69,39	75,11	67,76	55,69
	20,0	13,08	24,37	39,07	42,29	38,15	31,35

Table A.1: Eigenbuckling critical load results

Nonlinear ultimate load at 20 [°C] [kN]							
Support	**L [m]**	**f/L=0,05**	**f/L=0,10**	**f/L=0,20**	**f/L=0,30**	**f/L=0,40**	**f/L=0,40**
Pinned	5,00	21,35	33,34	44,71	51,29	47,15	33,59
	10,0	12,16	18,14	23,19	25,71	22,83	15,71
	15,0	7,20	11,35	14,92	16,60	14,25	9,81
	20,0	4,53	7,72	10,60	11,85	9,98	6,91
Fixed	5,00	26,70	38,57	49,55	56,15	57,47	46,04
	10,0	16,67	21,32	25,52	28,31	28,17	21,66
	15,0	11,01	13,93	16,44	18,10	17,99	13,24
	20,0	7,75	9,99	11,93	13,13	13,16	9,78

Table A.2: Nonlinear ultimate load at 20 [°C], steel S275

Nonlinear ultimate load at 400 [°C] [kN]							
Support	**L [m]**	**f/L=0,05**	**f/L=0,10**	**f/L=0,20**	**f/L=0,30**	**f/L=0,40**	**f/L=0,40**
Pinned	5,00	15,62	26,92	40,40	44,76	33,63	24,53
	10,0	7,68	12,26	17,72	19,28	14,03	10,10
	15,0	4,42	7,11	10,36	11,26	8,21	5,86
	20,0	2,80	4,72	6,95	7,53	5,54	3,95
Fixed	5,00	21,29	35,40	45,31	51,53	49,33	36,42
	10,0	11,38	16,72	21,52	24,79	23,06	16,54
	15,0	7,08	9,93	13,00	14,95	13,94	9,96
	20,0	4,81	6,76	8,93	10,27	9,60	6,92

Table A.3: Nonlinear ultimate load at 400 [°C], steel S275

Nonlinear ultimate load at 600 [°C] [kN]							
Support	**L [m]**	**f/L=0,05**	**f/L=0,10**	**f/L=0,20**	**f/L=0,30**	**f/L=0,40**	**f/L=0,40**
Pinned	5,00	7,10	12,39	18,83	20,57	15,31	11,27
	10,0	3,43	5,52	8,11	8,70	6,28	4,57
	15,0	1,95	3,17	4,71	5,04	3,65	2,64
	20,0	1,23	2,09	3,13	3,35	2,45	1,76
Fixed	5,00	9,76	15,76	21,13	23,95	22,44	17,29
	10,0	5,16	7,57	9,86	11,33	10,56	7,70
	15,0	3,15	4,54	5,89	6,80	6,34	4,58
	20,0	2,15	3,09	4,03	4,64	4,35	3,14

Table A.4: Nonlinear ultimate load at 600 [°C], steel S275

Nonlinear ultimate load at 700 [°C] [kN]							
Support	**L [m]**	**f/L=0,05**	**f/L=0,10**	**f/L=0,20**	**f/L=0,30**	**f/L=0,40**	**f/L=0,40**
Pinned	5,00	3,27	5,81	8,96	9,68	7,18	5,29
	10,0	1,51	2,49	3,73	3,96	2,88	2,09
	15,0	0,84	1,40	2,13	2,24	1,63	1,19
	20,0	0,53	0,91	1,39	1,47	1,07	0,78
Fixed	5,00	4,62	7,55	10,15	11,56	9,54	8,25
	10,0	2,37	3,52	4,65	5,33	4,90	3,62
	15,0	1,40	2,06	2,73	3,17	2,93	2,13
	20,0	0,94	1,40	1,84	2,13	1,98	1,43

Table A.5: Nonlinear ultimate load at 700 [°C], steel S275

Nonlinear ultimate load of S355 pinned steel arches [kN]							
Temp. [°C]	**L [m]**	**f/L=0,05**	**f/L=0,10**	**f/L=0,20**	**f/L=0,30**	**f/L=0,40**	**f/L=0,40**
400	5,00	17,65	33,88	51,21	56,67	42,61	31,00
	10,0	9,08	14,83	21,90	23,82	17,36	12,49
	15,0	4,96	8,96	12,51	13,57	10,01	7,15
	20,0	3,06	5,79	8,21	8,89	6,65	4,75
600	5,00	8,80	15,53	23,86	26,05	19,40	14,24
	10,0	4,03	6,71	10,02	10,73	7,80	6,83
	15,0	2,19	3,74	5,67	6,07	4,45	3,22
	20,0	1,35	2,39	3,69	3,94	2,93	2,11
700	5,00	4,02	7,27	11,34	12,23	9,05	6,69
	10,0	1,76	3,00	4,58	4,85	3,53	2,58
	15,0	0,94	1,63	2,54	2,68	1,96	1,44
	20,0	0,56	1,03	1,62	1,71	1,25	0,93

Table A.6: Nonlinear ultimate load of S355 pinned steel arches

Maximum axial force at ultimate load, 20 [°C] [kN]							
Support	**L [m]**	**f/L=0,05**	**f/L=0,10**	**f/L=0,20**	**f/L=0,30**	**f/L=0,40**	**f/L=0,40**
Pinned	5,00	122,43	104,10	83,83	68,93	55,95	37,27
	10,0	70,27	53,71	39,39	34,50	27,14	17,49
	15,0	41,68	33,69	25,36	22,29	16,97	10,92
	20,0	26,49	22,85	18,03	15,93	11,85	7,72
Fixed	5,00	121,28	104,10	83,83	78,05	71,66	53,54
	10,0	84,99	59,45	43,36	39,40	35,24	25,36
	15,0	56,59	38,79	27,88	25,16	22,55	15,59
	20,0	39,58	27,67	20,21	18,23	16,53	11,58

Table A.7: Maximum axial force at ultimate load, 20 [°C]

Maximum bending moment at ultimate load, 20 [°C] [kN.m]							
Support	**L [m]**	**f/L=0,05**	**f/L=0,10**	**f/L=0,20**	**f/L=0,30**	**f/L=0,40**	**f/L=0,40**
Pinned	5,00	7,17	8,18	9,31	9,72	9,83	9,94
	10,0	8,85	9,68	10,05	10,16	9,83	9,99
	15,0	9,29	9,97	10,21	10,25	9,79	9,81
	20,0	9,07	9,97	10,16	10,21	9,73	9,69
Fixed	5,00	7,27	8,18	9,31	9,68	10,06	10,49
	10,0	8,77	9,71	10,24	10,39	10,45	10,60
	15,0	9,64	10,12	10,33	10,41	10,33	10,53
	20,0	9,83	10,18	10,37	10,40	10,39	10,56

Table A.8: Maximum bending moment at ultimate load, 20 [°C]

Maximum axial force at ultimate load, 400 [°C] [kN]							
Support	**L [m]**	**f/L=0,05**	**f/L=0,10**	**f/L=0,20**	**f/L=0,30**	**f/L=0,40**	**f/L=0,40**
Pinned	5,00	90,17	81,47	68,37	60,23	39,98	27,45
	10,0	45,02	36,85	29,99	25,93	16,73	11,34
	15,0	25,76	21,24	17,52	15,14	9,78	6,60
	20,0	16,26	14,08	11,73	10,14	6,62	4,46
Fixed	5,00	108,13	92,68	75,89	71,65	61,90	43,70
	10,0	45,02	43,40	35,47	34,06	29,00	19,40
	15,0	36,73	25,79	21,42	20,61	17,54	11,74
	20,0	24,84	17,64	14,71	14,21	12,09	8,20

Table A.9: Maximum axial force at ultimate load, 400 [°C]

Maximum bending moment at ultimate load, 400 [°C] [kN.m]							
Support	**L [m]**	**f/L=0,05**	**f/L=0,10**	**f/L=0,20**	**f/L=0,30**	**f/L=0,40**	**f/L=0,40**
Pinned	5,00	7,09	8,11	8,95	8,92	8,07	8,26
	10,0	5,92	7,52	8,40	7,86	7,00	7,13
	15,0	5,49	6,63	7,61	7,18	6,23	6,41
	20,0	4,94	6,12	6,90	6,70	5,86	4,73
Fixed	5,00	6,51	8,32	9,25	9,41	9,87	10,36
	10,0	5,92	9,14	9,78	9,95	10,07	10,19
	15,0	6,69	8,56	9,31	9,42	9,45	9,77
	20,0	6,33	7,96	8,61	8,97	8,91	9,35

Table A.10: Maximum bending moment at ultimate load, 400 [°C]

Maximum axial force at ultimate load, 600 [°C] [kN]							
Support	**L [m]**	**f/L=0,05**	**f/L=0,10**	**f/L=0,20**	**f/L=0,30**	**f/L=0,40**	**f/L=0,40**
Pinned	5,00	43,02	37,49	31,56	27,60	18,22	12,62
	10,0	20,14	16,56	13,58	11,67	7,48	5,13
	15,0	11,40	9,50	7,90	6,76	4,35	2,97
	20,0	7,15	6,25	5,24	4,49	2,92	1,98
Fixed	5,00	49,22	43,33	35,06	33,23	28,17	20,27
	10,0	26,98	20,92	16,12	15,53	13,24	9,07
	15,0	16,28	12,50	9,62	9,33	7,97	5,43
	20,0	11,07	8,48	6,57	6,38	5,47	3,73

Table A.11: Maximum axial force at ultimate load, 600 [°C]

Maximum bending moment at ultimate load, 600 [°C] [kN.m]							
Support	**L [m]**	**f/L=0,05**	**f/L=0,10**	**f/L=0,20**	**f/L=0,30**	**f/L=0,40**	**f/L=0,40**
Pinned	5,00	2,88	3,78	4,15	4,04	3,85	3,84
	10,0	2,70	3,36	3,84	3,49	3,22	3,22
	15,0	2,46	3,06	3,44	3,20	2,84	2,87
	20,0	2,15	2,80	3,11	2,92	2,63	2,63
Fixed	5,00	2,98	3,96	4,34	4,40	4,64	4,87
	10,0	3,27	4,10	4,63	4,61	4,67	4,81
	15,0	2,96	3,78	4,35	4,34	4,40	4,61
	20,0	2,86	3,50	4,03	4,05	4,18	4,35

Table A.12: Maximum bending moment at ultimate load, 600 [°C]

Maximum axial force at ultimate load, 700 [°C] [kN]							
Support	**L [m]**	**f/L=0,05**	**f/L=0,10**	**f/L=0,20**	**f/L=0,30**	**f/L=0,40**	**f/L=0,40**
Pinned	5,00	19,90	19,60	14,96	12,99	8,55	5,95
	10,0	8,89	7,46	6,22	5,30	3,43	2,35
	15,0	4,88	4,18	3,54	3,00	1,94	1,34
	20,0	3,06	2,71	2,31	1,97	1,28	0,87
Fixed	5,00	23,23	20,76	16,76	15,96	12,01	9,69
	10,0	12,36	9,67	7,56	7,32	6,16	4,27
	15,0	7,25	5,68	4,45	4,35	3,70	2,53
	20,0	4,85	4,21	3,01	2,93	2,50	1,71

Table A.13: Maximum axial force at ultimate load, 700 [°C]

Maximum bending moment at ultimate load, 700 [°C] [kN.m]							
Support	**L [m]**	**f/L=0,05**	**f/L=0,10**	**f/L=0,20**	**f/L=0,30**	**f/L=0,40**	**f/L=0,40**
Pinned	5,00	1,36	1,83	2,02	1,93	1,85	1,89
	10,0	1,23	1,56	1,79	1,63	1,54	1,50
	15,0	1,05	1,37	1,59	1,42	1,28	1,33
	20,0	0,95	1,23	1,36	1,30	1,14	1,15
Fixed	5,00	1,41	1,95	2,13	2,16	2,06	2,38
	10,0	1,52	1,94	2,22	2,23	2,20	2,34
	15,0	1,36	1,78	2,10	2,13	2,16	2,23
	20,0	1,29	1,43	1,91	1,95	1,95	2,03

Table A.14: Maximum bending moment at ultimate load, 700 [°C]

Appendix B

Instability and collapse modes

B.1 Linear eigenbuckling solutions

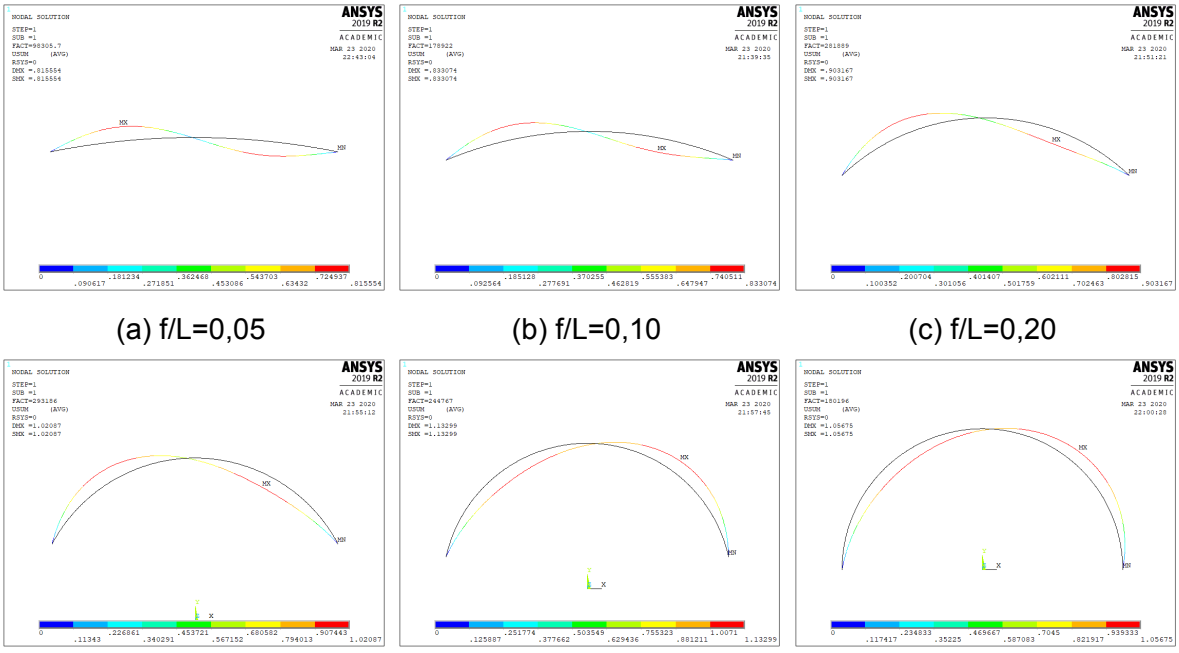

(a) f/L=0,05 (b) f/L=0,10 (c) f/L=0,20

(d) f/L=0,30 (e) f/L=0,40 (f) f/L=0,50

Figure B.1: Instability modes of pinned arches of 5 [m] span

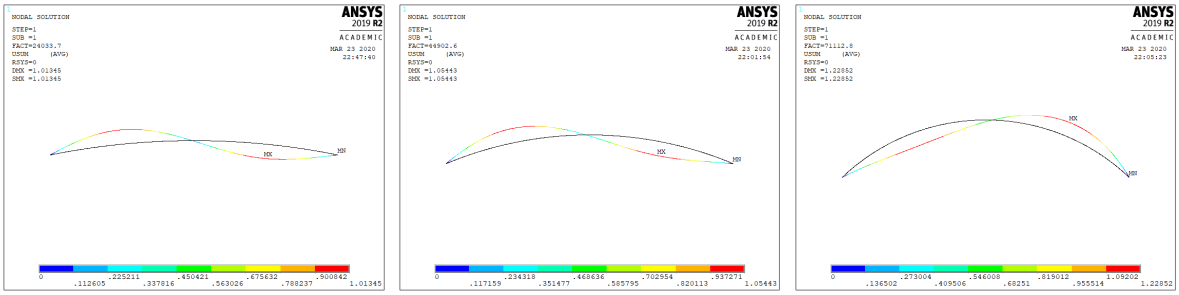

(a) f/L=0,05 (b) f/L=0,10 (c) f/L=0,20

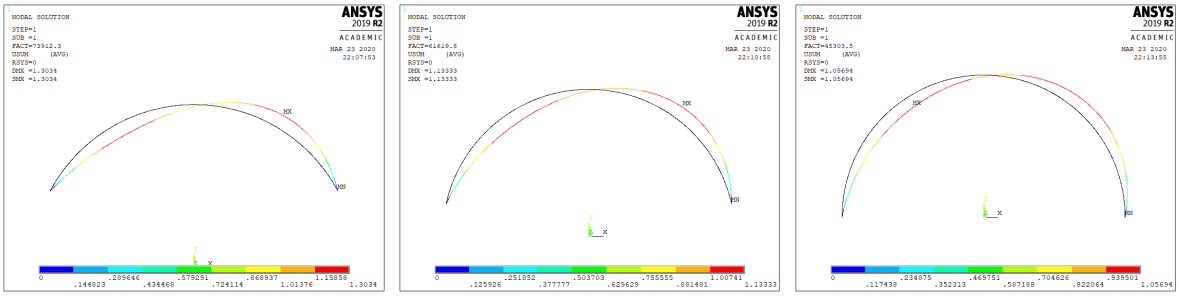

(d) f/L=0,30 (e) f/L=0,40 (f) f/L=0,50

Figure B.2: Instability modes of pinned arches of 10 [m] span

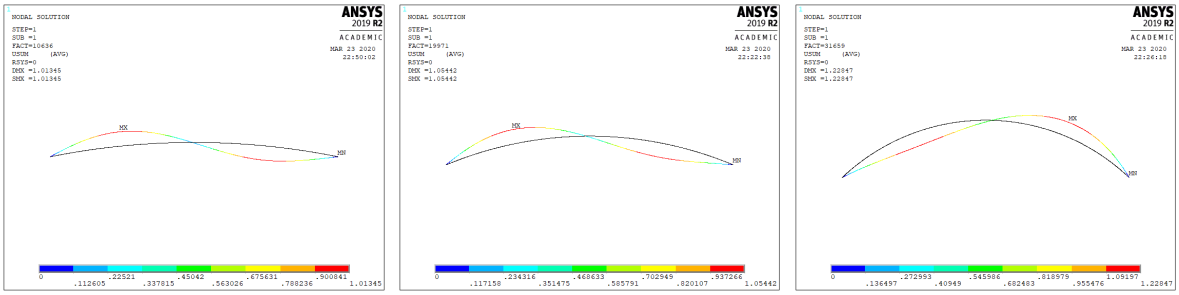

(a) f/L=0,05 (b) f/L=0,10 (c) f/L=0,20

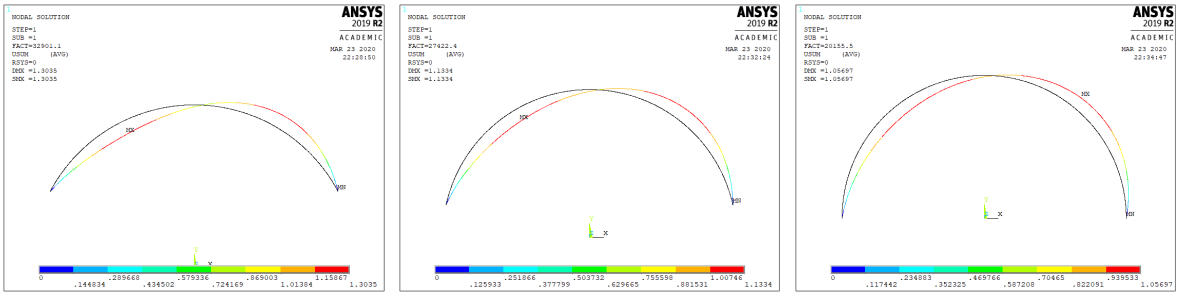

(d) f/L=0,30 (e) f/L=0,40 (f) f/L=0,50

Figure B.3: Instability modes of pinned arches of 15 [m] span

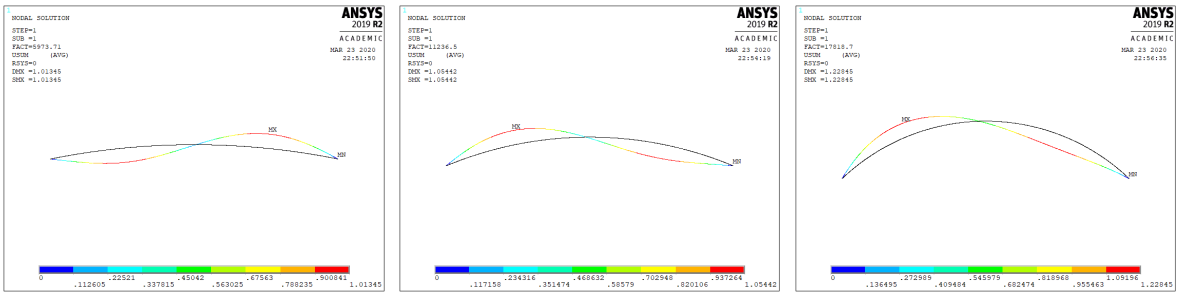

(a) f/L=0,05 (b) f/L=0,10 (c) f/L=0,20

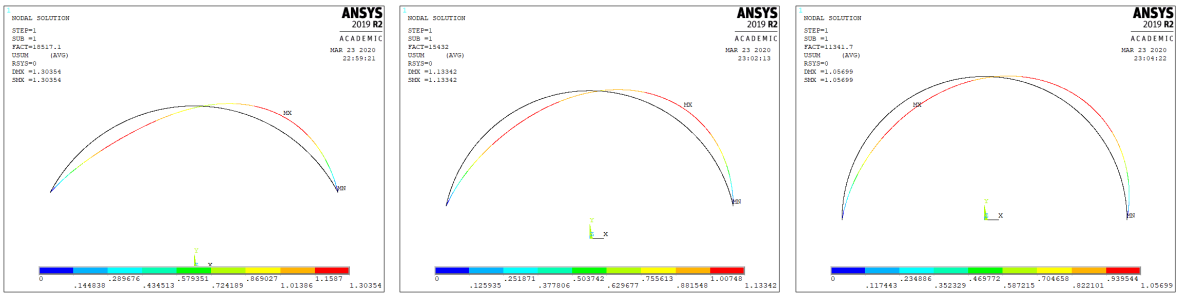

(d) f/L=0,30 (e) f/L=0,40 (f) f/L=0,50

Figure B.4: Instability modes of pinned arches of 20 [m] span

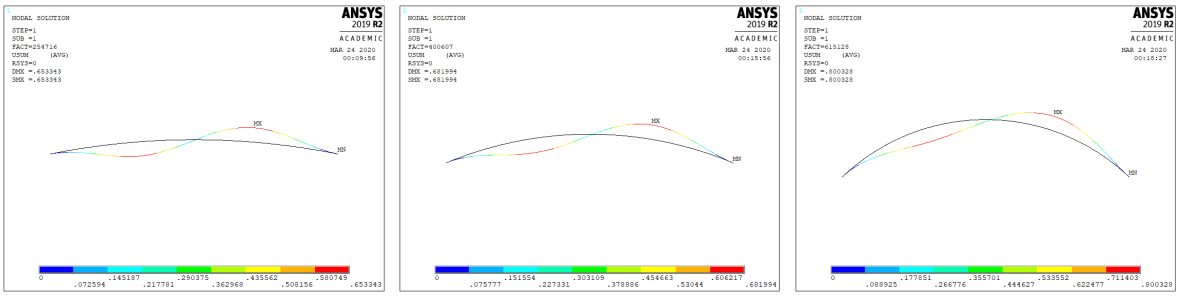

(a) f/L=0,05 (b) f/L=0,10 (c) f/L=0,20

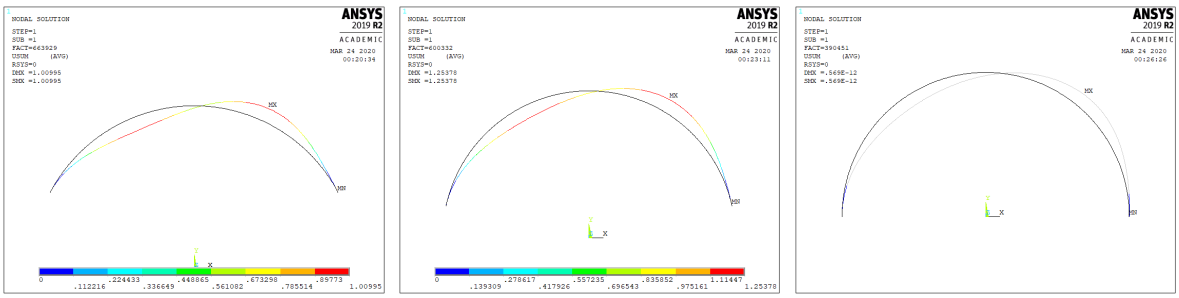

(d) f/L=0,30 (e) f/L=0,40 (f) f/L=0,50

Figure B.5: Instability modes of fixed arches of 5 [m] span

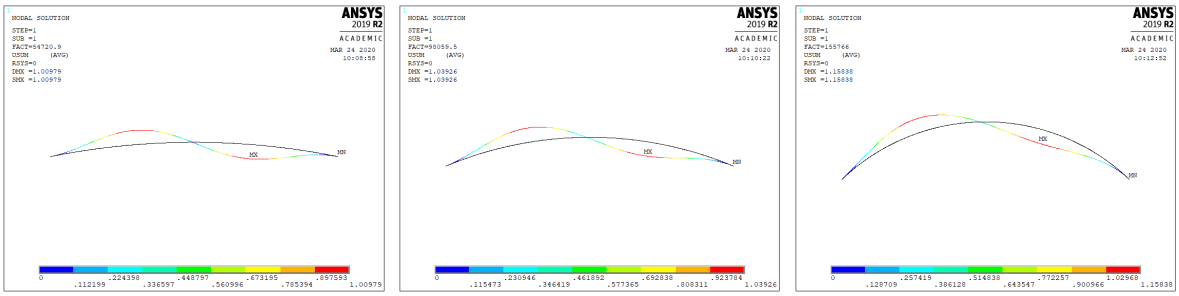

(a) f/L=0,05 (b) f/L=0,10 (c) f/L=0,20

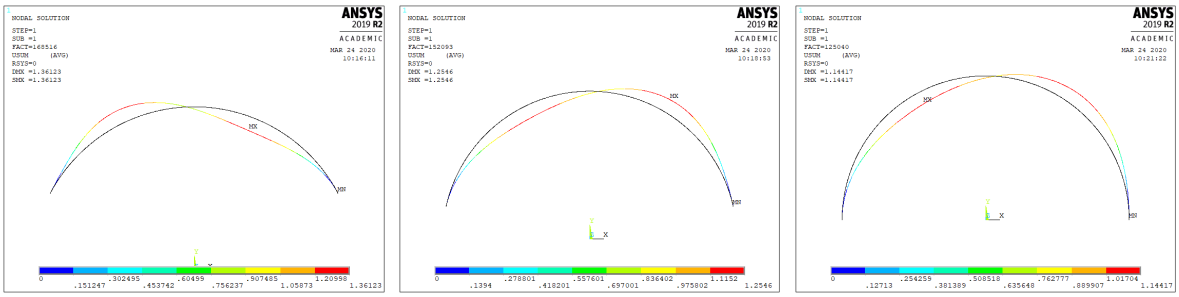

(d) f/L=0,30 (e) f/L=0,40 (f) f/L=0,50

Figure B.6: Instability modes of fixed arches of 10 [m] span

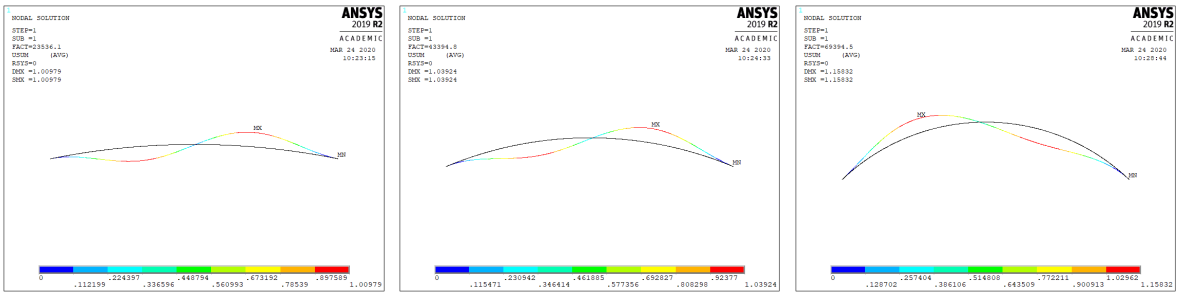

(a) f/L=0,05 (b) f/L=0,10 (c) f/L=0,20

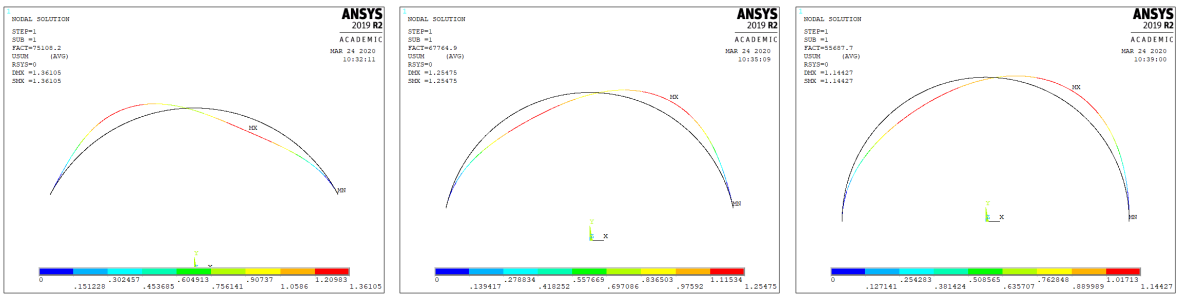

(d) f/L=0,30 (e) f/L=0,40 (f) f/L=0,50

Figure B.7: Instability modes of fixed arches of 15 [m] span

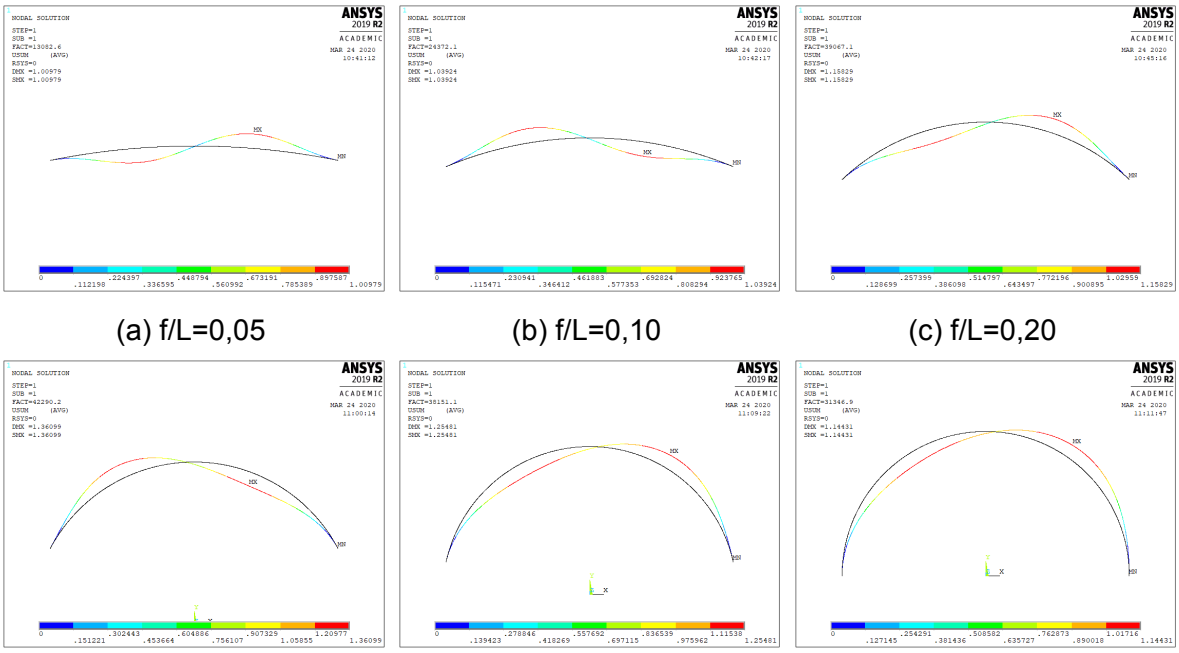

(a) f/L=0,05 (b) f/L=0,10 (c) f/L=0,20

(d) f/L=0,30 (e) f/L=0,40 (f) f/L=0,50

Figure B.8: Instability modes of fixed arches of 20 [m] span

B.2 Nonlinear ultimate load solutions

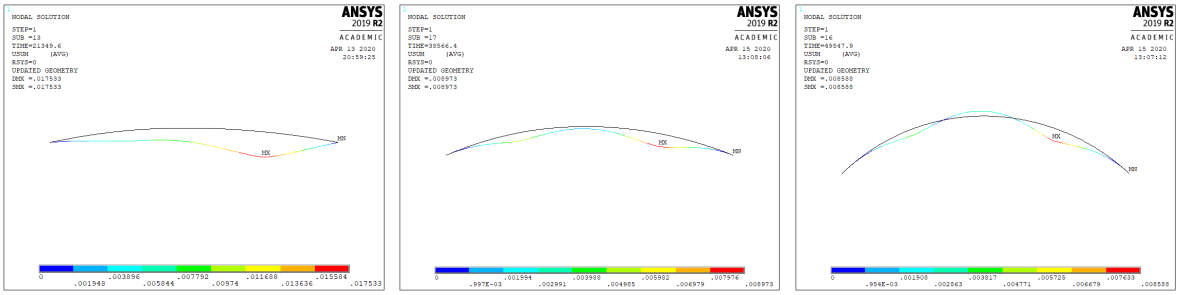

(a) f/L=0,05 (b) f/L=0,10 (c) f/L=0,20

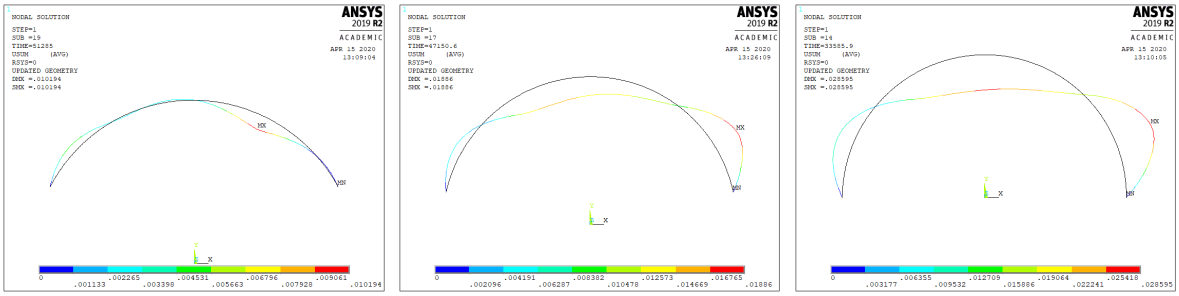

(d) f/L=0,30 (e) f/L=0,40 (f) f/L=0,50

Figure B.9: Collapse mode of S275 pinned arches of 5 [m] span at 20 [°C]

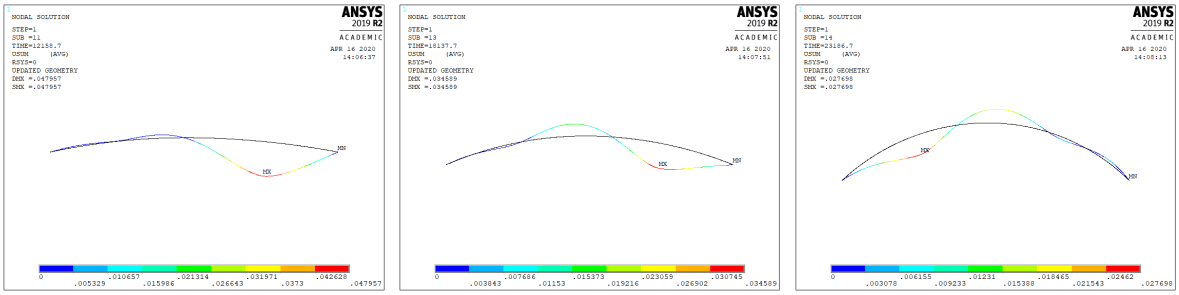

(a) f/L=0,05 (b) f/L=0,10 (c) f/L=0,20

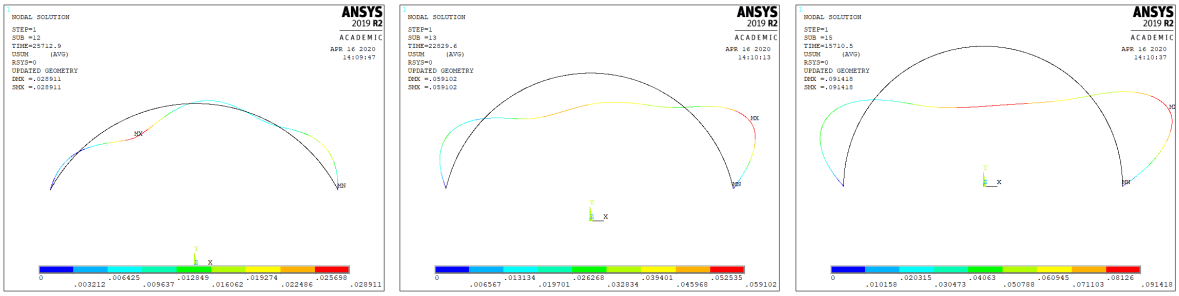

(d) f/L=0,30 (e) f/L=0,40 (f) f/L=0,50

Figure B.10: Collapse mode of S275 pinned arches of 10 [m] span at 20 [°C]

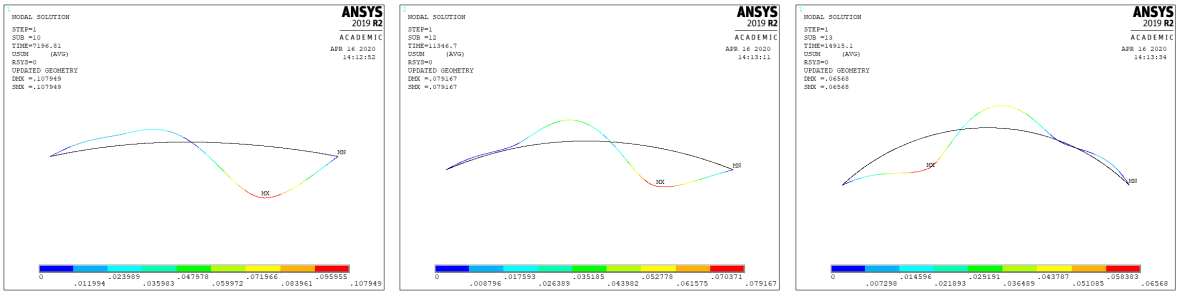

(a) f/L=0,05 (b) f/L=0,10 (c) f/L=0,20

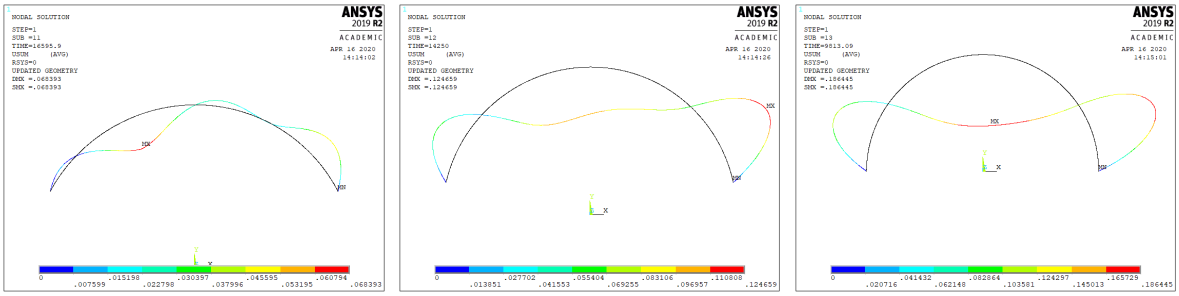

(d) f/L=0,30 (e) f/L=0,40 (f) f/L=0,50

Figure B.11: Collapse mode of S275 pinned arches of 15 [m] span at 20 [°C]

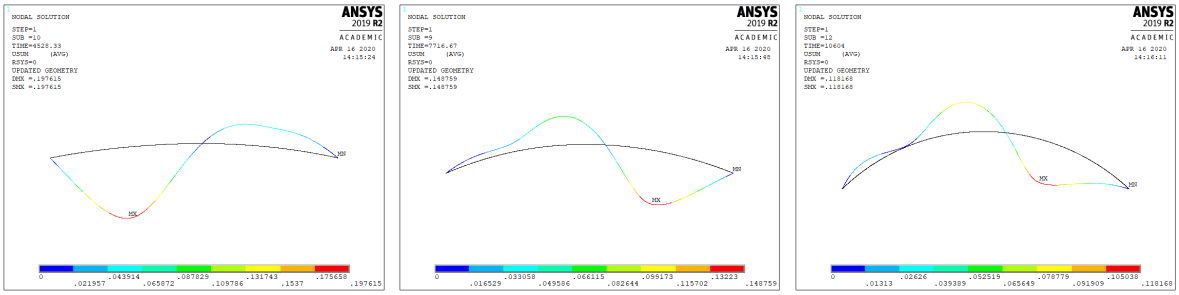

(a) f/L=0,05 (b) f/L=0,10 (c) f/L=0,20

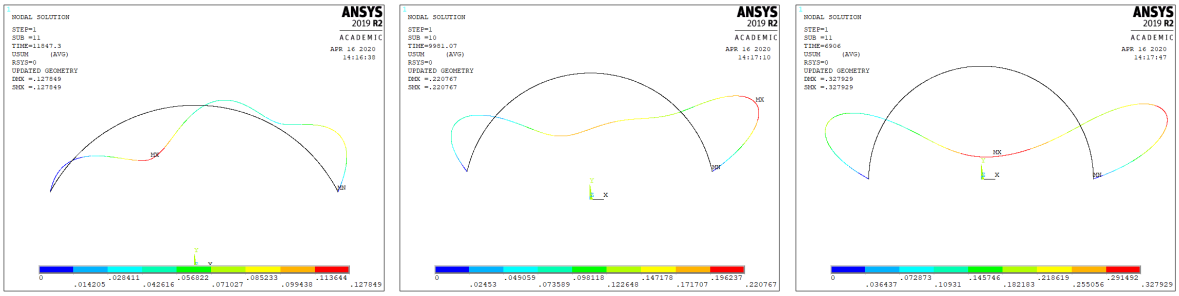

(d) f/L=0,30 (e) f/L=0,40 (f) f/L=0,50

Figure B.12: Collapse mode of S275 pinned arches of 20 [m] span at 20 [°C]

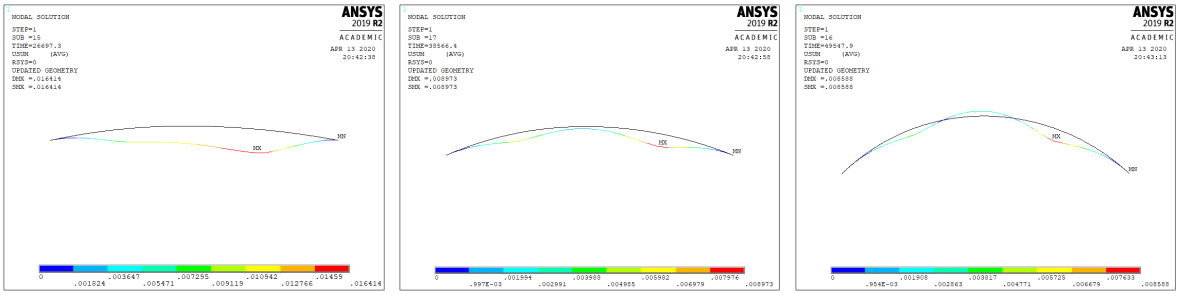

(a) f/L=0,05 (b) f/L=0,10 (c) f/L=0,20

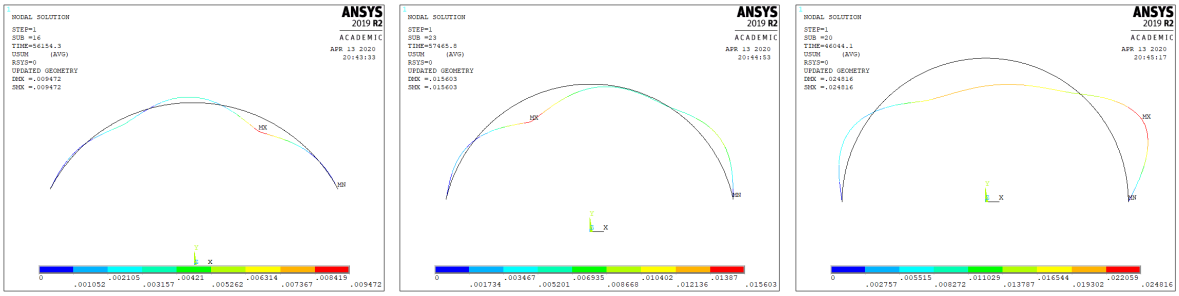

(d) f/L=0,30 (e) f/L=0,40 (f) f/L=0,50

Figure B.13: Collapse mode of S275 fixed arches of 5 [m] span at 20 [°C]

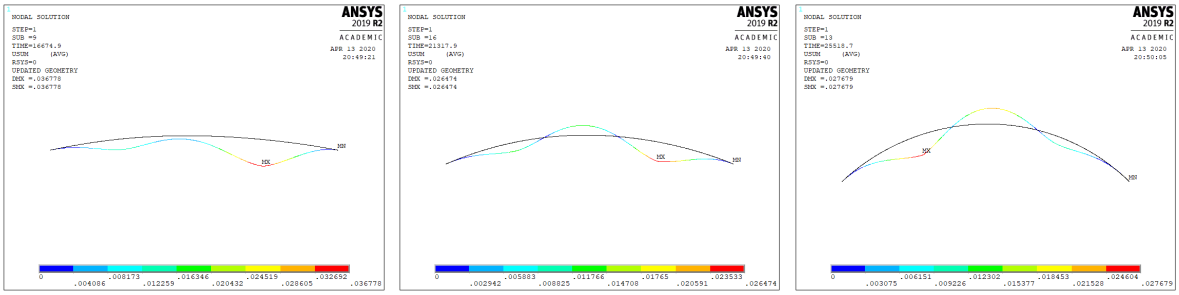

(a) f/L=0,05 (b) f/L=0,10 (c) f/L=0,20

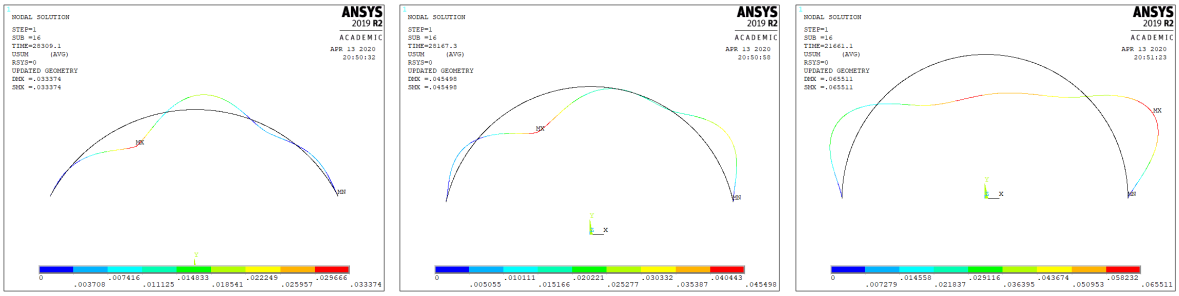

(d) f/L=0,30 (e) f/L=0,40 (f) f/L=0,50

Figure B.14: Collapse mode of S275 fixed arches of 10 [m] span at 20 [°C]

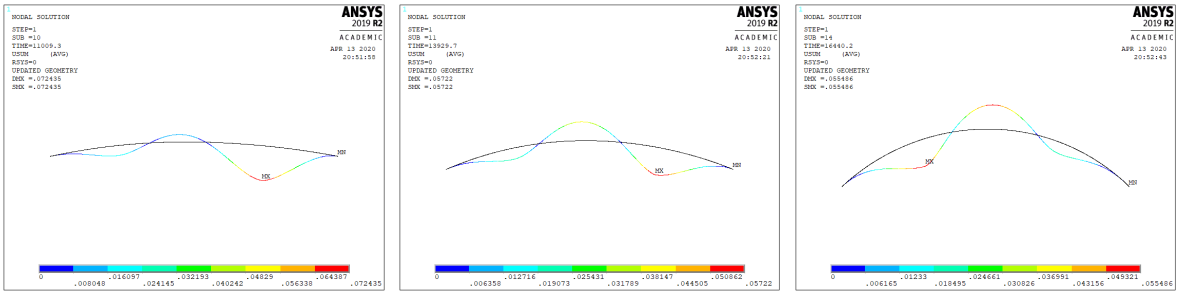

(a) f/L=0,05 (b) f/L=0,10 (c) f/L=0,20

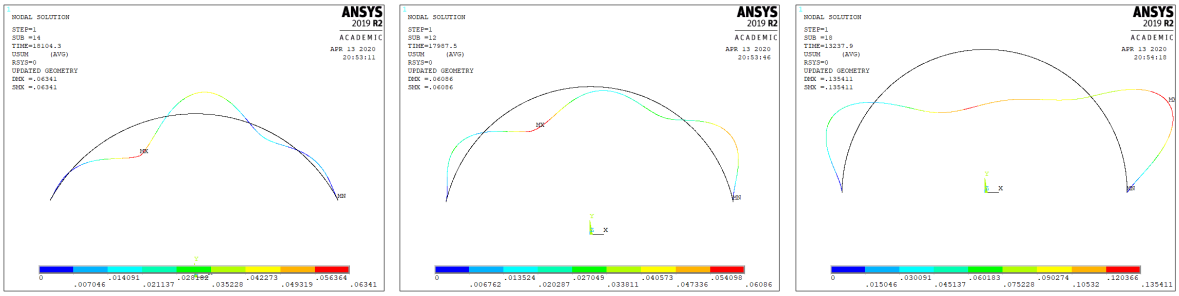

(d) f/L=0,30 (e) f/L=0,40 (f) f/L=0,50

Figure B.15: Collapse mode of S275 fixed arches of 15 [m] span at 20 [°C]

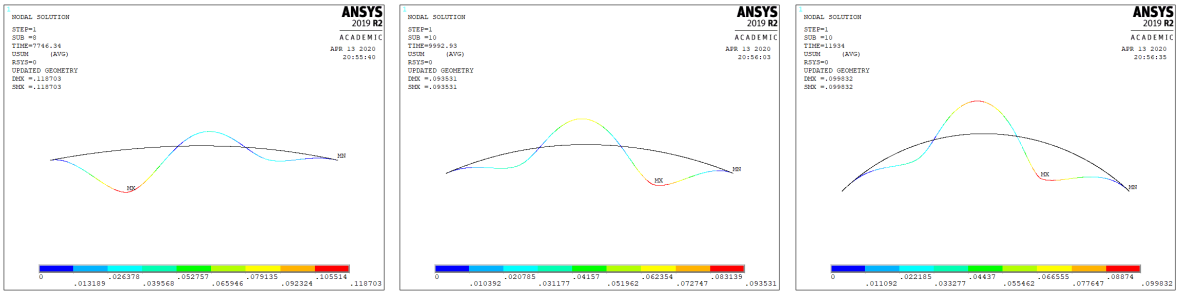

(a) f/L=0,05 (b) f/L=0,10 (c) f/L=0,20

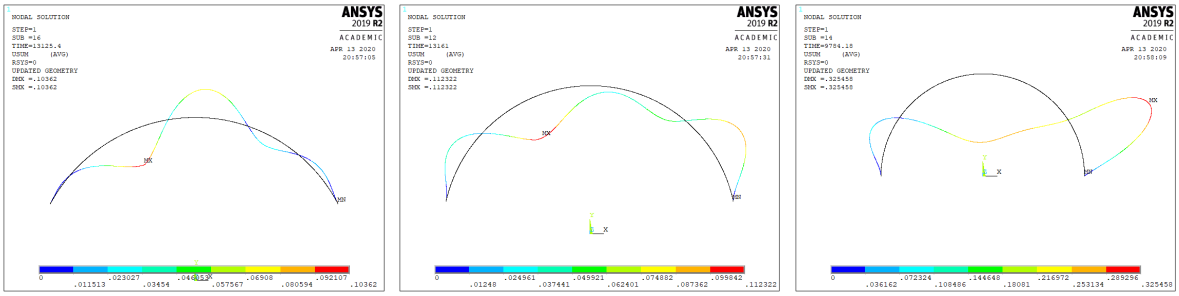

(d) f/L=0,30 (e) f/L=0,40 (f) f/L=0,50

Figure B.16: Collapse mode of S275 fixed arches of 20 [m] span at 20 [°C]

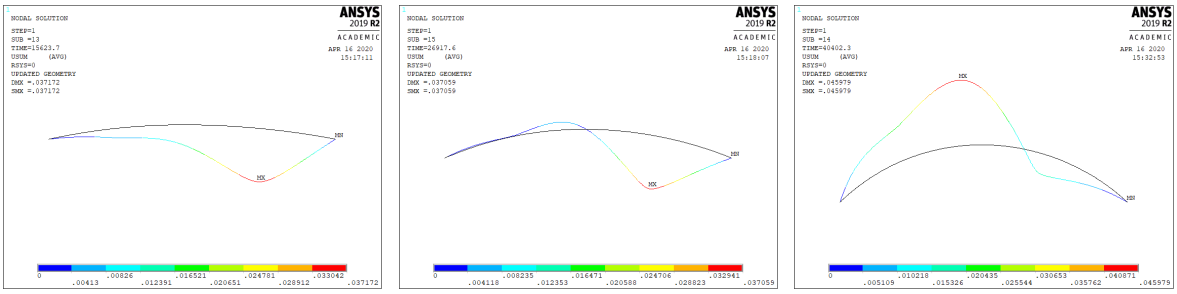

(a) f/L=0,05 (b) f/L=0,10 (c) f/L=0,20

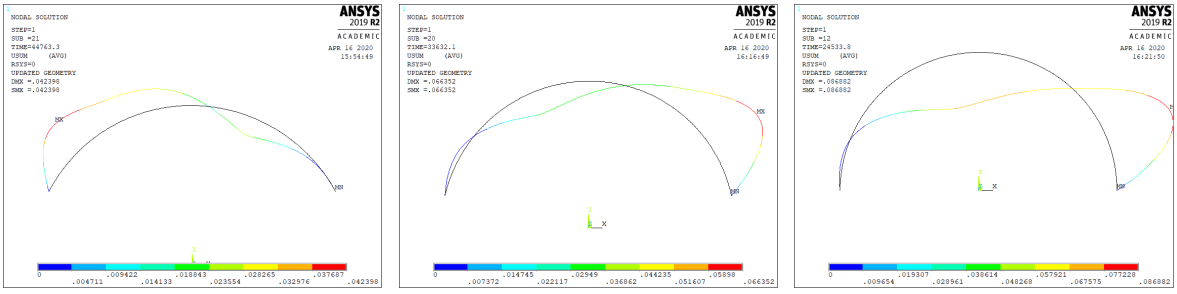

(d) f/L=0,30 (e) f/L=0,40 (f) f/L=0,50

Figure B.17: Collapse mode of S275 pinned arches of 5 [m] span at 400 [°C]

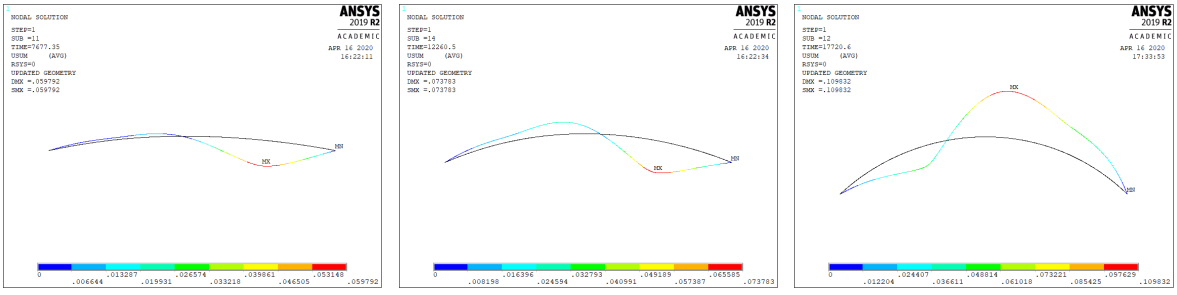

(a) f/L=0,05 (b) f/L=0,10 (c) f/L=0,20

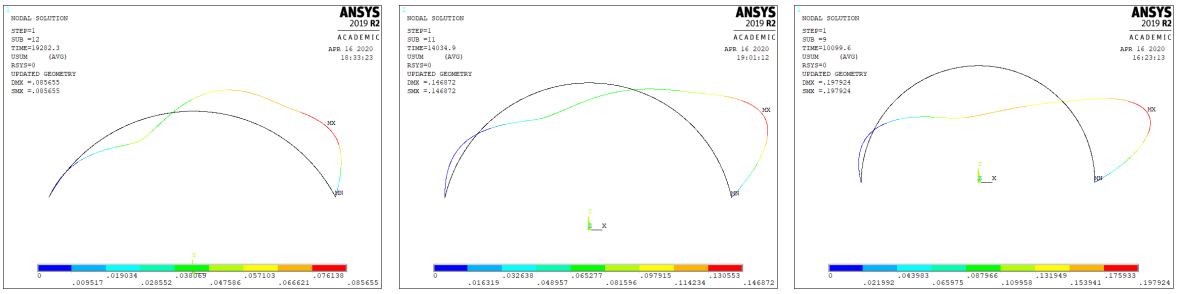

(d) f/L=0,30 (e) f/L=0,40 (f) f/L=0,50

Figure B.18: Collapse mode of S275 pinned arches of 10 [m] span at 400 [°C]

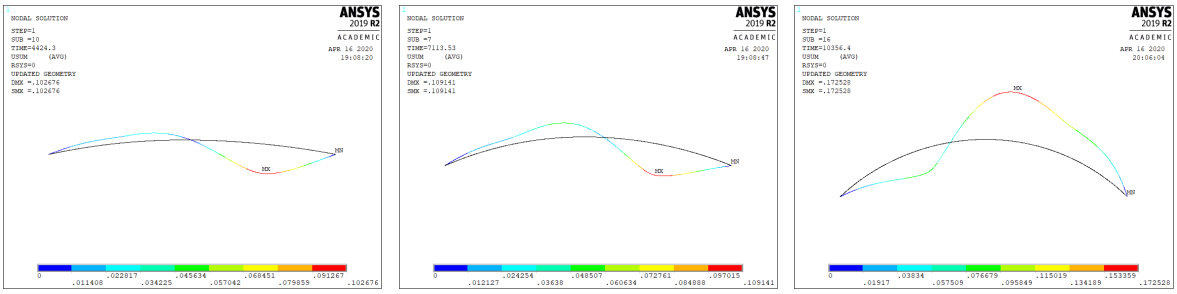

(a) f/L=0,05 (b) f/L=0,10 (c) f/L=0,20

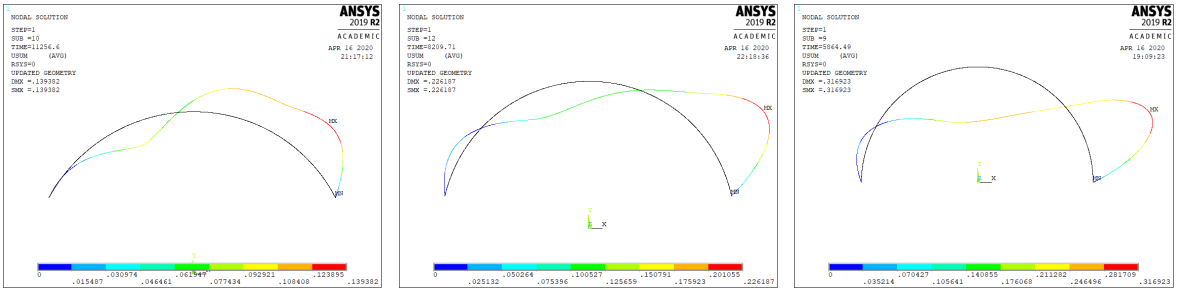

(d) f/L=0,30 (e) f/L=0,40 (f) f/L=0,50

Figure B.19: Collapse mode of S275 pinned arches of 15 [m] span at 400 [°C]

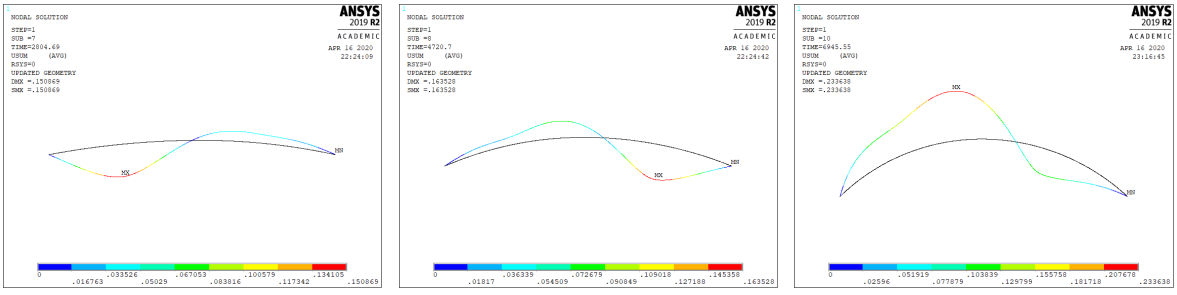

(a) f/L=0,05 (b) f/L=0,10 (c) f/L=0,20

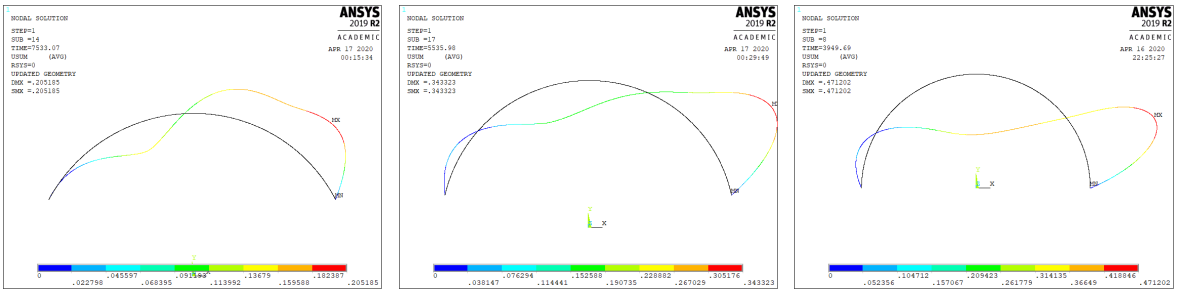

(d) f/L=0,30 (e) f/L=0,40 (f) f/L=0,50

Figure B.20: Collapse mode of S275 pinned arches of 20 [m] span at 400 [°C]

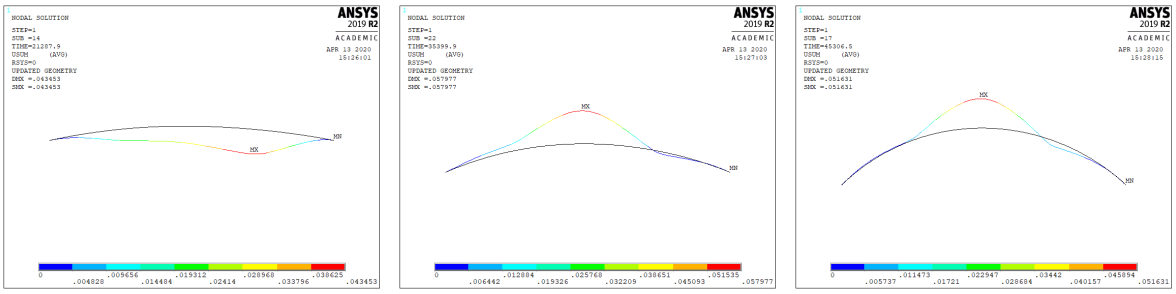

(a) f/L=0,05 (b) f/L=0,10 (c) f/L=0,20

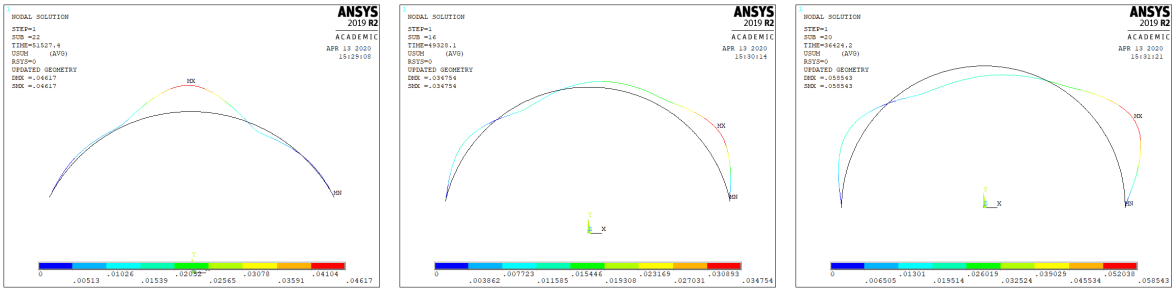

(d) f/L=0,30 (e) f/L=0,40 (f) f/L=0,50

Figure B.21: Collapse mode of S275 fixed arches of 5 [m] span at 400 [°C]

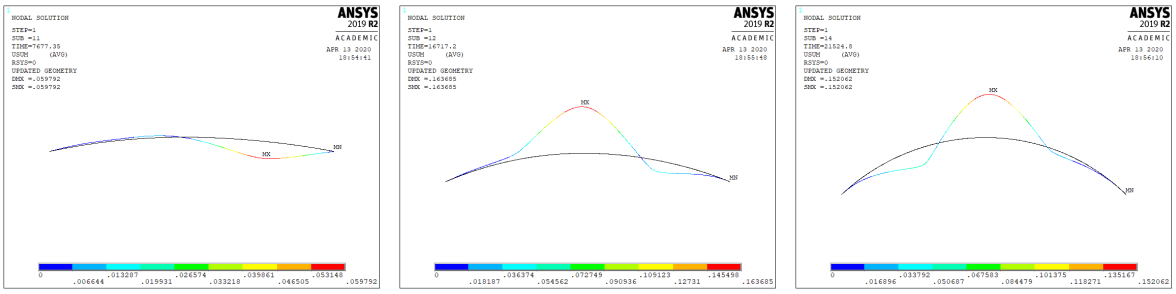

(a) f/L=0,05 (b) f/L=0,10 (c) f/L=0,20

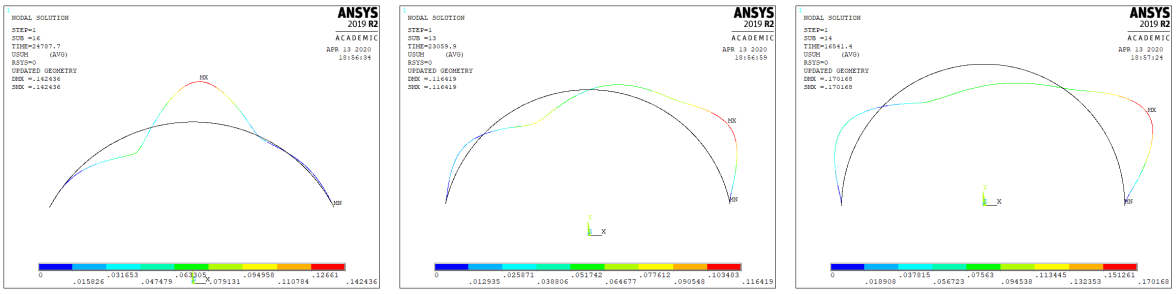

(d) f/L=0,30 (e) f/L=0,40 (f) f/L=0,50

Figure B.22: Collapse mode of S275 fixed arches of 10 [m] span at 400 [°C]

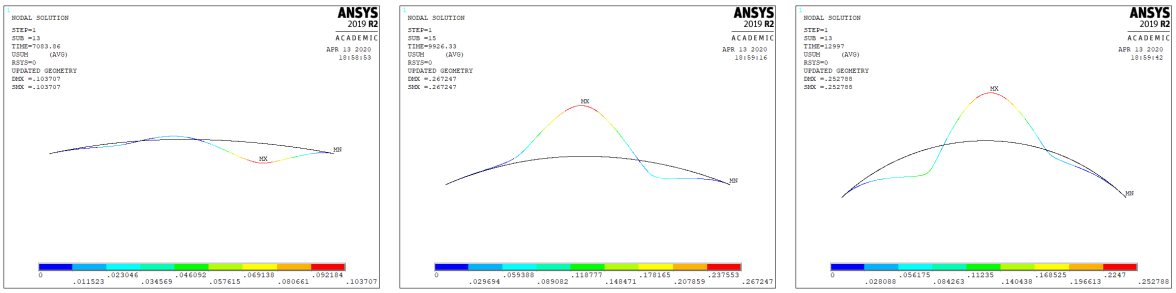

(a) f/L=0,05 (b) f/L=0,10 (c) f/L=0,20

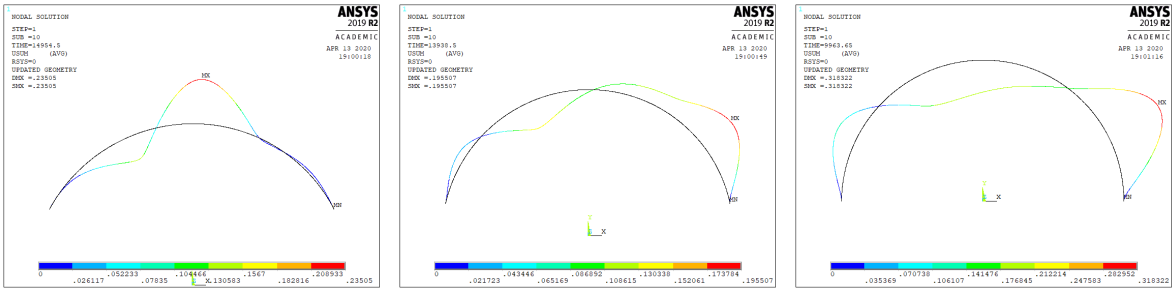

(d) f/L=0,30 (e) f/L=0,40 (f) f/L=0,50

Figure B.23: Collapse mode of S275 fixed arches of 15 [m] span at 400 [°C]

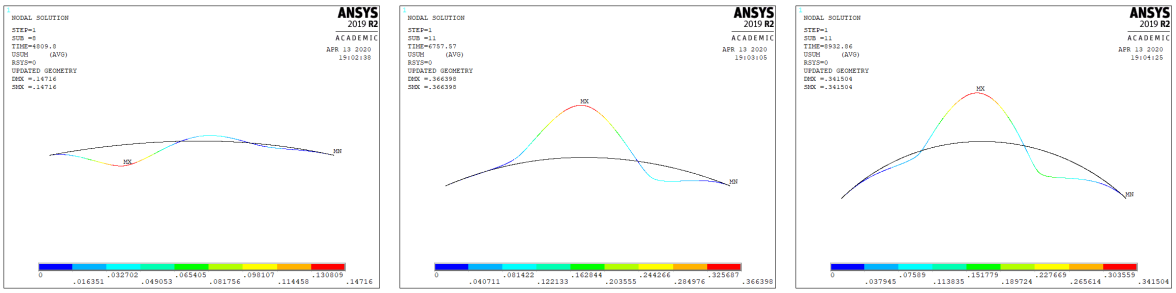

(a) f/L=0,05 (b) f/L=0,10 (c) f/L=0,20

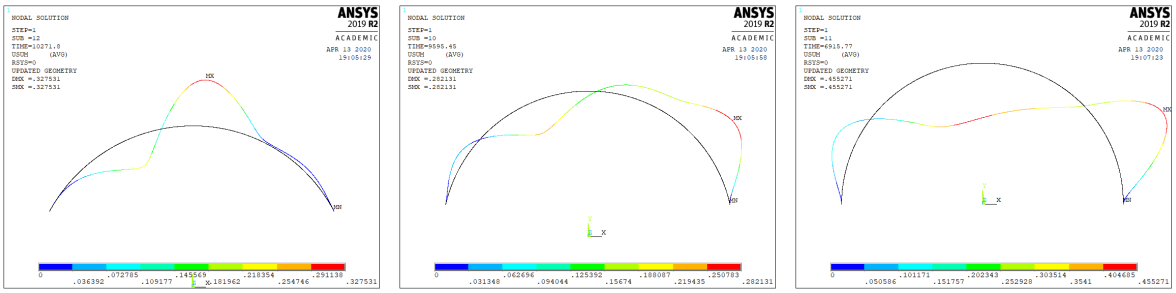

(d) f/L=0,30 (e) f/L=0,40 (f) f/L=0,50

Figure B.24: Collapse mode of S275 fixed arches of 20 [m] span at 400 [°C]

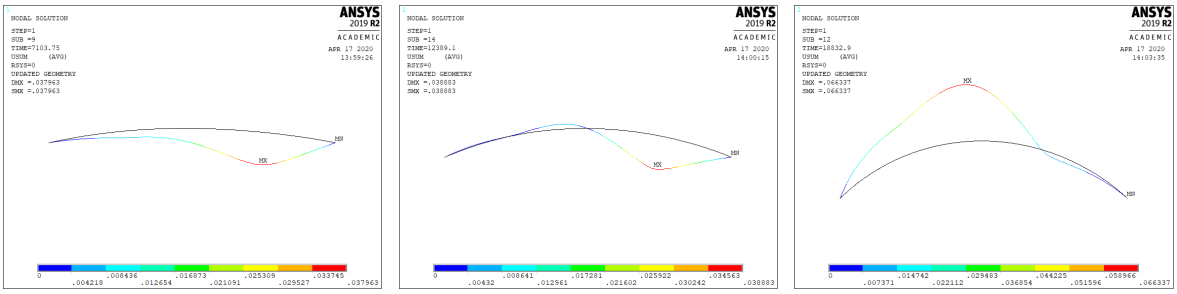

(a) f/L=0,05 (b) f/L=0,10 (c) f/L=0,20

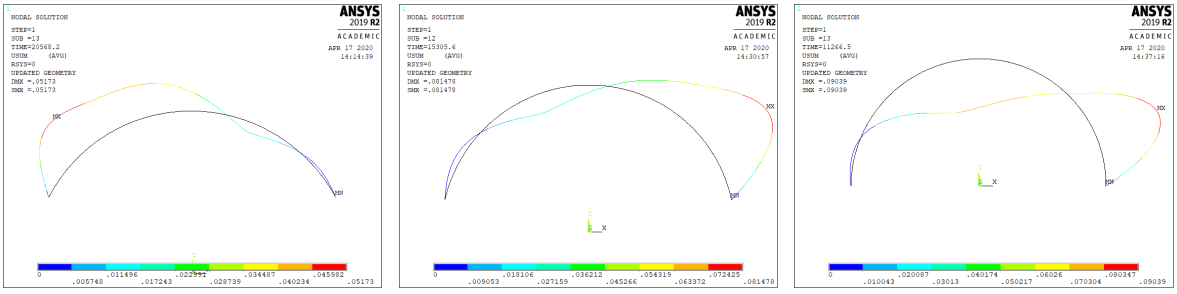

(d) f/L=0,30 (e) f/L=0,40 (f) f/L=0,50

Figure B.25: Collapse mode of S275 pinned arches of 5 [m] span at 600 [°C]

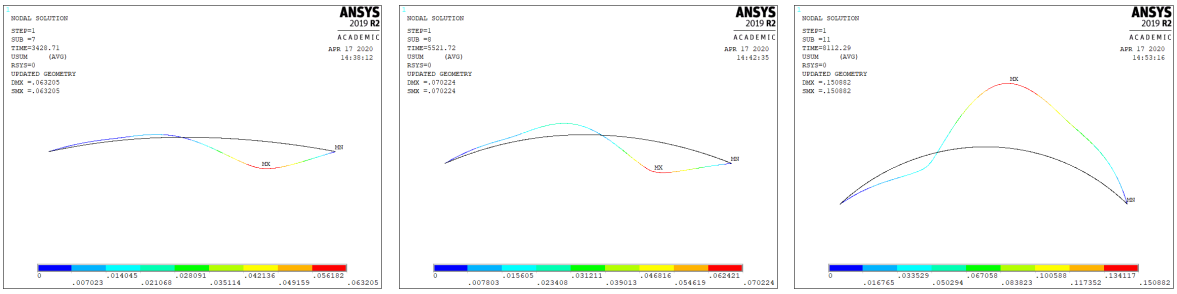

(a) f/L=0,05 (b) f/L=0,10 (c) f/L=0,20

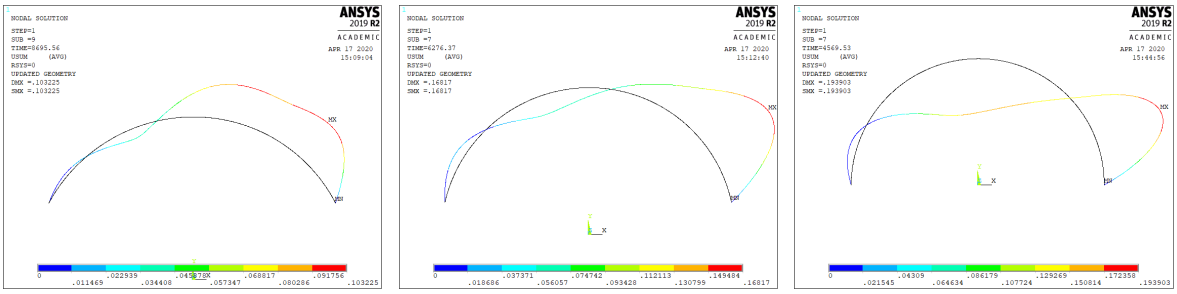

(d) f/L=0,30 (e) f/L=0,40 (f) f/L=0,50

Figure B.26: Collapse mode of S275 pinned arches of 10 [m] span at 600 [°C]

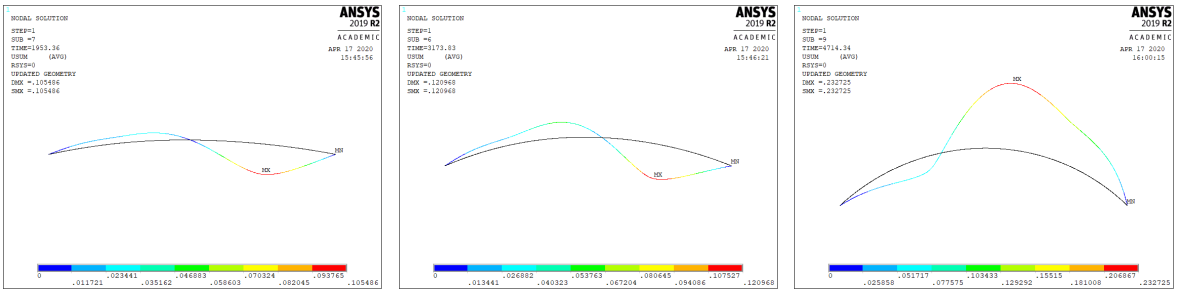

(a) f/L=0,05 (b) f/L=0,10 (c) f/L=0,20

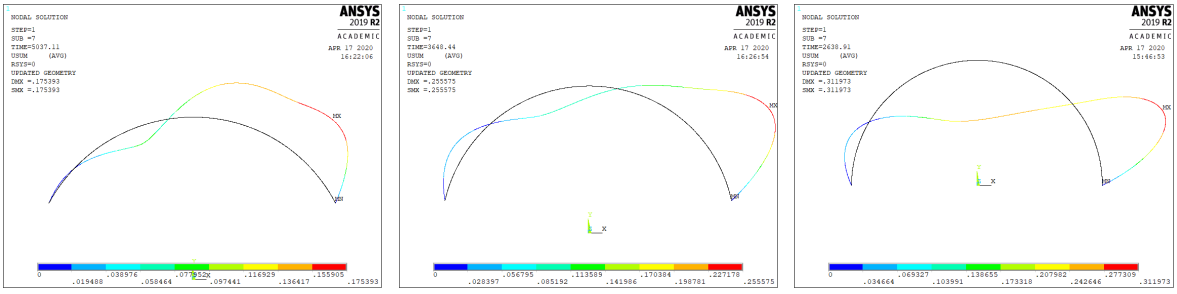

(d) f/L=0,30 (e) f/L=0,40 (f) f/L=0,50

Figure B.27: Collapse mode of S275 pinned arches of 15 [m] span at 600 [°C]

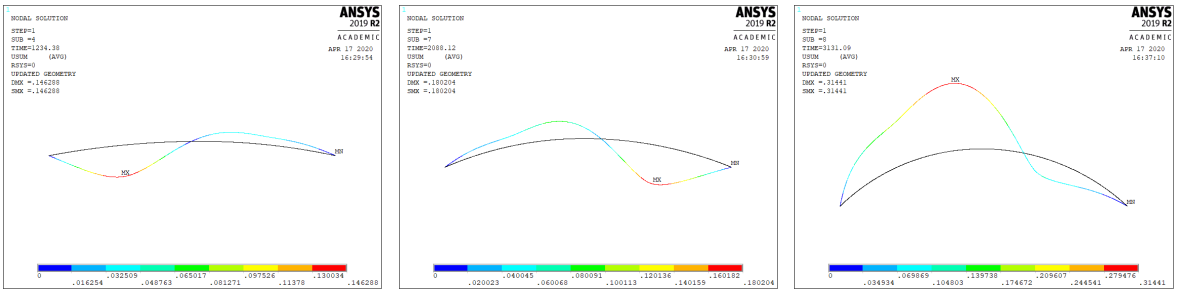

(a) f/L=0,05 (b) f/L=0,10 (c) f/L=0,20

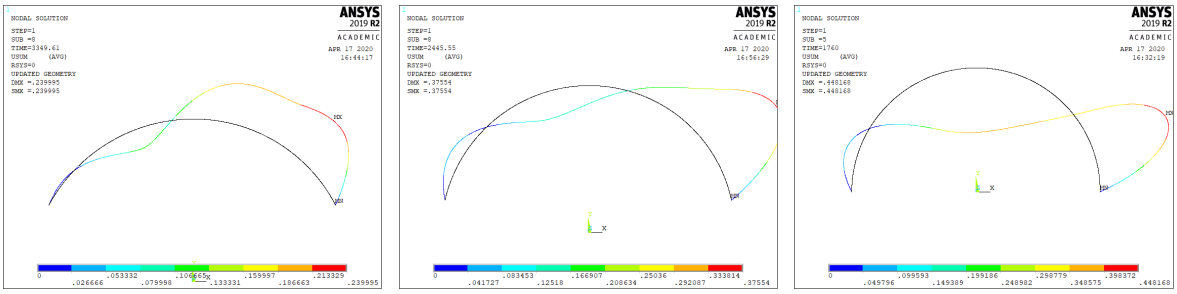

(d) f/L=0,30 (e) f/L=0,40 (f) f/L=0,50

Figure B.28: Collapse mode of S275 pinned arches of 20 [m] span at 600 [°C]

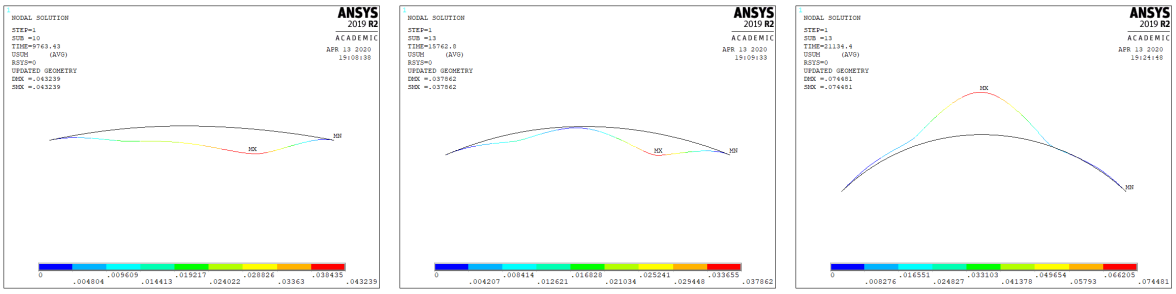

(a) f/L=0,05 (b) f/L=0,10 (c) f/L=0,20

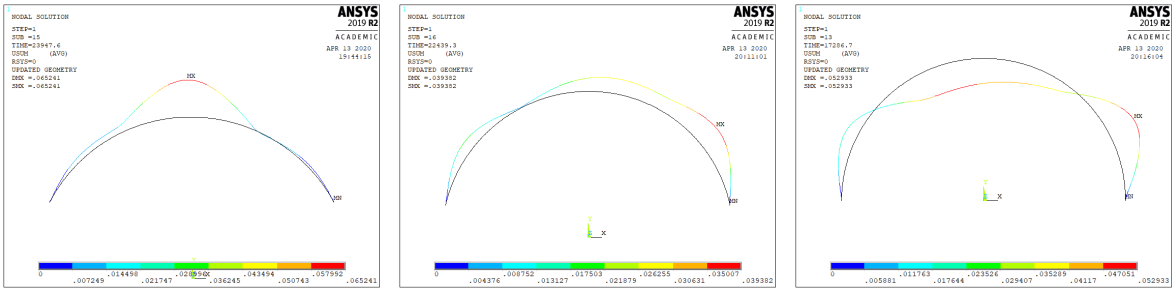

(d) f/L=0,30 (e) f/L=0,40 (f) f/L=0,50

Figure B.29: Collapse mode of S275 fixed arches of 5 [m] span at 600 [°C]

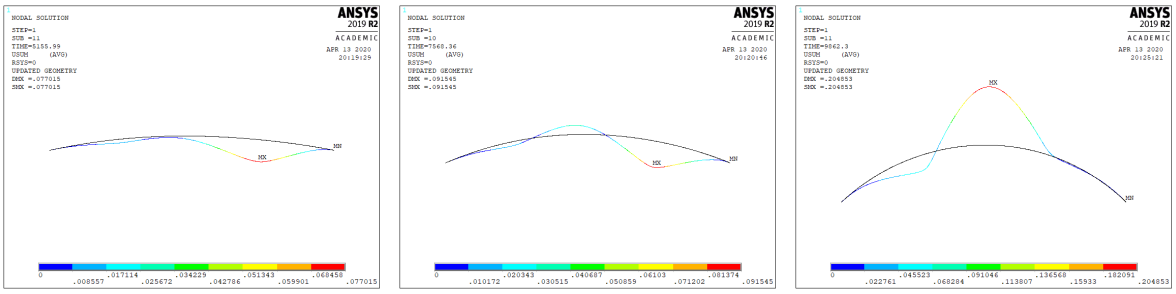

(a) f/L=0,05 (b) f/L=0,10 (c) f/L=0,20

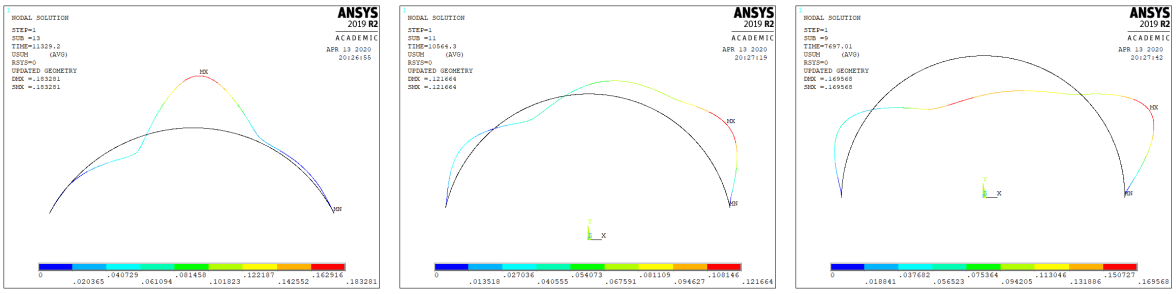

(d) f/L=0,30 (e) f/L=0,40 (f) f/L=0,50

Figure B.30: Collapse mode of S275 fixed arches of 10 [m] span at 600 [°C]

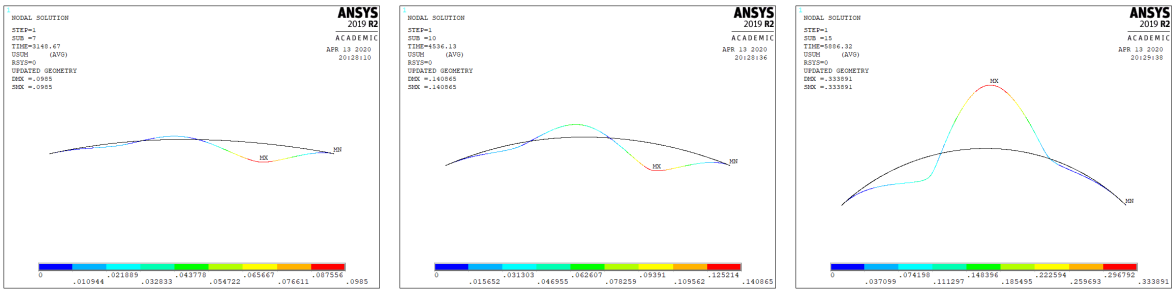

(a) f/L=0,05 (b) f/L=0,10 (c) f/L=0,20

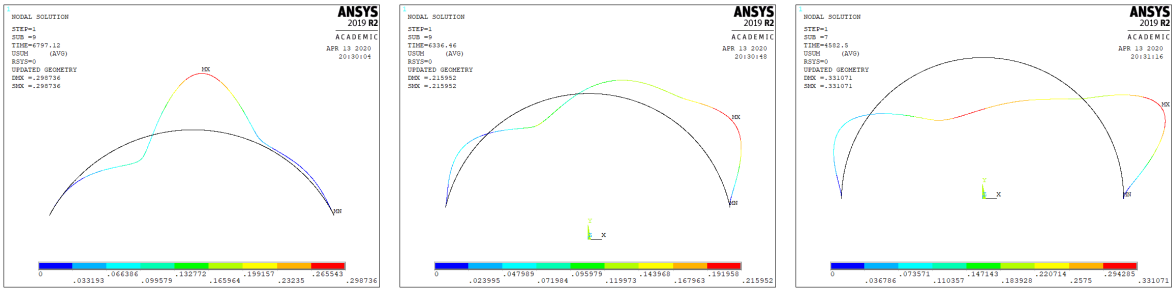

(d) f/L=0,30 (e) f/L=0,40 (f) f/L=0,50

Figure B.31: Collapse mode of S275 fixed arches of 15 [m] span at 600 [°C]

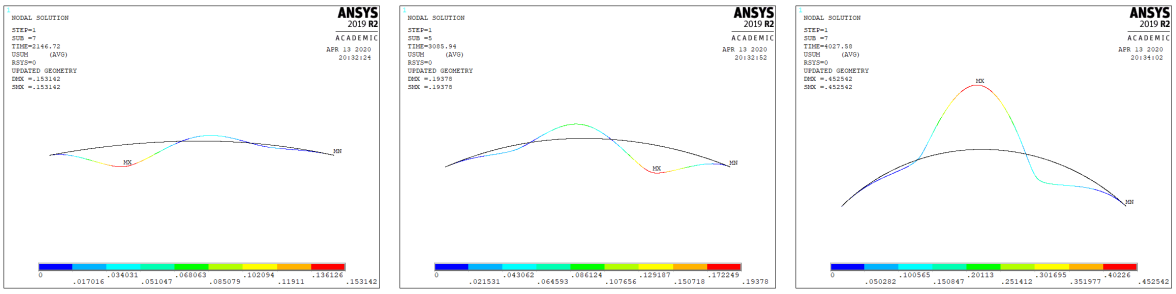

(a) f/L=0,05 (b) f/L=0,10 (c) f/L=0,20

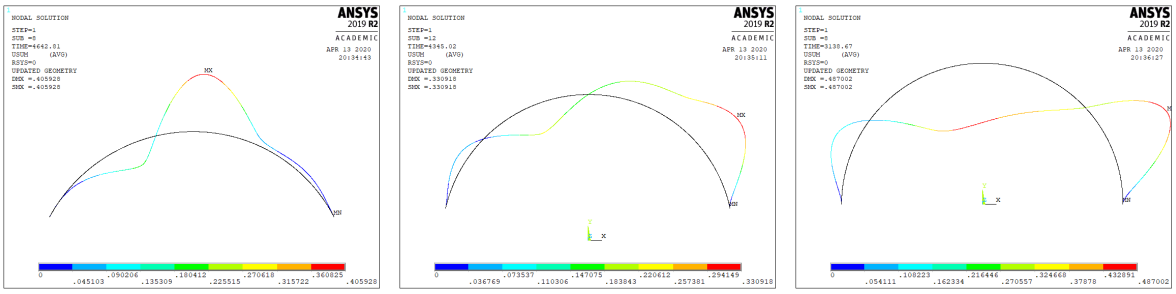

(d) f/L=0,30 (e) f/L=0,40 (f) f/L=0,50

Figure B.32: Collapse mode of S275 fixed arches of 20 [m] span at 600 [°C]

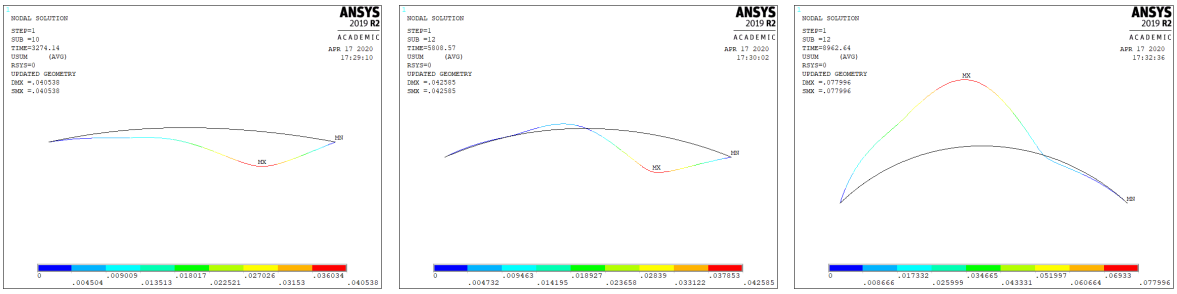

(a) f/L=0,05 (b) f/L=0,10 (c) f/L=0,20

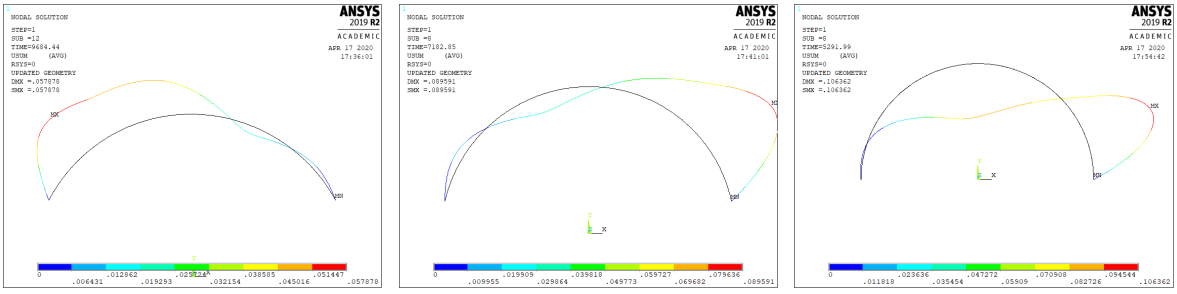

(d) f/L=0,30 (e) f/L=0,40 (f) f/L=0,50

Figure B.33: Collapse mode of S275 pinned arches of 5 [m] span at 700 [°C]

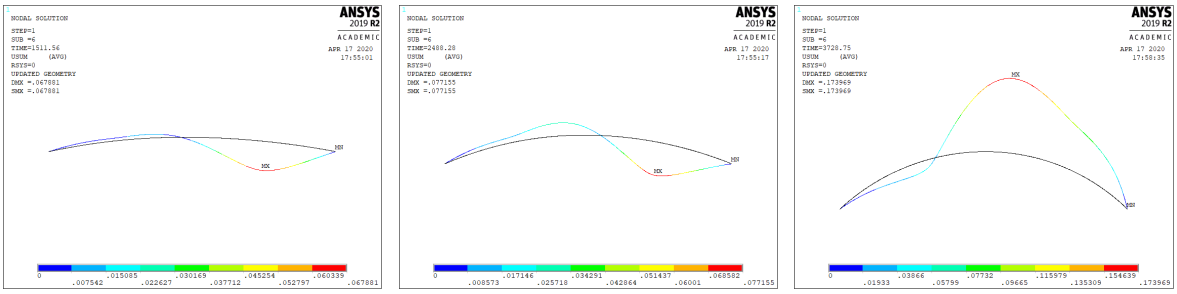

(a) f/L=0,05 (b) f/L=0,10 (c) f/L=0,20

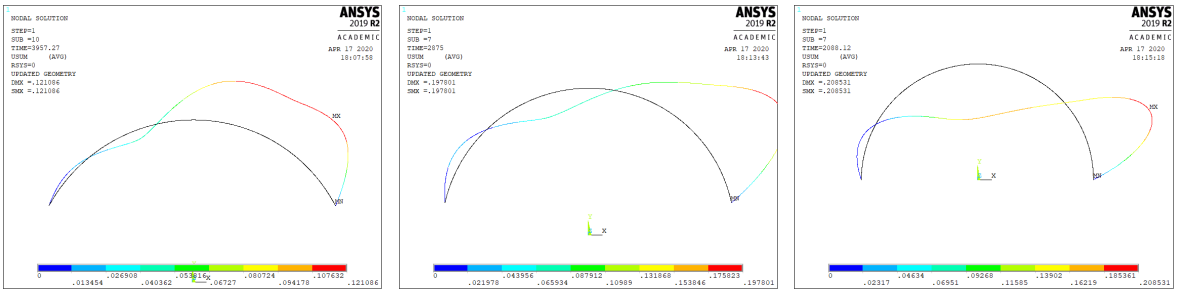

(d) f/L=0,30 (e) f/L=0,40 (f) f/L=0,50

Figure B.34: Collapse mode of S275 pinned arches of 10 [m] span at 700 [°C]

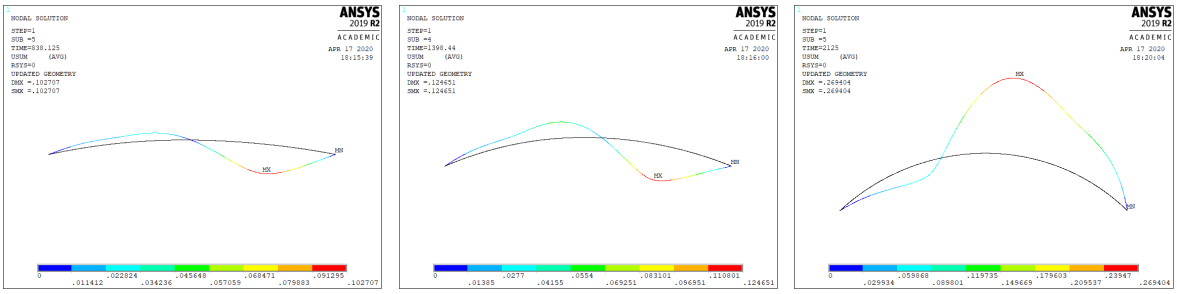

(a) f/L=0,05 (b) f/L=0,10 (c) f/L=0,20

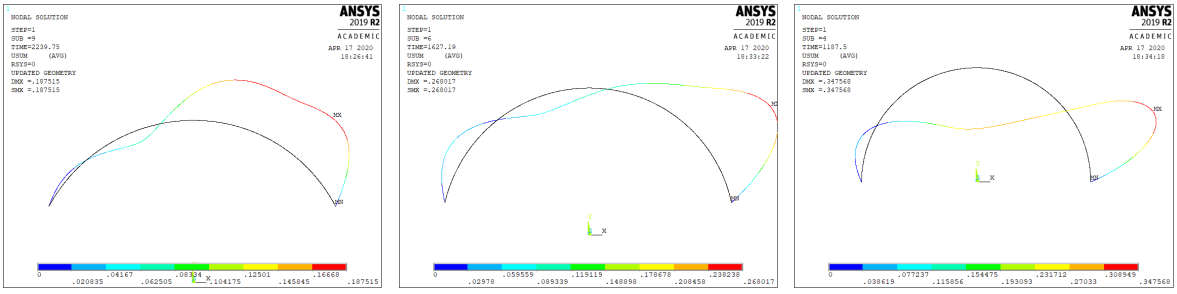

(d) f/L=0,30 (e) f/L=0,40 (f) f/L=0,50

Figure B.35: Collapse mode of S275 pinned arches of 15 [m] span at 700 [°C]

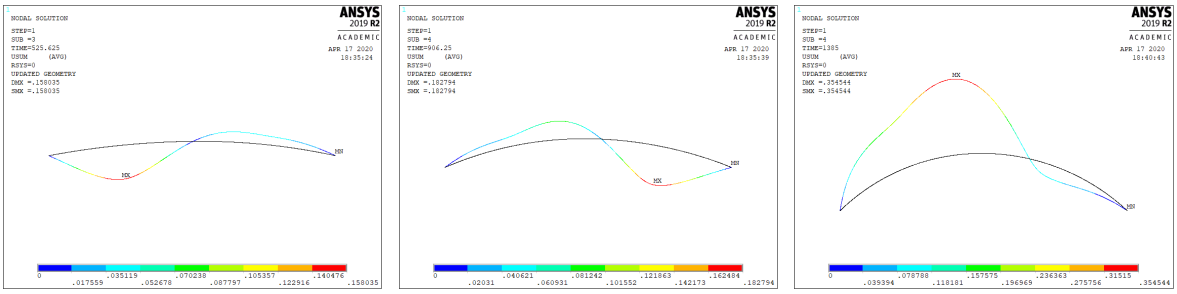

(a) f/L=0,05 (b) f/L=0,10 (c) f/L=0,20

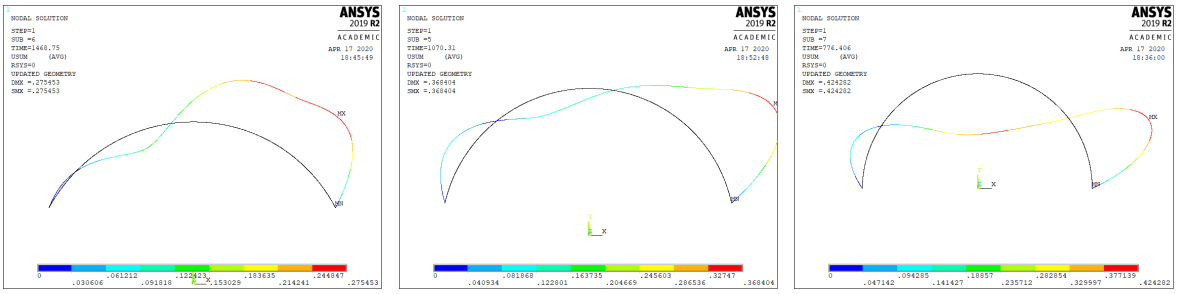

(d) f/L=0,30 (e) f/L=0,40 (f) f/L=0,50

Figure B.36: Collapse mode of S275 pinned arches of 20 [m] span at 700 [°C]

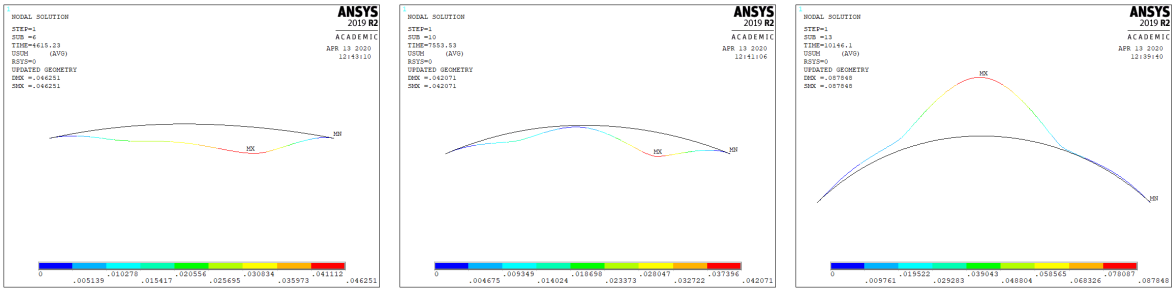

(a) f/L=0,05 (b) f/L=0,10 (c) f/L=0,20

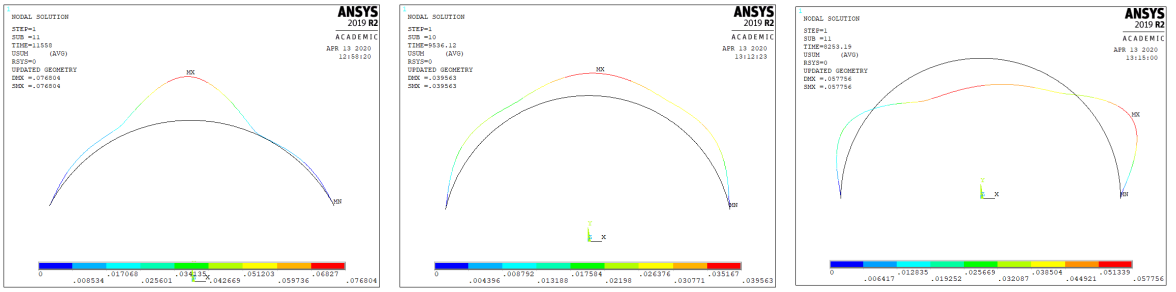

(d) f/L=0,30 (e) f/L=0,40 (f) f/L=0,50

Figure B.37: Collapse mode of S275 fixed arches of 5 [m] span at 700 [°C]

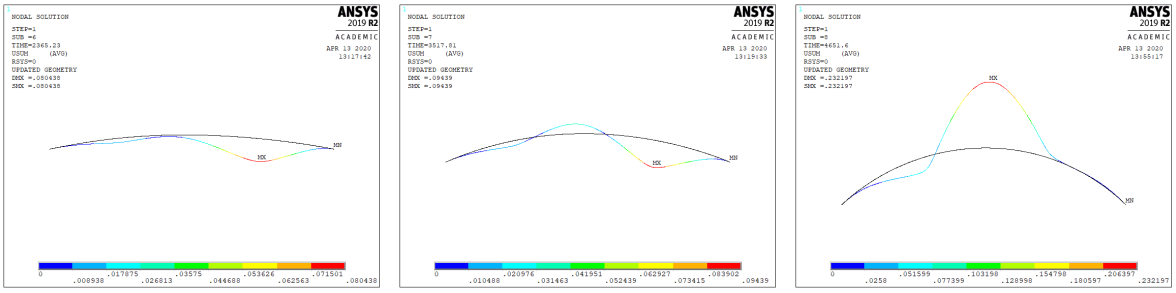

(a) f/L=0,05 (b) f/L=0,10 (c) f/L=0,20

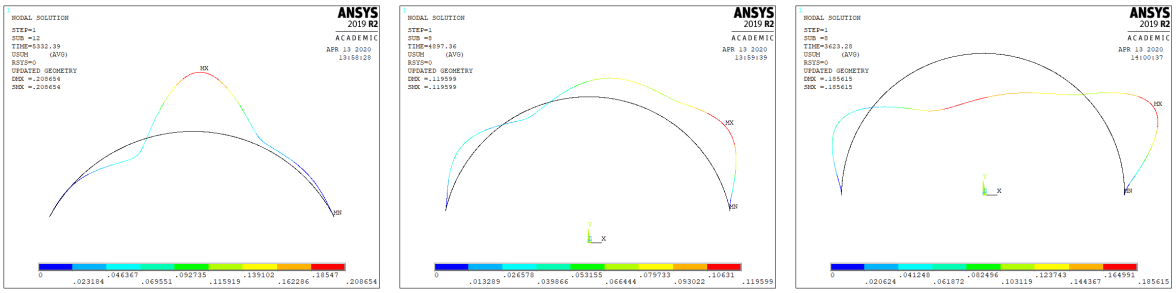

(d) f/L=0,30 (e) f/L=0,40 (f) f/L=0,50

Figure B.38: Collapse mode of S275 fixed arches of 10 [m] span at 700 [°C]

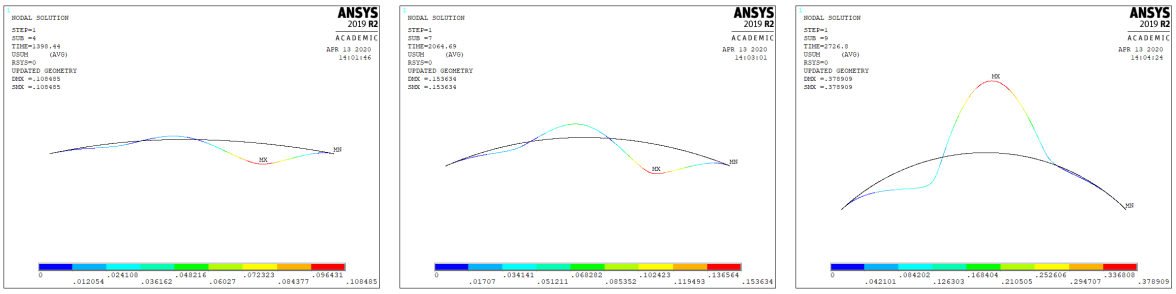

(a) f/L=0,05 (b) f/L=0,10 (c) f/L=0,20

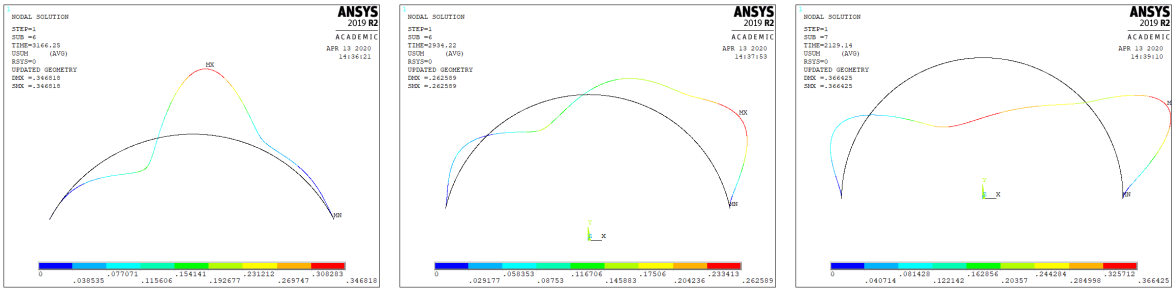

(d) f/L=0,30 (e) f/L=0,40 (f) f/L=0,50

Figure B.39: Collapse mode of S275 fixed arches of 15 [m] span at 700 [°C]

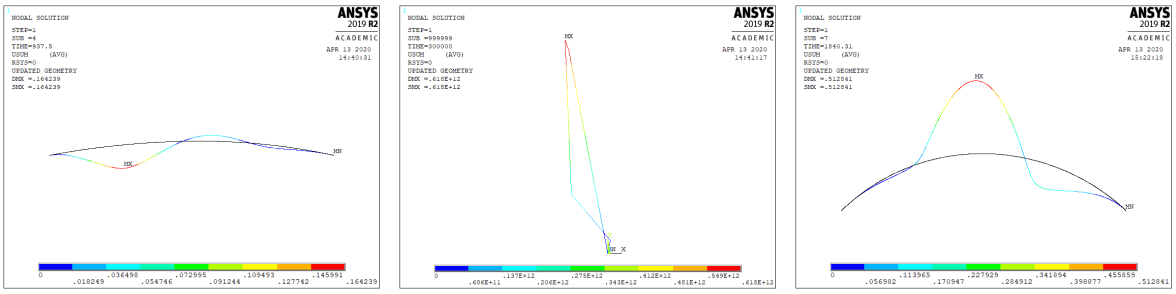

(a) f/L=0,05 (b) f/L=0,10 (c) f/L=0,20

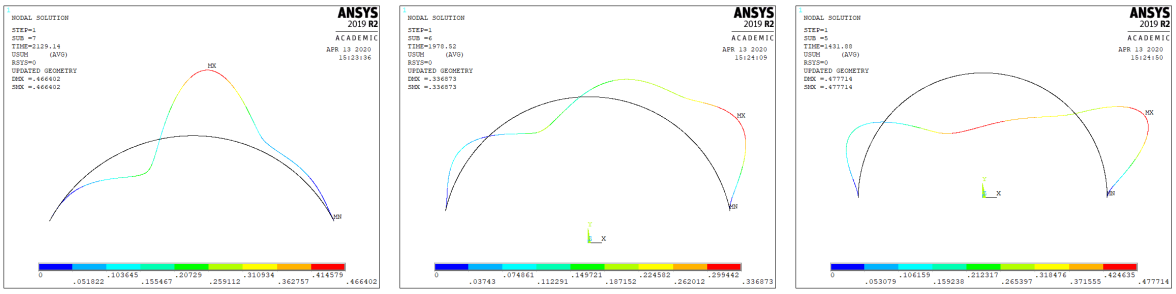

(d) f/L=0,30 (e) f/L=0,40 (f) f/L=0,50

Figure B.40: Collapse mode of S275 fixed arches of 20 [m] span at 700 [°C]

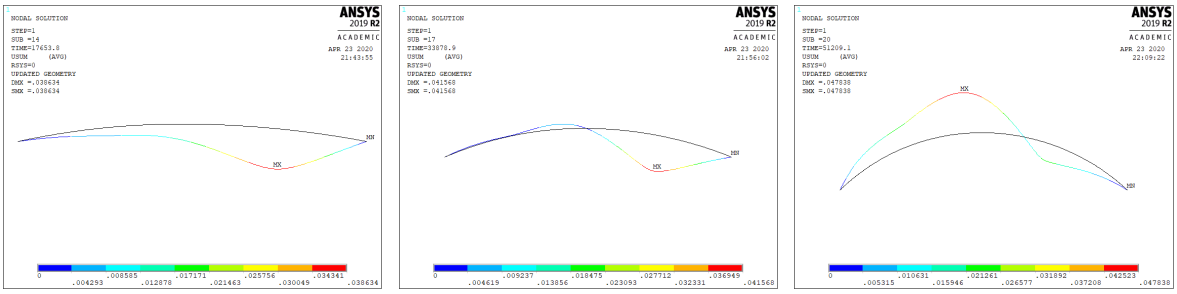

(a) f/L=0,05 (b) f/L=0,10 (c) f/L=0,20

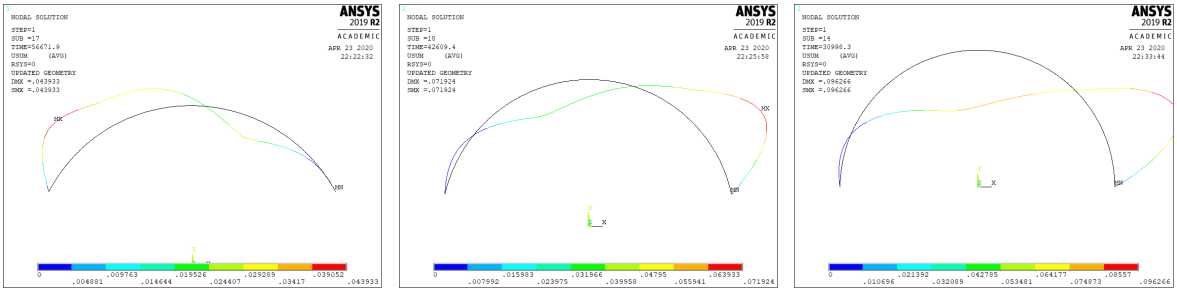

(d) f/L=0,30 (e) f/L=0,40 (f) f/L=0,50

Figure B.41: Collapse mode of S355 pinned arches of 5 [m] span at 400 [°C]

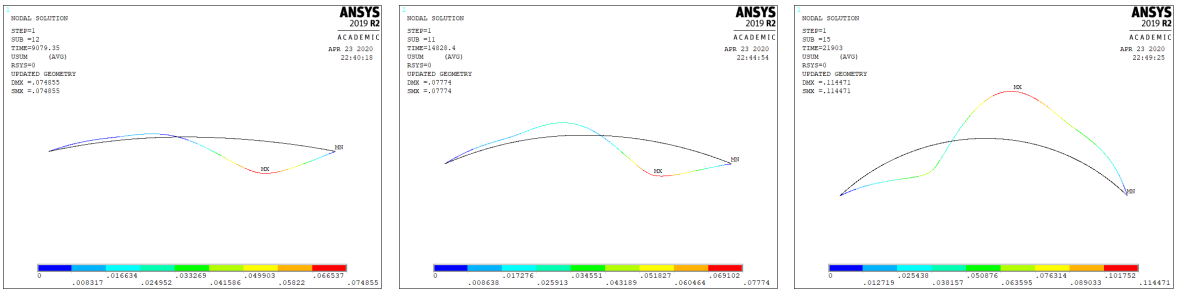

(a) f/L=0,05 (b) f/L=0,10 (c) f/L=0,20

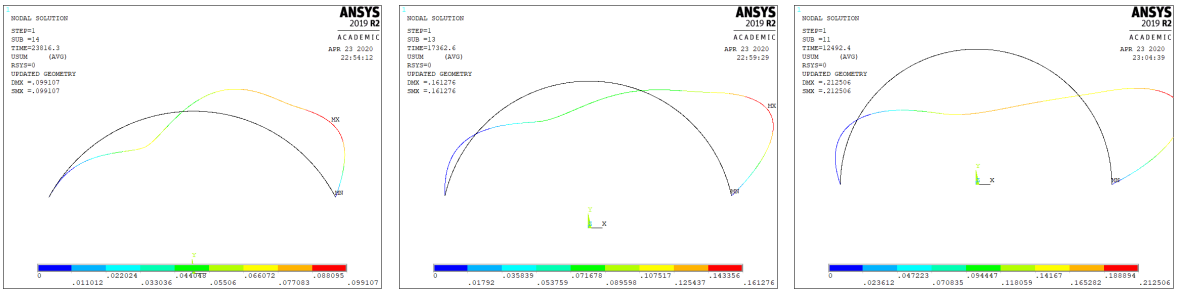

(d) f/L=0,30 (e) f/L=0,40 (f) f/L=0,50

Figure B.42: Collapse mode of S355 pinned arches of 10 [m] span at 400 [°C]

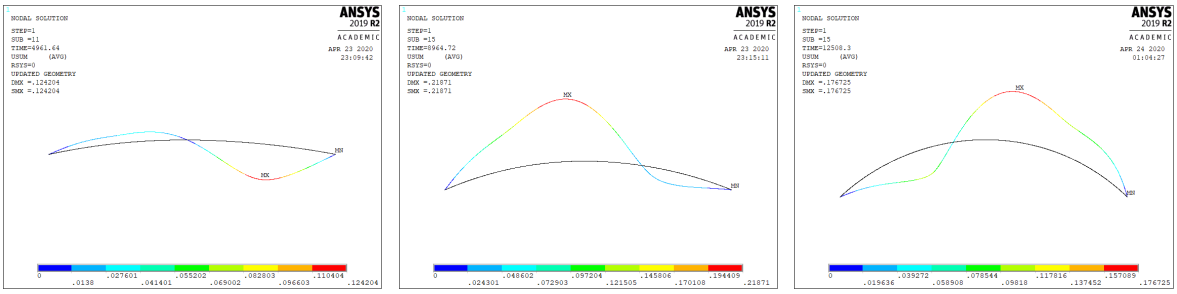

(a) f/L=0,05 (b) f/L=0,10 (c) f/L=0,20

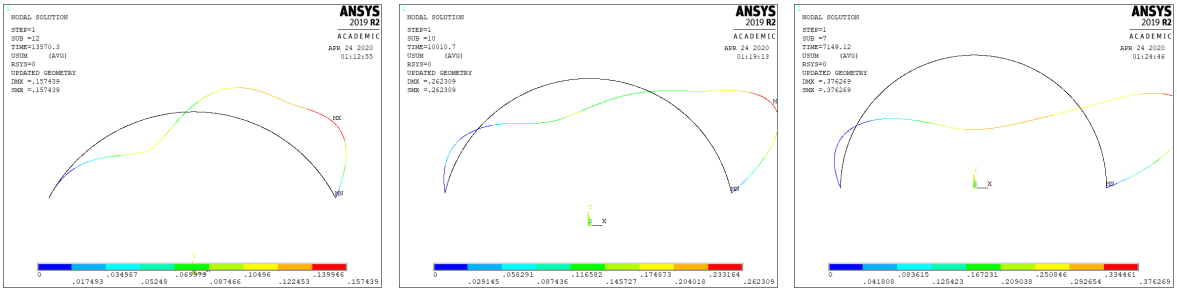

(d) f/L=0,30 (e) f/L=0,40 (f) f/L=0,50

Figure B.43: Collapse mode of S355 pinned arches of 15 [m] span at 400 [°C]

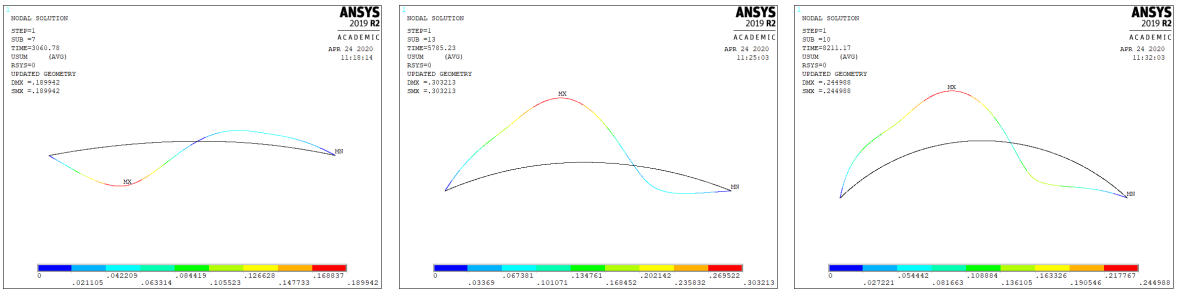

(a) f/L=0,05 (b) f/L=0,10 (c) f/L=0,20

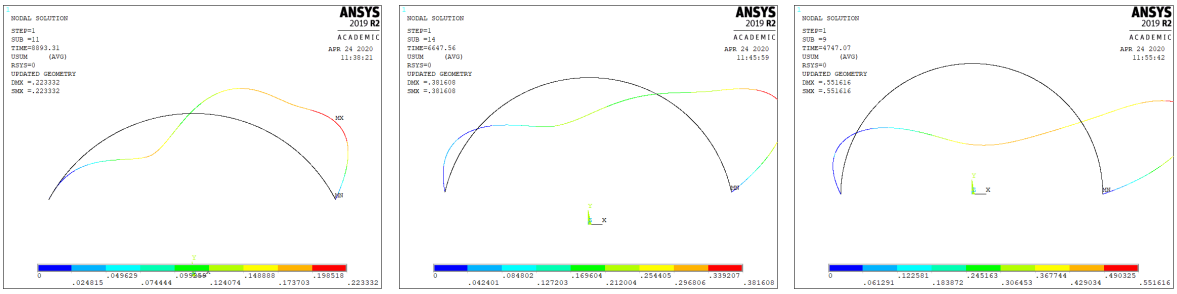

(d) f/L=0,30 (e) f/L=0,40 (f) f/L=0,50

Figure B.44: Collapse mode of S355 pinned arches of 20 [m] span at 400 [°C]

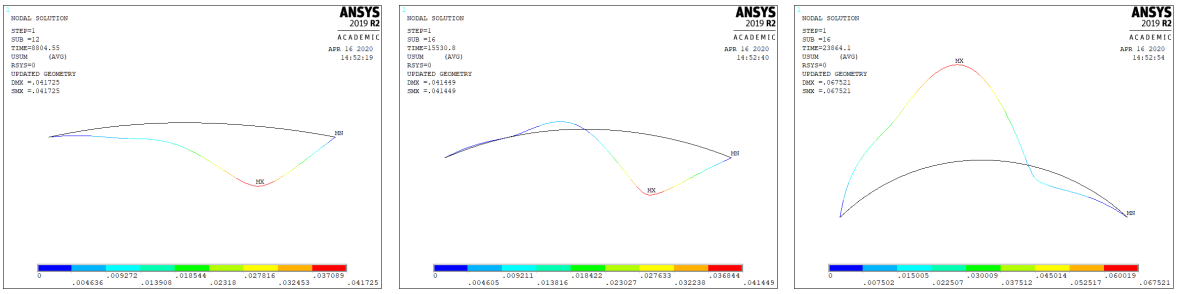

(a) f/L=0,05 (b) f/L=0,10 (c) f/L=0,20

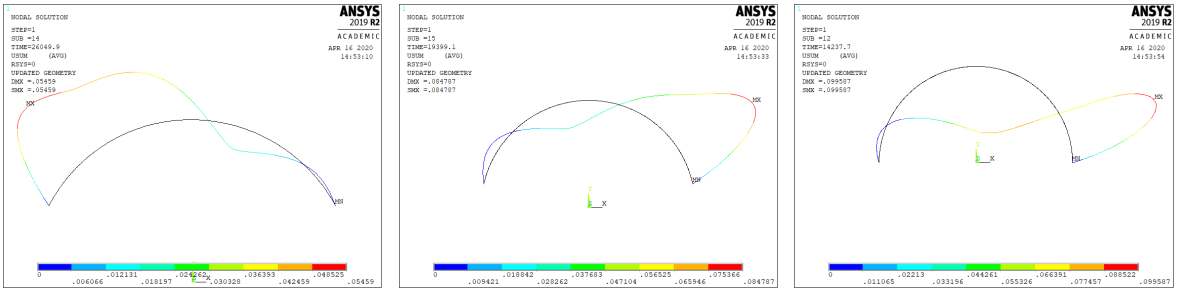

(d) f/L=0,30 (e) f/L=0,40 (f) f/L=0,50

Figure B.45: Collapse mode of S355 pinned arches of 5 [m] span at 600 [°C]

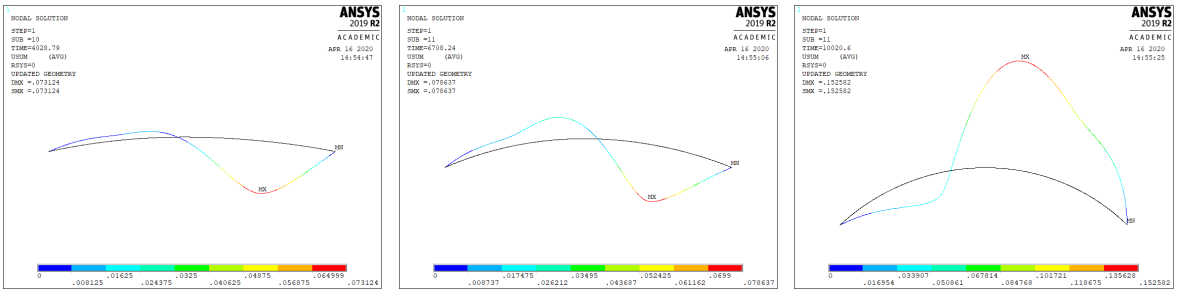

(a) f/L=0,05 (b) f/L=0,10 (c) f/L=0,20

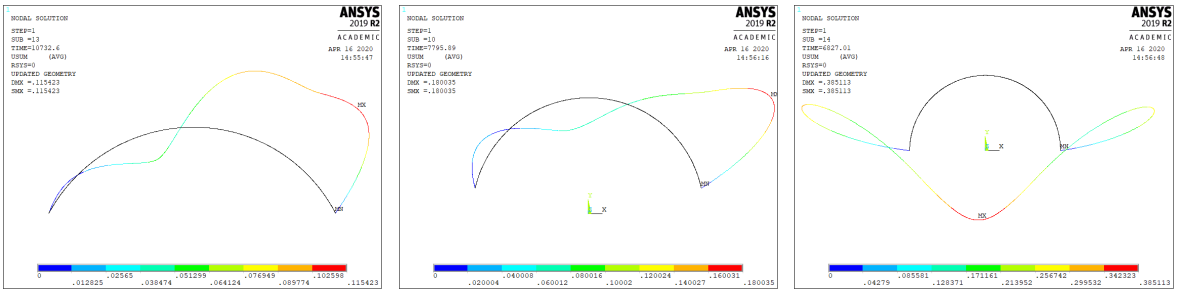

(d) f/L=0,30 (e) f/L=0,40 (f) f/L=0,50

Figure B.46: Collapse mode of S355 pinned arches of 10 [m] span at 600 [°C]

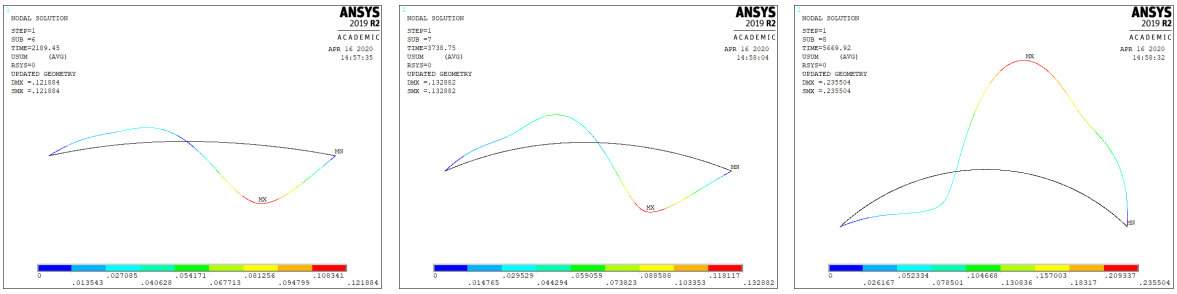

(a) f/L=0,05 (b) f/L=0,10 (c) f/L=0,20

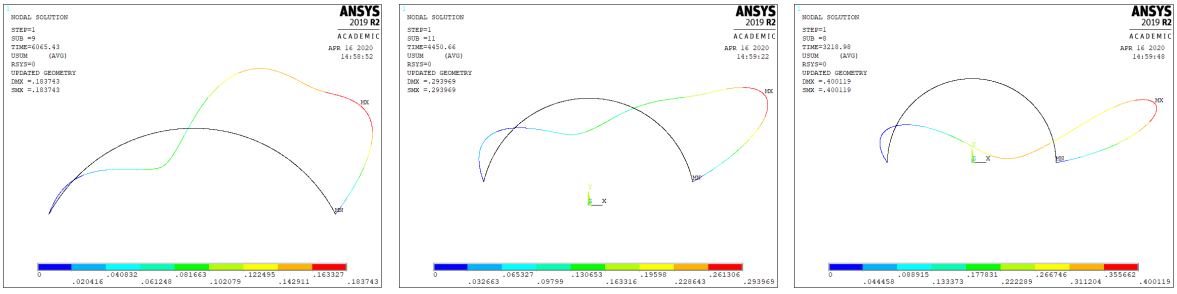

(d) f/L=0,30 (e) f/L=0,40 (f) f/L=0,50

Figure B.47: Collapse mode of S355 pinned arches of 15 [m] span at 600 [°C]

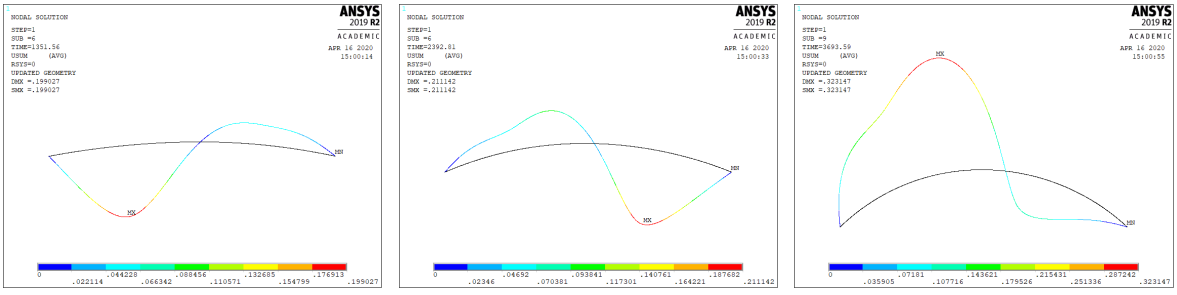

(a) f/L=0,05 (b) f/L=0,10 (c) f/L=0,20

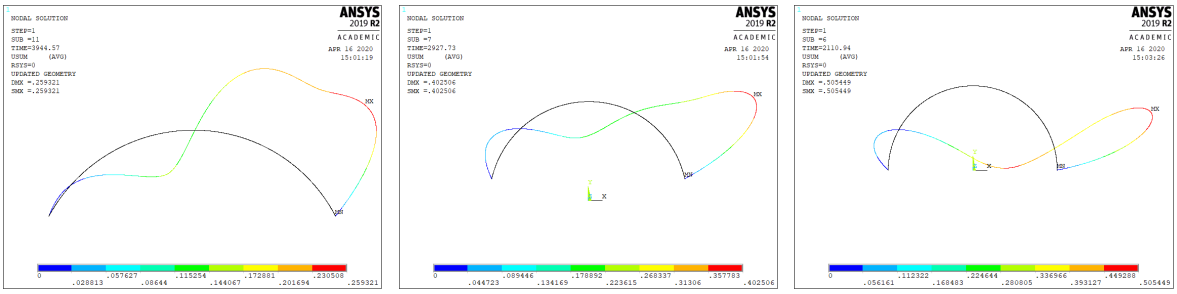

(d) f/L=0,30 (e) f/L=0,40 (f) f/L=0,50

Figure B.48: Collapse mode of S355 pinned arches of 20 [m] span at 600 [°C]

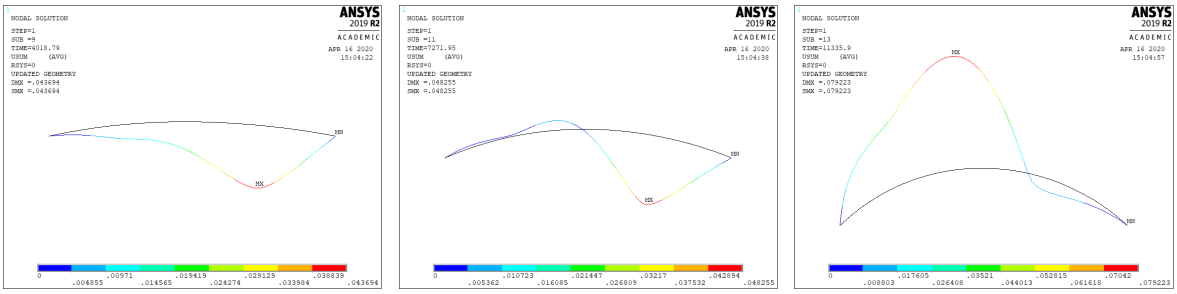

(a) f/L=0,05 (b) f/L=0,10 (c) f/L=0,20

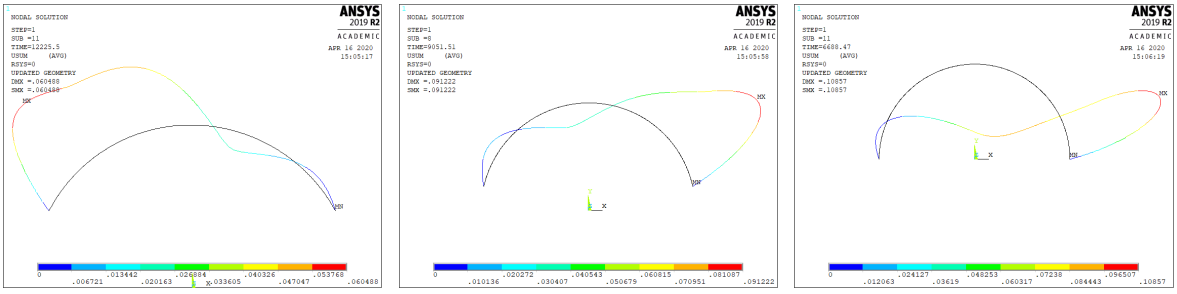

(d) f/L=0,30 (e) f/L=0,40 (f) f/L=0,50

Figure B.49: Collapse mode of S355 pinned arches of 5 [m] span at 700 [°C]

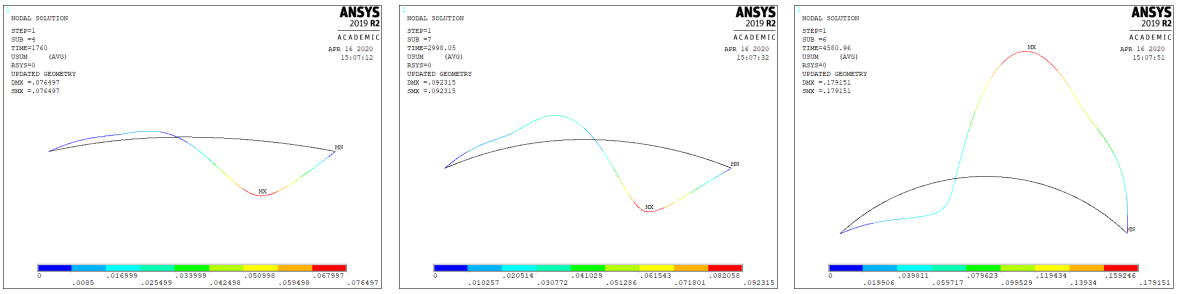

(a) f/L=0,05 (b) f/L=0,10 (c) f/L=0,20

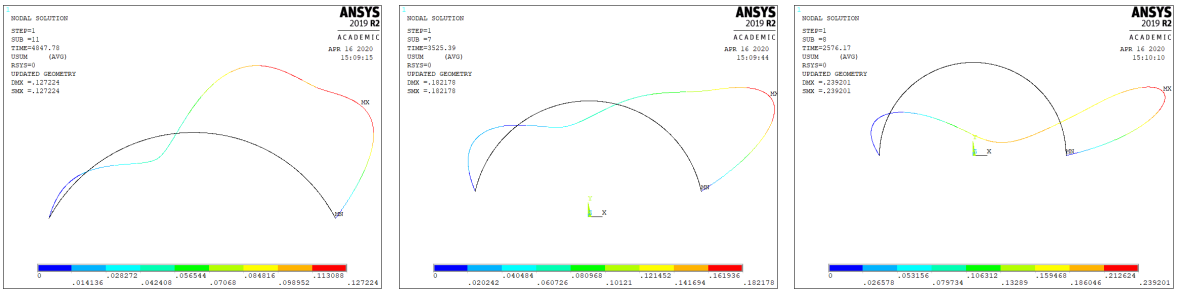

(d) f/L=0,30 (e) f/L=0,40 (f) f/L=0,50

Figure B.50: Collapse mode of S355 pinned arches of 10 [m] span at 700 [°C]

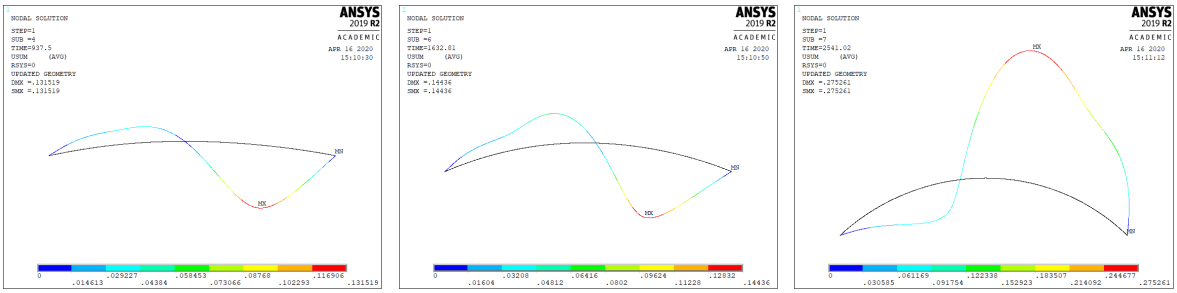

(a) f/L=0,05 (b) f/L=0,10 (c) f/L=0,20

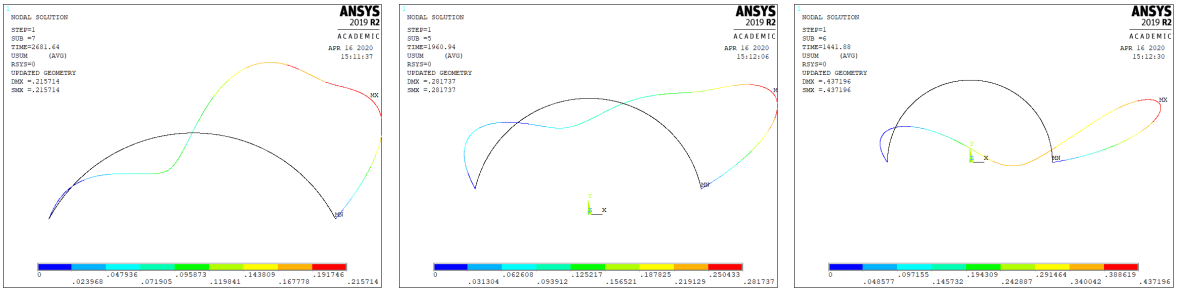

(d) f/L=0,30 (e) f/L=0,40 (f) f/L=0,50

Figure B.51: Collapse mode of S355 pinned arches of 15 [m] span at 700 [°C]

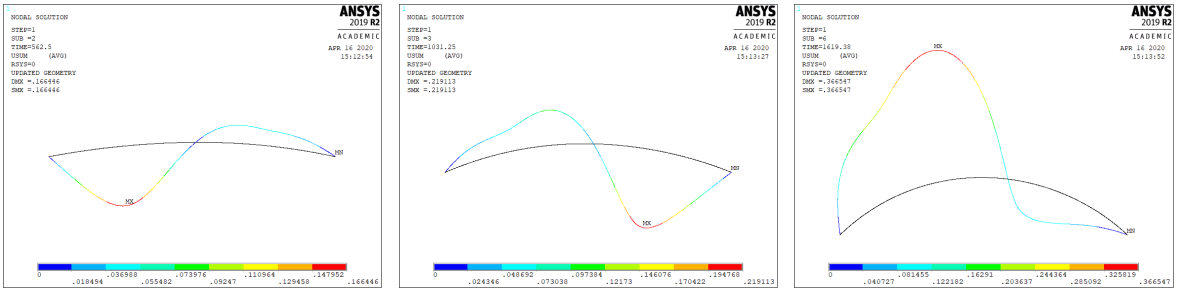

(a) f/L=0,05 (b) f/L=0,10 (c) f/L=0,20

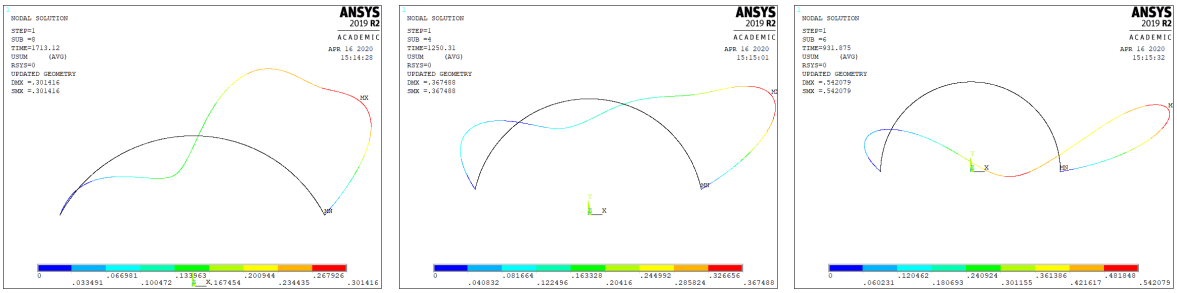

(d) f/L=0,30 (e) f/L=0,40 (f) f/L=0,50

Figure B.52: Collapse mode of S355 pinned arches of 20 [m] span at 700 [°C]

Appendix C

ANSYS Mechanical APDL solution routines

```
/CLEAR,NOSTART  ! Clear model since no SAVE found
*GET, JOBN, ACTIVE, 0, JOBNAM,  ,  ,! This gets the ANSYS jobname
WPSTYLE,,,,,,,,0
! General geometry
! Input Data (Span and rise-to-span ratio)
*SET,L,L ! span (5, 10, 15 and 20)
*SET,f,f/L ! rise (0,05 to 0,50)
! Calculated Data
*SET,L1,0.25*L ! load position
*SET,R,((L/2)**2+f**2)/(2*f)    ! radius
*SET,alpha,asin((L/2)/R)    ! half internal angle
*SET,theta1,asin(L1/R) ! load position angle
/PREP7
! Element type, material and section properties
ET,1,BEAM189
MPTEMP,,,,,,,,
```

```
MPTEMP,1,0
MPDATA,EX,1,,210e9
MPDATA,PRXY,1,,0.3
SECTYPE,  1, BEAM, I, IPE100, 3
SECOFFSET, CENT
SECDATA,0.055,0.055,0.1,0.0057,0.0057,0.0041,0,0,0,0,0,0
! Keypoints
K,1,0,0,0,
K,2,L/2,R-f,0,
K,3,L1,R*cos(theta1),0,
K,4,-L1,R*cos(theta1),0,
K,5,-L/2,R-f,0,
! Create arcs from keypoints
LARC,2,3,1,R,
LARC,3,4,1,R,
LARC,4,5,1,R,
! Meshing of arc lines
LSEL,ALL
LATT,1, ,1, ,0, ,1
LESIZE,all,0.02, , , , , , ,1
LMESH,all
! Support conditions and restraints
DK,2, ,0, ,0,UX,UY,UZ,ROTX,ROTY,ROTZ,  ! if pinned, ROTZ is removed
DK,5, ,0, ,0,UX,UY,UZ,ROTX,ROTY,ROTZ,  ! if pinned, ROTZ is removed
D,ALL, ,0, , , ,UZ,ROTX, , , ,! only in-plane buckling
! Apply forces on keypoints
FK,3,FY,-force
FK,4,FY,-force
! Static pre-buckling analysis
```

```
/SOL
ANTYPE,0
SOLVE
FINISH
/POST1
/EFACET,1
/RGB,INDEX,100,100,100, 0
/RGB,INDEX, 80, 80, 80,13
/RGB,INDEX, 60, 60, 60,14
/RGB,INDEX, 0, 0, 0,15
/DSCALE,ALL,AUTO     !PLOT SCALE
PLNSOL, U,SUM, 1,1.0
/IMAGE,SAVE,desl_estatica,png
FINISH
! Eigenvalue buckling analysis
/SOLU
ANTYPE,1
BUCOPT,LANB,5,0,0,CENTER
MXPAND,5,0,100e100,1,0.001,
SOLVE
! Postprocessing and results
/POST1
SET,,, ,,, ,1
PLNSOL, U,SUM, 1,1.0
/IMAGE,SAVE,modo1,png
!!!!!!!!!!!!!!!!!!!!!!!!!!!!!!!!!!!!!!!!!!!!!!!!!!!!!!!!
! Nonlinear solutions at natural temperature
! Material nonlinearities – S275 steel
TB,MISO,1,1,2,0
```

```
TBTEMP,0
TBPT,,1.3095e-3,275e6
TBPT,,0.15,278.15e6
! Update geometry
/PREP7
UPGEOM,f_imp,1,1,results_file,'rst','□'
! Load Table
*DIM,LOAD,TABLE,2,1,1,  ,  ,
!*
*SET,LOAD(1,0,1)  ,  0
*SET,LOAD(1,1,1)  ,  -1
*SET,LOAD(2,0,1)  ,  300000
*SET,LOAD(2,1,1)  ,  -300000
! Solution phase
FINISH
/SOL
ANTYPE,0
NLGEOM,1
DELTIM,500,10,10000
OUTRES,ERASE
OUTRES,ALL,ALL
NCNV,2,0,0,0,0
TIME,300000
! Apply Load Table
FDELE,ALL  !DELETE ALL NODE FORCES AND APPLY A DISTRIBUTED LOAD
FKDELE,all,ALL
FK,2,FY,  %LOAD%
FK,3,FY,  %LOAD%
!!!!!!!!!!!!!!!!!!!!!!!!!!!!!!!!!!!!!!!!!!!!!!!!!!!!!!!!!!!!!!!!
```

```
! Nonlinear solutions at elevated temperatures
TUNIF,TEMP,
! Material nonlinearities
MPDE,ALL,1
TBDE,ALL,1
MPTEMP,,,,,,,
MAT,1,
MPREAD,'material_file','SI_MPL',' ',LIB
! Deformed shape
/POST1
SET,LAST
SET,PREVIOUS
/DSCALE,ALL,15
/EFACET,1
PLNSOL, U,SUM, 1,1.0
concat='%JOBN%_%L%_s275_f'
/IMAGE,SAVE,concat,png
! Displacements
KSEL,S, , , 3
NSLK,S
*GET, FixNode,NODE,,NUM,MIN
*get,my_nsets,ACTIVE,,SET,NSET
*dim,slist,array,my_nsets,3
SET,,, ,,, ,my_nsets-1
*do,iset,1,my_nsets
set,,,,,,,iset
*GET,slist(iset,1), ACTIVE, 0, set, Time
*get,slist(iset,2),NODE,FixNode,U,x     ! horizontal DISP
*get,slist(iset,3),NODE,FixNode,U,y     ! vertical DISP
```

```
*enddo
*CREATE, ansuitmp
! to save the table slist IN THE FILE.csv
*cfopen,JOBN,csv ! ou extensão csv
*vwrite,'Load', 'X_disp', 'Y_disp'
(A8,,A8,,A8,,A8)
*do,iset,1, 1
*vwrite,slist(iset,1,1),slist(iset,2,1),slist(iset,3,1)
(F15.2,'□',F15.7,'□',F15.7,'□',F15.7)
*enddo
*cfclose
*END
/INPUT,ansuitmp
finish
```